Noise in coupled VECSEL array

Sopfy Karuseichyk

Doctoral Thesis
Sorbone Université

presented by

Sopfy Karuseichyk

pour obtenir le grade de Docteur de Sorbonne Université
sur le sujet:

Noise in coupled VECSEL array

Membres du jury :

Pr. Masimo Guidici	Rapporteur
Pr. Frederic Griliot	Rapporteur
Dr. Ghaya Baili	Examinatrice
Pr. Valia Voliotis	Président du jury
Pr. Fabien BRETENAKER	Examinateur
Pr. Nicolas TREPS	Membre invité

Dedicated to the people who have profoundly influenced my journey — those who are by my side now, and to those who left us too soon.

Abstract

Laser arrays are key components in many areas of science, technology, and civilian applications today. A remarkably new domain of application of laser arrays is the laser solver, which allows to parallelize the computation process spatially. For such applications a low noise array with identical laser's characteristics is required. At the same time, most of the listed applications require a coupling mechanism for the array. Most commonly, solid-state lasers are used today for such applications.

However, in this work we present a new type of laser array based on the VECSEL (Vertical External Cavity Surface Emitting Lasers) with the intracavity coupling control. Such lasers are well known to be extremely low noise lasers. Their dynamics are a remarkable example of class-A dynamical behavior. Such dynamics is accompanied with the filtering of the transferred pump noise above the cavity cut-off frequency. At the same time the VECSEL is a semiconductor laser, which has distinguishing peculiarities, when compared with the solid-state laser. For example, it has a non-negligible Henry factor. Dynamics of such phase-locked VECSEL arrays have not been studied yet.

This laser is developed with a planar spatially degenerate cavity. Thanks to cavity degeneracy we transform a multimode VECSEL into an array of independent lasers with a designed loss mask. Thanks to the method of array development with a mask, we gain control on the coupling between lasers by the diffraction on the mask. The coupling is determined by the diffraction on the edges of the mask holes and consequent reflection on the output cavity mirror. Reflected field of each laser is injected to the neighboring holes. The coupling coefficient is complex. We numerically quantify it and then develop several models for the laser array dynamics description with considered complexity of the coupling coefficient. Each model characterizes one of the investigated mask topologies. Changes of the mask position were shown experimentally to change the coupling between lasers from zero to values large enough to phase-lock the laser array. We performed a noise measurement both for the unlocked and phase-locked solutions. The measured relative intensity noise spectra of individual lasers confirmed the class-A dynamics of the developed VECSEL array. Based on the cross-correlation on the noises of different lasers we discovered a clear correlation between phase-locking and a noises spectral correlation. Then, we could reproduce numerically and analytically the same results based on the models we developed.

A particular interest of the project was situated on a ring laser array. Such arrays are known for their discrete series for the phase-difference solutions when phase-locked. We studied such solutions in our system. Each of them, except for the in-phase phase-locking, corresponds to a vortex with discrete phase increment between lasers. Since good quality vortices are extremely needed for particle micromotoring, information transfer, etc. we deeply studied such solutions in our system. We studied the limitations dictated by the Henry factor and derived a general analytical criterion

for the existence of such solutions. We studied asymmetric vortex generation with non-uniform loss masks.

Additionally, we studied theoretically the influence of optical feedback on the phase-locking in such a vortex. The noise model of such an array was experimentally confirmed with three lasers. Based on the model we found a simple method of the determination of the vortex sign (direction of the phase accumulation) based on the laser's noise measurements.

Résumé

Les réseaux de lasers sont des composants clés dans de nombreux domaines de la science, de la technologie et des applications civiles aujourd'hui. Un domaine remarquablement nouveau d'application des réseaux de lasers est le solveur laser, qui permet de paralléliser le processus de calcul spatialement. Pour de telles applications, un réseau de lasers à faible bruit ayant des caractéristiques identiques est nécessaire. En même temps, la plupart des applications répertoriées nécessitent un mécanisme de couplage entre les lasers du réseau. Les lasers à état solide sont les plus couramment utilisés aujourd'hui pour de telles applications.

Cependant, dans ce travail, nous présentons un nouveau type de réseau laser basé sur les VECSEL (Lasers à Émission de Surface à Cavité Externe Verticale) avec un contrôle de couplage intra-cavité. De tels lasers sont bien connus pour être des lasers à très faible bruit. Leurs dynamiques sont un exemple remarquable de comportement dynamique de classe A. Ces dynamiques s'accompagnent d'un filtrage du transfert du bruit de pompage au-dessus de la fréquence de coupure de la cavité. En même temps, le VECSEL est un laser à semi-conducteur, ce qui le distingue des lasers à état solide. Par exemple, il présente un facteur de Henry non négligeable. Les dynamiques de ces réseaux de VECSEL verrouillés en phase n'ont pas encore été étudiées.

Ce laser est développé à partir d'une cavité plan-plan spatialement dégénérée. Grâce à la dégénérescence de la cavité, nous avons transformé un VECSEL multimode en un réseau de lasers indépendants avec un masque de perte spécialement conçu dans ce but. Nous avons atteint un contrôle sur le couplage entre les lasers dû à la diffraction sur le masque. Le couplage est déterminé par la diffraction sur les bords des trous du masque et la réflexion consécutive sur le miroir de sortie de la cavité. Les champs réfléchis de chaque laser sont injectés dans les trous voisins. Ce couplage est complexe. Nous le quantifions numériquement, puis développons plusieurs modèles pour la description de la dynamique du réseau laser en tenant compte de la complexité du coefficient de couplage. Chaque modèle caractérise l'une des topologies de masque étudiées. Nous avons montré expérimentalement que changer la position du masque permet de changer le couplage entre les lasers de zéro à des valeurs suffisantes pour verrouiller en phase le réseau de lasers. Nous avons effectué une mesure du bruit à la fois pour les solutions non verrouillées et verrouillées en phase. Les spectres de bruit relatif en intensité mesurés des lasers individuels ont confirmé la dynamique de classe A du réseau de VECSEL développé. Sur la base de la corrélation croisée des bruits des différents lasers, nous avons découvert une corrélation claire entre le verrouillage en phase et une corrélation spectrale du bruit. Ensuite, nous avons montré numériquement et analytiquement les mêmes phénomènes basés sur les modèles développés.

Un intérêt particulier du projet concernait le réseau laser annulaire. De tels réseaux sont connus pour générer des solutions sous forme de série discrète de différences de phase lorsqu'ils sont verrouillés en phase. Nous avons étudié de telles solutions dans notre système. Chacune d'elles, à l'exception du verrouillage en phase, correspond à un vortex avec un incrément de phase discret entre les lasers. Nous avons étudié les limitations dictées par le facteur de Henry et dérivé une formule analytique générale. Nous avons étudié la génération de vortex asymétrique avec des masques de pertes non uniformes. De plus, nous avons étudié théoriquement l'influence de la rétroaction optique sur le verrouillage de phase dans un vortex. Le modèle de bruit d'un tel réseau a été confirmé expérimentalement avec trois lasers. Sur la base du modèle, nous avons trouvé une méthode simple pour déterminer le signe du vortex (direction de l'accumulation de phase) basée sur les mesures de bruit des lasers.

Contents

List of Abbreviations

AV	**A**symmetric **V**ortex
DBR	**D**istributed **B**ragg **R**eflector
FIR	**F**ar **I**nfa **R**ed
FSR	**F**ree **S**pectral **R**ange
Laser	**L**ight **A**mplification by **S**timulated **E**mission of **R**adiation
NIR	**N**ear **I**nfa **R**ed
OC	**O**utput **C**oupler
OF	**O**ptical **F**eedback
OP	**O**ptical **P**ump
OV	**O**ptical **V**ortex
SESAM	**SE**miconductor **S**aturable **A**bsorber **M**irror
SLM	**S**patial **L**ight **M**odulator
TC	**T**opological **C**harge
VCSEL	**V**ertical **C**avity **S**urface **E**emitting **L**aser
VECSEL	**V**ertical **E**xternal **C**avity **S**urface **E**mitting **L**aser

Chapter 1
Introduction

Contents

1.1 Laser arrays

Integration of lasers into communication technologies and computational systems is growing every day. One example of such applications of lasers relies on laser arrays. During the past few decades, such arrays have already been widely investigated with different kinds of lasers. The most studied examples of laser arrays include gas lasers (such as CO_2), solid-state lasers (such as Nd:YAG), and semiconductor lasers [Glova 2003].

Each of the mentioned laser systems has some benefits for specific applications. Some of the arrays are designed for high output power. More advanced applications cover beam shaping and optical computations. To clarify the importance of laser array development and coupling, we can see the main directions of the laser network applications shown in Fig. 1.1.

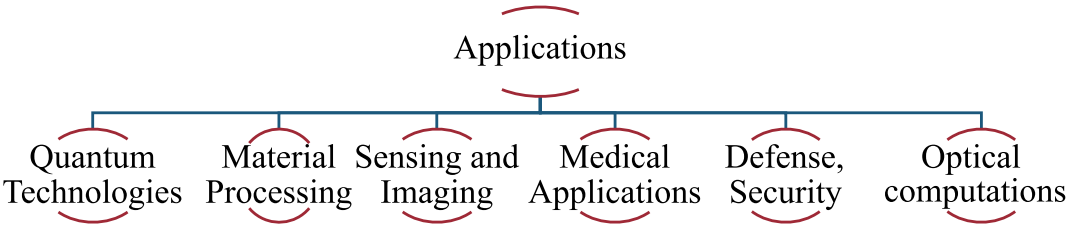

FIGURE 1.1: Laser array applications examples.

Both very new applications (such as quantum technologies) can benefit from laser array development as well as deeply developed applications (such as material processing, cutting, welding, and engraving). Laser arrays are highly valuable for optical sensing and imaging technologies. In the landscape of LiDAR systems, laser arrays bring new dimensions, enabling 3D mapping and imaging. Medical applications of laser arrays cover surgical procedures, dermatological treatments, and noninvasive imaging techniques such as Optical Coherence Tomography (OCT), particularly in ophthalmology for the retina imaging capabilities. Furthermore, laser arrays are irreplaceable in applications such as free-space optical communication. Their utility extends to defense and security, where they serve in target designation, range finding, and the development of directed energy weapons, delivering precision and controlled energy to designated targets. Beyond pragmatic applications, laser arrays are also used in entertainment, powering mesmerizing laser light shows, projectors, and display technologies.

There are many parameters of the laser array that characterize their quality. However, the equality of parameters of the lasers forming the array is the most valuable at the end of the day. This is particularly true if the application of the array is meant to be based on the far-field patterns of the coupled laser array or chaos-based cryptography [Spitz 2021; Spitz 2022].

1.2 Degenerate cavity laser arrays

A common approach used to create a laser array with uniform parameters is the spatially degenerate cavity. It is a class of optical systems, where rays retrace their path after a round trip between highly reflective mirrors. The field distribution in the "input" plane (given by the first lens focal distance) is re-imaged to itself after the round trip propagation inside the cavity.

Degenerate cavity lasers can have different cavity geometries [Arnaud 1969]. A common solution for degenerate cavity laser array development is the integration of the planar cavity with a self-imaging telescope. In this case, planar mirrors are placed at the focal planes of the telescope lenses as shown in Fig. 1.2.

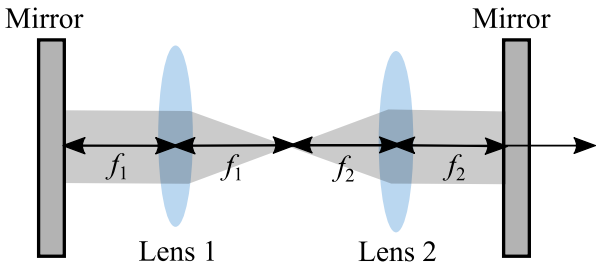

FIGURE 1.2: Planar degenerate cavity

Degenerate cavity lasers have been widely investigated with Nd:YAG crystal and CO_2 gas as active media. The solid-state Nd:YAG laser specifically has a widely developed background. It is possible to obtain thousands of lasers with the same crystal thanks to its strong gain. Such cavity geometry allows us to obtain a laser array and couple it by various techniques.

Before discussing the current state of the laser array development in VECSELs, we should pay attention to the wide range of possibilities of coupled laser arrays in general.

1.2.1 Coupled laser arrays applications

There are some applications of the laser array, where the uncoupled array operation is required (such as a power source or parallel data transmission). Nevertheless, the widest application area is covered by the coupled laser arrays. Indeed, such a system of many coupled oscillators recently became a promising device to solve several types of problems. The applications in total may be classified based on the laser array usage in its near-field or its far-field.

For example, the laser array near-field emission can find applications in extremely important areas, such as parallel data transmission [Grobe 2014; Lau 2008], optical memories [Alexoudi 2020; Gu 2014; Mitsugi 2002; Chen 2011], tweezers for atom arrays [Anderegg 2019; Burd 2016], and others. In such applications, the laser far-field is usually not accessible, for example, because the laser output light is coupled to

a fiber. One thus needs alternative methods to monitor the laser steady-state behavior. One such method consists of studying the intensity noises of the individual lasers, which permits in principle to access the laser dynamics and, in particular, the phase-locking behavior of the laser array.

On the other hand, utilization of the far-field emission of the laser addresses applications to beam shaping [Pal 2015; Pal 2017; Dev 2021]. The interest in beam shaping covers medical, material processing, information storage, and analytical applications. A laser array is a many-oscillator system that tends to find a beneficial steady-state solution. Then the investigation of the local and global steady-states can be used to solve complicated optimization problems for different physical systems [Takata 2012; Takata 2014; Takata 2016; Nixon 2013b; Tradonsky 2019; Pal 2020]. There is already significant progress in this domain, which covers matrix-vector optical operations, NP problems, and more in all-optical coherent laser solver machines (developed in LightSolver, group of Yamamoto, group of Nir Davidson, group of Claudio Conti, and more). Besides, it was recently demonstrated numerically that coherent laser arrays exhibit collective neural computing capabilities [Saxena 2022; Miri 2023], where the individual lasers act as the array nodes, and the coupling strength between the lasers plays the role of the weight coefficients.

Experimental realization of the hundreds and thousands of lasers in a degenerate cavity has been achieved only in solid slate lasers [Nixon 2011].

1.3 Degenerate cavity VECSELs

In this work, we are interested in the development of a new type of laser array. Vertical external cavity surface emitting laser (VECSEL) has some benefits, that we would like to study and introduce deeply in the manuscript. This type of laser has a gain region integrated with a mirror (DBR). The 1/2 VCSEL gain chip is placed in the front focal plane of the intracavity telescope and the highly reflective mirror is in the back focal plane as shown in Fig. 1.3.

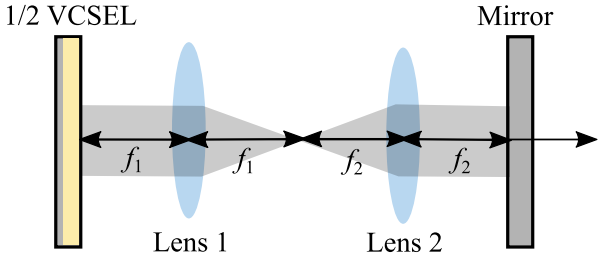

FIGURE 1.3: Planar degenerate cavity

A description of such laser is given in the chapter 2. Here we would like to highlight, that there is no real "external" cavity in the scheme. The term is used historically to distinguish the semiconductor chips with two DBRs (VCSELs) and a single DBR (VECSEL), i.e. requiring an external mirror (OC).

Several groups have already developed and studied the VECSELs with degenerate cavities in various domains.

VECSEL with controllable coherence

A significant branch of the degenerate cavity laser is dedicated to such VECSELs as a laser source with controllable spatial coherence. The method of control is shown in Fig. 1.4.

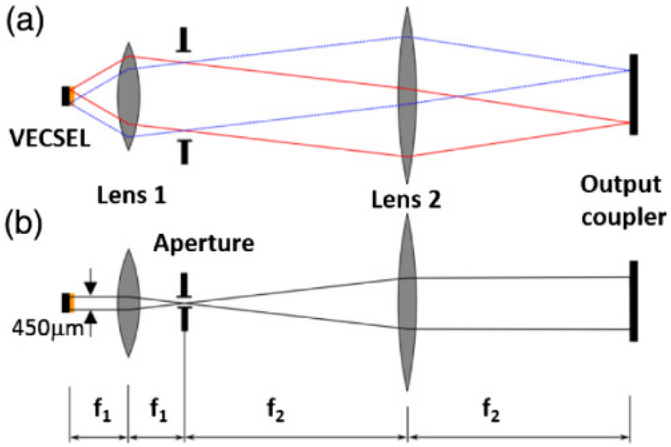

FIGURE 1.4: [Knitter 2016]. Schematic of the degenerate laser cavity (not to scale) with VECSEL, lens 1 (high numerical aperture), aperture, lens 2 (reimaging lens), and output coupler (OC) mirror. (a) In multimode operation locations on the VECSEL will be imaged onto the OC and vice versa, yielding a large number of independent spatial modes (low spatial coherence). (b) For few-mode operation an aperture is introduced in the mutual focal plane of lens 1 and lens 2, yielding plane-wave emission through the OC (high spatial coherence).

The cavity is a planar one. The 1/2 VCSEL gain chip is placed in the front focal plane of the intracavity telescope and the highly reflective mirror is in the back focal plane. We can control the coherence by the change of the aperture size. The aperture must be placed in the so-called far-field point of the intracavity telescope, i.e. in the focal plane of the telescope lenses. In this case, we can control spatial and spectral properties of the VECSEL output reducing the number of the speckles in the beam. This creates a powerful tool for laser imaging and holography [Knitter 2016; Eliezer 2021].

Temporal-localised spatial structures with degenerate cavity VECSEL

In some way the laser arrays can be compared with an array of localized light structures, which have been known for decades in VCSELS [Barland 2002; Genevet 2009; Pedaci 2008; Pedaci 2006].

Only during the last few years, this phenomenon was investigated in VECSELs [Bartolo 2022; Bartolo González 2022; Vigne 2023]. One of the works of this team is particularly interesting because it partially covers our future interests. In the series of the mentioned works the light structures were either exited by different optical pumps [Bartolo 2022] or by the same pump, but the gain was shaped by the deposited loss profile [Bartolo 2023]. By this, several pulse-shaped light structures were created in a degenerate cavity VECSEL. They were shown to work efficiently in the pulsed regime when the laser cavity is closed by a SESAM instead of the OC. See Fig. 1.5 for the scheme of the setup.

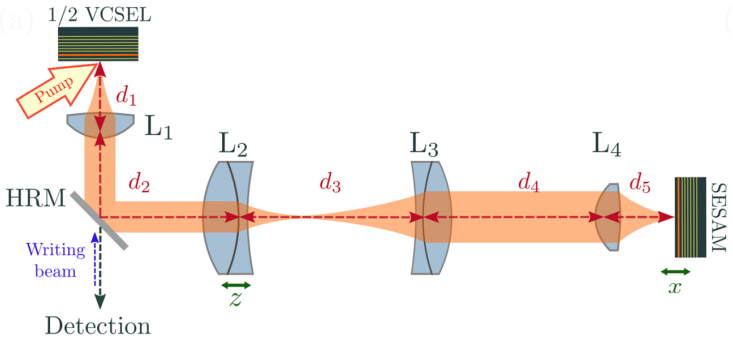

FIGURE 1.5: [Bartolo 2022]. Experimental setup showing the L-shape VECSEL. d_1, the distance between the gain mirror and lens 1; d_2, distance between f_1 and lens f_2; d_3, distance between f_2 and lens f_3; d_4, distance between f_3 and lens f_4; d_5, distance between f_4 and the SESAM; HRM, high-reflectivity beam splitter (>99.5% at 1.06 µm). For the telecentric configuration, the distances are $d_1 = f_1, d_2 = f_1 + f_2, d_3 = f_2 + f_3, d_4 = f_3 + f_4$, and $d_5 = f_4$.

This scheme represents a powerful method of developing light structures localized in space in time.

This series of results is very interesting and important. However, our main interest is the development of the CW VECSEL array and a study of the coupling effects on the VECSEL array phase-locking dynamics.

1.3.1 Coupling between lasers in an array.

There are multiple methods of laser array geometry manipulation and creating the coupling between lasers. All methods can be divided into two groups. The first group is the method of near-field manipulations, i.e. in the image planes of the intracavity telescope. The variations of the loss, gain, and other spatial properties in the input plane are imaged to the output of the laser and vice versa. The second group of methods is manipulation in the far-field, i.e. in the Fourier plane between two lenses of the telescope. Examples of these methods potentially applicable to the degenerate cavity VECSEL are collected in Fig 1.6.

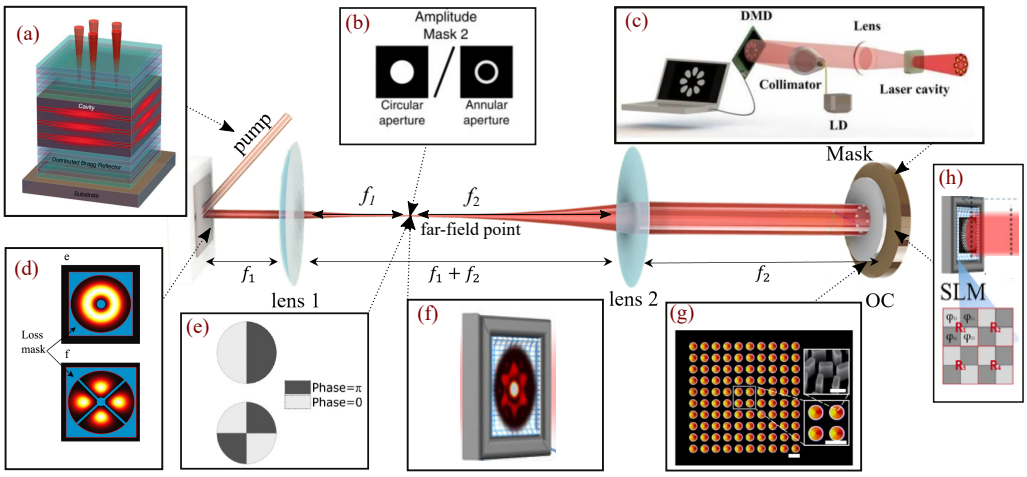

FIGURE 1.6: Examples of different methods to manipulate laser array geometry and phase-relation between lasers. Insets are given by (a) [Cookson 2021a], (b) [Chriki 2018] , (c) [Guo 2023], (d) [Bartolo 2023; Seghilani 2016], (e) [Mahler 2019a], (f) [Tradonsky 2019], (g) [Piccardo 2022], (h) [Tradonsky 2021]. The laser cavity consists of a 1/2 VCSEL gain chip, output coupler (OC), and two-lens imaging telescope.

The near-field manipulation methods illustrated by (a, c, d, h, g) in Fig. 1.6 and (b,e,f) stand for the far-field.

Methods of the laser array development with a loss-profile

To obtain a laser array different techniques can be used. For example, one can use pump beam-shaping (a), a loss layer can be deposited at the gain chip (d), or the loss profile can be introduced by a loss mask at the output coupler (OC) plane (c, h). The loss mask can be implemented with the help of a spatial light modulator (SLM) (h), digital micro-mirror device (DMD) (c), or a metal plate with holes.

Not all of the mentioned methods are possible to apply to degenerate cavity VECSEL today. OC can not be changed for DMD (c) or SLM (h) because of two factors: high precision of the loss boundaries and high reflection at the resonance wavelength of the VECSEL's gain chip. Both DMD and SLM must work as the OC and the high-precision loss pattern. The loss pattern precision is given by the pixel sizes of the DMD and SLM. The minimal pixel pitches are $\sim 3\,\mu$m for the most advanced and expensive devices nowadays. Unfortunately, it is also not possible to find such devices with enough reflectivity (>99%) for the VECSEL resonance wavelengths.

In our experiment we have a strong motivation to save the possibility of coupling strength adjustment, thus the mask integration with the gain chip (inset (d)) is not preferred. Pump shaping is a possible solution. At the same time, the beam-shaping system decreases the intensity of the pump beam and requires additional expenses.

Loss mask is the cheapest solution. At the same time, the quality of the mask depends a lot on the quality of production.

Methods of the laser array coupling

Among numerous laser array coupling methods, we would like to focus on the injection coupling typical of many solutions with laser arrays. The main idea is that we must create an exchange channel between lasers belonging to the array. These channels can be realized in various ways inside the optical cavity. They can be realized by the diffraction coupling controlled by the distance between the loss mask and OC position [Tradonsky 2017], passive or active intracavity element [Reddy 2022; Mahler 2019a; Chriki 2018; Mahler 2021; Tradonsky 2019] illustrated by (b,e,f,g) in Fig. 1.6 or some optical feedback configuring [Nixon 2012; Pabœuf 2011; Wang 2022]. Moreover, a single SLM can be used simultaneously to create the laser array, couple it, and improve the quality of the coupling decreased by some optical aberrations [Pando 2023].

The laser array can be also coupled outside the cavity to the optical fibers with the help of a lenslet (array of small lenses), by diffraction grating, beam-combining optics, waveguides, and more. This kind of coupling technique is passive. Scalability and flexible coupling realization immediately make those systems bulky. Additionally, these systems struggle with efficient power consumption and transfer and beam quality [Lau 2008].

1.4 Noise in laser arrays

It is well known that noise plays a crucial role in the dynamics of lasers [Petermann 1991]. The noise can greatly affect the phase-locking of lasers by reducing the number of phase-locked lasers. This will limit the scalability of the laser array. In case the laser array is designed as an optical solver, this will limit the capability of solving large-scale problems. Further, noise can prevent the laser array from phase-locking to a ground state. Therefore, to improve the performance of a laser array, it is very important to study the role of noise in such laser arrays.

Moreover, a complete characterization of such noise requires not only measuring the noise of individual lasers in the array but also their correlations. Such correlations have, for example, already been shown to play an important role in dual-frequency lasers used in atomic clock applications [Liu 2018a; Gredat 2018; Gredat 2020b], and also to be able to reveal the dynamics of lasers, depending in particular on whether they belong to the class-A or class-B dynamical regime [De 2013a; De 2013b].

Diagnosing the behavior of an array of coupled lasers by using its intensity noise properties requires to use a relatively quiet laser. However, till now, laser array phase-locking was mainly investigated in solid-state Nd:YAG lasers [Davidson 2022], fiber lasers [Fridman 2010a; Fridman 2010b], laser diodes [Kapon 1984; Winful 1988;

DAmato 1989], and CO_2 gas lasers [Glova 2003], which are usually quite noisy systems. Despite their versatility in the context of arrays of lasers based on degenerate cavity architectures [Friesem 2013], Nd:YAG lasers are not the best candidates to achieve low noise operation. Indeed, they are intrinsically very noisy because they belong to the class-B dynamic class [Arecchi 1984].

On the contrary, VECSELs (Vertical External Cavity Surface Emitting Lasers) are well known to be extremely quiet lasers, because their class-A dynamical behavior filters out the pump noise above the cavity cut-off frequency [Baili 2007; Baili 2008; Baili 2014]. However, one must take into consideration the fact that the semiconductor gain medium of VECSELs exhibits a non-negligible Henry α-coefficient (also called phase-amplitude coupling coefficient or linewidth enhancement factor), which tends to affect the laser phase-locking behavior [Bouchereau 2022]. Indeed, the value of this linewidth enhancement factor in different types of semiconductor gain chips typically ranges from 3 to 10 [Zilkie 2008; Consoli 2012; Fordell 2007; Sinquin 2023] and can even be much larger (up to 60) for shallow quantum wells chips [Stohs 2001]. These values are much larger than those of Nd:YAG lasers ($\alpha \sim 0.3$) [Thorette 2017].

1.4.1 Motivation

Based on the presented review we see an interest in the development of degenerate cavity VECSEL arrays. There is a strong interest in such optical cavities due to their unusual spatial properties. They allow us to obtain an array of almost identical lasers in the geometry determined by the simple loss mask. This is very valuable for beam-shaping applications including the generation of vortices.

Even more valuable is the class-A dynamics of each laser in the VECSEL array. Such dynamics of the laser array is unstudied yet. The phase-locking dynamics of such a system may be very different from the solid-state laser array also due to the non-negligible Henry factor. We see the interest in the study of the complex coupling influence on phase-locking and laser array noise characteristics. The main interest in the class-A laser array is its outstanding low-noise characteristics. Thus, it is also important to study the noise dependency of the coupling parameters. Especially we are interested in the study of the noise correlations in this case. One of the potential applications of the laser array is a laser solver and thus, the noise correlation between lasers may affect interpretations of the information at the final steady state.

1.4.2 Challenges

The main goal and the main challenge of this work is to develop a degenerate cavity VECSEL array. We chose an all-optical degenerate cavity scheme (without SLM and DMD) based on the literature review, which is presented in Fig. 1.7.

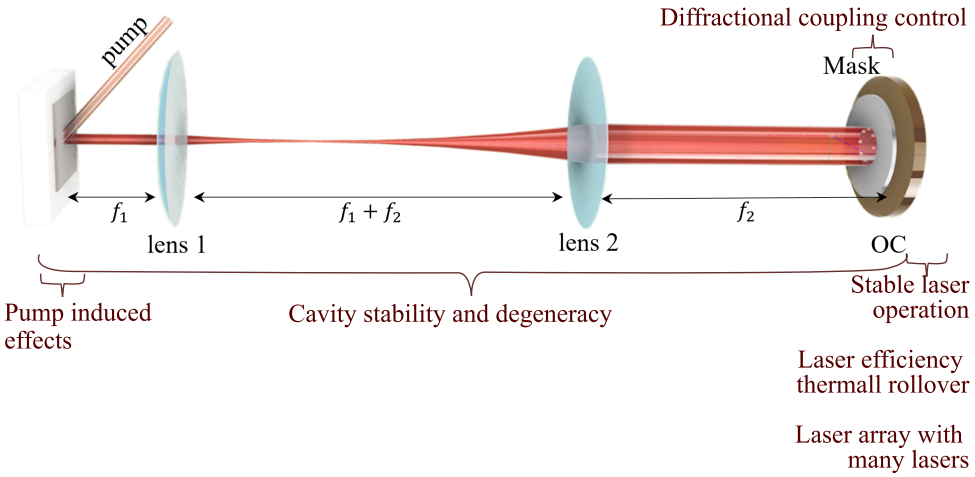

FIGURE 1.7: Degenerate cavity VECSEL: 1/2-VCSEL: optically pumped gain chip; lens 1, lens 2: lenses; OC: output coupler; M: mask.

Each part of the presented scheme leads to a corresponding challenge. Some of them are noted in Fig. 1.7. The pump is chosen to be optical. The array is created by the metal loss mask placed in the self-imaging cavity. The coupling between lasers is provided by the diffraction on the mask. Consequently, the coupling adjusting mechanism results in the adjustment of the distance between the mask and the OC. The choice of the system dictates a list of the preliminary challenges for the project listed in the frame below.

Then the main challenges are:

1. Cavity degeneracy;
2. Stable lasing operation of the laser array;
3. Thermal management;
4. Laser power and maximal number of lasers;
5. Mode composition of the single laser from an array;
6. Coupling control between the lasers.

The quality of the laser array is supported by the quality of cavity adjustment, the gain chip properties, and the loss mask profile precision. The gain chip of a VECSEL has typically a very low gain, thus the adjustment of the laser can be challenging. Additionally, those gain chips typically experience thermal lensing and efficiency rollover. The additional difficulty occurs due to the requirements of self-imaging telescope integration with a planar cavity. The optical system is on the border of stability then. The quality of this part of the work determines the coherence and consequently synchronization dynamics of the laser array.

Additional challenges occur when the VECSEL is transformed into a laser array by the mask. The choice of the mask dimensions must allow for obtaining a maximal number of lasers having the same parameters and preferably oscillating close to the fundamental mode of the cavity. Additionally, the mask must be movable to control the coupling between lasers.

1.5 Outline

The manuscript aims to describe both theoretical and experimental study of the laser array in degenerate cavity VECSEL.

- The manuscript starts with a general description of the VECSEL laser emission and dynamics description. This information is presented in chapter 2. In this chapter, the model for the diffraction coupling is presented. A rate-equation model integration with complex coupling is developed on the example of two lasers.
- In the chapter 3 we investigate a ring laser array theoretically. Specifically, the interest of this chapter is concentrated in the steady-states of the phase-locked ring laser array. Here we discuss what are the vortex solutions and the characteristics and application of different steady-states.
- Chapter 4 continues the theoretical study of the ring laser arrays with numerical experiments. Here we investigate probabilities of the phase-locking in different steady-states. Additionally, we studied methods of the non-uniform coupling and optical feedback influence on the probabilities of the different steady-state solutions.
- Experimental realization of the degenerate cavity is presented in Chapter 5. Here we study stability and degeneracy criteria with ABCD matrix analysis. We show the stages of the degenerate cavity alignment. We present some experimental signatures of spatial degeneracy. Finally, we present several examples of the laser arrays obtained with different masks.
- Chapter 6 presents the experimental, analytical, and numeral noise study in the array of the two and three lasers. We compare these results and give a conclusion and perspectives of the VECSEL laser array.
- The manuscript ends with a theoretical concept of the optical computations presented in the chapter 7. Here we show that boolean operations and information storage can be introduced in the developed VECSEL array.

The results of this project were presented at:

1. The Siegman International School on lasers (Poland, June 25-July 2, 2022)

2. IQFA-XII "Quantum Engineering, Fundamental Aspects to Applications“ (France, November 16-18, 2022)

3. FRISNO16 “French-Israel Symposium on Non-linear & Quantum Optics” (Israel, January 15-19, 2023)

4. CLEO/Europe-EQEC 2023, (Germany, Munich, June 26 – 30, 2023)

5. 26th International Conference on Noise and Fluctuations (ICNF) (France, Grenoble, October 17-21, 2023)

Parts of the thesis have been published in journals and some are currently prepared for submission:

1. [Bouchereau 2022]: Yann Bouchereau, Sopfy Karuseichyk, Raphael Guitter, Vishwa Pal, and Fabien Bretenaker, “Effect of linewidth enhancement factor on the generation of optical vortices in a class-A degenerate cavity semiconductor laser”. Opt. Express 30.9 (Apr. 2022), pp. 15648–15658;

2. [Karuseichyk 2023]: Sopfy Karuseichyk, Vishwa Pal, Sahil Sahoo, Grégoire Beaudoin, Isabelle Sagnes, and Fabien Bretenaker, “Investigation of noise correlations in the phase-locked class-A VECSEL array”. Opt. Express 31.25 (Dec. 2023), pp. 41713–41725;

3. In progress: Sopfy Karuseichyk, Vishwa Pal, Ilan Audoin and Fabien Bretenaker. "Non-symmetrical vortex beam shaping in VECSEL laser arrays".

CHAPTER 2

Fundamentals of VECSEL

Contents

This chapter introduces the operational principles of Vertical External Cavity Surface Emitting Lasers (VECSELs) and the description of their dynamics.

The first part provides a general introduction to semiconductor laser architecture, offering detailed explanations of laser cavity schematics and the modal composition specific to long-cavity VECSELs. An introduction of the light-matter interaction is given with a specific focus on the optically pumped (OP)-VECSELs gain chip. The VECSEL gain chip used in our experiment is based on the InGaAs/GaAs semiconductor structure, incorporating several Quantum Wells (QWs). Thus, a criterion to reach the VECSEL radiation threshold is given with particular emphasis on the role played by QWs. This part ends with a description of the Henry factor (α factor) and its role in VECSELs.

The second part of the chapter starts with the description of the laser dynamics classes. The main goal of this part is to introduce a general model for the VECSEL dynamics. A broad spectrum of numerical and analytical results is presented there. The numerical modeling of VECSEL dynamics is then presented in comparison with other types of lasers, such as Vertical Cavity Surface Emitting Lasers (VCSELs). After this, our approach for the injection coupling parameterization is described. Consequently, the rate equation model for two lasers coupled by the complex-valued coupling strength is introduced. Finally, the basic principles of the two phase-locked VECSELs are derived analytically in for most general case.

2.1 VECSEL architecture

The theoretical groundwork for the laser operational principle originates from Einstein's work from 1917 [Einstein 1917]. In this paper, the concepts of stimulated and spontaneous emission are introduced. The concept of stimulated emission found practical application in the 1940s in a framework of spectroscopy and in the 1950s with the invention of the maser and the laser. The first working laser was built by Theodore Maiman at Hughes Aircraft Company. Subsequent developments included the creation of the first diode laser made of GaAs in 1962. Nick Holonyak further advanced laser technology in the same year by developing the first semiconductor visible light-emitting diode (LED). The first room-temperature continuous-wave (CW) operation of VCSELs was realized only in 1988 by Koyama [Iga 1988].

The optically-pumped semiconductor laser with vertical geometry hasn't been implemented until 1992 even though the concept of laser geometry with "radiation mirrors" was proposed in 1966 [Basov 1966]. VECSEL's architecture is inherited from thin-disk solid-state lasers [Guina 2017a]. Those lasers involve a thin semiconductor gain mirror and an external cavity mirror. The gain chip consists of a highly reflective mirror and a semiconductor gain region with quantum well (QW) or quantum-dot (QD) layers separated by spacer or barrier layers. Its mirror is a semiconductor-distributed Bragg reflector (DBR)[1]. This combination of the DBR

[1] Alternatively, it can be replaced with a metallic, dielectric, or hybrid mirror

and external cavity mirror corresponds to the classic laser cavity architecture with two mirrors and follows the basic laser principles.

A demonstration of the first high-power, room-temperature VECSEL [Raja 1989] and its quantum efficiency improvement happened several years later. Thus, this type of laser still can be considered as a young technology. The gain chips are constantly improving. Today's VECSELs demonstrate versatility in covering various wavelengths from visible to mid-infrared $\sim 300-5300\,\text{nm}$ [Guina 2017a]. They stand out for their ability to achieve high output power (up to 100 W), maintain high brightness, operate in a single-frequency mode with low noise, and more. As a result, VECSELs are recognized as some of the most adaptive lasers today.

2.1.1 Fundamental laser scheme

The basic laser construction consists of an active medium (gain) positioned between two high-quality mirrors (shown in Fig. 2.1). The active medium needs to be pumped by an external energy source called a pump. Two mirrors form a laser cavity or a resonator. Usually, one mirror is highly reflective and the other one is partially transmitting ($R \sim 99\%$). The partially transmitting mirror is often called an output coupler (OC).

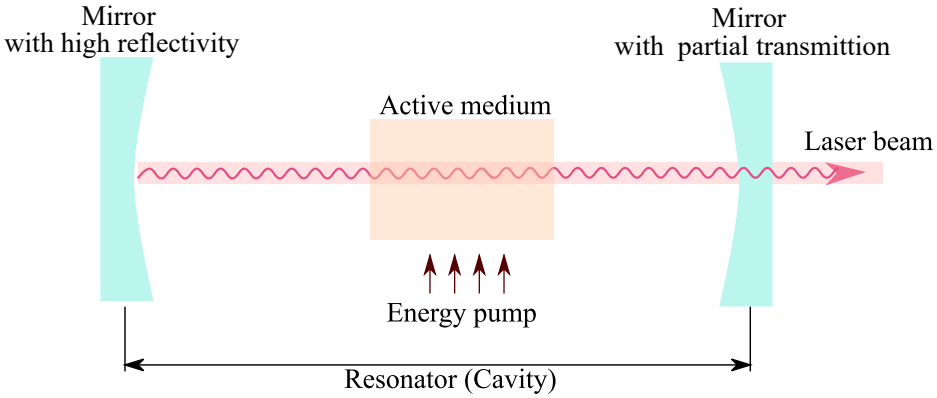

FIGURE 2.1: Principle scheme of the laser

The key components required for laser emission and their functions are the following:

- **Gain**. The gain medium is selected based on its ability to amplify light through stimulated emission.
- **Pump**. The pump source provides energy to the gain medium to achieve the inverted population of energy states. The pump source can be optical, electrical, thermal, chemical, or other, depending on the type of laser.
- **Optical cavity**. The cavity serves to reflect light back and forth through the gain medium, stimulating the emission of more photons and allowing for the

amplification of the coherent light. The partially transparent mirror allows a portion of the amplified light to exit the cavity and form the laser beam. The reflected light within the cavity stimulates further emissions, contributing to the amplification of the laser beam. This effect accumulates and enhances the stimulated emission, promoting the coherence and directionality of the laser beam.

The light propagates in the longitudinal direction of the resonator and is reflected by the mirrors. The interference of two counter-propagating optical waves with the same frequency leads to the formation of the standing wave, as illustrated in Fig. 2.2 (a).

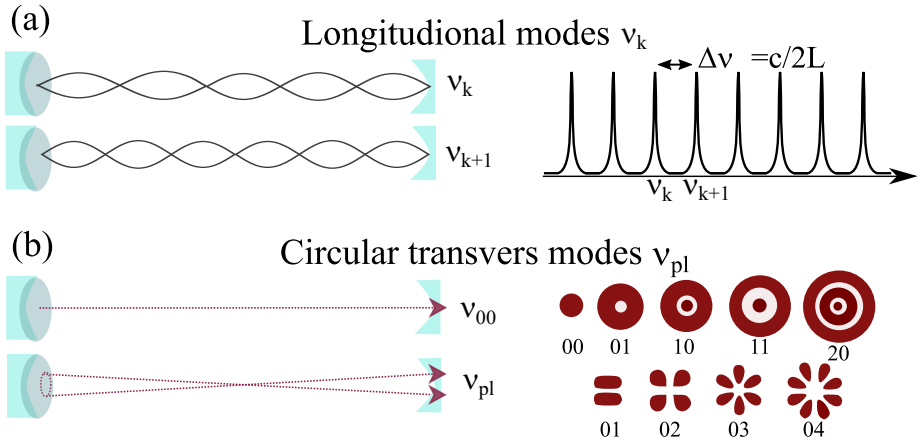

FIGURE 2.2: Illustration of the (a) longitudinal and (b) transverse modes formation in the laser cavity.

The cavity boundary conditions specify that $k\lambda/2 = L$ must hold for standing waves, where k is an integer, λ is the wavelength and L is the length of the laser cavity. Fig. 2.2 (a) shows the two standing waves of frequencies ν_k and ν_{k+1} with $k = 5$. The frequencies of the k-th mode $\nu_k = c_0 k/2Ln_0 = ck/2L$, where c_0 is the speed of light in vacuum, n_0 is a reflective index of the medium. From this, we can obtain a very important parameter for a resonator: its free spectral range (FSR):

$$\Delta\nu = \nu_{k+1} - \nu_k = c/2L.$$

This simple relation reveals that the frequencies of the modes are equally spaced. In the considered case, these standing waves belong to the fundamental mode TEM_{00}, which corresponds to some specific path in the cavity. However multiple geometries of the stable path can exist in the same laser cavity in the transverse direction. Different transverse modes accumulate different phases along the propagation. As a result of this, a set of different spatial patterns can occur Fig. 2.2 shows a series of the circular transverse modes. The frequencies of those stable field configurations will differ depending on the longitudinal k and spatial p, l indexes (see Fig. 2.3).

FIGURE 2.3: Spectrum of the transverse modes, where the indexes p, l of ν_{plk} gives the number of nods in the radial and angular profiles of the circular modes.

Transverse modes associated with a TEM_{00} axial mode have a frequency that differs from that of the axial, potentially leading to a broadening of the linewidth (and decrease in coherence length) for multi-spatial-mode lasers. The cavity resonances are then defined according to the formula eq. (2.1).

$$\nu_{plk} = \frac{c}{2L}\left[(k+\frac{1}{\pi}(p+l+1)\cos^{-1}\sqrt{(1-L/R_1)(1-L/R_2)}\right]. \tag{2.1}$$

Here R_1 and R_2 are the radii of curvature of the cavity mirrors. We can see, that in the case of the well-aligned planar cavity with $R_{1,2} \to \infty$, the term with $\cos^{-1}$ goes to zero, and the transverse resonances are frequency degenerate $\nu_{plk} = \nu_k = ck/2L$.

Optical amplification can only occur for a finite range of optical frequencies. Laser generation occurs in the bandwidth where the gain is larger than the cavity losses, as illustrated in Fig 2.4. Due to this, not all the cavity modes in Fig 2.2 can become lasing modes. In addition, the number of oscillating modes also depends on the mode competition in the considered laser medium.

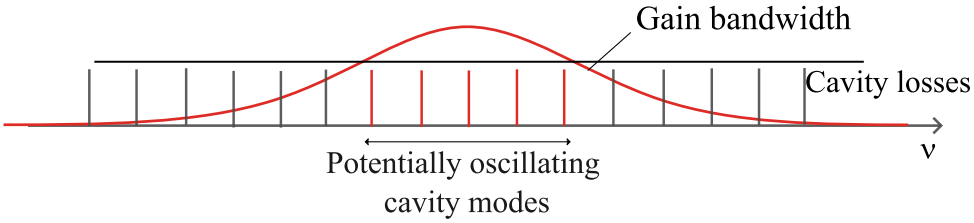

FIGURE 2.4: Potentially oscillating modes in the laser cavity. Only the ν_{plk}'s can oscillate, which fall in the bandwidth with the gain prevailing losses.

The losses are determined by the absorption and scattering of the cavity mirrors, optical components (such as lenses and beam-splitters), and gain medium. At the same time, the gain is determined only by the VECSEL gain chip. The process of regarding it has to be discussed in more detail in connection with the generation of laser radiation.

2.2 Semiconductor gain chips as an active medium

The existence of energy bands distinguishes semiconductor gain chips from other laser gain materials, such as solid-state, gas, and dye lasers. The laser transition in this case occurs between the wide energy bands of the host crystal which are different from the laser media mentioned above, such as, for example, ruby and Nd:YAG, which are characterized by the transitions between the narrow energy levels of impurity atoms.

The band structure of a crystal is explained by the nearly free electron model, where band electrons are only weakly perturbed by the periodic potential of the ion cores [Grundmann 2016]. Energy gaps arise from Bragg's reflection of electron waves in crystals. This means that the periodic boundary conditions induce discontinuities in the electron momentum at the nodes of the crystal lattice, leading to a band-organized energy diagram structure with a bandgap separating valence and conducting bands [Kittel 2004].

2.2.1 Light-matter interaction in semiconductors

Light-matter interaction in semiconductors results in the three main processes shown in Fig. 2.5 (a-c): absorption, spontaneous emission, and stimulated emission. A series of stimulated emissions results in the amplification of the light propagating in the laser cavity.

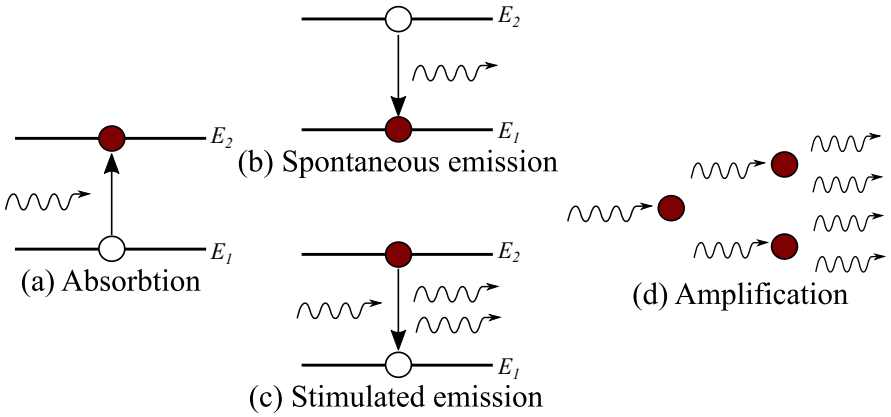

FIGURE 2.5: Light-matter interaction mechanism between two energy levels. Energy values E_1 and E_2 correspond to the ground state and excited state, respectively. (a) absorption, (b) spontaneous emission, (c) stimulated emission, (d) amplification.

The description of the process is the following: process (a) illustrates the absorption of a photon with energy $h\nu = E_2 - E_1$, when a system goes from the ground state to the excited state; subplot (b) shows spontaneous emission of a photon with

energy $h\nu = E_2 - E_1$, when a system in the excited level goes to the bottom energy level; process (c) shows stimulated emission when the exited system interacts with the photon. As a result, the system emits photons with identical characteristics; and (d) shows the amplification based on series stimulated emission by the photons thanks to multiple propagation in the cavity.

The flat bandgaps shown in Fig. 2.5 are of course a crude approximation. The energy difference depends on the electron momentum similar to the diagrams shown in Fig. 2.6.

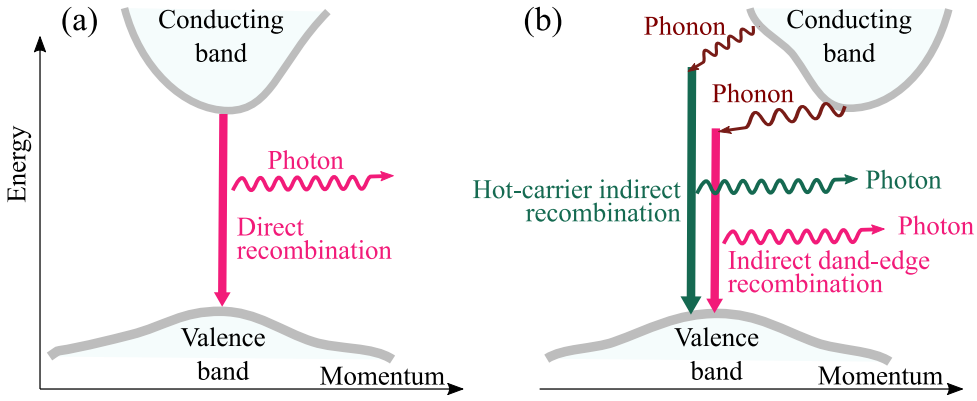

FIGURE 2.6: The difference between direct (a) and indirect (b) bandgap semiconductors. In the first case (a) transition is between the maximum and the minimum of the conducting and valence bands. In the case shown in subplot (b) the transition between bands is accompanied by phonon absorption.

The photon emission occurs as a result of the electron-hole recombination between the maximum and minimum of the conduction and valence bands correspondingly. This process is shown in Fig. 2.6 (a). Nevertheless, the band's extremums can be not matched for some semiconductors. Then, the photon emission is observed with an additional participation of the phonons. A more detailed scheme of this process is given in Fig. 2.6. In case recombination occurs directly with the electron transfer from the "upper" conducting band to the "bottom" valence band - the semiconductor is a direct bandgap material, otherwise - "indirect".

In a direct bandgap (shown in Fig. 2.6 (a)) semiconductor the top of the valence band and the bottom of the conduction band lie on top of each other (for example, GaAs). In indirect bandgap semiconductors, the valence band maximum and the conduction band minimum are not on top of each other (shown in Fig. 2.6 (b)). This makes, for example, Si and Ge indirect bandgap semiconductors. Only direct semiconductors are successfully used as a base for laser gain chips.

2.2.2 Quantum Wells

The main role of quantum wells is to confine charge carriers. The carriers can not be localized within the single semiconductor layer. They "leak" over the entire structure escaping the recombination area and heating it.

It is proposed to use a combination of semiconductors with different bandgaps E_g (see Fig. 2.7) to isolate the carriers in the active layer following Herbert Kroemer's idea. Then, the semiconductor with a wider bandgap acts as a barrier for both electrons and holes. The lattice constants given by the interatomic distances of those two semiconductors should be close. Reducing the thickness of the middle layer significantly affects the behavior of the electron. The proximity of the barriers on both sides results in the quantization of the electron's motion. Then, such a layer behaves as a quantum well (QW).

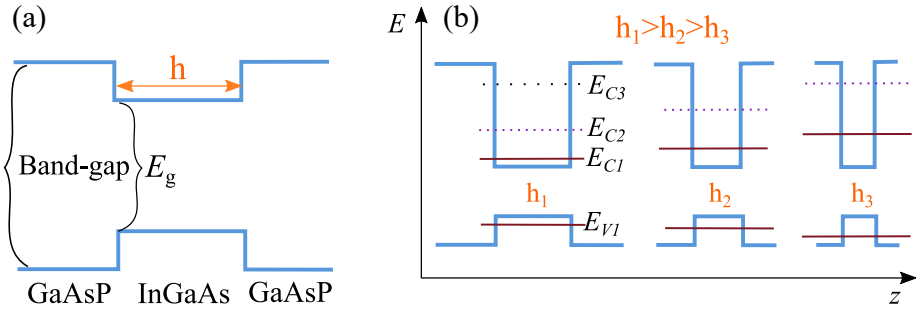

FIGURE 2.7: Illustration of the QW's energy levels dependency on the width of the QW. Subplot (a) gives an example of the combination of semiconductors with different bandgaps and compatible interatomic distances. The barrier layer is introduced by InGaAs and its width is noted h. Subplot (b) shows the illustration of the lowest energy levels shift with a change of the QW width.

The main feature of a QW is that electrons cannot be at the very bottom of the well. The lowest level at which they can be located is the first energy level of the quantum well, which is illustrated in Fig. 2.7 by a solid purple line E_{C1}. An electron can also occupy the higher energy levels - the second E_{C2}, the third E_{C3}, and so on.

The depth of the levels varies depending on the width of the quantum well h. Growing the quantum well layer wider leads to the level dropping deeper and growing the layer narrower leads to the rise of the energy levels. This means, that the energy of the laser transition, can be carefully adjusted by slightly changing the width of the quantum well, and therefore the wavelength of the radiation can be changed.

A typical gain chip architecture for VECSEL consists of DBR and several QWs incorporated inside. This kind of gain chip is also often called 1/2 VCSEL and a schematic of its bandgap profile is shown in Fig. 2.8.

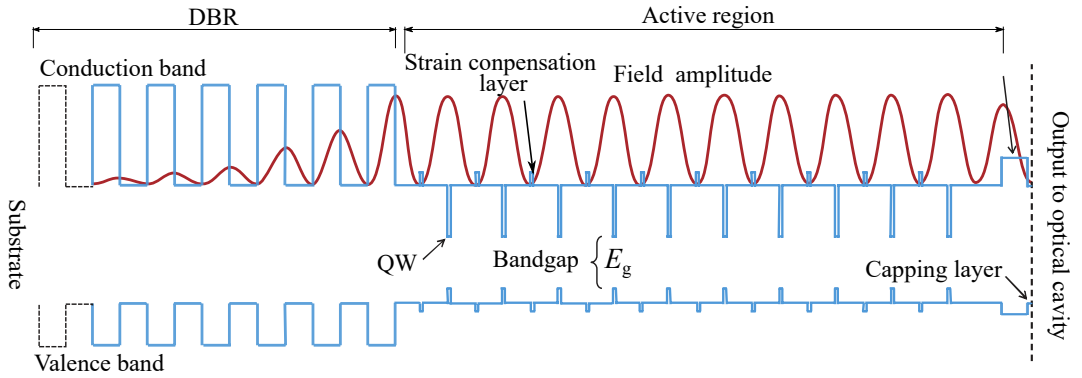

FIGURE 2.8: Adapted from [Guina 2017a]: Example of a bandgap profile of a VECSEL gain chip with 10 QWs. The red curve illustrates the intracavity field amplitude.

The physical dimensions of Fig. 2.8 are presented not to scale. A typical thickness of the QW layer is tens of nm. For example, the gain-chips used in the experiment have 27 pairs of GaAs/AlAs of total thickness around 1.1 µm, while the single QW's thickness is 0.06 µm. QWs are separated by the barriers and strain-compensating layers with different thicknesses, and in total the active region is around 1.2 µm. The number of the QW determines the gain of the laser gain-chip, but the dependency is not linear. The increase in the number of QWs is often accompanied by the increase of the mechanical strain in the structure, thus affecting the emission properties negatively.

The absorption and stimulated emission mechanisms between the valence band and the conduction band are induced by the photons of the optical pump. The transition from the bottom state of QW to the upper state respects the conservation of the absorbed energy of the photon. Due to extremely rapid intra-band relaxation processes, stimulated emission occurs more from the bottom of the valence band. The charge carriers stimulate the emission necessary for coherent amplification of the laser field after achieving population inversion when recombining inside the quantum wells.

The electrons obey the Fermi–Dirac statistics. According to this the probability that an electron state with energy $E = h\nu$ is occupied is given by:

$$f_{c,v} = \frac{1}{1 + \exp\left[\frac{E - E_{Fc,Fv}}{k_B T}\right]}. \tag{2.2}$$

Here $k_B = 1.38 \times 10^{-23} J/K$ stands for the Boltzmann constant, T is the temperature in K, and E_{F_v,F_c} are the Fermi energy levels of conducting and valence bands. Fig. 2.9 (a-c) illustrates the changes in the Fermi levels and population from the quantum well at the thermodynamic equilibrium (a), to the amplification threshold and the population inversion state (c) on the energy diagram. The Fermi level represents the energy state with a 50% probability of being filled. Then, the thermal equilibrium

gives the single Fermi level $E = E_{F_C} = E_{F_V}$, and it is situated exactly in the middle of the bandgap (see Fig. 2.7 (a)).

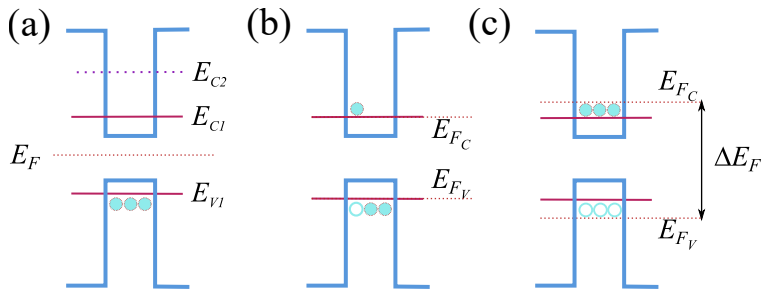

FIGURE 2.9: Illustration of the Fermi-levels shift from the thermal equilibrium to the population inversion of the QW-system.

The rates of absorption R_{abs} and stimulated emission R_{st} are linked to the probabilities of occupation by carriers of the energy levels of the transition [Gredat 2020a]. For stimulated emission, an electron should be in the conduction band and a hole in the valence band. The rates R_{abs} and R_{st} are expressed as follows:

$$R_{\text{abs}} = Bf_v(1-f_c),\ R_{\text{st}} = Bf_c(1-f_v),$$

where $f_{c,v}$ are given by the eq. (2.2) and B represents the rate of radiative recombination. At non-zero temperature, E_{F_C}, E_{F_V} strongly depend on the level of carrier injection into the quantum wells and differ from each other in the non-thermodynamic equilibrium situation achieved thanks to pumping. The system shown in Fig. 2.9(a) is at thermodynamic equilibrium. Then, photons with the energy $E \geq E_{\text{g}}$ are absorbed. The Fermi levels of the two bands E_{F_C}, E_{F_V} shift with the rising energy of the absorbed photons Fig. 2.9 (b). The difference between the Fermi levels of the two bands $\Delta E_F = E_{F_V} - E_{F_C}$ increases when the carrier number increases. Continuing to increase, a population inversion and the amplification threshold are obtained under the effect of enough carrier injection Fig, 2.9 (c).

The amplification condition amounts to imposing a rate of stimulated emission greater than the rate of absorption leading to:

$$\frac{R_{\text{st}}}{R_{\text{abs}}} = \frac{f_c(1-f_v)}{f_v(1-f_c)} \geq 1.$$

Then, using a $f_{c,v}$ definition according eq. (2.2) we obtain:

$$\exp\left[\frac{1}{k_B T}(\Delta E_F - h\nu)\right] \geq 1,$$

where $h\nu$ is the energy of a photon to be produced. Then, the amplification condition is

$$\Delta E_F \geq h\nu \geq \Delta E_{\text{g}},$$

which is known as the Bernard-Duraffourg condition [Bernard 1961]: quasi-Fermi level separation exceeds the energy of photons, which has a minimal energy of the bandgap.

In conclusion, we should also mark one of the benefits of semiconductors for optically pumped systems. Fig. 2.10 shows the absorption spectra for the most commonly used semiconductors.

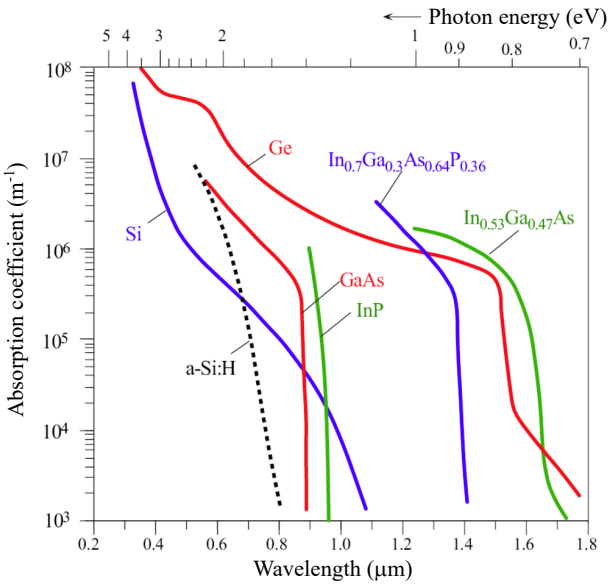

FIGURE 2.10: Absorption coefficient as a function of the wavelength and bandgap energy [Benedikovič 2020].

Since the absorption is observed in a wide range, it is easier to choose the appropriate wavelength for optical pumping.

Henry factor

Another peculiarity of semiconductor lasers is the linewidth enhancement factor, also often denoted as α or Henry factor. The fundamental laser linewidth is given by the Schawlow–Townes expression, which is essentially the contribution to the linewidth due to phase changes from spontaneous emission processes. The Schawlow–Townes formula agrees with measurements in the case of certain lasers, such as, for example, solid-state lasers. However, semiconductor lasers exhibit larger linewidths. Charles H. Henry found that the increased linewidth is a result of a coupling between intensity and phase noise, caused by a strong dependence of the refractive index on the carrier density in the semiconductor [Henry 1982].

The refractive index n depends on the carrier density ΔN. Changes in intensity I cause changes in ΔN, affecting the complex susceptibility of the active medium. This

change in refractive index alters the instantaneous frequency [Henry 1982]. In summary: amplitude-phase coupling can be represented as a chain of variations causing the consequent variations:

$\Delta I \rightarrow$	$\Delta N \rightarrow$	$\Delta n \rightarrow$	$\Delta\phi \rightarrow$	$\Delta\omega$
(intensity)	(carrier density)	(refractive index)	(phase)	(linewidth)

The formula derived by Henry corresponds to eq. (2.3), where $\Delta n''$ is a variation of the imaginary part of the refractive index and $\Delta n'$ is a real part of the refractive index variations.

$$\alpha = \frac{\Delta n'}{\Delta n''}. \tag{2.3}$$

In standard semiconductor gain chips, the α factor is significant, especially with weak carrier confinement in quantum wells. Unconfined carriers populate the barriers' continuum, reducing the differential gain, and increasing α. The Henry factor enlarges the Schawlow-Townes laser line by $1 + \alpha^2$, implying a coupling between the phase and amplitude of the laser field $A(z,t)$. The value of the Henry factor can vary depending on the number of the QW layers [Alkhazraji 2023], temperature, and pump regime of the structure. The experimentally estimated value of the linewidth enhancement factor in different types of semiconductor gain chips typically ranges from 3 to 10 [Zilkie 2008; Consoli 2012; Fordell 2007; Sinquin 2023] and can even be much larger (up to 60) for shallow quantum wells [Stohs 2001]. These values are much larger than those of solid-state lasers, for example, Nd:YAG laser characterized by ($\alpha \sim 0.3$) [Thorette 2017].

2.3 Basic classes of the laser dynamics

Laser dynamics is a result of the coupling between the cavity processes and the processes in the active medium. It can be categorized into different classes based on the relationship between the carrier population decay rate $\gamma_\parallel$, the dipolar polarization relaxation rate $\gamma_\perp$, and the field decay rate γ_{cav}. We consider here the simple set of so-called dimensionless Lorenz–Haken equations [Khanin 2006], which are sufficient to discuss dynamics classes. The model corresponding to a single-mode laser is then

$$\frac{\mathrm{d}E}{\mathrm{d}t} = \frac{\gamma_{\text{cav}}}{2}(P - E), \tag{2.4}$$

$$\frac{\mathrm{d}P}{\mathrm{d}t} = \gamma_\perp(\Delta n\, E - P), \tag{2.5}$$

$$\frac{\mathrm{d}\Delta n}{\mathrm{d}t} = \gamma_\parallel(W - \Delta n - P E). \tag{2.6}$$

The variables of this set of equations are the amplitude of the light electric field E, the amplitude of the medium polarization P, the population inversion per unit volume Δn, and the pumping parameter W.

- *Class-A:* $\gamma_{\text{cav}} \ll \gamma_{\parallel}, \gamma_{\perp}$. Class-A lasers are characterized by a long photon lifetime. This type of laser includes atomic gas lasers, dye lasers, and VECSEL. Based on the difference between decay rates, an adiabatic elimination[2] can be applied to reduce the number of equations. The laser system is then described with only one differential equation for the field. The evolution of the active medium variations is supposed to follow the variations of the field instantaneously. Both material variables are eliminated from the set of equations. The dynamical phase space is one-dimensional, and the family of attractors can be represented only by the fixed points. The transient processes in the laser are aperiodic.

- *Class-B:* $\gamma_{\perp} >> \gamma_{\text{cav}} \geq \gamma_{\parallel}$. The field decay rate γ_{cav} and the carrier decay rate $\gamma_{\parallel}$ are smaller than the medium polarization relaxation rate $\gamma_{\perp}$. Class-B is the most commonly used nowadays and includes Ruby, Nd: YAG, CO_2, and semiconductor lasers. Adiabatic elimination leads to the system description with two coupled nonlinear differential equations for the field and the population inversion. The transient process to the steady-state is oscillatory and quasi-periodic. The phase space is two-dimensional and the system trajectory corresponds to the point, limit cycle, and periodic or quasi-periodic attractors depending on the pump value.

- *Class-C:* $\gamma_{\text{cav}} \sim \gamma_{\perp}, \gamma_{\parallel}$. The class is often referred to as a class of lasers with chaotic dynamics. All decay rates have the same scales. Most FIR gas lasers belong to this class. The attractor of the system in the phase space is typically a strange attractor.

  The sketches of the attractors of the mentioned above dynamical classes are shown in Fig. 2.11 following [Wieczorek 2005].

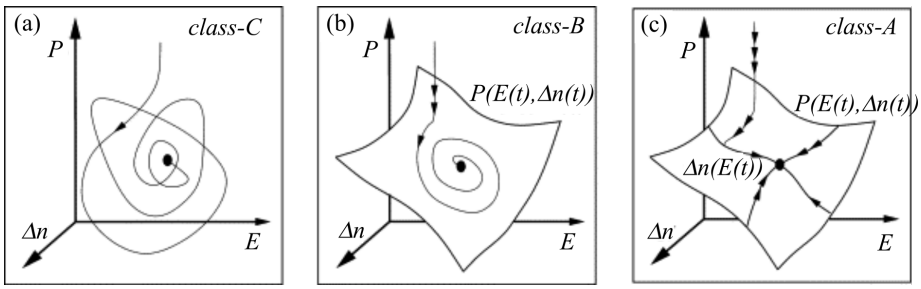

FIGURE 2.11: Sketches of a typical trajectory approaching a stable fixed point in class-C, class-B, and class-A free-running lasers [Wieczorek 2005].

[2] Adiabatic elimination in the context of dynamical systems, is a technique to simplify a complex system of equations by eliminating rapidly oscillating variables. The term "adiabatic" refers to a process that occurs slowly compared to the characteristic time scales of the system. The idea behind adiabatic elimination is to identify variables in a system that evolve much more rapidly than others. By assuming that these fast variables quickly reach quasi-equilibrium states, their dynamics can be effectively removed from the equations governing the slower variables.

- *Class-D:* $\gamma_{cav} >> \gamma_{\parallel}, \gamma_{\perp}$. In this case, the field is an inertia-free variable that follows the state of the atomic system and should therefore be adiabatically eliminated. The class-D lasers are not yet studied experimentally because they require very low-Q cavities and, hence, exotic active media with extremely high spatial density and spectral density of active centers.

The classification is summarised in Table 2.1.

Class	Relaxation rates relation	Eliminated variables	Examples
A	$\gamma_{cav} << \gamma_{\parallel}, \gamma_{\perp}$	P, n	Gas lasers, Dye lasers, VECSEL
B	$\gamma_{\perp} >> \gamma_{cav} >> \gamma_{\parallel}$	P	Ruby, Nd:Yag, CO_2 lasers, VCSEL
C	$\gamma_{cav} \sim \gamma_{\perp}, \gamma_{\parallel}$	–	FIR lasers (NH_3, CH_3F)
D	$\gamma_{cav} >> \gamma_{\parallel}, \gamma_{\perp}$	E	molecular beam masers (H_2, NH_3) lasers - not yet studied experimentally

TABLE 2.1: Classification of the laser dynamical classes with allowed variables for eliminating and examples of the laser active media allowing to observe a certain dynamical class

It is important to note that it is not straightforward to determine dynamics based on the dynamical class. Classification is performed based on the decay parameters of the system. At the same time, optical feedback (OF), multimode laser operation, coupling with neighbors, or any other additional nonlinearities make dynamic classification more complicated. Even the class-A laser (based on the decay rates classification) reveals chaotic behavior, as reported by [Kuwashima 2001].

2.4 Rate-equation model for OP-VECSELs dynamics

The description of the dynamic properties of VECSEL is based on the tracking of the electric field variations oscillating at the frequency ω inside the cavity. The field oscillates as a plane wave due to the fixed direction of polarization. The plane wave propagating in the cavity along z is given by the formula eq. (2.7).

$$\mathscr{E}(z,t) = E_0 E(z,t) e^{-i(\omega t - kz)} + c.c. \tag{2.7}$$

with $c.c.$ designating the complex conjugated term. The quantity $E(z,t)$ is the slowly varying field complex amplitude. It will be considered dimensionless thanks to the introduction of the factor E_0. VECSELs belong to semiconductor lasers, which requires taking into account some peculiarities for the rate-equation model:

- Active medium polarization P decays rapidly so that it can be adiabatically eliminated from the differential equation system, that is, $dP/dt = 0$. Then, at every instant $P(t)$ can be replaced with its steady-state value.

- The carrier lifetime of the semiconductor gain chips is typically a few nanoseconds. The lifetime is considered constant in the manuscript and is taken to be equal to 1 ns, which corresponds to the value we have in our experiment. At the same time, the cavity lifetime is given by the formula eq. (2.8), which represents the relation between the duration of the cavity round trip and the losses per round trip of the cavity:

$$\tau_{\text{cav}} = -\frac{n_0 L_{\text{cav}}}{c_0 \ln\left(R_{DBR} R_{OC}(1-\varepsilon)\right)}, \tag{2.8}$$

  where L_{cav} stands for the round-trip cavity length, c_0 -speed of light, ε - intracavity losses (diffusion, optical components, diffraction losses etc.), R_{DBR} and R_{OC} are reflection coefficients of the cavity-forming mirrors: (DBR - with a distributed Bragg reflector grown as a part of the gain chip and OC - output coupler closing the external cavity [3]).

  Thus the length and the losses of the VECSEL cavity critically determine the VECSEL dynamics.

- One of the fundamental parameters for semiconductor lasers is the above-mentioned (in section 2.2.2) linewidth enhancement factor α that describes the coupling between carrier-induced variations of real and imaginary parts of the media refractive index. This factor couples the equations for phase and amplitude, thus making phase-locking behave differently from other types of lasers.

The rate-equation model can be written phenomenologically or derived from the Maxwell-Bloch equations [Siegman 1986; Erneux 2010] leading to:

$$\frac{\mathrm{d}E}{\mathrm{d}t} = -\left(\frac{1}{2\tau_{\text{cav}}} - \frac{\kappa}{2}(\Delta n(1+i\alpha)\right) E, \tag{2.9}$$

$$\frac{\mathrm{d}\Delta n}{\mathrm{d}t} = \frac{1}{\tau}(\Delta n_0 - \Delta n) - \kappa \Delta n |E|^2. \tag{2.10}$$

- Δn is a carrier density per unit volume, Δn_0 is a non-saturated population inversion per unit volume.

- τ_{cav} is the photon lifetime in the cavity.

- κ is a coupling constant of the stimulated emission, given by $\kappa = \frac{c_0 \sigma}{n V_{\text{cav}}}$, where V_{cav} is a volume of the cavity occupied by the mode, σ - interaction cross-section.

- τ is the carrier lifetime.

[3] Notice that a VECSEl has only one cavity, the external one. There is no "internal" cavity in such structures. The name VECSEL was coined to shred the difference with respect to VCSELs.

- α is the Henry factor.

The field complex amplitude is defined as $E = Ae^{i\phi}$, where A is the amplitude of the field and ϕ is the phase. Both values are supposed to be real numbers. Then, one can separate the imaginary and real parts of the equation:

$$\frac{\mathrm{d}E}{\mathrm{d}t} = \frac{\mathrm{d}A}{\mathrm{d}t}e^{i\phi} + iA\frac{\mathrm{d}\phi}{\mathrm{d}t}e^{i\phi} = - \left(\frac{1}{2\tau_{\mathrm{cav}}} - \frac{\kappa}{2}\Delta n(1+i\alpha)\right) Ae^{i\phi}. \tag{2.11}$$

We modify eqs. (2.9) and (2.10) by introducing a carrier density at threshold defined as $\Delta n_{th} = 1/\kappa\tau_{\mathrm{cav}}$ and an excitation ratio $r = \Delta n_0 \kappa \tau_{\mathrm{cav}}$. The excitation ratio indicates how high the pumping is compared to the threshold, where $r = 1$. The saturation photon number is defined as $F_{\mathrm{sat}} = 1/(\kappa\tau)$. Then, the basic universal set of equations for the description of the dynamics of class B and class A is given by the system (2.12):

$$\begin{aligned} \frac{\mathrm{d}A}{\mathrm{d}t} &= -\frac{1}{2\,\tau_{\mathrm{cav}}}\left(1 - \frac{\Delta n}{\Delta n_{\mathrm{th}}}\right)A, \\ \frac{\mathrm{d}\phi}{\mathrm{d}t} &= \frac{\alpha}{2\,\tau_{\mathrm{cav}}}\frac{\Delta n}{\Delta n_{\mathrm{th}}}, \\ \frac{\mathrm{d}\Delta n}{\mathrm{d}t} &= \frac{r\,\Delta n_{\mathrm{th}}}{\tau} - \frac{\Delta n}{\tau} - \frac{1}{\tau}\frac{A^2}{F_{\mathrm{sat}}}\Delta n. \end{aligned} \tag{2.12}$$

The order of magnitude of the saturation photon number F_{sat} magnitude can be estimated from the experimental parameters:

Calculation of the saturation photon number F_{sat}.

We measured the output power of the VECSEL without any loss-mask. The power is equal to $P = 50\,\mathrm{mW}$ at pumping rate $r = 2.3$. The wavelength of the radiation is $\lambda = 1.06\,\mu\mathrm{m}$. The length of the cavity is $0.5\,\mathrm{m}$ and losses are estimated as 11%. Then, the photon lifetime in the cavity is $\tau_{\mathrm{cav}} = 30\,\mathrm{ns}$.
The photon flux is defined as $\Phi = \dfrac{P}{hc_0/\lambda}$, where $h = 6.62 \times 10^{-34}$ is a Planck constant. This gives the number of the photons in the cavity $F = \tau_{\mathrm{cav}}\Phi = F_{\mathrm{sat}}(r-1)$. Finally, the saturation number of photons is $F_{\mathbf{sat}} \sim 10^{10}$.

Let us illustrate the class-A and class-B transient laser behaviors by two examples. We consider two VECSELs with different cavity lengths. The first one labeled A corresponds to a cavity length of $0.5\,\mathrm{m}$ with 11% losses per round trip, which leads to the photon cavity lifetime $\tau_{A,cav} = 30\,\mathrm{ns}$. These parameters correspond to our experimental values. The second laser labeled B has the same total intracavity losses

(11%), but a significantly smaller cavity length 0.5 mm. This leads to its photon lifetime in the B cavity $\tau_{B,cav} = 30$ ps. Such a "0.5 mm"-cavity length is taken among the smallest ones and its value is close to the VCSELs's cavity length [Larisch 2020]. The plots for the transient amplitude dynamics obtained with the model given by the eq. (2.12) for both cases are shown in Fig. 2.12.

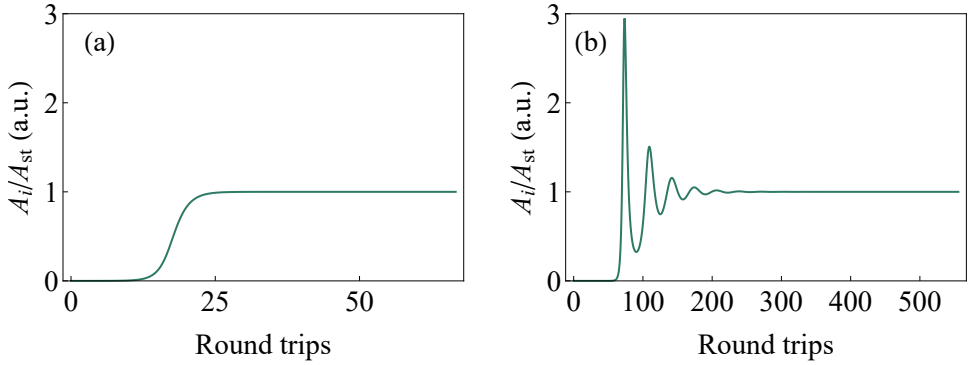

FIGURE 2.12: Amplitude dynamics of the semiconductor lasers with different cavity lifetimes are (a) $\tau_{A,\mathrm{cav}} = 30$ ns, (b) $\tau_{B,\mathrm{cav}} = 30$ ps. (a) represents class-A dynamical behavior, (b) represents class-B dynamical behavior. The plots are calculated with $\tau = 1$ ns, $\alpha = 4, r = 1.5, F_{\mathrm{sat}} = 10^{10}$. The cavity round trip time is $2L/c$, where L is the cavity length.

Fig. 2.12 (a) is a perfect illustration of the monotonous behavior of a class-A VECSEL, while Fig. 2.12 (b) shows the relaxation oscillations typical for class-B lasers. Indeed, the VECSEL laser with our experimental characteristics corresponds to the class-A dynamics without relaxation oscillations. A transition between dynamic classes -A and -B in VECSEL has been experimentally observed by varying the lifetime of the cavity with variations in length [Baili 2009].

Taking $\tau \ll \tau_{\mathrm{cav}}$, we may remove Δn from the equation as being equal to its instantaneous equilibrium value:

$$\Delta n(t) = \frac{r\Delta n_{\mathrm{th}}}{1 + A^2/F_{\mathrm{sat}}} = \frac{1}{\kappa\tau_{\mathrm{cav}}} \frac{r}{(1 + A^2/F_{\mathrm{sat}})}. \tag{2.13}$$

Finally, the equations for the class-A laser have the following form:

$$\begin{aligned} \frac{\mathrm{d}A}{\mathrm{d}t} &= -\frac{1}{2\,\tau_{\mathrm{cav}}} \left(1 - \frac{r}{1 + A^2/F_{\mathrm{sat}}}\right) A, \\ \frac{\mathrm{d}\phi}{\mathrm{d}t} &= \frac{\alpha}{2\,\tau_{\mathrm{cav}}} \frac{r}{1 + A^2/F_{\mathrm{sat}}}. \end{aligned} \tag{2.14}$$

The system eq. (2.14) is valid for a single-mode laser corresponding to the class-A dynamics. To modify the above-developed model for two lasers and later for a complete VECSEL array, it is necessary to parameterize a coupling mechanism.

2.5 Diffraction coupling in the laser arrays

To introduce the coupling between lasers to the rate equation model, we should follow its physical cause in the laser setup. We create a laser array employing a loss-mask close to the OC of the planar degenerate cavity VECSEL. The scheme of the laser cavity is shown in Fig. 2.13.

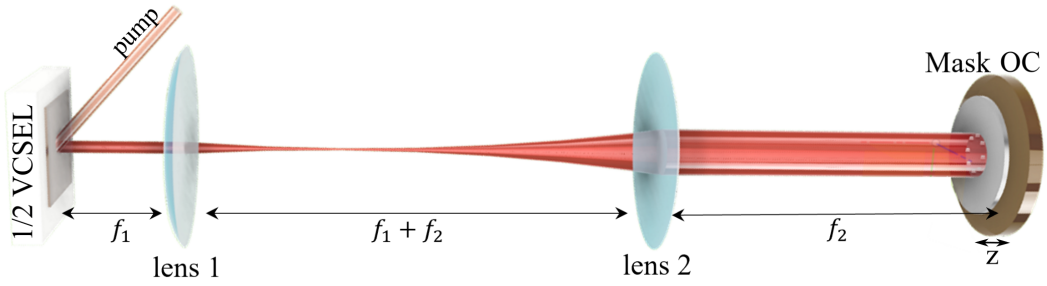

FIGURE 2.13: Scheme of planar degenerate cavity laser. Spatial degeneracy is supported by an intracavity telescope of two lenses with focuses f_1, f_2. Gain chip and output coupler (OC) placed in the focal points of the telescope. The loss-mask is placed very close to the OC.

An array of independent lasers can be obtained if the laser cavity is spatially degenerate (or self-imaging). We can call the cavity degenerate if the gain chip and OC are placed in the focal points of the intracavity telescope [4]. These focal points are given by the focal points of the first and second lenses consequently, when the lenses are separated by a distance equal to the sum of their focal lengths. The focal lengths are $f_1 = 50\,\text{mm}$ and $f_2 = 200\,\text{mm}$ in our experiment. The cavity stability and degeneracy condition are discussed in the sec. 5.3. A loss-mask is an absorbing material, such as metal, with a set of transparent holes. Alternatively, it can be implemented using a spatial light modulator (SLM) or glass plate with a deposited loss profile.

We consider the case when the distance between the Mask and OC z is not zero. Diffraction on the mask leads to an injection coupling between individual lasers. Let us now consider the diffraction path in detail, for example, with a focus on the laser created by the hole i. Fig. 2.14 shows the injection principle of the i-th laser radiation to the closest neighbors. Here, neighbors are the lasers created also by the loss-mask profile. Propagation of the i-th laser field is schematically illustrated by the red color.

[4] With assumptions of the perfect alignment and gain chip without thermal lensing and mechanical deformations.

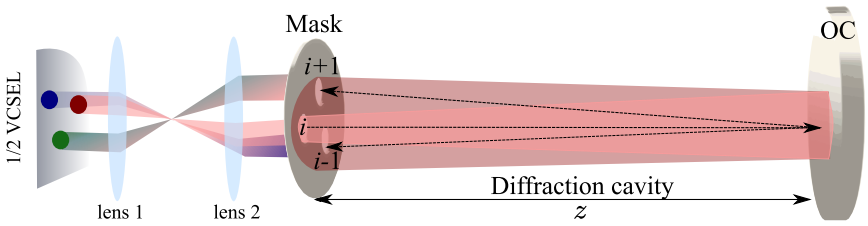

FIGURE 2.14: Principle of injecting coupling on the example of the ring laser array. Self-imaging telescope magnification in the degenerate cavity is not illustrated for simplification reasons.

The order of propagation is shown with black arrows. The field diffracts on the i-th aperture of the mask. Then, diffracted light propagates along the distance z separating the mask and OC. A significant portion of the light returns to the source hole. Another portion of the reflected light is directed toward neighboring holes $i-1$ and $i+1$. Then, these fields are affected by a portion of the diffracted light from the i-th hole.

In the diffraction coupling scenario, the coupling strength is proportional to the spatial overlap of the field between the two considered modes on the mask [Mehuys 1991; Glova 2003; Ma 2022]. The same process occurs on each hole of the loss-mask. The part of the setup between the loss-mask and OC is called the diffraction cavity. A majority of the experiments with solid-state laser arrays are based on a diffraction cavity in which the loss-mask is placed in the self-imaging position of the telescope. Depending on z it can behave as an imaging cavity thanks to the Talbot effect. Talbot effect means that if an optical grating or periodic structure is illuminated with coherent light, the image of the periodic object is self-replicated at certain distances. This self-replication occurs at regular intervals, known as Talbot distances given by the multipliers of Talbot length z_T:

$$z_T = \frac{2h^2}{\lambda}. \tag{2.15}$$

Here h is a center-to-center separation between the emitters or grating period and λ is the wavelength of the light illuminating a loss profile. The example of a diffracted light pattern of a plane periodic profile with a period h is shown in Fig. 2.15.

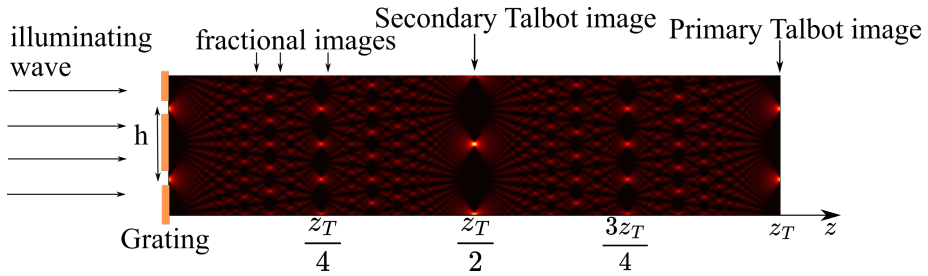

FIGURE 2.15: "Talbot carpet". Diffracted light forms complicated periodic patterns at fractions of the Talbot length.

Fig. 2.15 illustrates multiple fractional Talbot images. The choice of the cavity length z allows control of the phase of the laser field returning to the degenerate cavity. The cavity with a round-trip propagation length equal to z_T gives an in-phase self-imaging configuration of the field. This can be seen by comparison of the bright spots at distance z_T with initial emitters configuration at $z = 0$. Fractions of Talbot distance never give the "in-phase" image, for example, $z_T/2$ leads to π phase accumulation, etc. This type of diffraction cavity is then often called a Talbot cavity. In practice, the same relations are confirmed with solid-state 2D laser arrays, such as ring-array [Tradonsky 2017; Pal 2015].

2.5.1 Model for diffraction coupling

Let us now consider the case we have in our experiment with VECSEL. Considering the mask, presented in Fig. 2.16, the period of the circular array of holes is $h = \sigma + a$, where σ is the diameter of the mask's hole and a is the edge-to-edge distance. Then the Talbot distance is $z_T = \dfrac{2(\sigma + a)^2}{\lambda}$.

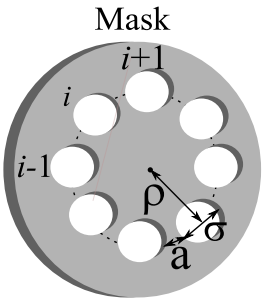

FIGURE 2.16: Graphical definition of the lass-mask parameters. The example is given by the mask with $n = 8$ holes.

The experiment that is performed in this work covers a ring laser array and a pair of lasers with $\sigma = 200\,\mu\text{m}$ and $a = 50\,\mu\text{m}$. Then the Talbot distance calculated with eq. (2.15) is $z_\text{T} = 2(\sigma + a)^2/\lambda = 62\,\text{mm}$. This distance should correspond to the imaging of the array. At the same time, it would create significant diffraction losses. Due to this and the small gain of the laser, the laser developed in our work has a "Talbot-cavity" with a variable length in the range $z = 0 \ldots 2$ mm, corresponding to $z < z_T/50$.

Working at such short distances means that coupling is not zero except at $z \sim 0$. Such a small distance will help us investigate the complex coupling case, which has not been considered for class-A lasers before.

Light diffracted by a given hole creates a coupling channel due to the overlap with the other holes all over the loss-mask. To calculate the overlap between the field diffracted by one aperture and the neighboring aperture we simply suppose that each laser exhibits a uniform distribution at the degenerate cavity output. The amplitude of the i-th laser $E_{0,i}$ is defined as shown in Fig. 2.17.

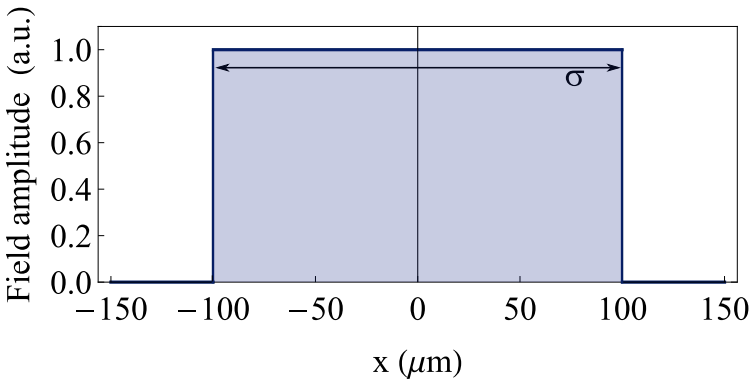

FIGURE 2.17: Distribution of the E_0 field's amplitude at the mask hole surface corresponding to the self-imaging cavity output. Blue – uniform top-hat field's amplitude profile.

The field of one laser diffracts on the edges of the loss-mask and then it transforms with propagation through the diffraction cavity according to the Huygens-Fresnel equation [Siegman 1986]:

$$E_{s,i}(\rho') = i\frac{2\pi}{B\lambda}\int_0^{\sigma_i/2} E_{0,i}\rho \exp\left\{-i\frac{\pi}{B\lambda}(A\rho^2 + D\rho'^2)\right\} J_0\left(\frac{2\pi}{B\lambda}\rho\rho'\right) d\rho, \qquad (2.16)$$

where the *ABCD* matrix describes propagation from the mask to the mirror and back, σ_i is the i-th hole diameter and ρ and ρ' are the radial coordinates for the input and output fields, respectively, described in cylindrical coordinates. Since the output coupler is flat, the matrix elements correspond only to the free-space propagation, $A = D = 1$, $C = 0$, and $B = 2z$. Here z is the distance between the mask and the mirror. It is worth noticing that a similar result would be obtained by considering propagation of the field in the opposite part of the cavity, i. e. from the mask, through the lenses to the gain chip, and back to the mask. Here $E_{0,i}$ holds for the definition of the source field from the hole with a diameter σ_i. The wavelength of the VECSEL is taken to be 1 µm. The diffracted beam profile is strongly oscillatory and mainly depends on the hole size σ and propagation distance z.

Taking into account ABCD coefficients, eq. (2.16) becomes:

$$E_{s,i}(\rho') = \frac{i\pi}{z\lambda}\int_0^{\sigma_i/2} E_{0,i}\rho \exp\left\{\frac{-i\pi(\rho^2 + \rho'^2)}{2z\lambda}\right\} J_0\left(\frac{\pi\rho\rho'}{z\lambda}\right) \mathrm{d}\rho\ . \qquad (2.17)$$

Fig. 2.18 shows a field transformation according to eq. (2.17). The initial field leaving the degenerate cavity comes from the left aperture. Edges of the mask holes are shown as black circles.

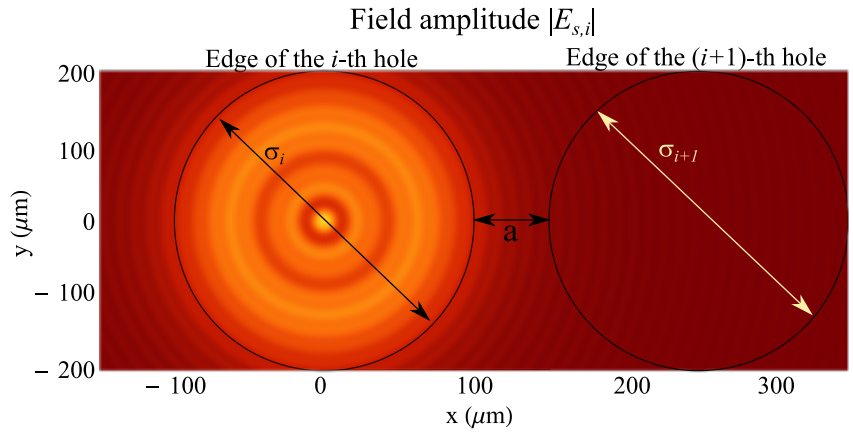

FIGURE 2.18: Top-hat beam ($E_{0,s} = 1$) diffracted on the i-th hole and propagated a round-trip in the diffraction cavity with $z = 500\,\mu$m. Balck circles represent the edges of holes i and $i+1$ with diameters σ_i, σ_{i+1} and edge-to-edge separation a. Diameters of the mask holes are $\sigma_i = 200\,\mu$m, $\sigma_{i+1} = 200\,\mu$m.

Coupling parameterization requires investigation of the overlap of the diffracted laser field with the neighbors. The coupling between the holes is a complex coefficient that is shown to be equivalent to the mode normalized overlap calculated in the following way (adapted from the paper [Ma 2022] to cylindrical coordinates):

$$\kappa_{i\to i+1} = \frac{\int_0^{2\pi} \mathrm{d}\phi_{i+1} \int_0^{\frac{\sigma_{i+1}}{2}} r_{i+1}\mathrm{d}r_{i+1} E^*_{0,i+1}(r_{i+1}) E_{s,i}\left(\sqrt{\rho^2_{i,i+1} + r^2_{i+1} + 2\rho_{i,i+1} r_{i+1}\cos\phi_{i+1}}\right)}{\sqrt{\int_0^{2\pi} \mathrm{d}\phi_i \int_0^{\frac{\sigma_i}{2}} r_i \mathrm{d}r_i |E_{0,i}(r_i)|^2 \int_0^{2\pi} \mathrm{d}\phi_{i+1} \int_0^{\frac{\sigma_{i+1}}{2}} r_{i+1}\mathrm{d}r_{i+1}|E_{0,i+1}(r_{i+1})|^2}}, \tag{2.18}$$

where $\rho_{i,i+1} = \sigma + a$, with a the distance between the edges of the two neighboring holes (see Fig. 2.14 (a)). The (r_i, ϕ_i) and (r_{i+1}, ϕ_{i+1}) are the cylindrical coordinates centered on holes number i and $i+1$, respectively.

We have also supposed that all the laser modes have a cylindrical symmetry and thus depend only on their radial coordinates r_i and r_{i+1}. Then, the denominator of eq. (2.18) simply becomes a constant $\pi\sigma_i\sigma_{i+1}$ in case the initial incident field on the mask holes is a top hat profile.

2.5.2 Dependence on the diffraction cavity length

The dependence of the coupling coefficient $\kappa_{i\to i+1}$ on z is complicated because of the highly oscillatory behavior of the diffracted field $E_{s,i}$. The overlap varies with z according to the curve presented in Fig. 2.19. It shows the evolution of the complex

overlap coefficient $\kappa_{i\to i+1}$ calculated according to eq. (2.16) and eq. (2.18) with the propagation distance z between the mask and the OC.

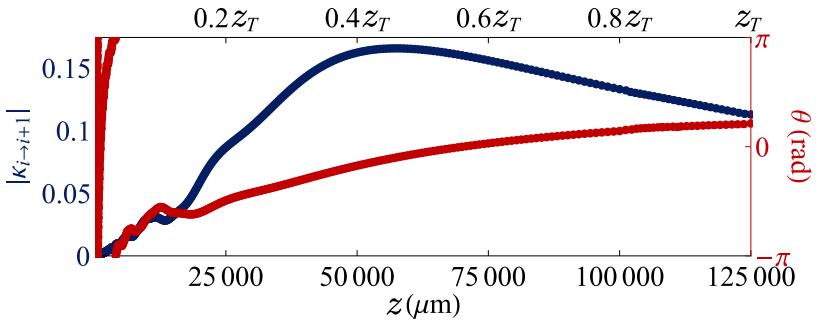

FIGURE 2.19: Evolution of the mode overlap coefficient $\kappa_{i\to i+1}$ versus propagation distance z between the mask and OC , when the incident mode $E_{0,i}$ is a top-hat field. Modulus (blue) and argument (red) of $\kappa_{i\to i+1}$, calculated with eq. (2.18).

This calculation is performed with the parameters of the experiment. The argument of the overlap $\kappa_{i\to i+1}$ tends to zero at z close to z_T. The coupling is then real and can be easily introduced to the equations for the laser dynamics [Bouchereau 2022; Glova 2003].

On the contrary, small values of z correspond to fast oscillations of the argument θ of $\kappa_{i\to i+1}$, which can't be neglected. Let us consider the range of small values of z between 200 µm and 1000 µm more precisely in Fig. 2.20. Distances below 200 µm correspond to rapid changes of the coupling argument θ and very small values of the coupling strength modulus. The control of the coupling argument then would require a micrometer precision of the diffraction length z control, which we can not implement in our experiment today.

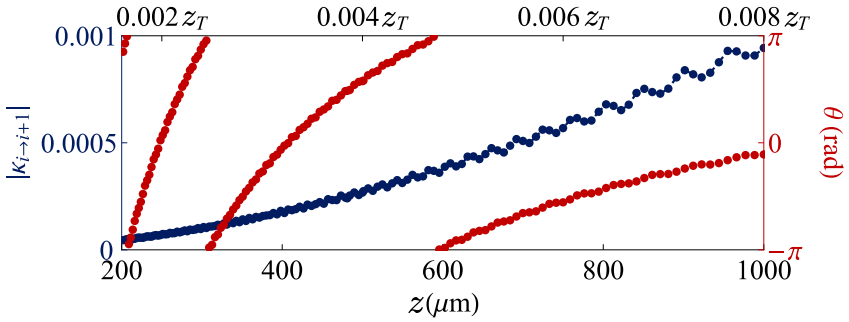

FIGURE 2.20: Evolution of the mode overlap coefficient $\kappa_{i\to i+1}$ versus propagation distance z between the mask and OC for $z \ll z_T$. Modulus (blue) and argument (red) of $\kappa_{i\to i+1}$, calculated with eq. (2.18).

Indeed, it is easy to see that small z values correspond to a fast increase of the argument of $\kappa_{i\to i+1}$, while its modulus varies slowly. This fact provides a wide degree

of freedom to adjust θ, while $|\kappa_{i\to i+1}|$ is marginally constant. It stresses the fact, as well, that the accuracy of z control is critical for the small propagation distances.

2.5.3 Second neighbor influence

Diffraction on the mask can affect more neighbors, than the closest lasers. Thus, it is important to estimate the influence of loss-mask parameters to build the coupling model accurately. In the experiment, we use only loss-masks, which create either an array of two lasers or n-dimensional ring arrays. Considering a ring-array of n lasers, one can notice that the center-to-center separation with the second neighbor $\rho_{i,i\pm2}$ increases with array dimension n according to the formula:

$$\rho_{i,i\pm2} = 2(a+\sigma)\sin\left[\frac{\pi(n-2)}{2n}\right]. \tag{2.19}$$

The center-to-center separation with the closest neighbor remains constant: $\rho_{i,i\pm1} = a+\sigma$. The limit $\lim_{n\to\infty}\rho_{i,i\pm2} = 2(a+\sigma)$ is easy to understand since it corresponds to the in-line laser array geometry. The center-to-center separation with the second laser $\rho_{i,i\pm2}$ reaches the neighborhood of its limiting values fast. Thanks to this, overlap with the second closest hole will not change its value significantly. For example, a difference between $\rho_{i,i\pm2}$ for $n = 30$ and $n = 100$ is less 1% for our experimental parameters.

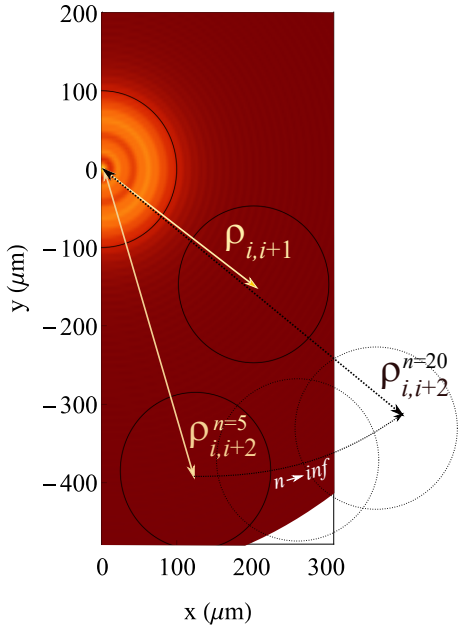

FIGURE 2.21: Mask edges of the first nearest neighbor, a second nearest neighbor in the $n = 5$ and $n = 20$ laser arrays. The background is a distribution of the field amplitude originating from the mask hole at (0,0) after passing a $z = 500\,\mu$m diffraction cavity at the mask plane.

Fig. 2.21 shows an illustration of the mask edges of the two closest neighbors. Separation between the i-th hole and the first neighbor is given by $\rho_{i,i+1}$. And the one for the second neighbor is given by $\rho_{i,i+2}$. The background in this figure is a diffracted wavefront of the top-hat beam in a $z = 500\,\mu$m cavity on the i-th hole. The evolution of the complex overlap coefficient with the second neighbor $\kappa_{i\to i+2}$ is shown in Fig. 2.22. It is calculated according to eq. (2.17), and eq. (2.18) for two different values of z depending on the ring-array dimensions and scaled for the overlap with the closest neighbor.

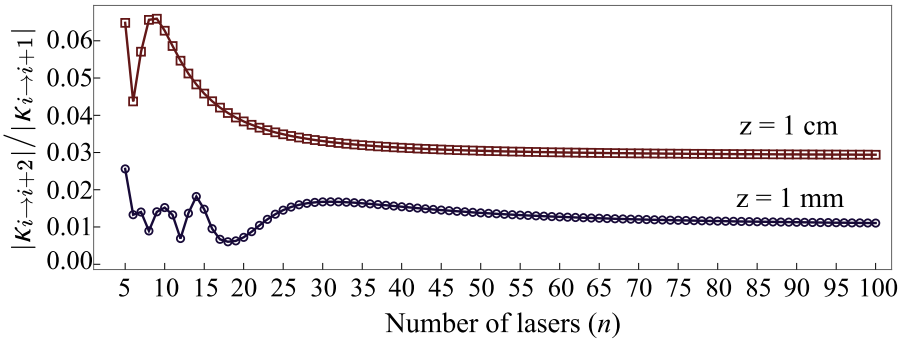

FIGURE 2.22: The ratio of the overlap amplitude with the second nearest neighbor $\kappa_{i\to i+2}$ and the first nearest neighbor $\kappa_{i\to i+1}$ at different z distances: the red line corresponds to $z = 1\,$cm, the blue line corresponds to $z = 1\,$mm.

The overlap with a second nearest neighbor gives just several percent of the overlap with the first neighbor. Considering the experimental range of z, it will not exceed 5% of $\kappa_{i\to i+1}$. This value is negligible and we don't consider the second-neighbour coupling in the upcoming models.

2.6 Phase-locked VECSELs with complex coupling

The coupling coefficient among neighboring lasers might be introduced in the rate equations as an additive term [Erneux 2010; Siegman 1986; Glova 2003]. For example, the system of rate equations for two coupled lasers with identical cavity parameters reads:

$$\frac{dE_1}{dt} = -\left(\frac{1}{2\tau_{cav}} - \frac{\kappa_0}{2}\Delta n_1(1-i\alpha)\right)E_1 + \frac{1}{2}\overbrace{|\kappa_{2\to1}|e^{i\theta_{2\to1}}\frac{c_0}{L_{cav}}E_2}^{\text{coupling with nearest neighbor}}, \tag{2.20}$$

$$\frac{dE_2}{dt} = -\left(\frac{1}{2\tau_{cav}} - \frac{\kappa_0}{2}\Delta n_2(1-i\alpha)\right)E_2 + \frac{1}{2}\overbrace{|\kappa_{1\to2}|e^{i\theta_{1\to2}}\frac{c_0}{L_{cav}}E_1}^{\text{coupling with nearest neighbor}}, \tag{2.21}$$

$$\frac{\mathrm{d}\Delta n_1}{\mathrm{d}t} = \frac{1}{\tau}(\Delta n_{01} - \Delta n_1) - \kappa_0 \Delta n_1 (A_1^2 + \overbrace{\xi_{12} A_2^2}^{\text{cross-saturation}}), \tag{2.22}$$

$$\frac{\mathrm{d}\Delta n_2}{\mathrm{d}t} = \frac{1}{\tau}(\Delta n_{02} - \Delta n_2) - \kappa_0 \Delta n_2 (A_2^2 + \overbrace{\xi_{21} A_1^2}^{\text{cross-saturation}}). \tag{2.23}$$

The notation here is inherited from the single VECSEL laser description in section 2.4. Complex amplitudes of the lasers E_1, E_2 now have additional coupling terms. The overlapped portion of the diffracted field is injected per each round-trip in the VECSEL cavity $1/\tau_{\text{round-trip}} = c_0/L_{\text{cav}}$. Variations of the carrier densities per unit volume $\Delta n_{1,2}$ are also modified due to the presence of a neighbor. A cross-saturation parameter ξ_{ij} characterizes the competition of the lasers due to the common gain media when the carriers are shared between lasers. Thanks to the spatial degeneracy of the laser cavity, the overlap in the gain region is negligible, and the cross-saturation is taken to be zero: $\xi_{ij} = 0$. For simplicity, we also take identical carrier lifetimes τ, photon lifetime in the cavity τ_{cav}, κ_0 coupling constants of the stimulated emission and, of course, Henry factor α.

Identical mask-holes lead to symmetry in the fields overlap, i.e. $(\kappa_{1\to 2} = \kappa_{2\to 1})$. We introduced a new variable to parameterize the coupling strength $|\kappa_{i\to j}| c_0/L_{\text{cav}} = |\eta_{i,j}|/\tau_{\text{cav}}$, which describes the overlap scaled by the intracavity losses. Following the same methodology as presented in section 2.4 we simplify eq. (2.23) with the help of adiabatic elimination of Δn_i, whose instant values are defined according to:

$$\Delta n_i(t) = \frac{\Delta n_{\text{th,i}} r}{1 + A_i^2/F_{\text{sat}}} = \frac{1}{\kappa_0 \tau_{\text{cav}}} \frac{r_i}{(1 + A_i^2/F_{\text{sat}})}, \tag{2.24}$$

where $i = 1, 2$, pumping rate $r = \Delta n_0 \tau_{\text{cav}} \kappa_0$ and saturation photon number $F_{\text{sat}} = 1/(\kappa_0 \tau)$. After substitution of the formula into eq. (2.23), we separate real and imaginary parts of the complex field amplitudes E_1, E_2. Finally, the rate equations for the two diffraction-coupled lasers in the degenerate cavity take the form:

$$\begin{aligned}
\frac{\mathrm{d}A_1}{\mathrm{d}t} &= -\frac{A_1}{2\tau_{\text{cav}}}\left(1 - \frac{r}{1 + A_1^2/F_{\text{sat}}}\right) + \frac{|\eta|}{2\tau_{\text{cav}}}\cos(\psi + \theta) A_2, \\
\frac{\mathrm{d}A_2}{\mathrm{d}t} &= -\frac{A_2}{2\tau_{\text{cav}}}\left(1 - \frac{r}{1 + A_2^2/F_{\text{sat}}}\right) + \frac{|\eta|}{2\tau_{\text{cav}}}\cos(\psi - \theta) A_1, \\
\frac{\mathrm{d}\psi}{\mathrm{d}t} &= \frac{\alpha}{2\tau_{\text{cav}}}\left(\frac{r}{1 + A_2^2/F_{\text{sat}}} - \frac{r}{1 + A_1^2/F_{\text{sat}}}\right) - \\
&\quad - \frac{|\eta|}{2\tau_{\text{cav}}}\left(\frac{A_1}{A_2}\sin(\psi - \theta) + \frac{A_2}{A_1}\sin(\psi + \theta)\right) + \Omega,
\end{aligned} \tag{2.25}$$

where A_1 and A_2 are the amplitudes of the two laser fields, normalized so that their squares correspond to the respective photon numbers. The third variable ψ is the

phase-difference between the lasers and Ω is the detuning between the laser's free-running oscillation frequencies.

2.6.1 Critical coupling

Our main interest is to estimate the parameters of the system when two lasers are phase-locked. This means the system of several oscillators has stabilized phase-differences and, thus, oscillates together as one. Depending on the coupling strength, it is known that coupled lasers with non-zero frequency detuning Ω can reveal different dynamical regimes [Erneux 2010; Siegman 1986; Glova 2003], which indicate proximity to phase-locking. Let us first visualize these regimes in the case of a real coupling ($\theta = 0$). Fig. 2.23 shows results of numerical integration of eqs. (2.25) with different values of detuning Ω between lasers, but with the same random initial conditions.

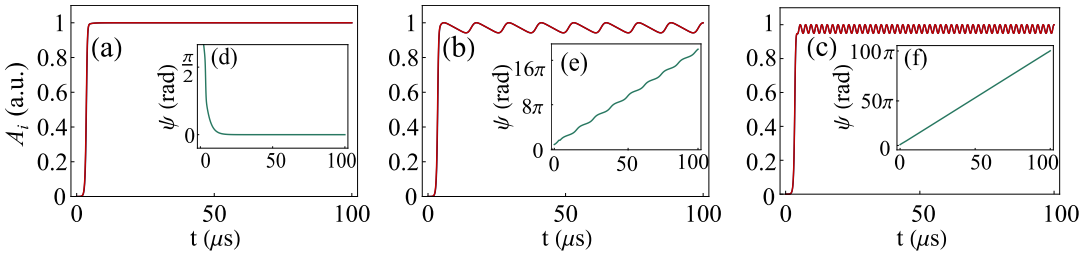

FIGURE 2.23: Phase-locking dynamics of two lasers with different detuning values. The subplots (a,b,c) represent the amplitudes A_i and the inset subplots (d,e,f) show the phase-difference ψ. Here (a, d) calculated with $\Omega = 0$, (b,e) with $\Omega/2\pi = 100$ kHz, and (c, f) - with $\Omega/2\pi = 500$ kHz. Coupling strength $|\eta| = 0.005$, $\alpha = 4, r = 1.2, F_{\text{sat}} = 10^{10}$.

Phase-difference ψ stabilizes around constant value $\psi = 0$ in the system with zero-detuning (subplot (d) of Fig. 2.23). This means that the lasers oscillate coherently "in-phase". The situation is different in the cases (e) and (f). Subplot (e) shows a "stairs"-like the behavior of the phase-difference, which tends to be locally stabilized [5]. However, the phase-difference constantly increases because the coupling strength is insufficient to balance the detuning. It is similar to the case (f), but this one doesn't have even local stability of the phase-difference. The modulus of the coupling strength is taken $|\eta| = 0.005$, which corresponds to a diffraction coupling length z around 700 μm.

To investigate the border between those regimes, we can numerically calculate the phase-difference at a fixed time[6] ($t = 0.1$ ms) with different values of $|\eta|$. The curves calculated for different detuning values are shown in Fig. 2.24.

[5] This regime is equivalent to the coherent spikes in class-B lasers [Nixon 2011]

[6] The time is chosen when the phase-looking is reliably expected.

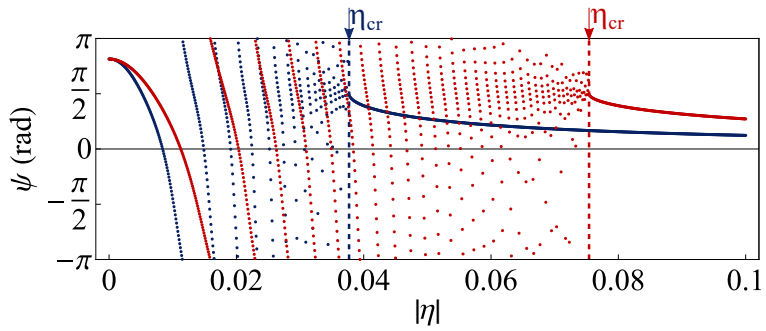

FIGURE 2.24: Phase-difference at $t = 0.1$ ms calculated with section 2.6. Different colors of the curves correspond to the different detuning values. Red - $\Omega/2\pi = 200$ kHz, Blue - $\Omega/2\pi = 400$ kHz. Steady-state phase-difference is $\psi = \pi/2$ at the coupling strength equal to the critical coupling value marked by the vertical dashed lines of the corresponding color.

It can be noticed that the minimal coupling strength allowing phase-locking corresponds to the phase-difference $\psi = \pi/2$. This fact is also noticed and reported by several groups [El-Nashar 2009; Silber 1993] in class-B lasers. Two lasers phase-locking requires an absolute value of the coupling strength to exceed the critical coupling value $|\eta| \geq \eta_{cr} = \Omega\tau_{cav}$ [Fabiny 1993].

The values of the critical coupling calculated with this formula are shown as dashed lines in Fig. 2.24. They are marked with arrows of color corresponding to the plotted data. A smaller detuning value is shown in red. This η_{cr} value is proportionally lower than the one shown in blue for the larger detuning. This formula is valid in the case where the lasers have identical parameters in terms of pumping rate, losses, cavity lifetime, and real-valued coupling strength η. To correct the formula $\eta_{cr} = \Omega\tau_{cav}$ for the case of the complex coupling we should first consider the steady-states of the system.

2.6.2 Steady-state solutions

Two lasers are phase-locked in the global steady-state when both amplitudes and the phase-difference are stabilized, i.e.

$$\frac{dA_1}{dt} = 0, \quad \frac{dA_2}{dt} = 0, \quad \frac{d\psi}{dt} = 0. \tag{2.26}$$

These derivatives are defined according to eqs. (2.25). One can see that equal amplitudes A_1, A_2 in the steady-state are only possible if the coupling is real, i.e. its argument is $\theta = 0$ or π. Real coupling leads to the simple analytical solutions for the

system's steady-state [Karuseichyk 2023]:

$$A_{1,st} = A_{2,st} = \sqrt{F_{\text{sat}}\left(\frac{r}{1-|\eta|\cos\psi_{st}} - 1\right)},$$
$$\psi_{\text{st}} = \begin{cases} \arcsin\dfrac{\Omega\tau}{|\eta|} + 2\pi m, m \in \mathbb{Z}, & \text{stable for } \theta = 0 \\ \pi - \arcsin\dfrac{\Omega\tau}{|\eta|} + 2\pi m, m \in \mathbb{Z}, & \text{stable for } \theta = \pi\ . \end{cases} \tag{2.27}$$

In the general case, we can estimate the steady-state amplitudes using a small coupling approximation. Then, two lasers are phase-locked with different amplitudes given by the solutions of the first two equations in the system (2.26):

$$A_{1,\text{st}} = \sqrt{F_{\text{sat}}(r-1)}\left(\frac{r}{r-1}\frac{|\eta|}{2}\cos(\psi_{\text{st}}+\theta)+1\right) + \mathscr{O}(|\eta|^2),$$
$$A_{2,\text{st}} = \sqrt{F_{\text{sat}}(r-1)}\left(\frac{r}{r-1}\frac{|\eta|}{2}\cos(\psi_{\text{st}}-\theta)+1\right) + \mathscr{O}(|\eta|^2). \tag{2.28}$$

Here the expansion over coupling strength $|\eta|$ is used, assuming that $|\eta| \ll 1$. We substitute these solutions into the third equation of the system (2.26) and after a series of simplifications we obtain an analytical formula for the phase-difference ψ_{st}:

$$\psi_{\text{st}} = \begin{cases} \arcsin\dfrac{\Omega\tau}{|\eta|(\cos\theta+\alpha\sin\theta)} + 2\pi m, m \in \mathbb{Z}, \\ \pi - \arcsin\dfrac{\Omega\tau}{|\eta|(\cos\theta+\alpha\sin\theta)} + 2\pi m, m \in \mathbb{Z}. \end{cases} \tag{2.29}$$

This expression takes real values indicating phase-locking when the argument of the arcsine is less than one, i.e.

$$|\eta| > \frac{\Omega\tau}{(\cos\theta+\alpha\sin\theta)}.$$

Then, a minimal modulus of the coupling strength, that allows the phase-locking is

$$\eta_{\text{cr}} = \frac{\Omega\tau}{(\cos\theta+\alpha\sin\theta)}, \tag{2.30}$$

and the phase-difference is $\psi_{st} = \pi/2$ as it is for the purely real coupling. In these analytical results we can see a similarity with a relation developed by several groups [Gao 2018; Dave 2020; Bouwmans 2000] for the micro-lasers and VCSELs.

We found our results comparable, even though these groups studied arrays phase-locking by different coupling mechanisms, and the dynamical class of their system is class-B. To check how legitimate is the obtained relation, we compare its values with numerical solutions of the eqs. (2.25) in Fig. 2.25.

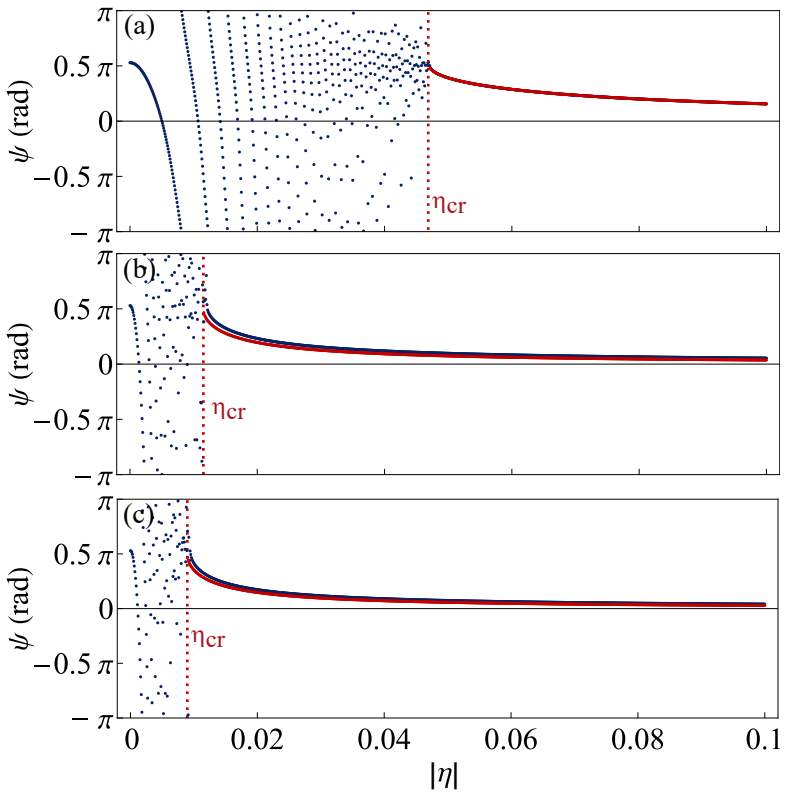

FIGURE 2.25: Phase-difference dependency of the coupling strength modulus with different values of the coupling argument. The blue color gives results of numerical solution eqs. (2.25) for ψ at $t = 0.1$ ms. The Red color shows the data calculated by approximation formula eq. (2.29). Subplots calculated with (a) $\theta = 0$, (b) $\theta = \pi/6$, (c) $\theta = \pi/4$. The vertical dashed lines illustrate critical coupling values given by the eq. (2.30). Here $\alpha = 4, \Omega/2\pi = 250$ kHz

One can see from Fig. 2.25, that the admitted approximation leads to the accurate solutions. Phase-difference at the critical coupling strength is equal to $\psi_{st} = \pi/2$. An interesting result is that the non-zero coupling argument θ leads to a lower critical coupling threshold. It means that detuned pairs of lasers are crucially easier to phase-lock at small z with non-zero θ, which leads to a decrease of $\mathrm{Re}[\eta]$.

Based on eq. (2.30) critical coupling value also depends on the value of the α factor. Its values characteristic for VECSEL's gain chips will also lower critical coupling if compared to solid-state lasers. Amplitudes defined according to eq. (2.28) with a substitution of eq. (2.30) give a deviation range of less than one percent when compared with numerical results. Due to this, we consider that the total solution is accurate.

Finally, the stability of the obtained steady-state must be assessed.

2.6.3 Stability of the steady-state solutions

Stability analysis of the differential equation system solutions is commonly performed with the help of Jacobian matrix **J**. We obtain this matrix by linearising the differential equations system 2.25 around the investigated steady-state solution $A_{1,st}, A_{2,st}, \psi_{\text{st}}$:

$$\mathbf{J}(A_{1,\text{st}}, A_{2,\text{st}}, \psi_{\text{st}}) \equiv \left(\begin{array}{ccc} \frac{\partial \frac{\mathrm{d}A_1}{\mathrm{d}t}}{\partial A_1} & \frac{\partial \frac{\mathrm{d}A_1}{\mathrm{d}t}}{\partial A_2} & \frac{\partial \frac{\mathrm{d}A_1}{\mathrm{d}t}}{\partial \psi} \\ \frac{\partial \frac{\mathrm{d}A_2}{\mathrm{d}t}}{\partial A_1} & \frac{\partial \frac{\mathrm{d}A_2}{\mathrm{d}t}}{\partial A_2} & \frac{\partial \frac{\mathrm{d}A_2}{\mathrm{d}t}}{\partial \psi} \\ \frac{\partial \frac{\mathrm{d}\psi}{\mathrm{d}t}}{\partial A_1} & \frac{\partial \frac{\mathrm{d}\psi}{\mathrm{d}t}}{\partial A_2} & \frac{\partial \frac{\mathrm{d}\psi}{\mathrm{d}t}}{\partial \psi} \end{array} \right) \Bigg|_{A_{1,st}, A_{2,st}\, \psi_{\text{st}}} \tag{2.31}$$

When the steady-state $(A_{1,\text{st}}, A_{2,\text{st}}, \psi_{\text{st}})$ experiences some perturbations, the response of the system is determined by the eigenvalues λ_i of the Jacobian matrix $\mathbf{J}(A_{1,\text{st}}, A_{2,\text{st}}, \psi_{\text{st}})$. In the general case, the eigenvalues are complex, their number is given by the rank of the Jacobian. Steady-state $(A_{1,\text{st}}, A_{2,\text{st}}, \psi_{\text{st}})$ is stable if all real parts of λ_i are negative.

It is easy to understand stability criteria following the changes in systems phase-trajectory. Instant amplitudes and phase-differences can be added to the three- dimensional phase space. It has three dimensions because our system has three variables A_1, A_2, ψ and the rank of the Jacobian is three. The distance between the two sequential points of the phase-trajectory is proportional to a combination of the $e^{\lambda_i t}$. If all real parts of Jacobian eigenvalues λ_i are negative all $e^{\lambda_i t}$ converge to the zero with time. This indicates the stability of the system and says that perturbations are damped. A positive eigenvalue, on the contrary, leads to the exponential growth $e^{\lambda_i t}$ in time. The solution diverges and potential steady-state $A_{1,\text{st}}, A_{2,\text{st}}, \psi_{\text{st}}$ is unstable then.

Steady-state solutions are developed in the previous section.

$$\begin{aligned} A_{1,st} &= \sqrt{F_{\text{sat}}(r-1)} \left(\frac{r}{r-1} \frac{|\eta|}{2} \cos(\psi_{\text{st}} + \theta) + 1 \right), \\ A_{2,st} &= \sqrt{F_{\text{sat}}(r-1)} \left(\frac{r}{r-1} \frac{|\eta|}{2} \cos(\psi_{\text{st}} - \theta) + 1 \right), \\ \psi_{\text{st}} &= \begin{cases} \arcsin \dfrac{\eta_{\text{cr}}}{|\eta|} + 2\pi m, m \in \mathbb{Z} \\ \pi - \arcsin \dfrac{\eta_{\text{cr}}}{|\eta|} + 2\pi m, m \in \mathbb{Z}, \end{cases} \\ \eta_{\text{cr}} &= \frac{\Omega\tau}{(\cos\theta + \alpha \sin\theta)}. \end{aligned} \tag{2.32}$$

It was shown, that there are two solutions for the phase-differences ψ_{st}, which we

would like to investigate. Each solution consequently leads to the corresponding Jacobian matrix and different sets of eigenvalues. Based on the calculated eigenvalues shown in Fig. 2.26 both steady-states ψ_{st} show symmetric stability regions around $|\eta| = 0$ for $\theta = 0$. The eigenvalue are real, when $|\eta| \geq \eta_{cr}$.

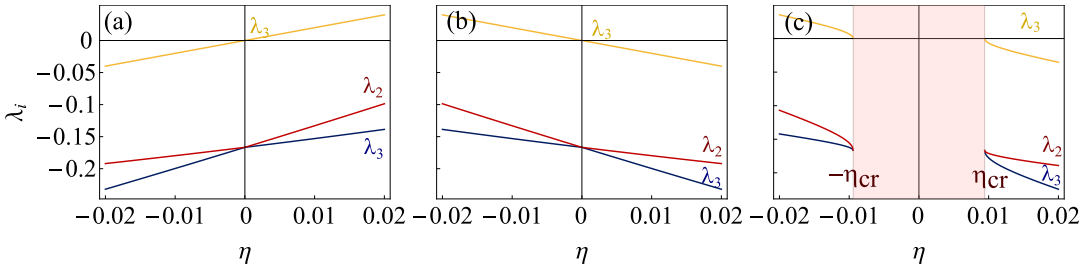

FIGURE 2.26: Jacobian eigenvalues $\lambda_1, \lambda_2, \lambda_3$. Subplot (a) represent stability of steady-state with $\psi_{st} = \pi - \arcsin\frac{\eta_{cr}}{|\eta|}$. Subplots (b,c) shows eigenvalues for $\psi_{st} = \arcsin\frac{\eta_{cr}}{|\eta|}$. Subplots (a, b) are calculated with $\Omega = 0$. Subplot (c) calculated with $\Omega/2\pi = 50\,\text{kHz}$ and shows an unstable region limited by η_{cr} marked with light-red. Here $\alpha = 4, r = 1.2, F_{sat} = 10^{10}, \theta = 0$.

The steady-state solution $\psi_{st} = \pi - \arcsin\dfrac{\eta_{cr}}{|\eta|}$ is stable if η is negative and $\psi_{st} = \arcsin\dfrac{\eta_{cr}}{|\eta|}$ is stable in case η is positive. A non-zero detuning Ω leads to a non-zero minimal coupling value required for laser phase-locking. This results in a shift of the stability regions for a constant η_{cr} (light red region if Fig. 2.26 (c)). At the same time, it does not affect conclusions regarding the sign of the required positive and negative coupling.

Among the three eigenvalues presented in Fig. 2.26, only λ_3-curve crosses zero and changes its sign. The global stability of the steady-state thus depends only on the sign of λ_3. Due to this, further plots represent only the values of λ_3.

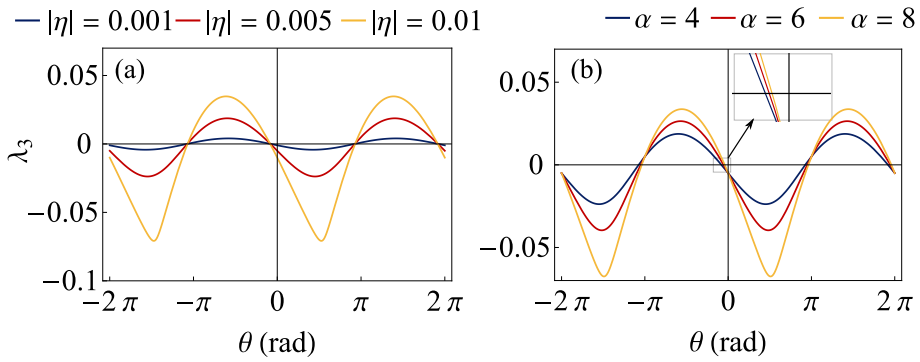

FIGURE 2.27: Dependency of the real parts of the eigenvalue λ_3 on θ. Subplot (a) shows the effect of different $|\eta|$ values, when when $\alpha = 4$ and. Subplot (b) shows the effect of α when $|\eta| = 0.005$. Here $r = 1.2, F_{sat} = 10^{10}, \Omega = 0$.

Fig. 2.27 shows the effect of the complex coupling argument and Henry factor on stability regions for steady-state phase-difference $\psi_{st} = \pi - \arcsin\frac{\eta_{cr}}{|\eta|}$. Both α and $|\eta|$ change the absolute value of the eigenvalues λ_3. More important is the range, where λ_3 is negative. The range doesn't depend on $|\eta|$, but different α weakly shift the boundaries, as shown in the inset. This shift is connected with the critical coupling dependency on the Henry factor. All conclusions here are valid for phase-locked cases, which clearly satisfy condition $|\eta| \geq \eta_{cr}$, as mentioned above. To conclude, we can also look at the signature of the critical coupling value $|\eta_{cr}|$ in λ_3 depending on detuning. Fig. 2.28 gives a dependence of $\mathrm{Re}[\lambda_3]$ for $\theta = 0$ in subplot (a) and $\theta = \pi/4$ in subplot (b) on coupling strength modulus and detuning.

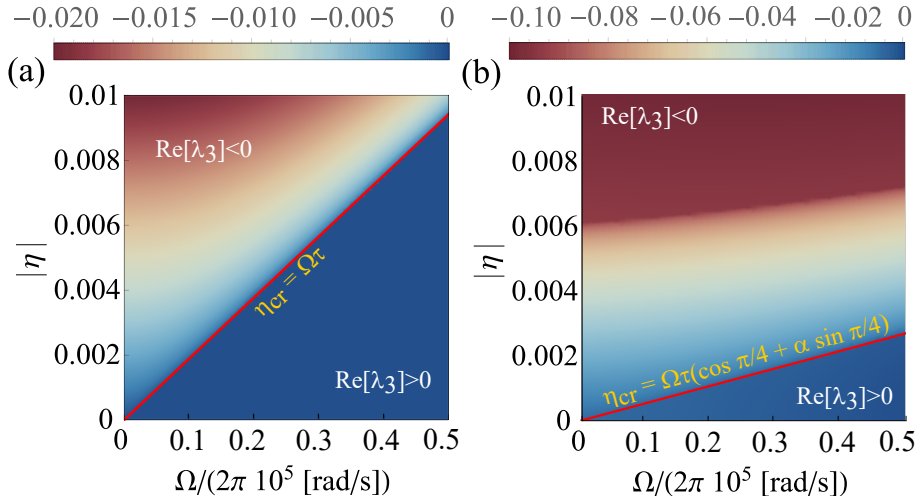

FIGURE 2.28: Real part of the eigenvalue λ_3 depending on the detuning values and the coupling value $|\eta|$ with fixed parameters $\alpha = 4, r = 1.2, F_{sat} = 10^{10}, \theta = 0$. The argument of the complex coupling is (a) $\theta = 0$ and (b) $\theta = \pi/4$.

The red line in Fig. 2.28 is given by the formula for the critical coupling value η_{cr} for correspondent detuning Ω and coupling argument θ. The line separates the region of positive and negative values of $\mathrm{Re}[\lambda_3]$. Positive values lay below the red curve for both (a) and (b) subplots and correspond to the unstable region of parameters.

This analysis confirms the analytical results of eq. 2.30. At the same time, θ affects the laser dynamics in a complicated manner. There is a range of parameters in Fig. 2.28 (b), where the system is stable ($\mathrm{Re}[\lambda_3] < 0$) but the imaginary part of the eigenvalue λ_3 is not equal to zero. A non-zero imaginary part indicates the existence of oscillation of the system's parameter around the steady-state on the way to synchronization. Fig. 2.29 shows the imaginary part of λ_3 for $\theta = 0$ in subplot (a) and $\theta = \pi/4$ in subplot (b) as a function of the coupling strength modulus $|\eta|$ and detuning Ω.

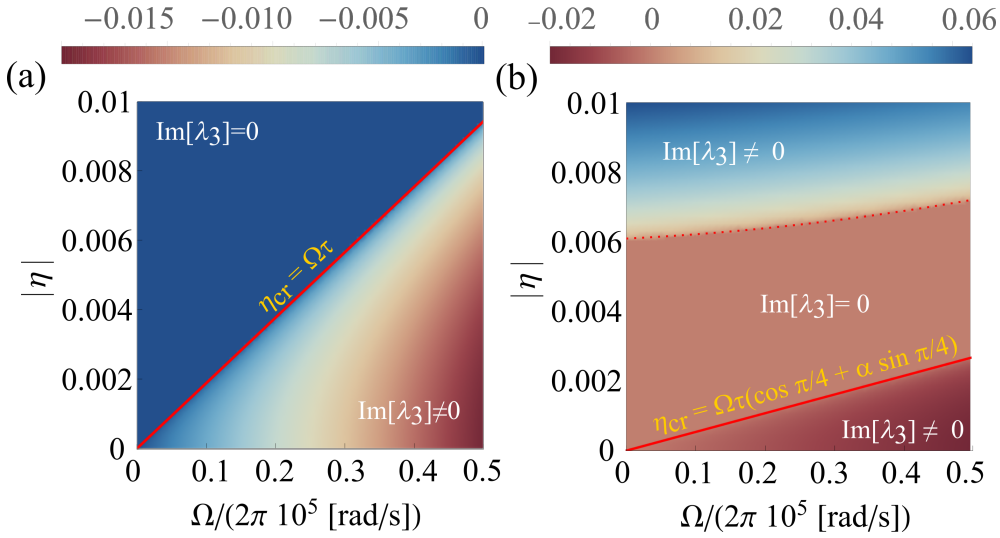

FIGURE 2.29: Imaginary part of the eigenvalue λ_3 depending on the detuning values and the coupling value $|\eta|$ with fixed parameters $\alpha = 4, r = 1.2, F_{\text{sat}} = 10^{10}, \theta = 0$. The argument of the complex coupling is (a) $\theta = 0$ and (b) $\theta = \pi/4$.

The stable region (above the red line in Fig. 2.29) reveals different valued of $\text{Im}[\lambda_3]$ at fixed $|\eta|$ and Ω with different θ ($\theta = 0$ in subplot (a) and $\theta = \pi/4$ in subplot (b)). Thus, this suggests to expect θ to influence the steady-state reaching time.

Indeed, Fig. 2.30 shows a difference in the stabilization time of the system's amplitudes A_1, A_2 and phase-difference ψ with different θ values. Here coupling strength modulus $|\eta|$ is taken identical among all cases. A two-laser system reaches its steady-state more rapidly with $\theta = \pi/8, \theta = \pi/4$, than with $\theta = 0$, i.e. when the imaginary part of the coupling coefficient increases.

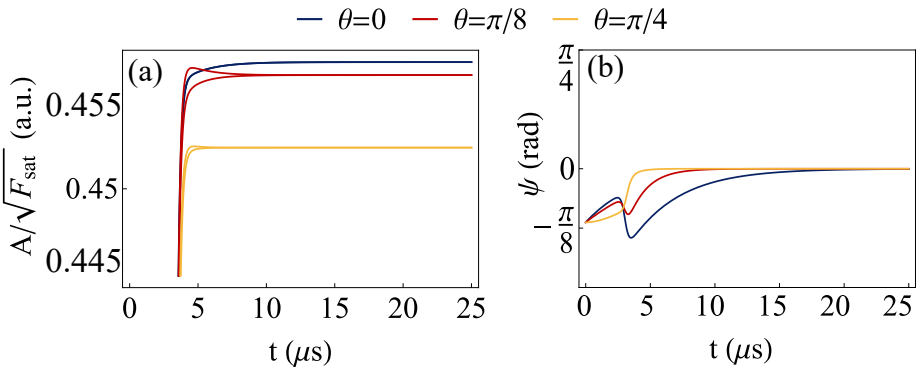

FIGURE 2.30: Phase-locking dynamics of two lasers with different values of the coupling argument θ shown in different colors. Subfigure (a) shows amplitude dynamics A_1, A_2 and (b) shows dynamics of phase-difference. $\alpha = 4, r = 1.2, F_{\text{sat}} = 10^{10}, |\eta| = 0.007, \Omega/2\pi =$ 50 kHz.

However, physically, different θ values correspond to a different modulus of the coupling coefficient $|\eta|$ and this comparison is not very accurate. However, the modeled case can be compared with a value corresponding to a small diffraction distance length, such as z around 340 µm (see Fig. 2.20), where the absolute value of the overlap changes much slower than the argument. All curves correspond to the same initial conditions.

2.6.4 Coupled VECSELs with different cavity parameters

Before, the asymmetry of the two laser systems was introduced only through the detuning Ω between the lasers. This can be caused by mechanical misalignments of the optical system, aberrations, and other factors that alter the details of the laser cavity. Additionally, variations in the pumping rate r may occur due to non-uniform processes across the semiconductor gain chip. The same factors can impact the losses in the cavity and lead to variations in the cavity length, thereby influencing the photon lifetime in the cavity (τ_{cav}). In case these laser parameters are different from one laser to the other, the rate-equation system must be modified. The rate equations for a pair of lasers with non-symmetrical system parameters read as follows:

$$\begin{aligned}
\frac{\mathrm{d}A_1}{\mathrm{d}t} &= -\frac{A_1}{2\tau_{\mathrm{cav},1}}\left(1-\frac{r_1}{1+A_1^2/F_{\mathrm{sat}}}\right)+\frac{|\eta|}{2\tau_{\mathrm{cav},1}}\cos(\psi+\theta)A_2\ ,\\
\frac{\mathrm{d}A_2}{\mathrm{d}t} &= -\frac{A_2}{2\tau_{\mathrm{cav},2}}\left(1-\frac{r_2}{1+A_2^2/F_{\mathrm{sat}}}\right)+\frac{|\eta|}{2\tau_{\mathrm{cav},2}}\cos(\psi-\theta)A_1\ ,\\
\frac{\mathrm{d}\psi}{\mathrm{d}t} &= \frac{\alpha}{2}\left(\frac{r_2}{(1+A_2^2/F_{\mathrm{sat}})\tau_{\mathrm{cav},2}}-\frac{r_1}{(1+A_1^2/F_{\mathrm{sat}})\tau_{\mathrm{cav},1}}\right)\\
&\quad -\frac{|\eta|}{2}\left(\frac{1}{\tau_{\mathrm{cav},2}}\frac{A_1}{A_2}\sin(\psi-\theta)+\frac{1}{\tau_{\mathrm{cav},1}}\frac{A_2}{A_1}\sin(\psi+\theta)\right)+\Omega\ . \qquad (2.33)
\end{aligned}$$

The laser phase-locking can still be observed in this case as well if the coupling strength $|\eta|$ is large enough to compensate for these differences.

We are interested again in the estimation of the critical coupling strength with a simple analytical formula. The rate-equation system is more complicated in this case, however, we repeat the earlier established approach for the approximation of the amplitude steady-state solution when the coupling is small. Then, the steady-state amplitudes are given by:

$$\begin{aligned}
A_{1,\mathrm{st}} &= \left(\sqrt{F_{\mathrm{sat}}(r_2-1)}\frac{r_1}{r_1-1}\frac{|\eta|}{2}\cos(\psi_{\mathrm{st}}+\theta)+\sqrt{F_{\mathrm{sat}}(r_1-1)}\right),\\
A_{2,\mathrm{st}} &= \left(\sqrt{F_{\mathrm{sat}}(r_1-1)}\frac{r_2}{r_2-1}\frac{|\eta|}{2}\cos(\psi_{\mathrm{st}}-\theta)+\sqrt{F_{\mathrm{sat}}(r_2-1)}\right). \qquad (2.34)
\end{aligned}$$

Then, we make an additional approximation, considering $\psi_{\mathrm{st}}=\pi/2$ at the critical coupling. Using this, we obtain a critical coupling value given by the eq.(2.35).

$$\eta_{cr} = \frac{\alpha|\tau_2 - \tau_1| + 2\tau_1\tau_2\Omega}{\left(\sqrt{\frac{r_1-1}{r_2-1}}\tau_1 + \sqrt{\frac{r_2-1}{r_1-1}}\tau_2\right)(\cos\theta + (\tau_1+\tau_2)\alpha\sin\theta)}. \tag{2.35}$$

When parameters are identical ($r_1 = r_2$ and $\tau_1 = \tau_1$) the formula becomes eq. (2.30). The phase-difference is based on the same arcsine dependency given by eq. (2.36) on the updated critical coupling value η_{cr}.

$$\psi_{st} = \begin{cases} \arcsin\dfrac{\eta_{cr}}{|\eta|} + 2\pi m, m \in \mathbb{Z} \\ \pi - \arcsin\dfrac{\eta_{cr}}{|\eta|} + 2\pi m, m \in \mathbb{Z}\,, \end{cases} \tag{2.36}$$

To validate the obtained formula, we calculate phase-difference at a fixed time $t = 0.5\,\text{ms}$ with different values of the coupling strength. We are doing this in the same manner, as we did for identical lasers parameters case (shown in Fig. 2.24). Numerically calculated phase-differences with eqs. (2.33) are presented in blue and red color in Fig. 2.31 for three different values of coupling argument $\theta = 0, \pi/6, \pi/4$.

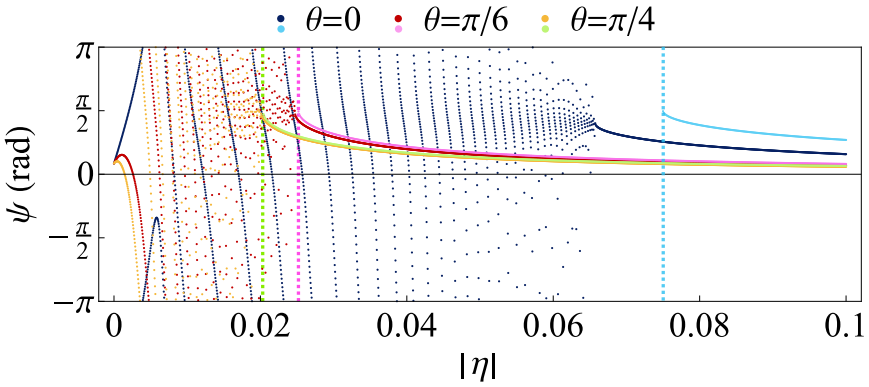

FIGURE 2.31: Phase-locking process of two lasers with different pumping rates ($r_1 = 1.2, r_2 = 1.1$) and photon lifetimes in the cavity $\tau_1 = 30.15\,\text{ns}, \tau_2 = 30\,\text{ns}$, $\Omega/2\pi = 250\,\text{kHz}$. Other parameter $\alpha = 4, F_{sat} = 10^{10}$.

Approximated values with eq. (2.32) and eq. (2.35) are shown in bright blue, pink, and green colors. These data overlap with numerically calculated curves completely for $\theta = \pi/6$ and $\pi/4$. Eventually, the maximal difference between approximated and numerically calculated values is given by $\theta = 0$. It occurs because the phase-difference is notably different from $\pi/2$ at the critical coupling value in this case. This deviation leads to an overestimation of the minimal coupling strength value with eq. (2.35). Nevertheless, this does not contradict phase-locking criterion $|\eta| > \eta_{cr}$.

2.7 Conclusion to chapter 2

This chapter introduces a first step in the understanding of the VECSEL array phase-locking dynamics. Herein, we introduced principles governing laser emission generation in this type of laser.

We highlighted the advantage of VECSEL class-A dynamics over class-B VCSEL dynamics due to the absence of relaxation oscillations. Then, we introduced a list of VECSEL laser peculiarities, such as the Henry factor, which happened to be dramatically important and affect the phase-locking criterion. More importantly, we prepared a basis for a many-laser array dynamics description given by the rate equation model with diffraction coupling. This model was used to develop analytical relations characterizing phase-locking among these lasers.

These analytical results are summarized in a framed list below.

- Phase-locking between two lasers requires coupling strength modulus exceeding a critical coupling value.

$$|\eta| \geq \eta_{\mathrm{cr}} = \frac{\alpha|\tau_2-\tau_1|+2\tau_1\tau_2\Omega}{\left(\sqrt{\frac{r_1-1}{r_2-1}}\tau_1+\sqrt{\frac{r_2-1}{r_1-1}}\tau_2\right)(\cos\theta+(\tau_1+\tau_2)\alpha\sin\theta)}.$$

- Two phase-locked lasers steady-state is given by the formulas:

$$\begin{aligned}
A_{1,\mathrm{st}} &= \left(\sqrt{F_{\mathrm{sat}}(r_2-1)}\frac{r_1}{r_1-1}\frac{|\eta|}{2}\cos(\psi_{\mathrm{st}}+\theta)+\sqrt{F_{\mathrm{sat}}(r_1-1)}\right),\\
A_{2,\mathrm{st}} &= \left(\sqrt{F_{\mathrm{sat}}(r_1-1)}\frac{r_2}{r_2-1}\frac{|\eta|}{2}\cos(\psi_{\mathrm{st}}-\theta)+\sqrt{F_{\mathrm{sat}}(r_2-1)}\right),\\
\psi_{\mathrm{st}} &= \begin{cases} \arcsin\dfrac{\eta_{\mathrm{cr}}}{|\eta|}+2\pi m, m\in\mathbb{Z}, \text{if } \mathrm{Re}[\eta]>0,\\ \pi-\arcsin\dfrac{\eta_{\mathrm{cr}}}{|\eta|}+2\pi m, m\in\mathbb{Z}\ , \text{if } \mathrm{Re}[\eta]<0. \end{cases}
\end{aligned} \tag{2.37}$$

  with a small-coupling approximation.

CHAPTER 3

Ring-shaped array of VECSELs

Contents

This chapter aims at describing theoretically the fundamental regularities of the ring laser array phase-locking. The ring topology of the loss mask promotes the widest range of applications among the other topologies. It naturally creates conditions for the phase-locking in a vortex configuration. This was experimentally and numerically studied in the case of class-B laser dynamics [Pal 2017; Pal 2015; Cookson 2021b]. At the same time, the system has never been investigated for class-A lasers with a complex coupling. Vortex solutions correspond to the persistence of a gradient in the phase differences between the array's elements. Those optical structures exhibit a zero intensity in the center of their intensity profile accompanied by a phase singularity. The chapter starts with the introduction of the rate equations generalized to describe a ring laser array with n members. The complex coupling between the nearest-neighbors is introduced in the model. In total, the main goal of the chapter is to derive analytical formulas for the steady-state solutions and investigate ring laser array stability.

3.1 Rate equations with near-neighbor coupling in ring geometry

In a ring configuration with n lasers, each laser field obeys the following set of coupled equations of evolution:

$$\begin{aligned}
\frac{\mathrm{d}A_i}{\mathrm{d}t} &= -\frac{1}{2\tau_{\mathrm{cav}}}\left(1-\frac{r}{1+A_i^2/F_{\mathrm{sat}}}\right)A_i + \\
&\qquad \frac{|\eta|}{2\tau_{\mathrm{cav}}}\left[\cos(\phi_{i+1}-\phi_i+\theta)A_{i+1}+\cos(\phi_{i-1}-\phi_i+\theta)A_{i-1}\right], \\
\frac{\mathrm{d}\phi_i}{\mathrm{d}t} &= \frac{\alpha}{2\tau_{\mathrm{cav}}}\frac{r}{1+A_i^2/F_{\mathrm{sat}}} + \\
&\qquad \frac{|\eta|}{2\tau_{\mathrm{cav}}}\left[\frac{A_{i+1}}{A_i}\sin(\phi_{i+1}-\phi_i+\theta)+\frac{A_{i-1}}{A_i}\sin(\phi_{i-1}-\phi_i+\theta)\right]+\Delta\omega_i.
\end{aligned} \tag{3.1}$$

Each laser labeled by $i = 1\ldots n$ is described by a field complex amplitude $E_i = A_i(t)\,\mathrm{e}^{i\phi_i(t)}$. All notations are inherited from the case of only two lasers in chapter 2. We use identical photon lifetime in the cavity τ_{cav} and excitation ratio r for all lasers, $\Delta\omega_i$ is the frequency detuning of the i-th laser from the closest cavity resonance. Henry factor is denoted as α, and F_{sat} stands for the saturation photon number ($F_{\mathrm{sat}} = 10^{10}$). The real amplitude A_i is normalized in such a way that its square corresponds to the photon number in the corresponding laser.

The behavior of the system is encapsulated in the phase differences between neighboring lasers that we denote $\psi_i \equiv \phi_{i+1} - \phi_i$. We introduce a new variable $\Omega_i \equiv \Delta\omega_{i+1} - \Delta\omega_1$ as a detuning from the first laser. Then the rate equations (3.1)

expressed in terms of the ψ_i's become:

$$\frac{dA_i}{dt} = -\frac{1}{2\tau_{cav}}\left(1-\frac{r}{1+A_i^2/F_{sat}}\right)A_i + \frac{|\eta|}{2\tau_{cav}}\left[\cos(\psi_i+\theta)A_{i+1}+\cos(-\psi_{i-1}+\theta)A_{i-1}\right]$$

$$\frac{d\psi_i}{dt} = \frac{\alpha}{2\tau_{cav}}\left(\frac{r}{1+A_{i+1}^2/F_{sat}}-\frac{r}{1+A_i^2/F_{sat}}\right)+\frac{|\eta|}{2\tau_{cav}}\left(\frac{A_{i+2}}{A_{i+1}}\sin(\psi_{i+1}+\theta)-\right.$$
$$\left.-\frac{A_i}{A_{i+1}}\sin(\psi_i-\theta)-\frac{A_{i+1}}{A_i}\sin(\psi_i+\theta)+\frac{A_{i-1}}{A_i}\sin(\psi_{i-1}-\theta)\right)+\Omega_i. \tag{3.2}$$

The steady-state solutions are easy to extract for the case of zero-detuning between the lasers ($\Omega_i = 0$) and identical laser parameters (same r, τ_{cav}) following [Bouchereau 2022]. Identical parameters lead to the phase-locking with the same amplitude all over the array $A_i = A_{st}$ for every i given by the eq. (3.3). The phase-differences are also identical $\psi_i = \psi_{st}$ and given by eq. (3.4).

$$A_{st} = \sqrt{F_{sat}}\sqrt{\frac{r}{1-2|\eta|\cos\psi_{st}\cos\theta}-1}\,, \tag{3.3}$$

$$\psi_{st} = \frac{2\pi q}{n}\,, \tag{3.4}$$

here $q \in \mathbb{Z}$ is an integer number. The steady-state solutions given by eq. (3.4) are consistent with the results previously published for class-B lasers [Pal 2017]. The number q in this case is associated with the topological charge (TC) of the beam formed by superposing the emission of n lasers.

3.1.1 Topological charge multistability

The term "topological" is used because the properties are preserved under continuous deformations of the wavefront. The topological charge q is the number of times a 2π-phase shift accumulates around the center of the beam. This parameter is equivalent to the orbital angular momentum (OAM) integer index in terms of laser beam topology or winding number. The phase accumulates equal portions $\Delta\phi = \psi_{st}$ between neighboring lasers. The more lasers form a ring array, the smaller portions of the phase increment for a fixed q, and the smoother the field and the phase distribution. This leads to a better quality of the vortex intensity profile. The beam becomes closer to the Laguere-Gaussian beam with the OAM index equal to the TC, i.e. $l \equiv q$.

An example of the phase relations for a phase-locked array of $n = 10$ lasers with different topological charges is presented in Fig. 3.1. Each circle illustrates a laser according to its position in a ring array. The color of the circle corresponds to the instant phase when the phase differences are stabilized. The phase-difference increment for an array of $n = 10$ lasers corresponds to $2\pi/10$ for TC $q = 1$ and $4\pi/10$ for $q = 2$ for example.

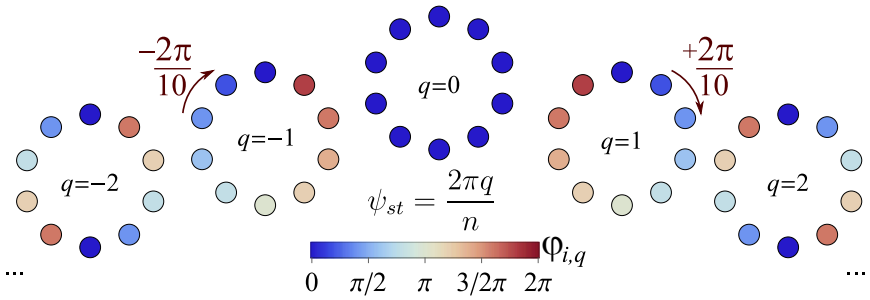

FIGURE 3.1: The steady-states phases ϕ_i for the $n = 10$ laser array phase-locked with different topological charges. The phase differences along the array are constant and defined according to eq. (3.3).

Based on the circle's colors in Fig. 3.1 it is easy to see that $q = 0$ corresponds to the "in-phase" oscillation of the laser array. TC-carrying arrays with $q = \pm 1, \pm 2$ show a phase gradient. Phase distribution for $q = \pm 2$ leads to the twice faster phase accumulation and "in-phase" oscillation of the opposite pairs of lasers.

Let us now investigate phase-locking dynamics for an array of ten lasers ($n = 10$). Fig. 3.2 shows numerical solutions of eq. (3.2) with five different sets of initial conditions. Different colors correspond to different sets of initial conditions. Each curve corresponds to the dynamics of one laser, thus one color represents n curves. The phase difference solutions include a redundant curve for $\psi_{10}(t)$, which is connected to the other solutions through $\psi_{10} = \phi_1 - \phi_{10} = -\sum_{i=1}^{n-1} \psi_i$.

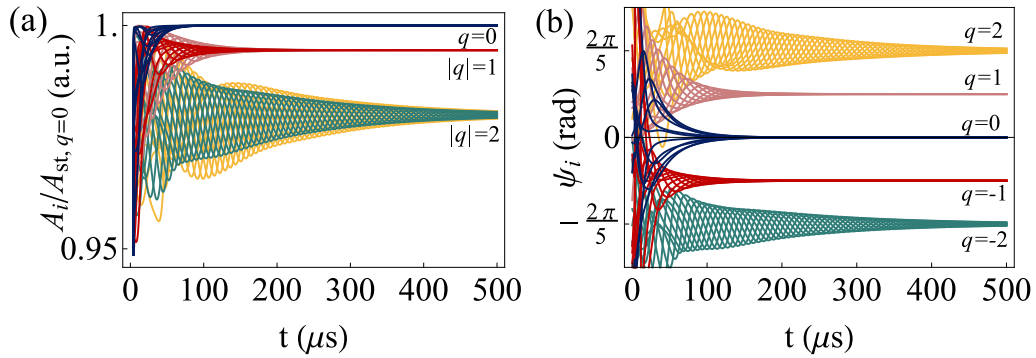

FIGURE 3.2: Time evolution of the amplitudes A_i normalized to the zero-TC ($q = 0$) steady-state value (a) and phase differences ψ_i (b) for $n = 10$ lasers in a ring array. Different sets of initial conditions correspond to the different colors. Each curve represents the dynamics of one laser from the array or one phase difference. The different initial conditions can lead to phase locking with different topological charges equal to $q = 0, -1, +1, -2$, and $+2$. Parameter values: $\alpha = 1$, $\eta = 0.005, \theta = 0$, $\tau_{cav} = 30\,\text{ns}$, $r_i = r = 1.2$, $\Omega_i = 0$.

We can see that different initial conditions lead to phase-locking with different TCs q. It is easy to notice in Fig. 3.2 that synchronization time increases with an

increase of the topological charge. Amplitude and phase-difference stabilization for $|q| = 2$ takes longer duration than for $|q| = 1$. Both cases show longer synchronization time then the "in-phase" solution ($q = 0$). It is also easy to notice that the positive and negative solutions are degenerate in amplitudes. They can't be identified based on power measurements.

Total amplitude degeneracy

The argument θ of the complex coupling coefficient does not affect the steady-state solution for the phase differences with zero-detuning. They always satisfy $\psi_{st} = 2\pi q/n$ (see eq. 3.4). At the same time, the coupling argument affects the solution for the amplitudes. The amplitude's dependency on θ is $\pi-$periodic.This leads to interesting points for $\theta = \pi/2 \pm \pi k, k \in \mathbb{Z}$, where the amplitudes are degenerate for all q.

Usually, the coherent "in-phase" state, with the $\psi_{st}(q = 0) = 0$ is always characterized by the maximal output power and thus preferred by the system. This means that $q = 0$ is always a predominant solution even though stability conditions allow different values of q to be generated. However, the case $\theta = \pi/2$ leads to the situation, where any q has a potentially equal chance to be generated by the array.

Let us investigate this case numerically by solving eqs. 3.2 with $\theta = \pi/2$. To do this, we generate a different set of initial conditions, leading to phase-locking with $q = 0, 1, -1$. Additionally, we introduce a perturbation in the shape of a Gaussian pulse to the rate equations to check how stable the steady-states are. A Gaussian pulse of a 1 µs full width at half maximum (FWHM) is added at $t = 100$ µs to the equation for the first laser amplitude as an additive term. Dynamics of the ten amplitudes and phase-difference stabilization are shown in Fig. 3.3.

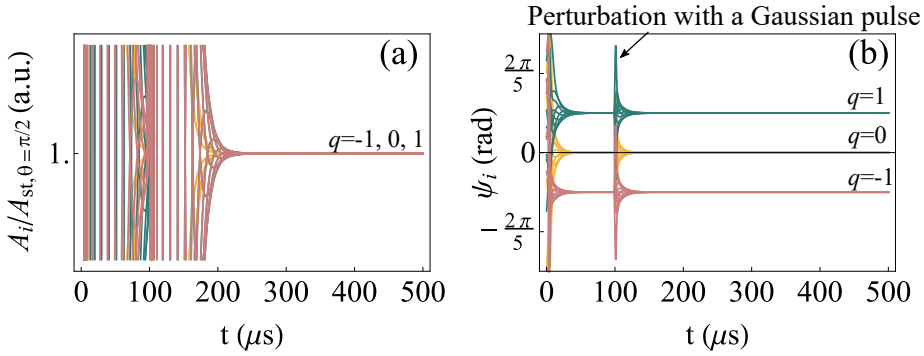

FIGURE 3.3: Time evolution of the amplitudes A_i (a) and phase differences ψ_i (b) for $n = 10$ lasers. Different colors correspond to different initial conditions: $q = 0$ yellow, $q = 1$ green, and $q = -1$ pink. The complex coupling argument is $\theta = \pi/2$. Other parameters have the same values as in Fig. 3.2. Amplitude of the Gaussian pulse is $8 \times 10^{-3}\sqrt{F_{sat}}$.

Indeed, these numerical calculations confirm the degeneracy of the amplitudes for different topological charges if the coupling argument is $\theta = \pi/2$. Moreover, all three solutions are shown to be stable and conserve their TC under an additional perturbation. This kind of system response is observed in all investigated cases when the amplitude of the perturbation is in a range from 0 to $0.8 \times 10^{-3}\sqrt{F_{\text{sat}}}$. The additional energy brought by the Gaussian pulse to the first laser is transferred between all lasers in the array and then dissipated. Both transient regimes starting at $t \sim 0\,\mu\text{s}$ and after Gaussian pulse perturbation have the same duration for different q. This is different from results with any values of θ different from $\pi/2$. Thus we conclude that the difference in the transient time duration is connected only with this amplitude stabilization mechanism.

3.1.2 Topological charge distinguishibility

How can one distinguish experimentally TC of the phase-locked solution if the amplitudes are degenerate in $|q|$? Even though the cases with different charges q are indistinguishable based on the power measurements, they have different interference patterns. The coherent "in-phase" phase-locking $\psi_{\text{st}} = 0$ leads to constructive interference with a strong intensity maximum in the center of the beam. Contrary to this, any non-zero topological charge leads to destructive interference in the center of the beam, i.e. to a field singularity. We can model the far-field patterns with corresponding TCs to help their identification.

The far-field region is also known as the Fraunhofer zone. The specific distance that marks the transition between the near field and the far field of a laser beam depends on the wavelength of the laser light and the characteristics of the optical system. It is important to note that this is a general guideline, and the transition between the near-field and the far-field is not a sharp boundary. The beam characteristics gradually change over a certain distance. However, a common rule of thumb used to approximate this transition is the Rayleigh length $z_R = \frac{\pi w_0^2}{\lambda}$, where w_0 is beam-waist and λ is a wavelength of the radiation.

To illustrate this, we can approximate each laser leaving the VECSEL cavity by a Gaussian beam. The following formula gives the propagation of the Gaussian beam along z in cylindrical coordinates:

$$E_i(r,z) = E_{i,0}\frac{w_0}{w(z)}\exp\left\{\frac{r^2}{w(z)^2}\right\}\exp\left\{-i\left(kz + k\frac{r^2}{R(z)} - \psi_{Gouy}\right)\right\}, \tag{3.5}$$

Here $w_0 = 200\,\mu\text{m}$ is the beam-waist of the laser beam, $\lambda = 1\mu\text{m}$ is the wavelength of the radiation, $k = 2\pi/\lambda$ is the wave number, z_R is the Rayleigh length, and Gouy phase-shift is $\psi_{Gouy} = \arctan\frac{z}{z_R}$ and accumulates with propagation. The beam radius $w(z)$ and its radius of curvation $R(z)$ depend on the propagation distance according

to:

$$w(z) = w_0\sqrt{1+\left(\frac{z}{z_R}\right)^2},\ R(z) = z\left(1+\left(\frac{z_R}{z}\right)^2\right). \tag{3.6}$$

Fig. 3.4 illustrates the far-field patterns of the arrays of $n = 5$ and $n = 10$ lasers phase-locked with different topological charges and with a distance between the center of the mask to each hole equal to 350 µm.

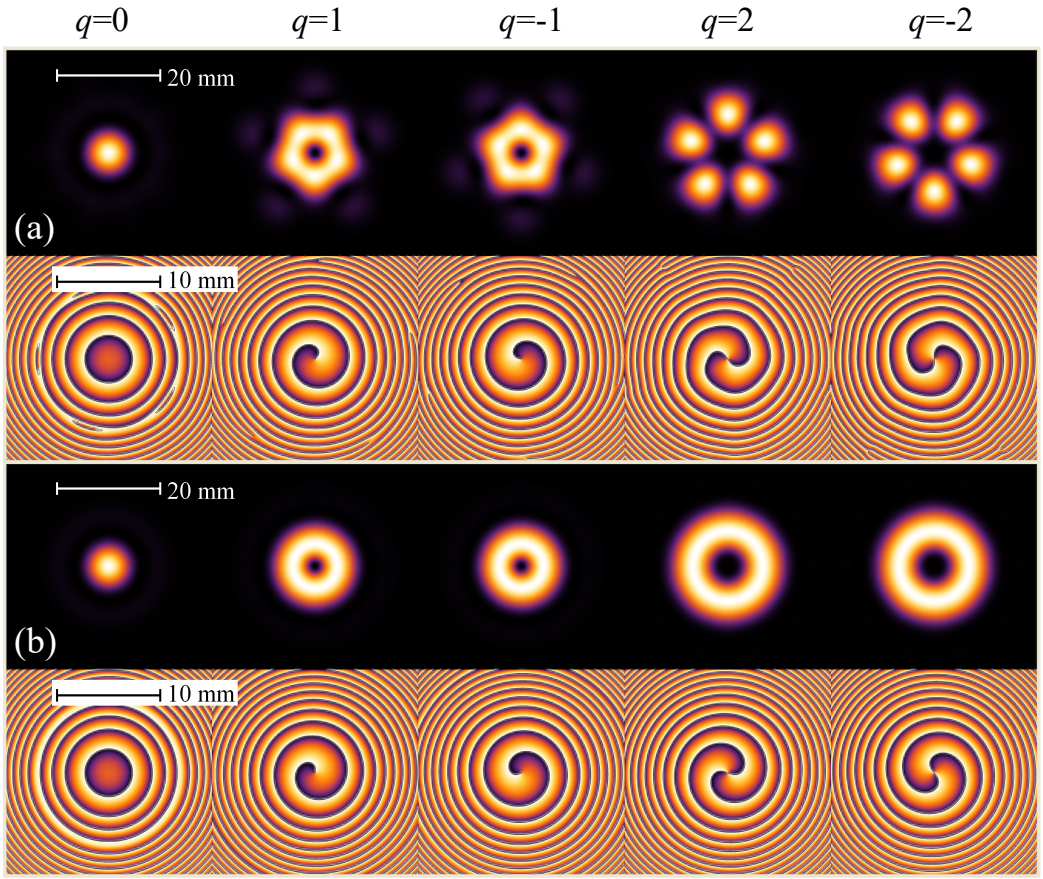

FIGURE 3.4: Calculated field patterns and phase profiles for (a) $n = 5$ and (b) $n = 10$ lasers. Upper row: Calculated far-field intensity patterns for $n = 5$ lasers with topological charges $q = 0, 1, -1, 2, -2$. Lower row: corresponding phase of the field. The patterns are calculated for $\lambda = 1\,\mu$m with mask hole diameters equal to 200 µm and a distance between the center of the mask to the holes equal to 350 µm. Propagation distance from the mask: $z = 50\,z_R$, where z_R is the Rayleigh length.

The patterns in Fig. 3.4 are calculated for $z = 50z_R$ and correspond to the far-field zone. It is easy to notice that in the case when the array has a few members ($n = 5$

in subplot (a) of Fig. 3.4), the far-field gives clear information about its topological charge including its sign. Each intensity pattern is unique. In the case $n = 10$ (shown in (b)) the positive and negative q lead to the situation when they are indistinguishable. The diameter of the beam increases with the increase of TC. Thanks to this the modulus of TC $|q|$ can be obtained, but not the sign of it.

The smooth far-field of the $n = 10$ array is an example of a perfect vortex, but the unsmooth case $n = 5$ can be even more valuable. The star-shaped structures in the center of the patterns corresponding to $|q| = 1$ are analogous to flower-shaped-optical vortex arrays (FOVAs) [Fan 2021]. Such structures provide a resource for complicated manipulation of particles, as evidenced by their distributions of linear and angular momenta shown in Fig. 3.5.

Indeed, Fig. 3.5 shows that, unlike the usual single Gaussian beam, the considered ring-shaped array of beams with a non-zero TC carries a non-zero linear momentum density, which is proportional to the Pointing vector projection, and some time-averaged angular momentum density. These values are computed with reference to [Allen 1992]. The projection of these vector fields and the gradient force are shown in Fig. 3.5 by arrows of different lengths.

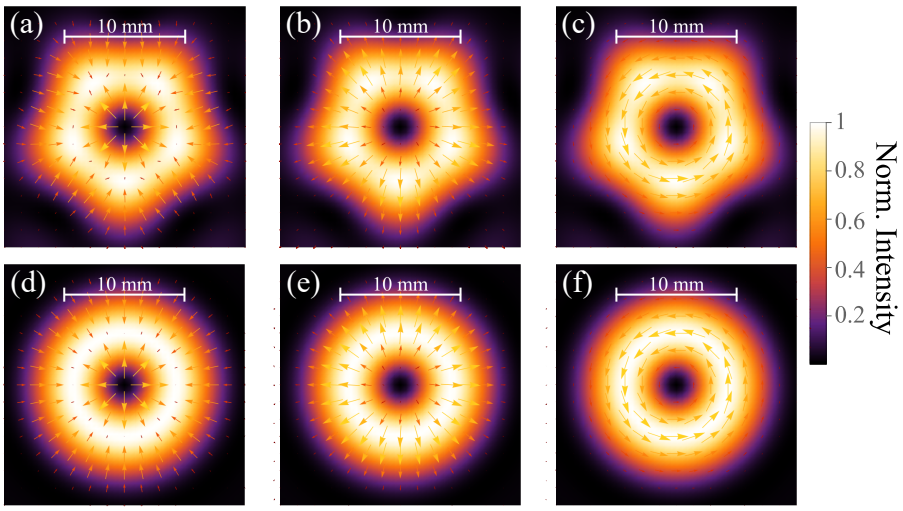

FIGURE 3.5: Intensity profile of $n = 5$ laser array (a,b,c) and $n = 10$ laser array (d,e,f) phase-locked with $q = 1$, corresponding to the ones shown in Fig. 3.4. Each subplot illustrates projection of the (a, d) gradient force $\mathscr{G} = \nabla(\vec{E}\vec{E}^*)$, (b, e) Poyting vector $\mathscr{P} \propto \vec{E} \times \vec{B}$ and (c, f) time-averaged angular momentum density profiles $\mathscr{M} \propto r \times \langle \vec{E} \times \vec{B} \rangle$. The length of the arrows is proportional to the normalized values of represented parameters.

If a particle is placed inside the laser beam, the change in light intensity creates a gradient in the radiation pressure (see (a,b) in Fig.3.5). Then, the particle experiences a force pushing it towards the region of higher intensity. Additionally, the particle will experience a momentum change forcing the particle to propagate along

the FOVA/OVA light corridor (star-shape or ring in Fig. 3.5). Due to this, such far-field structures can be potentially useful as micromotors, optical tweezers, etc.

3.1.3 Henry factor influence on the ring laser array phase-locking

Characterization of multi-oscillator systems is often performed with the use of the order parameter r_{op} defined according to the formula:

$$r_{\text{op}} = \frac{1}{n}\left|\sum_{i=1}^{n} e^{-i\phi_i}\right|. \tag{3.7}$$

A completely ordered system corresponds to the coherent synchronous "in-phase" phase-locking of the array given by $q = 0$ and $r_{\text{op}} = 1$. Any non-zero TC $q \neq 0$ leads to $r_{\text{op}} = 0$.

Let us now follow the order parameter in time, when an array of ten lasers $n = 10$ tends to be phase-locked. The data for different values of the Henry factor calculated with the same set of initial conditions are shown in Fig. 3.6.

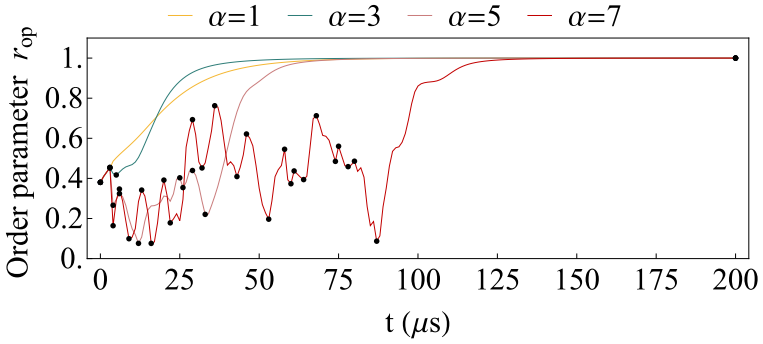

FIGURE 3.6: Time evolution of order parameter r_{op} for solutions, for which the laser array is phase-locked with $q = 0$ for different values of α. Critical points are shown as black dots. Parameter values: $\eta = 0.005, \theta = 0, \tau_{\text{cav}} = 30\,\text{ns}, r_i = r = 1.2, \Omega_i = 0$.

From this figure, we can see that the linewidth enhancement factor α plays a significant role in the stabilization dynamics of the system. The cases presented in Fig. 3.6 tend to be phase-locked with $r_{\text{op}} = 1$, which means the "in-phase" solution with $|q| = 0$. The TC of the steady-state is predefined by initial conditions and none of the system parameters can affect it. At the same time, the α factor affects the phase-locking time. One can notice that there is a certain number of critical points corresponding to the local minima and maxima of each curve. These critical points are marked with black dots. Their number increases with an increase in the Henry factor.

These points seem to correspond to an attempt of the laser array to partially phase-lock when the phase-difference of a certain pair of lasers is $\psi_i \sim \pi/2$ [El-Nashar 2009]. The origin of these critical points is complicated to trace as a function

of some specific parameters. However, we can visualize which pair of lasers has this difference in a particular case. To do this, we calculate the order parameter again for $\alpha = 7$, but different initial conditions. The new curve is plotted in Fig. 3.7 (a). Then, we extract time moments of these critical points and calculate all phase-differences ψ_i at each of them[1]. The obtained phase-differences are presented in subplot (b) of Fig. 3.7 by the circles of a certain color in a ring array. The index position i in the array gives the index of calculated phase-difference ψ_i.

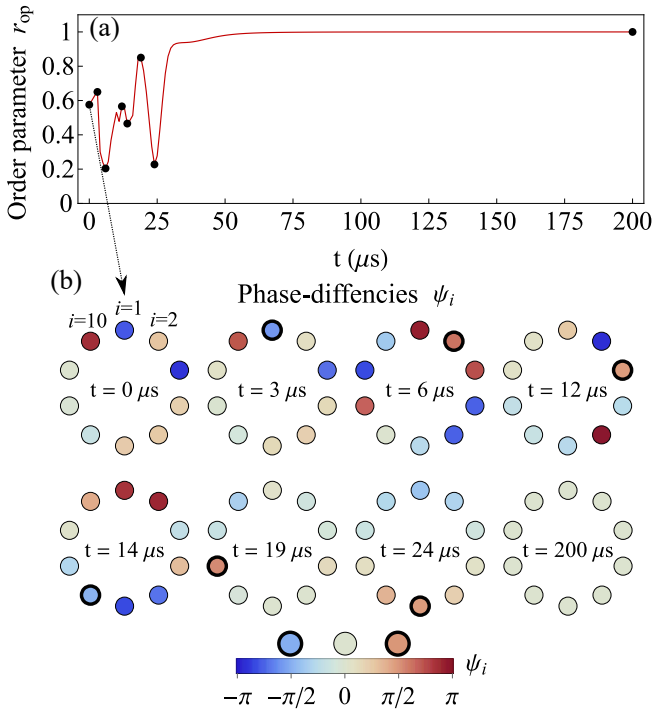

FIGURE 3.7: Time evolution of order parameter r_{op} (a) and phase-differences ψ_i at the instants given by the critical points of the order parameter. Critical points are shown as black dots. Parameters used for the computations are $\alpha = 7$, $\eta = 0.005, \theta = 0$, $\tau_{cav} = 30$ ns, $r = 1.2$, $\Omega_i = 0$. Solutions for the phase differences ψ_i are illustrated in ring arrays according to their indexes i. The black thick edges of the circles indicate a value $|\psi_i| = \pi/2$.

First of all, one can notice that the new initial conditions leading to the curve shown in subplot (a) of Fig. 3.7 exhibit a smaller number of critical points than shown in Fig. 3.6 for the same Henry factor $\alpha = 7$. This confirms again the strong role of initial conditions. The thick black border of the circles in subplot (b) of Fig. 3.7 corresponds to the phase differences satisfying $|\psi_i| \sim \pm\pi/2$. The index of the circle corresponds to the index of the index of phase-difference ψ_i. We can conclude each "critical" time moment corresponds to one pair of lasers exhibiting $|\psi_i| \sim \pm\pi/2$.

[1]Including the redundant curve for $\psi_{10}(t)$, which is connected to the other solutions as $\psi_{10} = \phi_1 - \phi_{10} = -\sum_{i=1}^{n-1} \psi_i$

3.1.4 Role of the detuning in the ring laser array phase-locking

In this section we investigate phase-locking in the case of a non-zero detuning Ω_i between the lasers. Unfortunately, there are no elegant analytical solutions for the steady-states of the system 3.2 in this case. Once the lasers in a ring array do not oscillate at the same frequency the amplitudes and phase-differences $A_{i,\mathrm{st}}, \psi_{i,\mathrm{st}}$ are different in steady-state. Even a single laser detuned from the array ($\Omega_i \neq 0$) leads to the redistribution of the phase-increment asymmetry between all lasers and consequently, to different steady-state phase-differences and amplitudes. This happens because the ring coupling geometry acts as a transfer bus equalizing the system disturbance. A variation of the lasers phase or amplitude increments immediately affects the neighbors. None of the laser amplitudes and phase-differences are degenerate, thus we investigate phase-locking only with the help of numerical modeling.

We choose randomly distributed detuning values Ω_i for the ring laser array of $n = 10$ laser. The Ω's are distributed with a zero mean value and standard deviation $\Delta\Omega_i/2\pi = 10^5$ rad/s.

First of all, we investigate the changes of the behavior of the global parameter characterizing the system phase-locking, i.e. the order parameter r_{op}. Fig. 3.8 shows its dependence on the Henry factor with the same initial conditions.

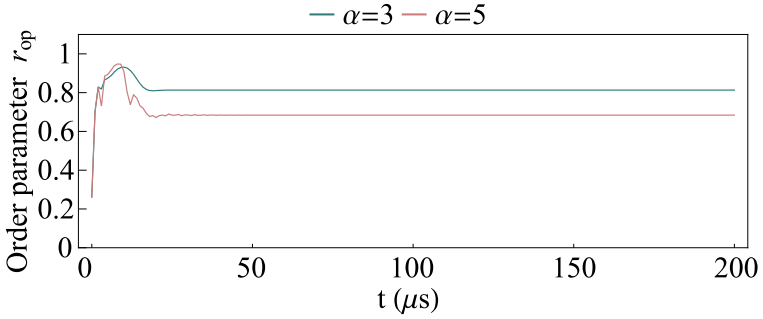

FIGURE 3.8: Time evolution of order parameter r_{op} with different values of α factor. Other parameter values are $\eta = 0.005, \theta = 0$, $\tau_{\mathrm{cav}} = 30\,\mathrm{ns}$, $r = 1.2$.

We can see that the order parameter is not equal to zero for all cases in Fig. 3.8. The system with non-zero detuning can be only phase-locked with $0 < r_{\mathrm{op}} < 1$. The perfect order of the system ($r_{\mathrm{op}} = 1$) corresponds to zero phase-differences ψ_i between all neighbouring lasers. This can't be achieved unless the detuning impact is negligible, i.e. it is completely compensated by large enough coupling strength [El-Nashar 2009].

Fig. 3.8 also shows the impact of the α factor on the steady-state value. The impact is not the same as with a zero-detuning system (cf. eq. 3.6), for which α dependence was not observed. This is similar to the results obtained for two lasers in the preceding chapter. Indeed, the steady-state solution depends on α only in the presence of different detunings for the different lasers.

Phase-locked ring laser array at critical coupling

Now, we wish to determine the minimal coupling strength for which a ring laser array with non-zero detuning can be phase-locked. To this aim we numerically calculate phase-differences at a fixed time moment[2] ($t = 1\,\mathrm{ms}$) with different values of $|\eta|$, but with the same set of initial conditions. The detuning values are the same as in the previous subsection. The curves calculated for different detuning values are shown in Fig. 3.9 for three different values of the α factor.

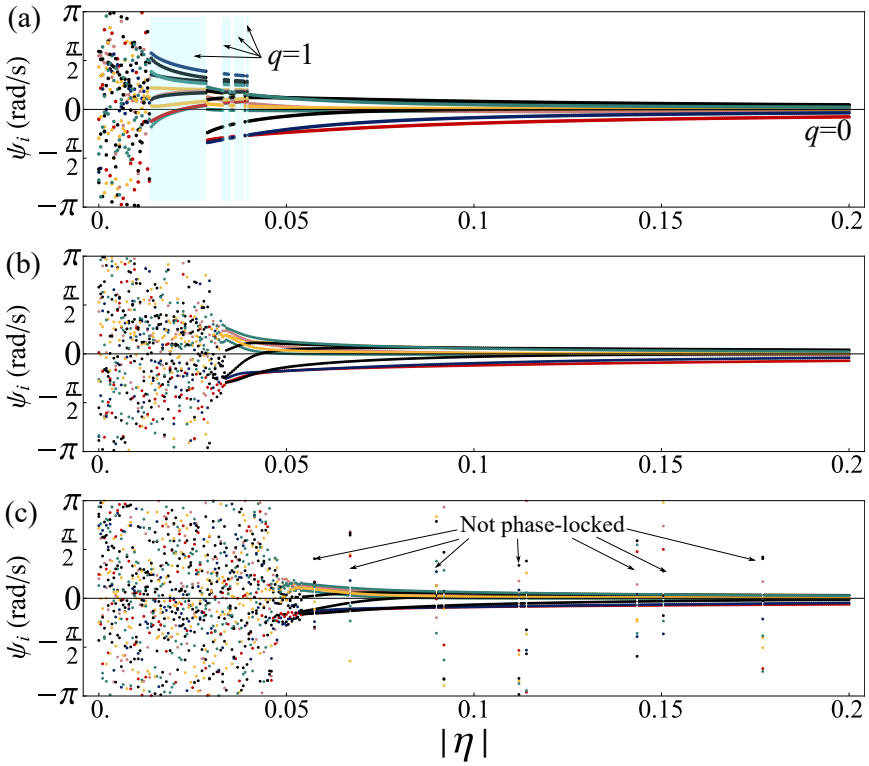

FIGURE 3.9: Phase-difference at $t = 1\,\mathrm{ms}$ calculated with eq. (3.2) as a dependency on $|\eta|$ with different α values. Henry factor is $\alpha = 2$ in subplot (a), $\alpha = 4$ in (b) and $\alpha = 8$ in (c). Other parameters are the same for each subplot: $\theta = 0$, $\tau_{\mathrm{cav}} = 30\,\mathrm{ns}$, $r_i = r = 1.2$. Different colors correspond to different lasers

The minimal coupling strength $|\eta|$ separating the stochastic range of the phase-difference ψ_i distribution and phase-locked range gives us a critical coupling value η_{cr}. Comparing its values in subplots (a), (b), and (c), it is easy to see that the increase of α factor destabilizes the phase-locking of the laser array: in (a) η_{cr} is close to 0.008, in (b) η_{cr} is around 0.03 and (c) η_{cr} reaches 0.048.

Let us first focus on the phase-locked solutions in the coupling range $|\eta| > \eta_{\mathrm{cr}}$. Subplot (a) in Fig. 3.9 shows us that some $|\eta|$ values lead to the phase-locking of the

[2]This duration is taken to be long enough for phase-locking to have time to happen.

ring array with an average phase-difference associated with TC $q = 1$. These ranges of $|\eta|$ are shown in a light blue background. We cannot see similar results for $\alpha = 4$ and $\alpha = 8$. Moreover, when $\alpha = 8$ (see subplot (c) in Fig. 3.9) some $|\eta|$ parameters do not allow our system to phase-lock with chosen initial conditions within a duration $t = 1\,\text{ms}$.

Additionally, one can notice that the stochastic range becomes limited in values of ψ_i close to η_{cr} right before the stable phase-differences range. It is of interest to study this range in more detail for the examples $\alpha = 4$, and $\alpha = 8$. These transient regions of the subplots (b, c) in Fig. 3.9 are given in Fig. 3.10 (a, b) respectively.

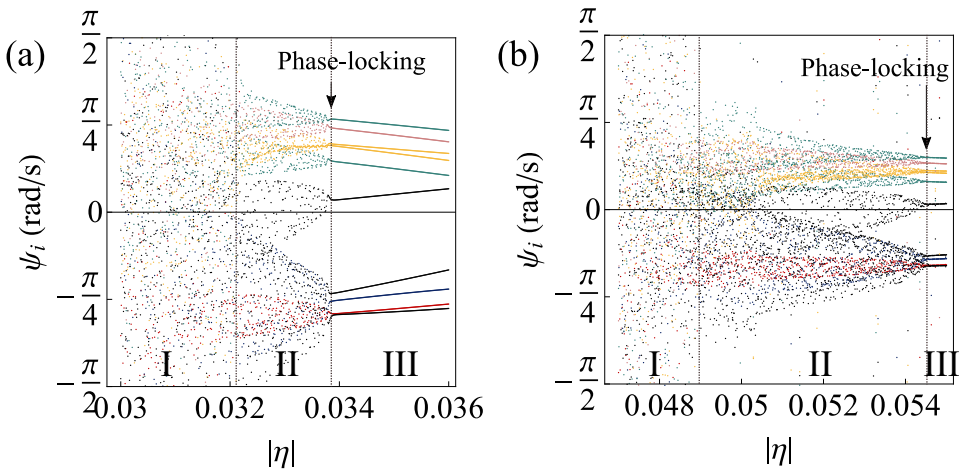

FIGURE 3.10: Phase-difference at $t = 1\,\text{ms}$ calculated with eq. (3.2) as a dependency on $|\eta|$ with different α values. These subplots show detailed parts of Fig. 3.9 (b,c) at the border of the laser array phase-locking. Henry factor is (a) – $\alpha = 4$, (b) – $\alpha = 8$. Parameter values: $\theta = 0$, $\tau_{cav} = 30\,\text{ns}$, $r_i = r = 1.2$.

Three characteristic ranges of coupling strength can be recognized in these plots. The first region (range number I) corresponds to values of $|\eta|$ for which the lasers are not phase-locked.

It corresponds to $|\eta|$ from 0 to 0.0317 in subplot (a) and $|\eta|$ from 0 to 0.0488 in subplot (b). The range in between gives an intermediate regime (range number II) of coupling strength values, where phase-differences are not stabilized but are limited in values. This range corresponds to $|\eta|$ from 0.0317 to 0.0338 in subplot (a) and to $|\eta|$ from 0.0488 to 0.0545 in subplot (b). The ranges $|\eta| \geq 0.0338$ in subplot (a) and $|\eta| \geq 0.0545$ in subplot (b) evidence the laser array phase-locking with unequally distributed phase-differences ψ_i (range number III). It is clear that the width of the stochastic range number I and the intermediate range II increase with an increase of the α factor.

Dynamical regimes characteristic of each of these ranges can be visualized in the phase-space of the system. The full phase-space has $2n - 1$ dimensions, but its projection on any pair of variables permits to have an idea of the global attractor

shape. This projection on the plane based on the values of A_1, A_2 is shown in Fig.3.11 for $\alpha = 8$. It illustrates the changes of laser amplitudes A_1, A_2 within the time period t from 0.4 ms to 0.5 ms.

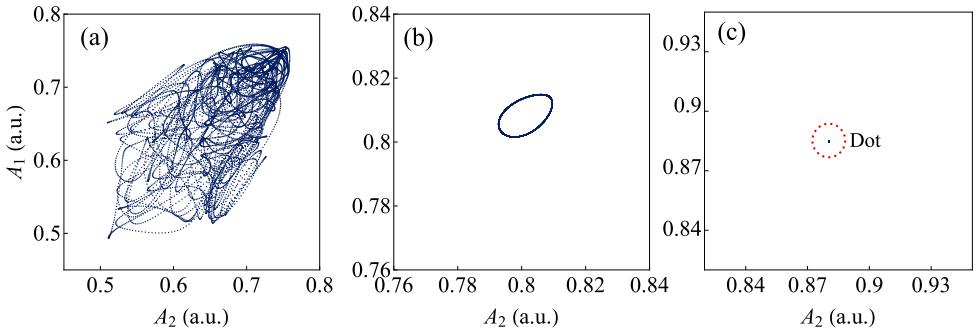

FIGURE 3.11: Dynamic trajectories in the A_1, A_2 phase-space for different values of the coupling strength within the time period t from 0.4 ms to 0.5 ms. Subplot (a) calculated with $\eta = 0.036$ (range I), while subplots (b) with $\eta = 0.051$ (range II), and (c) with $\eta = 0.07$ (range III). Here $\alpha = 8$, $\theta = 0$, $\tau_{cav} = 30\,\text{ns}$, $r = 1.2$.

Subplot (a) corresponds to the value of the coupling strength from the range number I defined in Fig. 3.10 (b). It clearly shows stochastic trajectories without any regular patterns. The laser array is not phase-locked in this case and this behavior is very typical for the transient laser dynamics. The opposite case is shown in subplot (c). Here coupling strength lies in the range number III in Fig. 3.10 (b). Here the transient regime is over and the amplitudes are constant. The attractor is shown by a single dot and the system is phase-locked. The intermediate regime is shown in Fig. 3.11 (b). The coupling strength used for this calculation belongs to the range number II in Fig. 3.10 (b). Here the coupling is not strong enough to allow phase-locking between the lasers. The amplitudes draw an orbit trajectory in the phase-space. All laser amplitudes and phase-differences exibit infinite oscillations in this regime without reaching fixed steady-state.

3.2 Ring laser array stability analysis

In this section, we come back to the investigation of the ring laser array steady-states, when the detunings are all equal to zero ($\Omega_i = 0$). As we have seen in chapter 2, the analysis of the Jacobian gives a clear picture of the system stability. At the same time, with an increase in the number of lasers, the rank of the Jacobian increases as $(2n-1)$, where n is the number of lasers. Then, the analysis requires a study of the $(2n-1)$ eigenvalues, which is not easy to compute even for $n = 10$ lasers.

Eventually, the query can be simplified. We can isolate the sub-system consisting in one of the lasers interacting with its neighbors [Bouchereau 2022]. Let us consider the steady-state amplitude and phase of the selected laser $\{A_q, \psi_q\}$ with a variation

of its parameters around this steady-state solution according to the rate-equations eq. (3.2).

The Jacobian matrix obtained by linearization of eq. (3.2) around steady-state is then:

$$\mathbf{J}(A_q,\psi_q) \equiv \begin{pmatrix} \frac{\partial \frac{\mathrm{d}A_i}{\mathrm{d}t}}{\partial A_i}\big|_{A_q,\psi_q} & \frac{\partial \frac{\mathrm{d}A_i}{\mathrm{d}t}}{\partial \psi_i}\Big|_{A_q,\psi_q} \\ \frac{\partial \frac{\mathrm{d}\psi_i}{\mathrm{d}t}}{\partial A_i}\big|_{A_q,\psi_q} & \frac{\partial \frac{\mathrm{d}\psi_i}{\mathrm{d}t}}{\partial \psi_i}\Big|_{A_q,\psi_q} \end{pmatrix}$$
$$= \frac{1}{2\tau_{\mathrm{cav}}} \begin{pmatrix} r\frac{1-A_q^2/F_{\mathrm{sat}}}{\left(A_q^2/F_{\mathrm{sat}}+1\right)^2} - 1 & -|\eta|A_q \sin\left(\psi_q+\theta\right) \\ 2\alpha r \frac{A_q/F_{\mathrm{sat}}}{\left(A_q^2/F_{\mathrm{sat}}+1\right)^2} + \frac{|\eta|\left(2\sin\left(\theta-\psi_q\right)+\sin\left(\psi_q+\theta\right)\right)}{A_q} & -2|\eta|\cos\psi_q\cos\theta \end{pmatrix} \tag{3.8}$$

As discussed in chapter 2, the steady-state solution is stable if all eigenvalues of $\mathbf{J}(A_i,\psi_i)$ have a negative real part. When applied to the presented Jacobian, this is equivalent to claiming that $\mathrm{Tr}(\mathbf{J})<0$ and $\mathrm{Det}(\mathbf{J})>0$. Here we consider these criteria separately.

Trace of Jacobian $\mathrm{Tr}(\mathbf{J})<0$

The condition for the negative Jacobian trace has the shape of eq. 3.9, when the calculated trace is simplified.

$$\mathrm{Tr}(\mathbf{J}\cdot\tau_{cav}) = \frac{4|\eta|^2\cos^2\theta\cos^2\psi_q - 4\eta\cos\theta\cos\psi_q}{r} + \frac{1-r}{r} < 0, \tag{3.9}$$

This condition is a quadratic equation of $|\eta|$ and it leads to the following requirement for the phase-locking:

$$-\frac{1}{2}\left(\sqrt{r}-1\right)\frac{1}{\cos\psi_q} < |\eta|\cos\theta < \frac{1}{2}\left(\sqrt{r}+1\right)\frac{1}{\cos\psi_q}. \tag{3.10}$$

If the coupling is real ($\theta=0$), this condition is always true [Bouchereau 2022]. Additionally, it is worth mentioning that the factor $(\sqrt{r}\pm 1)>0$ is always positive when the pumping rate is above the laser threshold $r>1$. The stable region for η given by the condition is very broad. Its borders are unreachable in our experiment and thus the condition is always true in practice.

Nevertheless the left border containing $\frac{1}{2}(\sqrt{r}-1)$ can be reached in some exotic cases. Numerically, we checked this case with eq. (3.2). Eventually, this border separates the region of the global laser array phase-locking with equal phase-differences $\psi_i=\psi_q$, and the array separates in at least two phase-locked ensembles. Within these ensembles all lasers have the same amplitude, but the lasers are phase-locked only within their group of lasers.

Determinant of Jacobian $\mathrm{Det}(\mathbf{J}) > 0$

Let us now consider the condition determined by the Jacobian determinant. Its formula can be simplified considering a small coupling strength, which is typical for a small length z of the diffraction cavity:

$$\mathrm{Det}(\mathbf{J}\cdot\tau_{cav}) = \frac{|\eta|(r-1)\left(\cos\psi_q(\alpha\sin\theta+2\cos\theta)+\alpha\cos\theta\sin\psi_q\right)}{2r} + \mathscr{O}\left(\eta^2\right) > 0. \tag{3.11}$$

From this, we obtain a new requirement, which says that the stable phase-locking with ψ_q is possible with $\alpha < \alpha_{\mathrm{lim}}$ given by:

$$\alpha_{\mathrm{lim}} = \frac{2\cos\theta\cos\psi_q}{\sin\left(\psi_q-\theta\right)}. \tag{3.12}$$

It is clear that the limitations are different for different topological charges ($\psi_q = 2\pi q/n$). The limiting value of the α factor is π periodic in θ. A graphical illustration of the formula is given in Fig. 3.12 for $|q| = 1,2,3$. The coupling argument θ range from $-\pi/2$ to $\pi/2$.

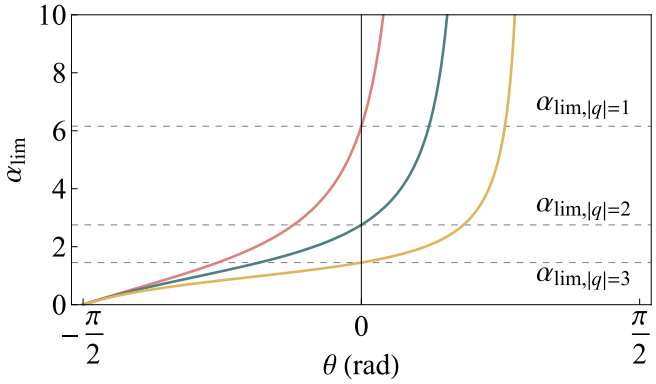

FIGURE 3.12: Dependency of the limiting values of the Henry factor for different topological charges: pink curve is for $|q| = 1$, green is for $|q| = 2$ and yellow curve is for $|q| = 3$. Dashed lines cross-sections with each curve give a limiting value of the Henry factor for a real positive coupling ($\theta = 0$).

We can see that the choice of θ crucially affects the stability range for each presented TC q. The α range below the q-curves corresponds to the stability of this phase-locked solution. Conversely, the α factor values above these curves correspond to a negligible probability of observing the corresponding topological charge. The eq. 3.12 can be simplified for a long diffraction cavity length z, where the coupling argument θ tends to 0.

Then, the limiting Henry factor is given by [Bouchereau 2022]:

$$\alpha_{\text{lim}} = \frac{2}{\tan\dfrac{2\pi q}{n}}, \tag{3.13}$$

and its simplified expression given by a Taylor expansion is:

$$\alpha_{\text{lim}} = \frac{2}{\tan\frac{2\pi}{n}} \simeq \frac{n}{\pi} - \frac{2}{3}\frac{2\pi}{n} + \mathcal{O}(\frac{1}{n^3}). \tag{3.14}$$

3.2.1 Orbit solution

The simplified model presented above is approximate. We expect the calculation of the full set of eigenvalues to provide more detailed information about the dynamical regimes of the array. For example, this can be done with the simplest ring configuration, such as a three-laser array ($n = 3$). It is easy to calculate all of the five eigenvalues λ_i. The first three eigenvalues $\lambda_{1...3}$ are always negative, while $\lambda_{4,5}$ change their sign depending on the system's parameters. Fortunately, the eigenvalues $\lambda_{4,5}$ are degenerate, and thus, the stability analysis of the system can be encapsulated into the behavior of a single parameter, such as λ_4. The dependency of the real part of the eigenvalue λ_4 on real-valued coupling strength is shown in Fig. 3.13 for different steady-states of the system ($q = 0, \pm 1$) and Henry factors.

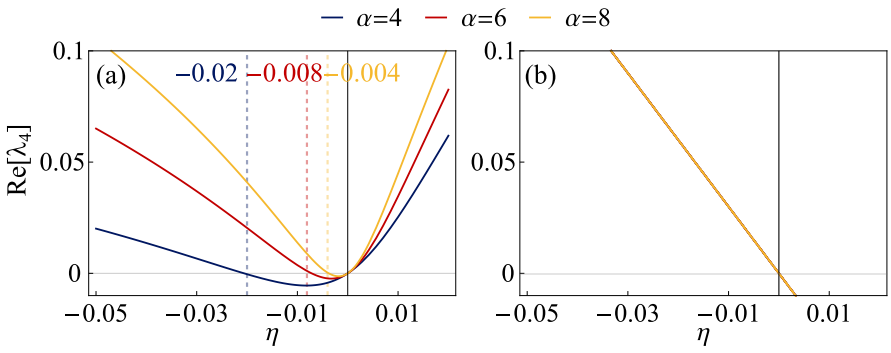

FIGURE 3.13: The real part of the eigenvalue λ_4 dependency on the coupling strength for the (a) vortex $|q| = 1$ and (b) "in-phase" $q = 0$ steady-state of the system. The curves were calculated with $r = 1.2, F_{\text{sat}} = 10^{10}$. All curves for different α overlap in subplot (b). The positive coupling values correspond to $\theta = 0$ and negative to $\theta = \pi$.

The range of the coupling values for which the solution $q \neq 0$ is stable decreases with an increase of the Henry factor (see subplot (a) of Fig. 3.13). From this, we can say that the large value of the α factor limits the chances of phase-locking in an OV. A zero topological charge $q = 0$ however is always stable in the positive coupling

range (see subplot (b) in Fig. 3.13), and its stability does not depend on the values of α.

In the presented case of $n = 3$ lasers, the choice between the stable OV and the "in-phase" solution can be done with the choice θ. But the stable coupling range for $|q| = 1$ solution shifts to the positive range of coupling strength with an increase in the number of lasers n. Examples of the real part of the sign-changing eigenvalues dependencies on coupling value for arrays of three, four, five, and six lasers are shown in Fig. 3.14

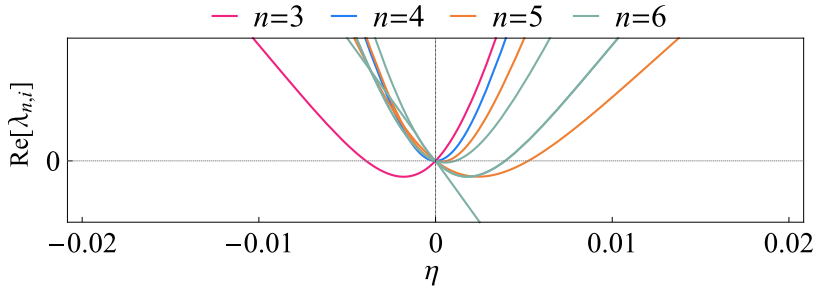

FIGURE 3.14: The real part of the eigenvalues $\lambda_{n,i}$ dependencies on the coupling strength for the vortex $|q| = 1$ steady-state of the systems on n lasers. The curves were calculated with $r = 1.1, F_{\text{sat}} = 10^{10}, \alpha = 6$. The positive coupling values in this figure correspond to $\theta = 0$ and negative to $\theta = \pi$.

The figure shows that the choice between the vortex and in-phase solution is possible to do in our system only for three lasers. Any other arrays will be multistable in the positive coupling range. The positive coupling values in this figure correspond to $\theta = 0$ and negative to $\theta = \pi$. The case of the vortex solution with four lasers is exceptional. It is given only by one coupling strength value $\eta = 0$. This means that we will not be able to observe it. Thus the vortex with $|q| = 1$ can be observed with three lasers or more than four.

Let us focus on the investigation of the three lasers case. We now investigate the borders of the stable region in subplot (a) in Fig. 3.13. At the border, the real part of λ_4 is equal to zero but its imaginary part is zero only at zero coupling strength $|\eta| = 0$. Due to this, the left borders of the stable regions (marked with vertical dashed lines in subplot (a)) correspond to the purely imaginary eigenvalues, i.e. correspond to Hopf bifurcation. Then, the laser array dynamics is described by the undamped periodic fluctuations of the amplitudes and phase-differences around their mean values. The amplitude dynamics are visualized in Fig.3.15 for two different sets of initial conditions. One set of initial conditions leads to the laser array phase-locking with a mean phase-difference $\sum_{i=1}^{n} \psi_i$ corresponding to $q = -1$. This case is shown in the subplot (a) in Fig. 3.15. Another initial condition leads to phase-locking with $q = 1$. This case is shown in subplot (b). In the figure, one can notice a Gaussian pulse (with

FWHM 1 µm at 50 µs) added to perturb the amplitude of the first laser A_1 to check how stable the system is with the considered parameters.

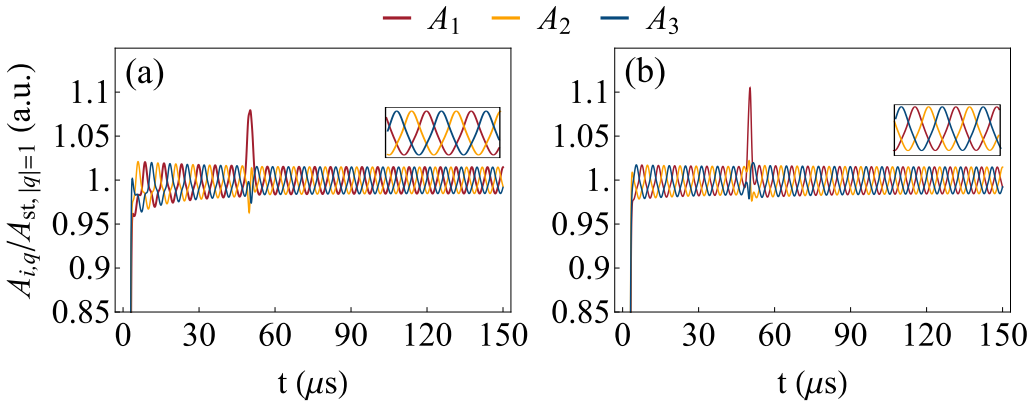

FIGURE 3.15: Amplitude dynamics of tree-lasers array with parameters ($|\eta| = 0.008, \theta = \pi, r = 1.2$) correspondent to the "orbit" solution with zero eigenvalues $\lambda_{4,5}$, while the rest are negative. The total phase accumulation between the lasers corresponds to $(a)\, q = -1, (b)\, q = 1$.

The fact that the amplitudes of the three lasers exhibit similar oscillations but with a phase-shift one with respect to the other shows the existence of a periodic transfer of power between the lasers. For example, in the case of subplot (a) in Fig. 3.15, some power is transferred to laser 3, then to laser 2 and back to laser 1. The direction is reversed in this case of Fig. 3.15 (b).

The solutions are shown to be stable and self-healing in time. We can see that the array restores the order of laser-to-laser energy transfer after a Gaussian pulse perturbation during a short transient process. The order gives the direction of the energy transfer and can be visualized in Fig.3.16.

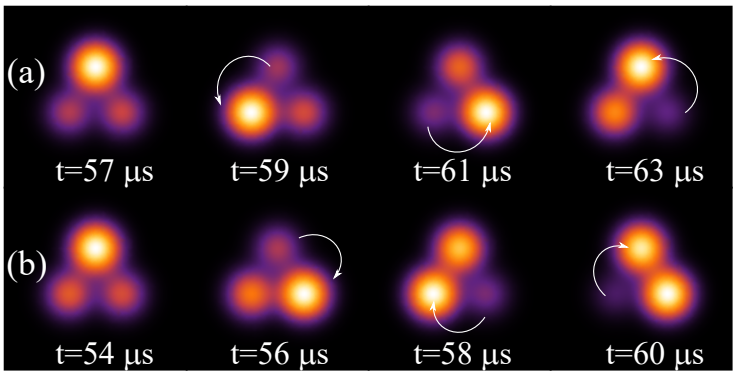

FIGURE 3.16: Near-field intensity variations of a $n = 3$ lasers ring array around ($A_{st,|q|=1}$). (a) $q = -1$, (b) $q = 1$. All of the parameters correspond to the parameters used to calculate (Figs. 3.13, 3.15) $|\eta| = 0.008, \theta = \pi, r = 1.2, \alpha = 6$.

Each laser of the array is approximated with a Gaussian beam ($w_0 = 1$ mm) located at a distance $\rho = 2$ mm from the center of the array. The amplitudes and phases are given by the solution shown in Fig. 3.15. This realization corresponds to the intensity kink propagating along the laser array with the energy transfer from laser to laser in time. The direction of the transfer depends on the phase relations, i.e. TC sign. For example, subplot (a) shows counterclockwise energy transfer and subplot (b) shows the clockwise direction of the intensity kink travel. If α increases, we can stay in this periodic solution by decreasing the coupling strength $|\eta|$ (see Fig. 3.15). In this case, the amplitude of the oscillations increases. Contrary to this, the frequency of the oscillations then decreases. Identical solutions exist in the arrays with larger dimensions. For example, Fig. 3.17 shows the case of vortex and anti-vortex solutions in the $n = 5$ laser array.

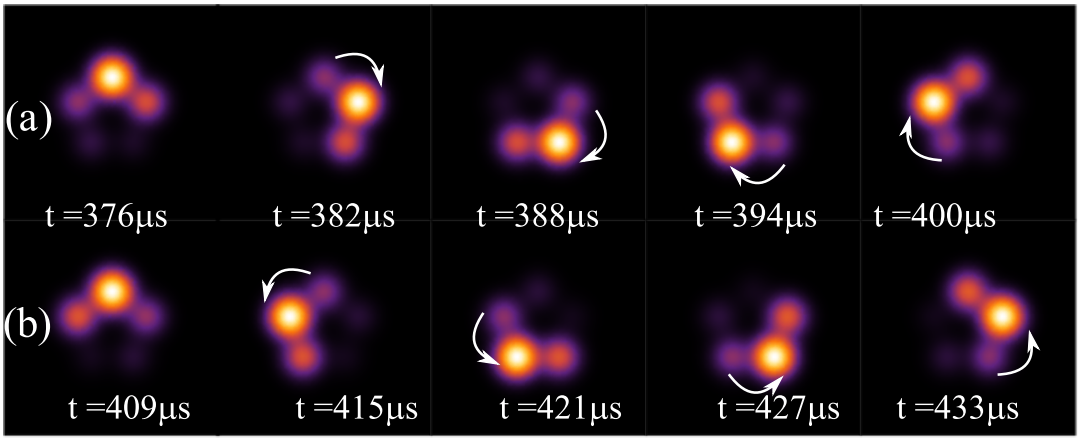

FIGURE 3.17: A set of intensity variations around ($A_{st,|q|=1}$) in the near field of the laser array of $n = 5$ lasers. $\eta = 0.0012, r = 1.2, \alpha = 6$.

The direction of the kink rotation always corresponds to the TC q. Those "orbit" solutions give information about the charge without the far-field or interference analysis. The information is accessible through the intensity fluctuations of the lasers and its readout requires only power measurement with some spatial resolution.

3.3 Conclusion to chapter 3

To conclude this chapter, we stress the fact that we have developed a generalized model for a ring laser array with n lasers, where the next-neighbor complex coupling is introduced. Phase-locking of the array is characterized by a discrete number of solutions for phase-differences. The amplitudes have equal values for positive and negative TCs. We also obtained an analytical formula for α_{lim} giving the limit of the Henry factor where non-zero TC can be observed.

These analytical results are summarized in a framed box below.

- Ring lasers array steady-state is given by the formulas:

$$A_{\text{st}} = \sqrt{F_{\text{sat}}}\sqrt{\frac{r}{1-2|\eta|\cos\psi_{\text{st}}\cos\theta}-1}\,,$$
$$\psi_{\text{st}} = \frac{2\pi q}{n}\, q \in \mathbb{Z}.$$

- We derived an analytic formula for the critical value of the α factor, which gives boundaries for the stable phase-locking with TC q and includes a dependency on the complex coupling argument θ.

$$\alpha_{\text{lim}} = \frac{2\cos\theta\cos\psi_q}{\sin\left(\psi_q-\theta\right)}.$$

We numerically studied the phase-locking dependence of the ring laser array with non-zero detuning on the α factor and discovered the range of coupling strengths, where the infinite oscillations, i.e. "the orbit solution" occur. This range increases with an increase in the Henry factor.

A simple method for TC recognition through the far-field intensity patterns is introduced. As well, an additional method for TC sign recognition is introduced based on the periodic intensity changes between the lasers of the array. The second method requires adjusting coupling strength down to the limit of the phase-locking stability to see continuous amplitude oscillations.

We also noticed that exceptional points of the coupling argument $\theta = \pi/2 \pm \pi$ potentially promise equal chances for all TCs generation. These values of the coupling argument give zero-limiting Henry factor based on presented dependency $\alpha_{\text{lim}}(\theta = \pi/2) = 0$. It is complicated to give a conclusion about steady-state stability in this case and we are interested in continuing the investigation in the next chapter.

CHAPTER 4

Topological charge and its control

Contents

In this chapter, we continue the theoretical study of the ring laser array with a focus on the probability of phase-locking in a vortex solution (TC $q \neq 0$). Those beams can be very useful in many applications. Such TC-carrying beams show robustness to random perturbations and the ability to conserve their charge [Eshaghi 2021; Kovalev 2021; Ikonnikov 2020]. They find a wide range of applications for example to STED microscopy [Gould 2017], particle manipulation (such as optical trapping, spanners, tweezers, and microscale mass transport [Rafferty 2021; Xiang 2022; Shen 2021; Zhou 2018; Ambrosio 2012]), for optical communications, improvement of the bandwidth of cryptography protocols [Wang 2016; Yang 2022], and even coronography [Engay 2020]. These beams are typically formed by passing the light through a spatially phase-modulating element, such as SLM, birefringent liquid crystal, axicon, phase-plate [Shen 2019], phase-grating [Harshith 2019], hologram [Li 2018], or integrating a gain and a loss mask [Seghilani 2016]. Phase-locking of the laser array with $q \neq 0$ has a probabilistic nature. No additional elements are required then. A generation of topological defects was studied and observed quite recently in the coupled class-B laser arrays [Mahler 2019b; Pal 2017; Nixon 2013b]. However, the benefits or disadvantages of the VECSEL array for vortex generation are not clear yet.

In this chapter, we analyze the results of numerical calculations obtained with the same rate equation system, as investigated in the previous chapter given by eqs. 3.2. The first part of the chapter investigates the probabilities of the natural phase-locking to different topological charges q with different parameters of the system. In particular, we study the influence of the coupling strength and the number of lasers in the ring array. Additionally, we investigate the effect of the coupling with the next-nearest neighbor, when each laser is coupled with the four closest lasers. We also wonder whether the fact that the lasers that we consider here belong to the class-A dynamical class makes them more robust to the Henry factor than class-B lasers. The second part of the chapter discusses available methods to force phase-locking with the desired topological charge. Here we consider a technique of diffraction engineering when the mask topology is non-uniform and its topology is chosen specifically for a predetermined solution. A method of the laser array steady-state manipulation through non-isotropic optical feedback is presented.

The study in this section is performed considering a zero detuning $\Omega_i = 0$, and cavity parameters inherited from the previous section and considered constant ($F_{\text{sat}} = 10^{10}, \tau_{\text{cav}} = 30\,\text{ns}$). To investigate the probability of laser array phase-locking P_q with TC q in this chapter we calculate the outcomes with hundreds of randomly generated sets of different initial conditions. The outcomes are then checked for the phase-differences stabilization ψ_i within the $t = 10\,\text{ms}$ time interval (extremely long comparing the round-trip in the laser cavity). After this, the number of outcomes with each q is calculated based on the total phase accumulation from laser to laser. Even though the vortices are highly desired, the beams with TC $q = 0$ also have a wide application area thanks to the intense peak in the center of the far field. Thus, a reliable range of parameters in which any q dominates is of interest.

4.1 Uniform Coupling

Let us first investigate the possibility of phase-locking with different topological charges q for a uniformly coupled ring laser array. The coupling is uniform, when all holes in the array have the same size, and the holes are equally distant from each other and to the center of the array. The mask should be carefully aligned inside the laser cavity without tilts.

4.1.1 Influence of the coupling strength

First, we consider only the effect of the coupling strength amplitude $|\eta|$, taking the value of the coupling argument equal to zero $\theta = 0$. For example, this assumption is legitimate in the case of diffraction cavity length z close to 220 µm or 400 µm. In these cases, the coupling is real and positive. The dependence of the overlap on z is shown in Fig. 2.20 in chapter 2.

The rate equation system (eq. (3.2)) for $n = 20$ laser array is solved with 1000 random initial conditions to calculate the probability of the different steady-sate solutions. The outcomes of phase-locked cases are sorted according to their TCs. Probabilities to obtain q from -2 to 2 for these cases are shown in Fig. 4.1 for different values of the real positive coupling strength $|\eta|$.

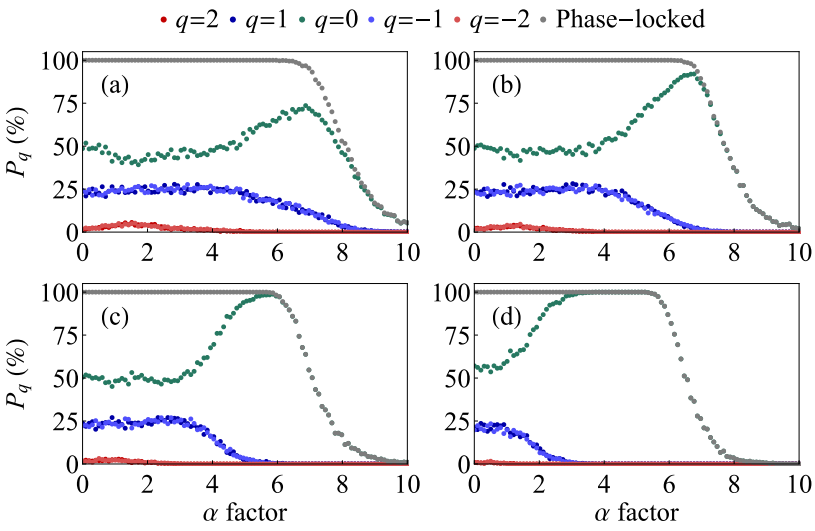

FIGURE 4.1: Probabilities $P_{|q|}$ to obtain a topological charge $|q|$ versus Henry factor α in a $n = 20$ lasers array for different values of the coupling strength $|\eta|$: (a) $|\eta| = 0.00125$, (b) $|\eta| = 0.0025$, (c) $|\eta| = 0.005$, (d) $|\eta| = 0.025$.

The total proportion of phase-locked outcomes is shown as gray dots. This proportion decreases with an increase of the α factor in each subplot in Fig. 4.1. The value of the coupling strength increases from subplot (a) to subplot (d). We can see

that the probability of phase-locking with non-zero TC ($q \neq 0$) increases for small values of the coupling amplitude $|\eta|$ (compare for example (a) and (d)). At the same time, the probability $P_{|q|=1}$ of phase-locking in a vortex with $|q| = 1$ never exceeds the probability of "in-phase" phase-locking $P_{q=0}$. The probabilities of positive and negative vortices ($\pm q$) are equal in all cases. Also, the probabilities to observe non-zero TC reveal the limit of α parameter, as is predicted with eq. (4.1):

$$\alpha_{\text{lim}} = \frac{2\cos\theta\cos\psi_q}{\sin\left(\psi_q - \theta\right)}. \tag{4.1}$$

The limiting α value gives the maximal value of the Henry factor, where the stable phase-locking with a certain TC may be observed. The formula gives $\alpha_{\text{lim},|q|=1} = 6.6$, $\alpha_{\text{lim},|q|=2} = 3.6$ for $n = 20$. These values should be compared with the maximum values of α when phase-locking happens almost every time. Subplots (a) and (b) agree with the analytical prediction. Nevertheless, eq. (4.1) was obtained with an assumption of small $|\eta|$. This explains the decrease of the numerically obtained α_{lim} with an increase of the coupling strength in sub-figures (c,d).

4.1.2 Influence of the coupling argument

The above mentioned formula (eq. (4.1)) also predicts a dependence of α_{lim} on the coupling argument θ. We expect positive values of θ to extend the phase-locking range of α_{lim}. Conversely, negative values of θ should reduce this range for all TCs. Probabilities calculated for several coupling argument values are shown in Fig. 4.2.

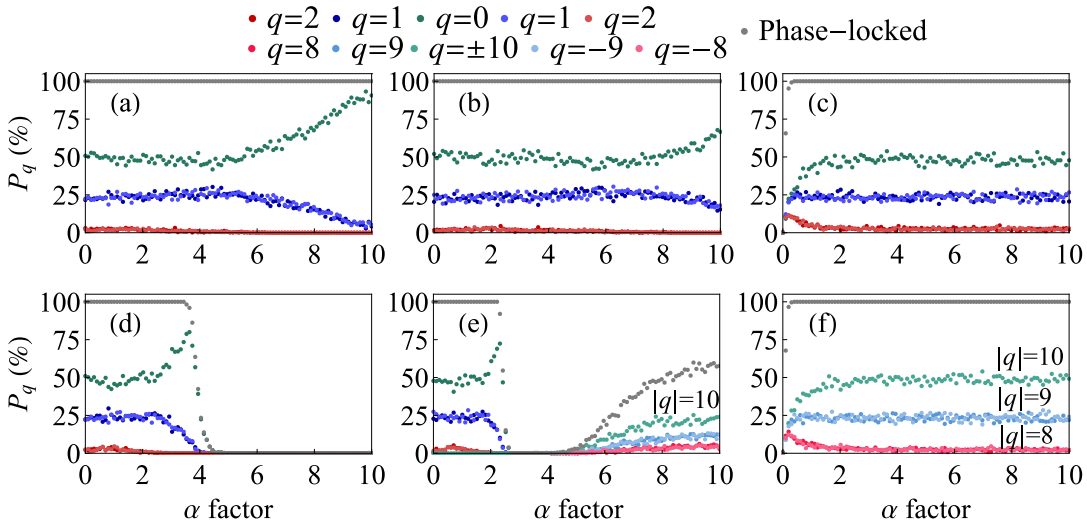

FIGURE 4.2: Probabilities $P_{|q|}$ to obtain a topological charge $|q|$ versus Henry factor α in an array of $n = 20$ lasers for different values of the coupling argument θ: (a) $\theta = \pi/20$ (rad), (b) $\theta = \pi/10$ (rad), (c) $\theta = \pi/2$ (rad), (d) $\theta = -\pi/20$ (rad), (e) $\theta = -\pi/10$ (rad), (f) $\theta = -\pi/2$ (rad). Modulus of the coupling strength is $|\eta| = 0.0025$.

The coupling argument values we used are typical for diffraction coupling length z around 500 to 600 µm. Indeed, the limiting values α_{lim} of the Henry factor change in agreement with the analytical formula eq. (4.1). In subplots (a), (b), and (c) for positive θ the limiting values α_{lim} are at least equal to 10. An opposite situation is shown in subplots (d), (e) and (f) for negative coupling arguments θ. The limiting Henry factor for $|q| = 1$ decreases in these cases, such that α_{lim} is close to 4 in subplot (d), α_{lim} is around 2.8 in (e) and α_{lim} is around 0 in (f). The range α from 4 to 10 in subplot (d) and α from 2.8 to 4.6 in subplot (e) gives a negligible chance to see a phase-locked laser array.

At the same time, subplots (e) and (f) show a new range, where the system phase-locks close to the out-of-phase solution. The most probable TC is given then by $q = \pm 10$, $\psi_q = \pm\pi$, and $|q| = 8, 9$. The portion of the phase-locked cases increases with the α factor in this case (see α in the range from 5 to 10). The subplots (c) and (f) show a negligible proportion of phase-locked solution at $\alpha_{\text{lim}} = 0$. However, as soon as α is more than zero there seems to be no upper limit on α to set a possible $q = 1$ solution. The values of α determined numerically for $|q| = 1$ are plotted in Fig. 4.3 along with the analytical expression of eq. (4.1).

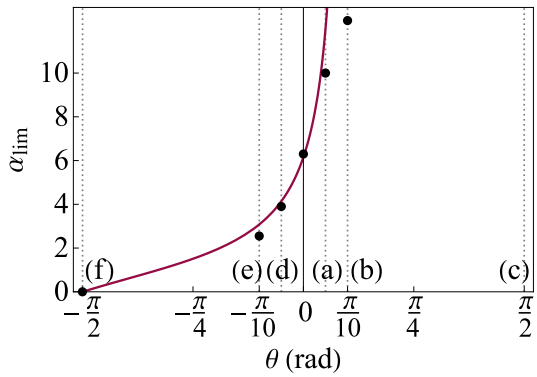

FIGURE 4.3: Graphical illustration of the limiting Henry factor α_{lim} for $q = 1$ calculated according to eq. (4.1) and compared with numerically calculated data from Fig. 4.2.

The analytical formula (4.1) is in good agreement with numerical results. Vertical dashed lines indicate the coupling argument θ values illustrated in Fig. 4.2. The point $\{\pi/10, 12.6\}$ is obtained by extrapolation of the probability data $P_{|q|=1}$ shown in Fig. 4.2 (b).

4.1.3 Effect of the number of lasers in the array

In this section, we investigate the influence of the number of lasers in the ring array on the probability of phase-locking in the vortex ($|q| \neq 0$). Eq. 4.1 gives the dependence on n through the steady-state phase-difference $\psi_q = 2\pi q/n$. Thus α_{lim} should increase with the increase of number n of lasers. Fig. 4.4 shows the evolution of

$P_{|q|}$ versus α for different numbers of lasers $n = 5, 10, 15, 20$ in the array for a real coupling strength $|\eta| = 0.0025$. The number of lasers increases from plot (a) to (d).

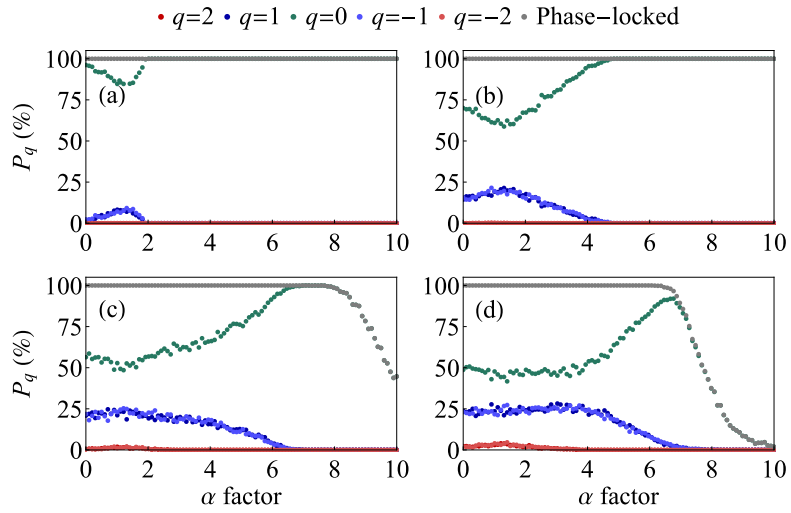

FIGURE 4.4: Probabilities $P_{|q|}$ to obtain a topological charge $|q|$ versus Henry factor α for different values of the number n of lasers: (a) $n = 5$, (b) $n = 10$, (c) $n = 15$, (d) $n = 20$ with $\eta = 0.0025$

The increase in the number of lasers n positively affects probabilities. The range of α values for non-zero values of probability $P_{|q|=1}$ increases with a n. For example, this can be seen when comparing the subplots (a) for $n = 5$ lasers and (b) for $n = 10$ lasers, where the peak probability values are $P_{\max,|q|=1} = 10\%$ and $P_{\max,|q|=1} = 20\%$. At the same time, the vortex probability never exceeds 25% and it is always smaller than $P_{q=0}$, which is shown in Fig. 4.4 as green dots. Furthermore, one can notice that the high-order vortices with $q = \pm 2$ have a negligible probability for n from 5 to 10.

We can collect all values of the probability calculated for n from 5 to 20 and stack them to visualize the border of non-zero probability P_q. Such data are composed in Fig. 4.5 for $|q| = 1$ in subplot (a) and $|q| = 2$ in subplot (b).

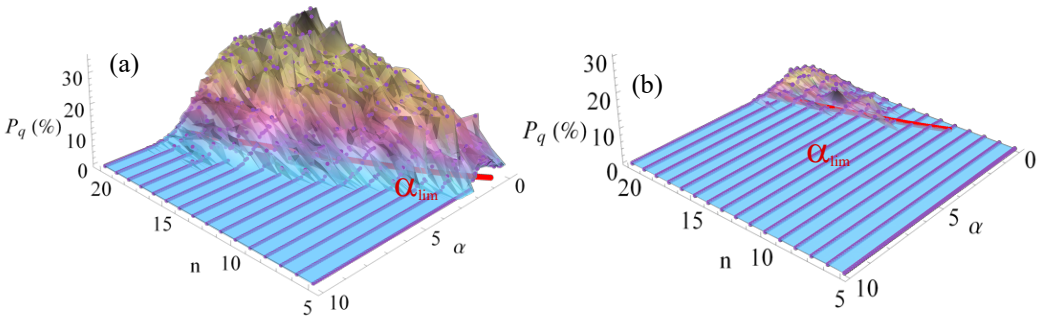

FIGURE 4.5: Probabilities P_q to obtain a topological charge q versus Henry factor α and n for real positive $\eta = 0.0025$. Red curves are given by the formula eq. 3.13. Plots (a), (b) are for $|q| = 1$ and $|q| = 2$.

Negative topological charges have the same stability regions as the positive TCs. We can see, that the red line of analytical solution (obtained with eq. 3.13) fits well the border of the numerically calculated probabilities.

By this, we can conclude, that eq. 4.1 is a good guide to estimate α_{lim} range that permits obtaining a non-zero TC with a small complex coupling in the ring arrays with any number of lasers n.

4.1.4 Effect of the next-nearest neighbor

The coupling of the laser indexed i with its second nearest neighbors $i \pm 2$ was estimated to be small ($\kappa_{i\to(i\pm2)} < 0.05\kappa_{i\to(i\pm1)}$, see Fig. 2.22). This value seems negligible. Nevertheless, its influence on the probabilities can reveal its influence on system stabilization in general. The are three subplots in Fig. 4.6 showing the results of numerical calculations for $n = 5, 10, 15$. The coupling with the second neighbor is taken as 5% of coupling with the nearest neighbor ($|\eta| = 0.0025$).

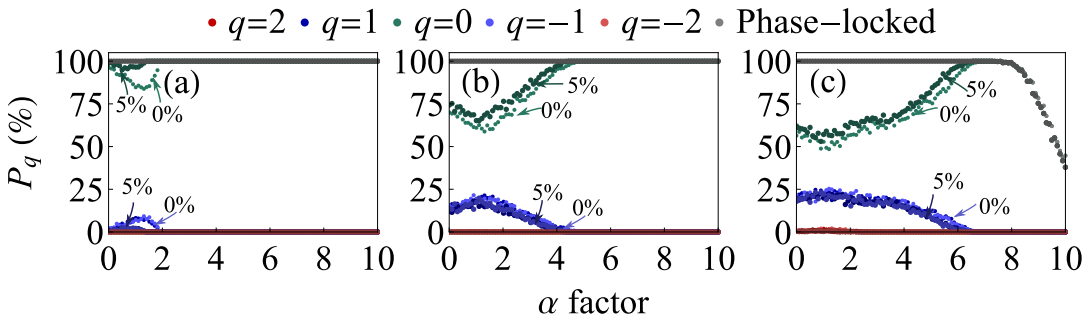

FIGURE 4.6: Probabilities $P_{|q|}$ to obtain a topological charge $|q|$ versus Henry factor α for different values of the number n of lasers with 0% (in legend colors) and 5% (in darker legend colors) of $|\eta| = 0.0025$ coupling between next-neighbouring lasers of the ring array. The nearest-neighbor coupling strength is $|\eta| = 0.0025$. Here (a) $n = 5$, (b) $n = 10$, (c) $n = 15$.

The three corresponding subplots of Fig. 4.4 (a,b,c) without second neighbor influence are used as backgrounds. Those data are marked by 0%. The data obtained with 5% coupling are given in a darker color and marked correspondingly. Each of the calculated cases shows that the influence of the second neighbors is to make $q = 0$ more probable. At the same time, the corresponding decrease of P_q when one considers coupling to the next-nearest neighbor becomes smaller with an increase of n. From this, we can also conclude that the smaller the edge-to-edge separation between the holes, the more phase-locked solutions will have $q = 0$, because of the increase of the overlap with the second nearest neighbor. However, we can also notice that an increase in the number n of lasers makes the laser array less sensitive to the coupling with the second nearest neighbor. Consequently, most of the time the model can be kept simple, i.e. one can consider only the coupling with the closest neighbors.

4.1.5 Comparison with class B lasers

This section addresses the question of whether the class-A dynamical class is more robust to the Henry factor than class-B lasers. The comparison of the dynamics for those classes was discussed in section 2.4 for the example of a single laser. Here we expand the system of the rate equations for class-B lasers with the nearest neighbors coupling description in the same way as was performed for the class-A VECSEL ring array. The rate equations system for class-B lasers become:

$$\begin{aligned}
\frac{dA_i}{dt} &= -\frac{1}{2\tau_{cav}}\left(1-\frac{\Delta n_i}{\Delta n_{th}}\right)A_i + \frac{|\eta|}{2\tau_{cav}}\left[\cos(\phi_{i+1}-\phi_i+\theta)A_{i+1}+\cos(\phi_{i-1}-\phi_i+\theta)A_{i-1}\right] , \\
\frac{d\phi_i}{dt} &= \frac{\alpha}{2\tau_{cav}}\frac{\Delta n_i}{\Delta n_{th}} + \frac{|\eta|}{2\tau_{cav}}\left[\frac{A_{i+1}}{A_i}\sin(\phi_{i+1}-\phi_i+\theta)+\frac{A_{i-1}}{A_i}\sin(\phi_{i-1}-\phi_i+\theta)\right]+\Omega_i , \\
\frac{d\Delta n_i}{dt} &= \frac{r_i\Delta n_{th}}{\tau} - \frac{\Delta n_i}{\tau} - \frac{1}{\tau}\frac{A_i^2}{F_{sat}}\Delta n_i ,
\end{aligned} \tag{4.2}$$

where τ is the carrier lifetime, Δn_i the carrier density providing gain to laser i, and Δn_{th} the carrier density at threshold. Results of the simulations with these equations are shown in Fig. 4.7 for different numbers of lasers and must be compared with identical simulations for class-A lasers shown in Fig. 4.4.

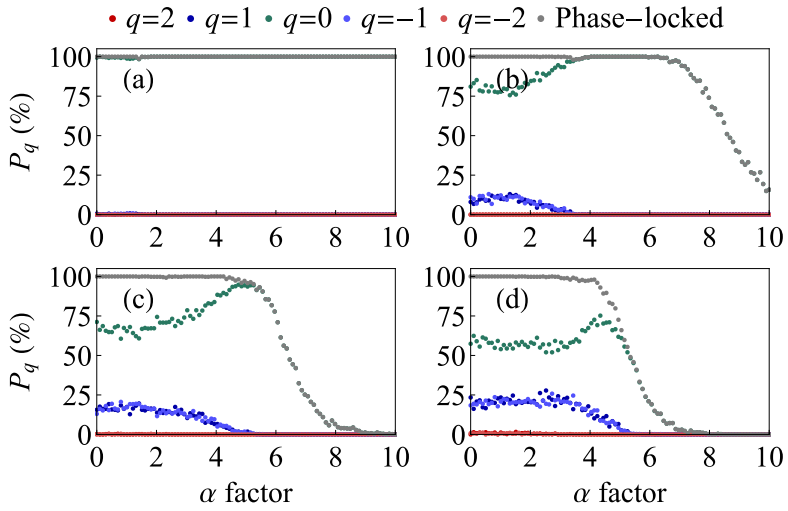

FIGURE 4.7: Probabilities $P_{|q|}$ to obtain a topological charge $|q|$ versus Henry factor α with class-B laser array ($\tau_{cav} = 30\,ps$, $\tau = 1\,ns$) for different values of the number n of lasers and fixed $\eta = 0.0025$. Sub-figures (a) $n = 5$, (b) $n = 10$,(c) $n = 15$, (d) $n = 20$ consistent with Fig 4.4.

The subplots (a-d) in both Fig. 4.7 and Fig. 4.4 correspond to $n = 5, 10, 15, 20$, respectively. These simulations show that the probability for a TC $q \neq 0$ becomes much smaller in class-B lasers than in the case of a class-A laser with the same parameters. For example, Fig. 4.7 (a) shows that with $n = 5$ it is impossible to generate

a TC-carrying beam with the class-B laser, while it is observed in $\sim 10\%$ cases with a class-A laser (see Fig. 4.4 (a)).

Also, by comparing Figs. 4.7 (b) and 4.7 (c) with Figs. 4.4 (b) and 4.4 (c), respectively, one can see that the class-A laser exhibits larger probabilities for TC-carrying beams to be emitted than the class-B laser. Furthermore, the limiting value α_{lim} of the Henry factor over which no TC-carrying beam can occur is larger for the class-A laser than for the class-B laser. This shows the larger interest of class-A lasers compared with class-B lasers in this context. The probability of generating non-zero values of q for a class-B laser can be increased by increasing r, as already observed in [Pal 2017]. For example, probabilities similar to those of a class-A laser with $r = 1.2$ can be obtained with $r > 2.4$ in a class-B laser.

4.2 Non-Uniform Coupling

The previous section showed that uniform coupling can't change the symmetry between the positive and negative values of TC. It is also unable to provide a "winning" vortex solution $P_{|q|=1} > P_{q=0}$. The uniform coupling is provided by perfectly symmetrical masks. The concept developed in this section is the opposite. Here we consider the breaking of the array's rotational symmetry by altering the geometry of the loss-mask profile.

The difference of such masks with respect to the case of uniform hole parameters is expected to affect the coupling coefficient between the lasers and thus affect the dynamics of the system and the choice of the system steady-state. Thus we investigate the generation of asymmetric vortex (AV) beams by introducing different kinds of asymmetries in the array, called "Gradient", "Random", and "Point defect" masks and presented in Fig. 4.8.

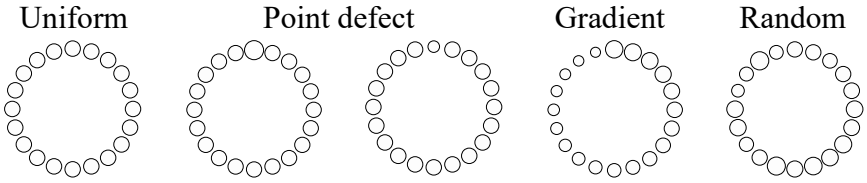

FIGURE 4.8: Schematic shapes of the different loss-mask patterns, called Uniform, Point defect, Gradient, and Random. The hole diameters are not to scale.

Here we continue investigations of an array of $n = 20$ lasers. In the Point defect case, one of the holes has a smaller or bigger diameter than the rest of the holes. In the gradient case, the hole diameter increases gradually from the first to the last hole, while in the random configuration, the hole diameters are randomly chosen around 200 µm. The hole diameters in Fig. 4.8 are presented not to scale with the array geometry. The dimensions are taken in agreement with our experimental possibilities, the standard hole diameter is taken to be 200 µm, and the center-to-center separation

between two successive holes is 250 µm. The details of the different masks are given in Table 4.1.

Hole Index	1	2	10	19	20
“Big" defect	202	200	200	200	200
“Small" defect	197	200	200	200	200
Gradient	197	197.25	199.25	201.5	201.75
Random	197.25	198.25	201	199.5	200

TABLE 4.1: Values of the hole diameters in the different chosen configurations of 20 lasers. The standard deviation of the hole diameters in the random configuration is chosen equal to 1.5 µm, mean value of 200 µm.

Coupling between neighboring lasers

Fig. 4.9 shows the computed values of the modulus and argument of coupling coefficients $\kappa_{i\to i+1}$ in solid lines and $\kappa_{i\to i-1}$ in dashed lines versus laser index i calculated with eq. (2.18).

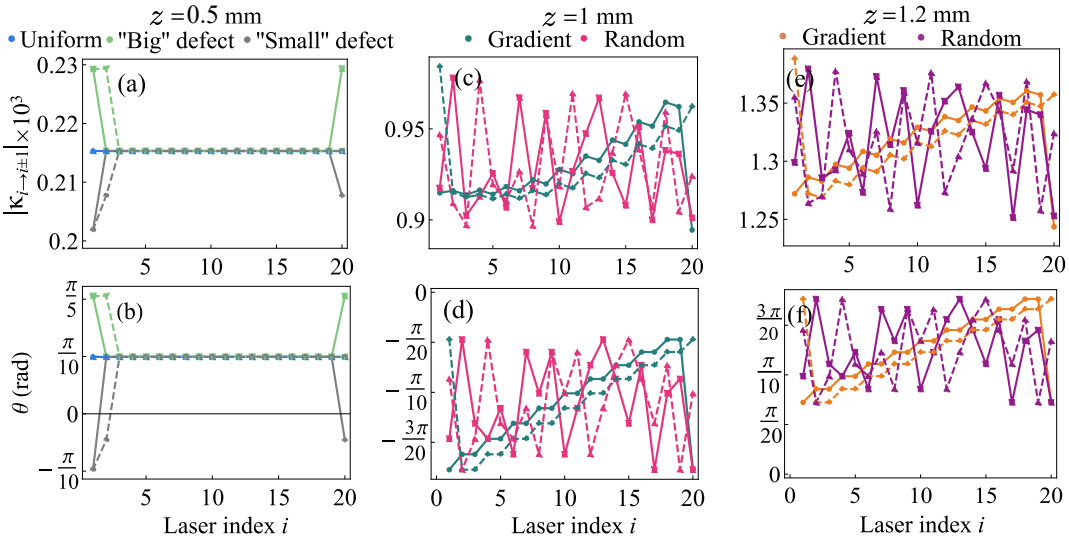

FIGURE 4.9: (a,c,e) Modulus and (b,d,f) argument of the coupling coefficients between neighboring lasers for the different masks. (a,b) Uniform and point defect masks studied with $z = 500$ µm; (c,d) Gradient and Random mask studied both with $z = 1000$ µm and $z = 1200$ µm (e,f). Solid lines: $\kappa_{i\to i+1}$; dashed lines: $\kappa_{i\to i-1}$. The hole diameters are given in Table 4.1.

Different colors of the lines correspond to the different masks shown in Fig. 4.8, with the values of the hole diameters given in Table 4.1. The distance between the centers of the holes is constant and equal $h = 250$ µm. These coupling coefficients

do not depend on i in the case of the uniform mask, while here we can see how the variations of the hole diameters affect not only the modulus of the coupling but also its phase for non-uniform masks. The "Big" and "Small" defect masks are chosen to observe the positive and negative coupling of the first hole with its neighbors respectively. These variations around the mean value are large (up to $\sim 12\%$) because of the small value of the distance z that we have chosen ($z = 500\,\mu$m to $1200\,\mu$m). The $\theta_{i\to i\pm1}$ are all positive for $z = 1200\,\mu$m, while the distance $z = 1000\,\mu$m leads to the situation, when the $\theta_{i\to i\pm1}$ are negative for certain laser indices i and positive for others. We have already seen that the θ value determines stability limits and preferred topological charge.

4.2.1 Phase-locked solutions with non-uniform complex coupling

The final steady-state depends a lot on the initial conditions. At a certain run, it is possible to generate a vortex solution for each of the loss patterns we investigate. Phase-difference solution is given in Fig. 4.10 for two different sets of initial conditions, leading to the non-vortex $q = 0$ (a), (c) and vortex $|q| = 1$ (b), (d) solutions.

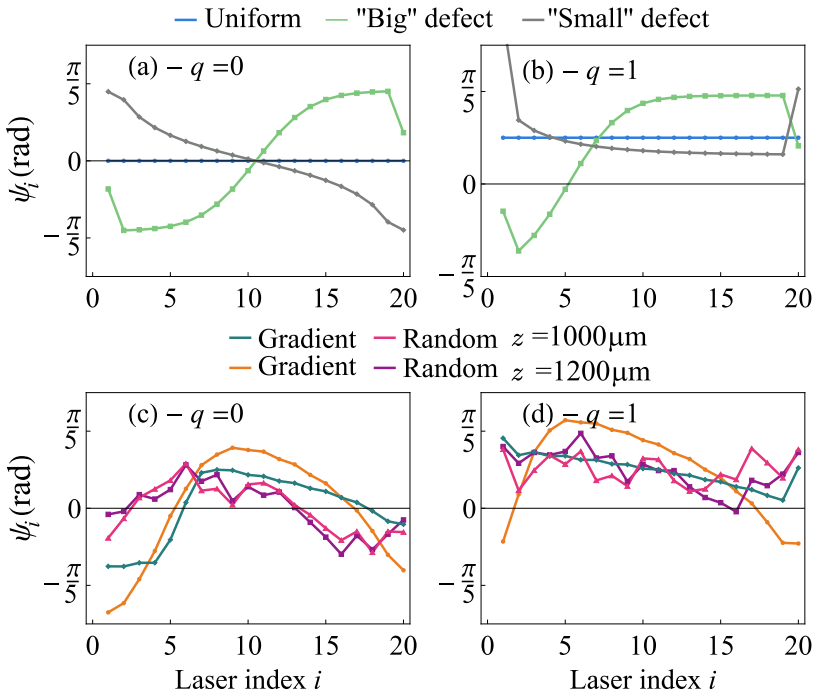

FIGURE 4.10: Phase-differences solutions calculated for different mask shapes with the coupling values shown in Fig. 4.9. Subplots (a) and (b) show the phase differences with Uniform and Point defect masks at diffraction cavity distances $z = 500\,\mu$m. Subplots (c) and (d) show the phase differences with Gradient and Random masks at two diffraction cavity distance $z = 1000, 1200\,\mu$m. System parameters used for the calculations are $r = 1.2, \alpha = 2$.

The Gradient and Random masks can be investigated for $z = 500\,\mu m$ also. But in this case, only a high-value TC, such as $q = 9, 8$, can be observed. Results for the cases of $q = 9$ with Gradient mask and $q = 8$ with the Random mask are presented in Fig. 4.11, where the far-field is calculated with the method introduced in Sec.3.1.2. Each laser is approximated with a Gaussian beam with 200 µm beam-waist.

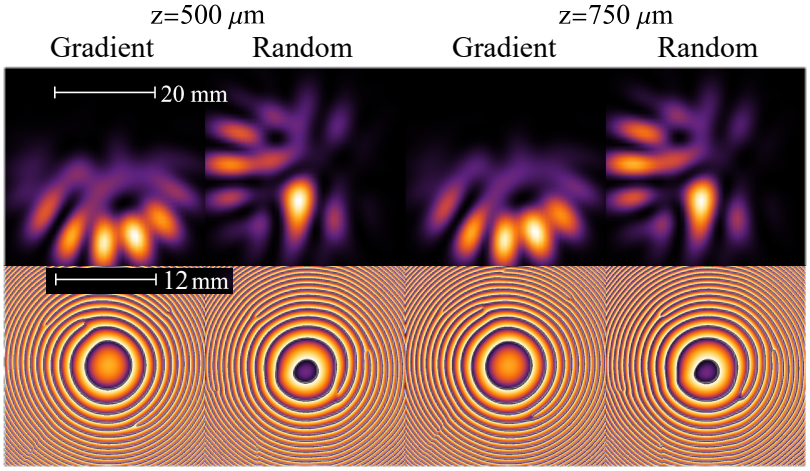

FIGURE 4.11: Intensity patterns and phase distribution patterns calculated for $z = 500, 750\,\mu m$ for Gradient and Random masks. Phase difference for the gradient mask corresponds to the topological charge $q = 9$ for the Gradient mask and $q = 8$ for the Random mask. No cases with q close to ± 1 are found.

The phase differences in these cases fluctuate in a wide range and lead to very complicated far-field intensity patterns inapplicable for regular vortex applications. Thus, we investigate these topologies at two different distances $z = 1000$ and $1200\,\mu m$. It is important to mention that vortex is always associated with topological charge q which has two definitions: though the neighboring phase-difference $q = \frac{n}{2\pi}(\phi_{i+1} - \phi_i)$ or through the total phase $q = \frac{1}{2\pi}\sum_{i=1}^{n} arg(E_i^* E_{i+1})$ [Pal 2015], where arg takes values in a range $[-\pi, \pi]$. Non-uniform masks can't satisfy the first definition. Here we associate the topological charge with a total phase accumulation. The variance of the phase distribution depends not only on the mask parameters but also on the values of the Henry factor and the pumping rate. It increases with the increase of r and α.

Using the amplitudes and phase differences of the steady states we can visualize the far field of the VECSEL array with the calculated phase differences. Fig. 4.12 illustrates the far fields of a laser array of $n = 20$ lasers with non-uniform masks, where each laser is approximated by a Gaussian beam with 200 µm beam-waist (see section 3.1.2 for details of the method).

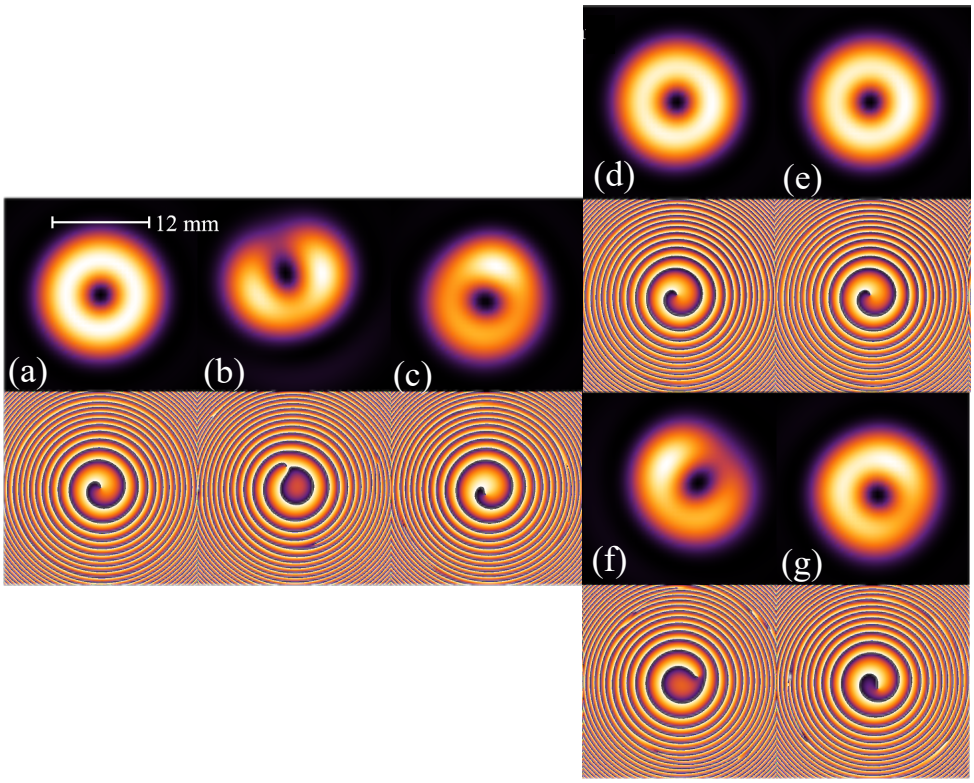

FIGURE 4.12: Intensity patterns (top row) of the phase-locked laser array ($n = 20$, $q = 1$) with phase differences (bottom row). Sub-figures named (a-c) correspond to the "Uniform", "Big" defect, and "Small" defect mask profiles. Sub-figures (d,f) correspond to the Gradient mask at (d) $z = 1000\,\mu$m and (f) $z = 1200\,\mu$m. Far-field profile with a Random mask with $z = 1000\,\mu$m and $z = 1200\,\mu$m are shown in sub-figures (e), (g) correspondingly. Intensities normalized to the beam's maximum, phase patterns show the phase variation from 0 to 2π. The patterns correspond to solution of the rate-equation with coupling parameters shown in Fig. 4.9.

The doughnut shape and phase singularity are preserved with the non-uniform masks but with strongly varying qualities. It is easy to see, that the vortices shown in Fig.4.9 (c), (d), (e) have a better phase profile and a more symmetric intensity beam profile. These cases are calculated with the mean coupling argument $\theta_{i\to i\pm1}$ closer to $2\pi/n$ than other cases, thanks to the coupling argument having both positive and negative values. The uniform mask leads to the perfectly symmetric beam structure and perfect vortex phase profile with a phase singularity in the center, even though $\theta_{i\to i\pm1}$ is not zero. As discussed in the previous chapter, the steady-state phase-differences ψ_q do not depend on θ with the uniform coupling (see eq. 3.4).

The patterns (b), (f), (g) give an asymmetric beam structure and complicated phase profiles with a singularity point shifted from the center of the beam with respect to the coupling argument distribution around its mean $\theta_{i\to i\pm1}$. For example,

the strongest deviation of the coupling strength is found for the "Big" defect mask between the $i = 20, 1, 2$ lasers, where the defect hole corresponds to $i = 1$. This leads to a spatial shift of the beam topological effect, as can be seen in Fig. 4.12 (b).

Each intensity pattern presented in Fig. 4.12 (b-g) is useful as an asymmetric vortex (AV). It has been shown that better results in the particle trapping and micromotoring domain can be achieved with an AV beam. For example, the rate of microparticle motion is shown to increase linearly with the asymmetry of vortex-carrying Bessel- or Laguerre-Gaussian beams [Kotlyar 2016; Kovalev 2016]. The thermal damage of the live cells is also reported to be better managed when the OV symmetry is broken [Kotlyar 2016].

Another example is that the vortex-based information storage using the topological charge can be improved through additional information encoded in the non-symmetrical intensity profile [Singh 2023]. The shape of the beam is conserved through propagation and thus constitutes a unique parameter, similar to the phase profile of the beam. A strong asymmetry can allow the beam to increase its storage capacity. However, a strong deformation of the optical vortex can make the information carried by the phase profile more difficult to read.

4.2.2 Vortex probability with non-uniform loss-mask profile

Probabilities for the Uniform, "Big" and "Small" defect loss profiles are presented in Fig. 4.13.

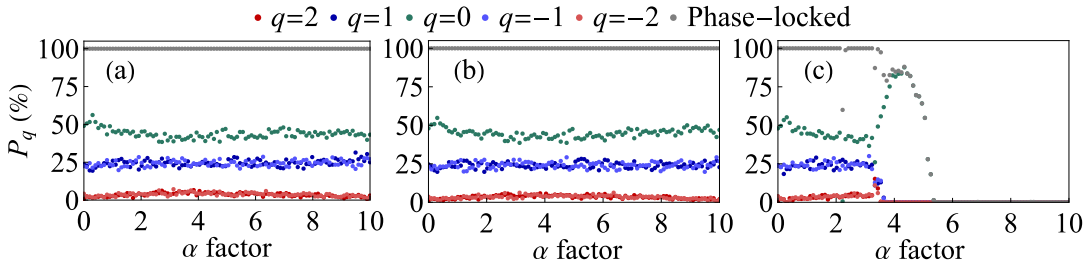

FIGURE 4.13: Probabilities to phase-lock laser array with topological charge q. Different subplots correspond to different masks: (a) is Uniform, (b) "Big" defect, (c) "Small" defect.

The data in Fig. 4.13 are calculated with 500 random initial conditions for each value of α. The probabilities for the Uniform and "Big" step mask remain very close. The argument of the coupling has the same sign for each pair of lasers in the array. The limiting α factor is very high.

A very different case is presented in sub-figure (c) for the "Small" defect. The limiting Henry factor value $\alpha_{\text{lim}} = 3.8$ is seen only in this subplot. Then, a new stability range only for $q = 0$ appears in the range α from 3.8 to 5.3, where 100% of the phase-locked solutions lead to the "in-phase" array synchronization with $q = 0$. There is an interesting effect close to $\alpha = 2$, where 100% of the phase-locked

cases lead to a non-zero topological charge. The width of the region increases with a decrease of the coupling strength $|\eta|$, but the physical explanation of this effect requires further investigation. None of these masks changes the symmetry between the positive and negative values of q.

The influence of the Gradient and Random masks calculated for two different values of distance z of the diffraction cavity is shown in Fig. 4.14.

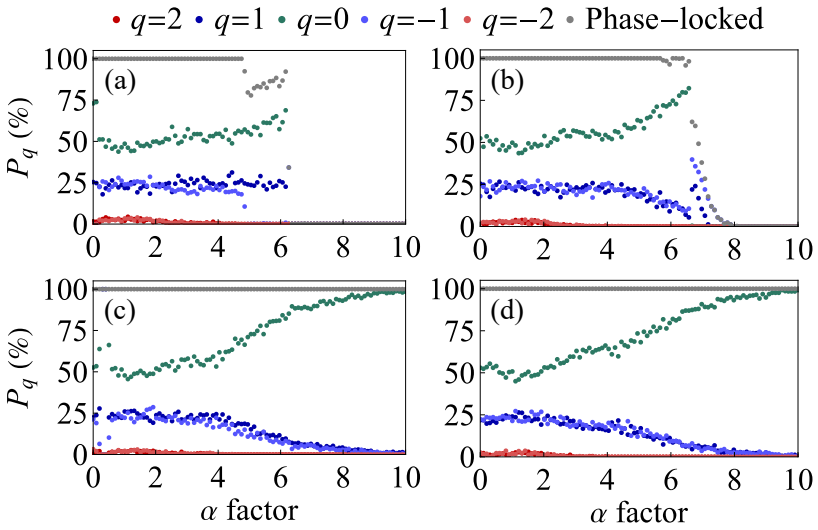

FIGURE 4.14: Probabilities to phase-lock laser array with topological charge q. Subplots (a) and (c) represent the effect of the Gradient mask, while (b) and (d) show results with the Random holes distribution. Top row (a, b) is calculated with $z = 1000\,\mu$m. The bottom subplots (c) and (d) are calculated with $z = 1200\,\mu$m.

The first row of the figure is calculated for $z = 1000\,\mu$m, where the sign of $\theta_{i\to i\pm1}$ is both positive and negative for different pairs of lasers. The Gradient mask shows a small symmetry break in the α factor range from 4.5 to 10 in subplot (a). This symmetry break is given by only several percent of the probabilities $P_{q=1} > P_{q=-1}$. Also, a small range α around 0.4 shows destabilization of $q = 1$ and consequent symmetry break between positive and negative vortex in subplot (c).

Let us focus on the comparison of the data presented in sub-figures (a), (b). Both mask geometries show symmetry breaking between $+q$ and $-q$ close to the end of the α factor stability range. The probability of observing laser array phase-locking with $q = 1$ in the range α from 4.8 to 6.3 prevails over $P_{q=-1}$. At the same time, the "in-phase" solution is still more likely to occur. Random mask shows a small range, where $P_{q=0} = 0\%$ in the range α_{lim} from 6.8 to 8. The "winning" solution is then $q = -1$. At the same time, the number of phase-locked cases decreased dramatically in this range.

In total, we noticed that there are several cases of dramatic mask geometry impacts. Those cases are shown in Fig. 4.13 (c) for the small "Point defect" mask and Fig. 4.14 (a,b). Each of the cases occurs when the coupling argument $\theta_{i\to i\pm1}$ has

both positive and negative signs within the same laser array. Other investigated cases (i.e. Uniform, "Big" defect at $z = 500\,\mu m$ and Gradient and Random masks at $z = 2000\,\mu m$) have only positive values of $\theta_{i\to i\pm1}$.

Then in the next step, we investigate a case, when we consider a virtual mask, which adds $\theta_{i\to i+1} = 2\pi/n$ and $\theta_{i\to i-1} = -2\pi/n$ between lasers to force the system phase-locking with an anti-vortex $q = -1$. The result is shown in Fig. 4.15, where among the uniformly coupled lasers the condition is satisfied for only one one of them $i = 1$ (a), for two lasers with for $i = 1,2$ (b), for half of the array $i \in [1,10]$ (c) and (d) for each laser in the array $i \in [1,20]$.

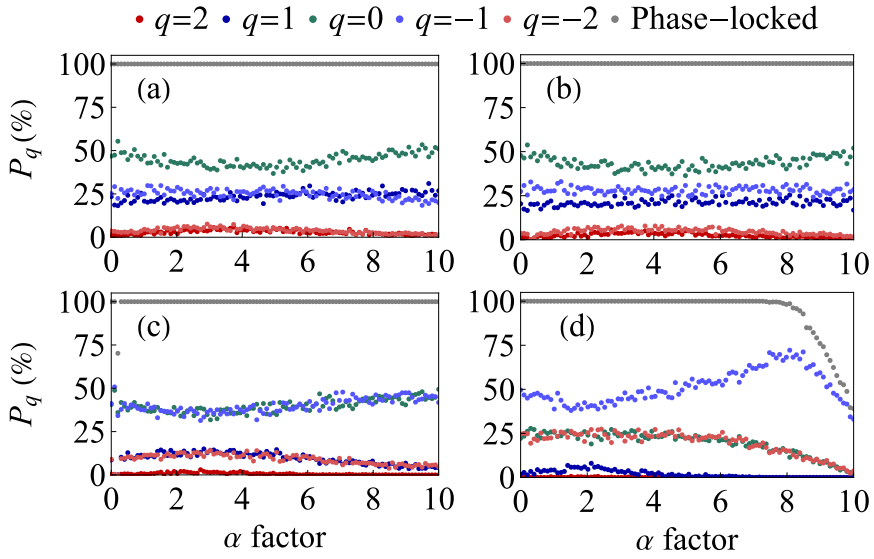

FIGURE 4.15: Probabilities to obtain topological charge with a specially designed mask satisfying the criteria $\theta_{i\to i-1} = 2\pi/n$ and $\theta_{i\to i+1} = -2\pi/n$ for (a) holes $i = 20,1,2$, (b) holes $i = 20,1,2,3$, (c) half of the array. (d) each hole satisfies the condition. Zero holes satisfying these criteria correspond to the probability shown in Fig. 4.13 (a).

Fig. 4.15 shows that this technique indeed allows to increase the value of $P_{q=-1}$. This increase happens thanks to a decrease of $P_{q=0}$. Moreover, when one increases the number of hole pairs for which $\theta_{i\to i\pm1} = 2\pi/n$, the probability $P_{q=-1}$ increases, as can be seen by comparing Fig. 4.15 (a) where the only value of $\theta_{i\to i+1}$ is equal $\pm2\pi/n$, (b) where two holes satisfy $\theta_{i\to i+1}$ is equal $\pm2\pi/n$, (c) where half of the array satisfies $\theta_{i\to i+1}$ is equal $\pm2\pi/n$ and (d) where the whole array satisfies $\theta_{i\to i+1}$ is equal $\pm2\pi/n$. In particular, when the number of lasers for which $\theta_{i\to i+1}$ is equal to $\pm2\pi/n$ exceeds $n/2$, one obtain $P_{q=-1} \geq P_{q=0}$. In this case the solution with non-zero topological charge becomes dominant, like for example in Fig. 4.15 (d).

4.3 Influence of the optical feedback

There are multiple ways to implement injection feedback for an optically pumped laser. Here we are interested in optical self-injections of the laser array field with the help of an external cavity. The main goal of this study is to investigate the role of optical feedback (OF) in vortex probability manipulation. The OF is known for inducing complicated nonlinear phenomena in laser dynamics [Erneux 2010] including relatively stable class-A lasers [Kuwashima 2001]. We wish to avoid the investigation of the unstable dynamics and focus on the selective properties of the external cavity modes. A simple scheme to obtain non-homogeneous OF, i.e. which is not the same for all lasers is shown in Fig. 4.16.

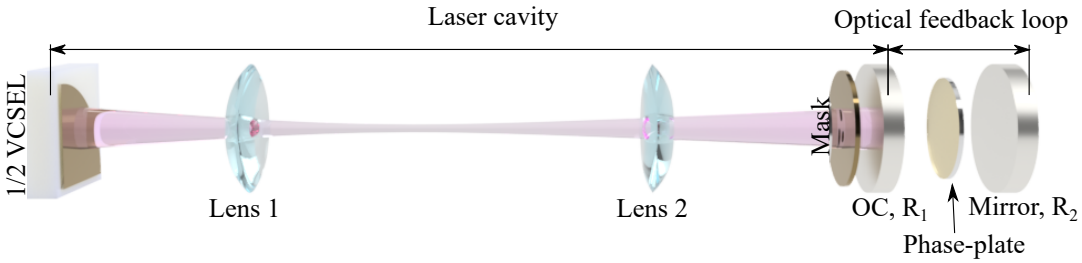

FIGURE 4.16: Optical scheme for the optical feedback realization. The planar degenerate cavity VECSEL array output is directed to the phase-plate and OF mirror. The scheme doesn't show the imaging optics in the feedback loop.

Let us assume that we have a perfect degenerate cavity in which all lasers oscillate with the same frequency close to the cavity resonance. A part of the radiation leaves a laser cavity and circulates in the external cavity. The external cavity as a classic Fabry-Perot resonator allows the oscillation at its resonant frequencies. Because the feedback cavity is very lossy, the feedback can be approximated by considering just one round-trip in the external cavity. Then, the returning field of each laser will be decreased in amplitude by the factor γ [Tartwijk 1995; Rogister 2009; Flunkert 2011]:

$$\gamma = (1 - r_1^2)\frac{r_2}{r_1}, \tag{4.3}$$

where γ^2 is the part of the intensity reflected from the external cavity relative to the intensity reflected from the laser mirror and γ itself is called the "feed-in" coefficient. The amplitude reflection coefficient of the laser cavity OC is $r_1 = \sqrt{R_1}$ and the one of the external cavity mirror is $r_2 = \sqrt{R_2}$.

To expand the rate equation model to include the OF, we adapt the Lang-Kobayashi equations (see [Rogister 2009] eq.2.144) for a class-A laser array. The time delay in the optical feedback loop is taken $\tau_{OF} = 0$. Then, each laser field obeys the following

set of coupled equations:

$$\begin{aligned}
\frac{dA_i}{dt} =& -\frac{1}{2\tau_{cav}}\left(1-\frac{r_i}{1+A_i^2/F_{sat}}\right)A_i+\frac{|\eta|}{2\tau_{cav}}\left[\cos(\phi_{i+1}-\phi_i+\theta)A_{i+1}\right.\\
&\left.+\cos(\phi_{i-1}-\phi_i+\theta)A_{i-1}\right]+\frac{c_0\gamma}{2L_{cav}}A_j(t)\cos\left(\phi_j(t)-\phi(t)+\phi_{OF,i}\right),\\
\frac{d\phi_i}{dt} =& \frac{\alpha}{2\tau_{cav}}\frac{r_i}{1+A_i^2/F_{sat}}+\frac{|\eta|}{2\tau_{cav}}\left[\frac{A_{i+1}}{A_i}\sin(\phi_{i+1}-\phi_i+\theta)+\frac{A_{i-1}}{A_i}\sin(\phi_{i-1}-\phi_i+\theta)\right]\\
&+\frac{c_0\gamma}{2L_{cav}}\frac{A_j(t)}{A_i(t)}\sin\left(\phi_j(t)-\phi(t)+\phi_{OF,i}\right),
\end{aligned} \tag{4.4}$$

where notations are inherited from the previous chapters, A_j, ϕ_j is the amplitude and phase of the laser injected into i-indexed laser.

There are several cases, that could potentially lead to the maximization of the $q=1$ probability:

1. Adding a phase=plate inside the OF loop providing an additional phase-difference $-\psi_{OF}=\phi_{OF,i}-\phi_{OF,i+11}=2\pi q/n$ between each pair of lasers. This requires the phase-plate to exhibit an angular gradient phase-shift.

2. Inserting a Dove prism inside the OF. Each laser would then receive a part of the neighbor radiation. This case can be implemented with an additional $\phi_{OF}=0$ or $-\psi_{OF}=\phi_{OF,i}-\phi_{OF,i+1}=2\pi q/n$.

Fig. 4.17 shows the effect of the feed-in coefficient $\tilde{\gamma}$ scaled for intracavity losses $\tilde{\gamma}=\frac{c_0\tau_{cav}}{L_{cav}}\gamma$ on the probabilities to obtain different TCs.

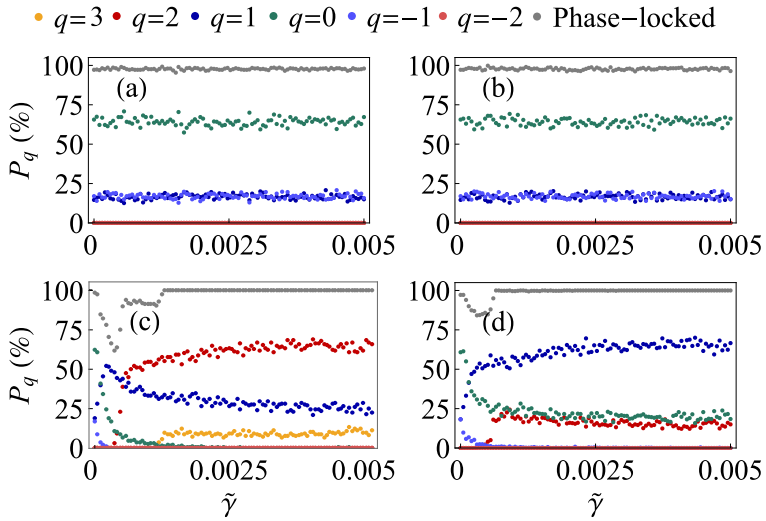

FIGURE 4.17: Probability of phase-locking with TC q in a $n=10$ laser array system with self-injection (a, b) and injection from the next-neighbor (c,d). Here (a, c) shows data for $\psi_{OF}=0$ and (b, d) for $\psi_{OF}=-2\pi/n$. The data are calculated with $\alpha=4, |\eta|=0.0025$.

Subfigures (a) and (b) correspond to the case of self-feedback, i.e. $A_j = A_i, \phi_j = \phi_i$. The second row (c, d) corresponds to the injection from the next nearest neighbor, i.e. $A_j = A_{i+1}, \phi_j = \phi_{i+1}$. Here are presented both the effect of the injection with a $\psi_{OF} = 0$ in subplots (a,c) and $\psi_i - \psi_{i+1} = 2\pi/n$ in (b,d).

Self-injection (a, b) stabilizes the array phase-locking in the $q = 0$ solution. There is no increase in the vortex solution observed both with and without phase-plate. The situation is very different from this in subplots (c,d). The injection of the signal from the following neighbor immediately leads to a predominance of vortex solution with $q = 1$ over $q \leq 0$. An increase of $\tilde{\gamma}$ leads to the predominance of $q = 2$ etc.

At the same time, a very small value of $\tilde{\gamma}$ (see (c) with $\tilde{\gamma}$ less than 0.001) leads to a small range of unstable dynamics with a small fraction of phase-locked solutions. Subplot (d) illustrates that the predominant solution can be controlled by the phase plate. In this case, we add the torsion by injection of the $i+1$st laser. The phase-shift induced by the phase-plate is $\psi_{OF} = -2\pi/n$. Thanks to this, the phase-locking in a vortex with TC $q = 1$ is the only predominant solution in the wide range of values of $\tilde{\gamma}$. Fig. 4.18 shows how the probabilities depend on the α factor in these cases of the injection from the neighbor.

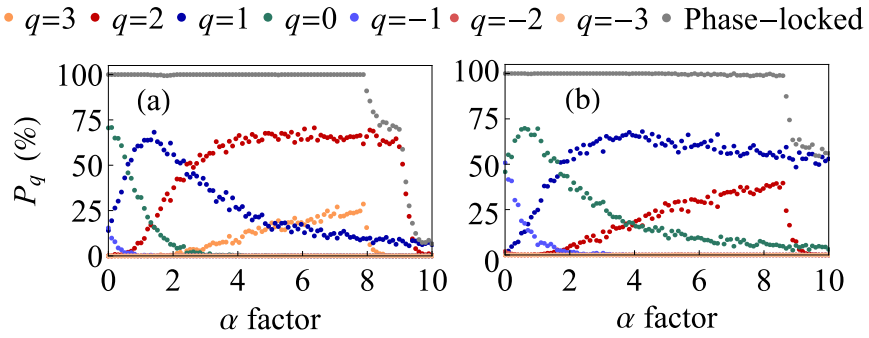

FIGURE 4.18: Probability of phase-locking with TC q in a $n = 20$ laser array system with a self-injection (a, b) and injection from the next-neighbor (c,d). Here (a,c) shows data for $\phi_{OF} = 0$, (b,d) shows $\phi_{OF} = 2\pi/n$. The data is calculated with $\alpha = 4, |\eta| = 0.0025$.

In both cases of next-neighbor injection with $\phi_{OF} = 0$ or $-2\pi/n$ the symmetry between the positive and negative vortices is broken. There are signatures of the different limiting values of the α factor for $q = 3$, $q = 2$, and $q = 1$ around 8, 9, and 10 at the abscissa axis of sub-figure (a). In the second case (b) the limiting factor for $q = 2$ has the same value around 9, while $q = 1$ has a wider phase-locking range and higher probability than in the case (a). The solution $q = 3$ can not be observed anymore in this case. The decrease of the probability $P_{q=1}$ in Fig. 4.18 is caused by the increasing number of phase-locked cases with $q > 1$.

The method has some common points with the one presented before for two VCSELs with injection coupling [Genevet 2010]. It was shown that the stable light structure can be switched between different steady-states including vortexes having

different chiralities. This made the light structure to be a so-called addressable vortex. The method was based on the self-injection of the fraction of the same light structure. In our case, the role of the light structure plays a phase-locked output beam. Its fracture in our case is well defined. We injected the same rotated light structure back. But we are also interested in a single laser injection to its neighbor.

We now turn to a smaller number of lasers in the array, namely $n = 3$ and we can see the same effect. Fig. 4.19 shows that, in this case, the $q = 1$ solution has a prevailing probability in the array phase-locking.

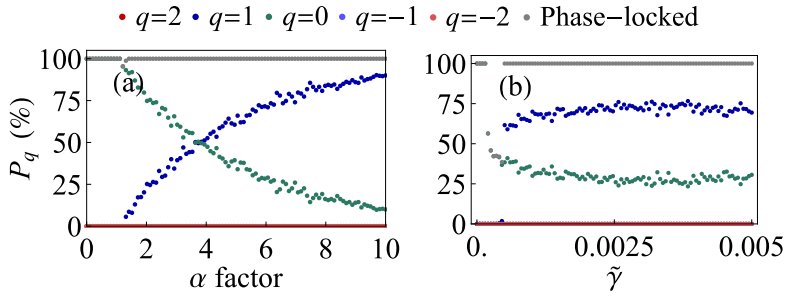

FIGURE 4.19: Probability of phase-locking with TC q in a $n = 3$ laser array with injection from the next-neighbor as a function of (a) α factor with $\tilde{\gamma} = 0.0025$ and (b) $\tilde{\gamma}$ with $\alpha = 6$. Here $\phi_{OF} = 0$. The data are calculated with $|\eta| = 0.0025$.

The OV solution probability $P_{q=1}$ prevails over others with a value of α more than 4. The probability slowly increases with $\tilde{\gamma}$. Starting from $\tilde{\gamma}$ equal to 0.003 it increases affects negatively the probability of OV. In a three-laser array, the TC does not exceed $|q| = 1$. This case is potentially the simplest case for the OV generation. Finally, we inquire whether it is feasible to enhance the probability of phase-locking in a vortex solely by introducing the neighboring field into a single laser.[1]. The calculated results are shown in Fig. 4.20.

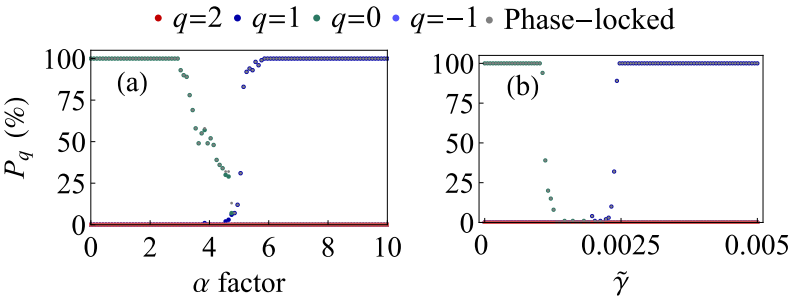

FIGURE 4.20: Probability of phase-locking with TC q in a $n = 3$ laser array with injection from the next-neighbor to the first laser as a function of (a) α factor with $\tilde{\gamma} = 0.0025$ and (b) $\tilde{\gamma}$ with $\alpha = 6$. Here $\phi_{OF} = 0$. The data are calculated with $|\eta| = 0.0025$.

[1]I.e. $\tilde{\gamma} = \delta_{i,1}\tilde{\gamma}$, where $\delta_{i,1}$ stand here for Kronecker delta equal to 1, when $i = 1$, i.e. only for the first laser and $A_j = A_2, \phi_j = \phi_2$

This case is similar to the one shown in Fig. 4.19. However, the probabilities $P_{q=0}$ and $P_{q=1}$ are now reach 100%. It is clear that in this case, the large Henry factor $\alpha = 6$ permits the vortex solution to be observed in 100% phase-locked cases. Of course, it occurs if the OF feeding rate is at least equal to 0.0025. Based on a α factor around $4-6$, we can obtain OV beams in the experiment with quite a weak OF. For example $\tilde{\gamma} = \frac{c_0 \tau_{\text{cav}}}{L_{\text{cav}}}(1-R_1)\sqrt{\frac{R_2}{R_1}} = 0.005$ corresponds to R_2 round 1% with our experimental values ($R_1 = 99.2\%$, $L_{\text{cav}} = 1\,\text{m}$, $\tau_{\text{cav}} = 30\,\text{ns}$).

By this, we can conclude that a couple of new methods of TC control have been discovered for the ring laser arrays. The complex coupling is a powerful instrument to control phase-locking relations between lasers.

4.4 Conclusion to chapter 4

Symmetric ring laser array was shown to always have the maximal probability of phase-locking with TC $q = 0$. A decrease in the coupling strength affects positively the OV probabilities. The same also happens for an increase in the number of lasers. A ring array with many lasers does not only give a better quality vortex but also has a higher probability of phase-locking in non-zero TC. We also studied the effect of the non-zero coupling argument on the probabilities of the different solutions.

One of the most important results is a numerical validation of the analytical formula obtained earlier:

$$\alpha_{\text{lim}} = \frac{2\cos\theta\cos\psi_q}{\sin\left(\psi_q - \theta\right)}.$$

The case of the laser array phase-locking with $\pm\pi/2$ hasn't shown the expected results. Equal intensities was potentially expected to lead to equal probabilities of phase-locking with different topological charges. However, the numerical calculations of this case confirmed phase-locking difficulty met in the solid-state lasers with zero Henry factor [Arwas 2022].

In the remaining part of the chapter, we studied methods of TC modifications. The study of the impact of non-symmetric complex coupling leads to the following conclusions. The stabilized phase differences of the phase-locked solution compensate for the variations of the coupling argument. Consequently, significant fluctuations in mask dimensions are detrimental to phase-locking. Diffraction engineering is a complex tool that cannot be universally applied to every system or application. In the case of the Random mask, this implies that the standard deviation should not exceed approximately 2 µm at $z = 1$ mm for investigated mask parameters.

The quality of the vortex beam is found to be strongly dependent on the complex coupling argument, and it can be effectively characterized by the order parameter. Contrary to expectations, a Gradient mask profile did not demonstrate any benefits for vortex beam generation. However, we have established a connection between the number of lasers satisfying $\theta_{i\to i+1} = 2\pi/n$ and $\theta_{i\to i-1} = -2\pi/n$ and a dominant vortex probability.

The optical feedback showed the most promising results for a phase-locking with OV. The probability of the OV solution with $q = 1$ will prevail, in case the optical feedback allows sending a fraction of the neighboring radiation to each laser. Moreover, a 100% case phase-locked in a vortex with $q = 1$ was numerically shown to be achieved in three laser arrays. This occurs when vorticity is only created between two lasers, i.e. the array phase-locking driven by the second laser injection into the first one. In total, we showed that even three lasers in the VECSEL array are enough to implement the method of phase-locking in OV. We believe this method will be useful for selecting vortex phase-locked solutions in a laser array.

CHAPTER 5

Experimental implementation of a Degenerate Cavity VECSEL

Contents

This chapter describes the experimental realization of the degenerate cavity VECSEL and the development of the VECSEL array. It can be separated into two parts: laser development and laser characterization. First, the main stages of the degenerate cavity VECSEL design and the explanation of key laser component choices are given. The scheme is inherited from the series of works in the degenerate cavity laser arrays discussed in the introduction section. It includes an optical pump delivery system, a thermally stabilized gain chip, and a planar degenerate cavity. The experimental scheme of the optically pumped (OP)-VECSEL is shown in Fig. 5.1.

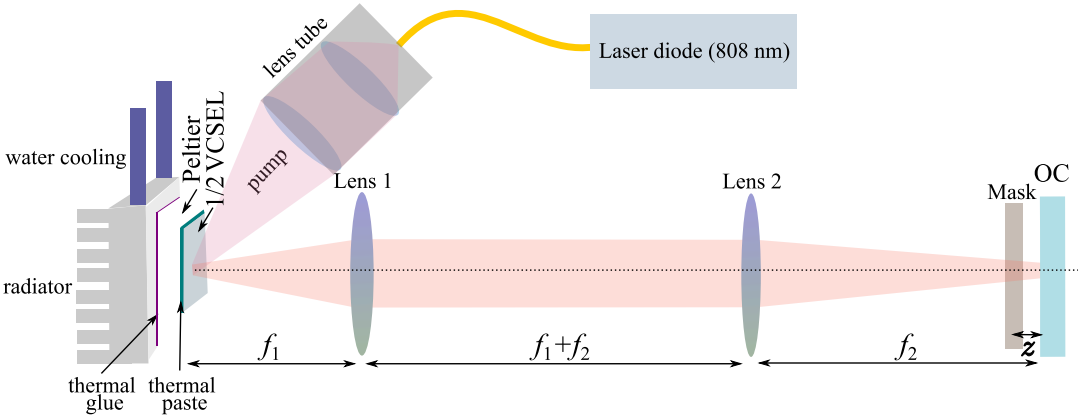

FIGURE 5.1: Scheme of the degenerate cavity VECSEL. The pump power is delivered by the multimode fiber (∅105 µm) to the two lens system placed in a lens tube. The output coupler is a highly reflective mirror ($R \sim 99\%$ at $\lambda = 1\,\mu m$). 1/2 VCSEL gain chip is attached to the Peltier with thermal paste. Heat excess from the Peltier is dissipated through the metal radiator. The intracavity telescope consists of two best-form lenses coated with respect to the gain-chip resonance wavelength (B-coated). The second lens has a four-times longer focal distance than Lens 1. Thus the telescope provides an enlarged image of the excited area on the gain chip. The loss mask is a metal plate with circular holes ($\sigma = 200\,\mu m, a = 50\,\mu m$).

The present chapter sequentially presents the laser development starting from the optical pump to the VECSEL laser array. It starts with a discussion of the pump delivery system. We then discuss the pump interaction with the gain chip focusing on dependent problems, such as the thermal lens effects and thermal rollover of the laser efficiency. In the same part, the characterization of several VECSEL gain chips is presented to clarify our choice of the final gain chip samples.

Then, the discussion of the laser cavity schematics and the choice of its elements is presented. It is accompanied by the corresponding study of cavity stability based on the ABCD matrix analysis. Finally, we demonstrate the experimental signatures of spatial degeneracy and our degenerate cavity VECSEL sustaining oscillation of an array of several lasers.

5.1 Optical pump

Semiconductor gain chips can be pumped optically or electrically [Guina 2017a]. Electrical pumping is usually characterized by better noise figures than optical ones. Unfortunately, it cannot provide uniformity in the pumping area, and pump shaping is not easily applicable in this case either. At the same time, the uniformity of the gain excitation is highly required for the laser array under study here. Unequal laser parameters make phase-locking observation and description much more complicated. Fig. 5.2 shows different possible pumping delivery schemes.

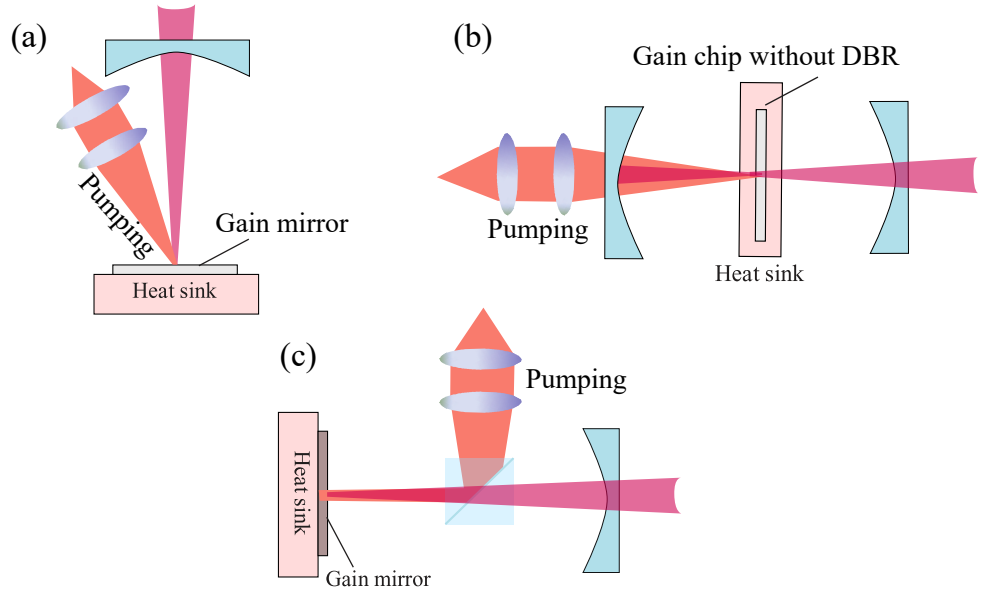

FIGURE 5.2: Typical stable cavity architectures of OP-VECSELs: (a) linear cavity, (b) DBR-free cavity in transmission, (c) Orthogonal pumping delivery thanks to a beamsplitter.

The optical pump beam is most often sent under some incidence angle to the gain chip as shown Fig. 5.2 (a) [Liu 2018b; De 2015; Baili 2009]. Alternatively, the orthogonal pumping without pumping spot deformation can be delivered using a beam-splitter as shown in Fig. 5.2 (c) [Bartolo 2022]. However, this would require inserting the beam splitter inside the cavity at the cost of extra losses. VECSEL gain chips have a small gain ($< 10\%$), thus the intracavity loss control is critical. Due to this, inclined pumping is preferable. The incidence angle must be kept smaller than the Brewster angle to minimize the pump reflection. Moreover, one could think of a more complicated solution with a shaped pump beam or several pumps.

5.1.1 Pump delivery system

In the experiment, our pump is a diode laser (Aerodiode, LD808-0-0 with a $\lambda = 808\,\text{nm}$) with multimode fiber output with a core diameter equal to $\varnothing 105\,\mu\text{m}$). The

pump beam passes a custom two-lens telescope with magnification $\Gamma = 0.8$. It is formed by two best-form spherical lenses (LBF254-040-B, LBF254-050-B). The best form spherical lenses are double-convex lenses designed with asymmetrical faces to achieve minimal spherical aberration while still using spherical surfaces to form the lens. The lenses are mounted using the lens tube. The lens LBF254-040-B is chosen to be the output lens of the lens tube.

The output of the lens tube corresponds to the image of the facet of the pumping diode fiber. The beam intensity is decreased with neutral density filters (NDF) and beam-splitters from the power $P_{\text{pump}} = 780\,\text{mW}$ to $5\,\text{mW}$ to prevent the saturation of the camera. The electrical current $I = 1.1\,\text{A}$. Typically the VECSEL arrays are investigated around this current value in our experiment. The cross-section of the pump beam is characterized in the focal plane of the lens tube, i.e. at the focal distance of the output lens. The output pattern captured by the CCD camera is shown in Fig. 5.3.

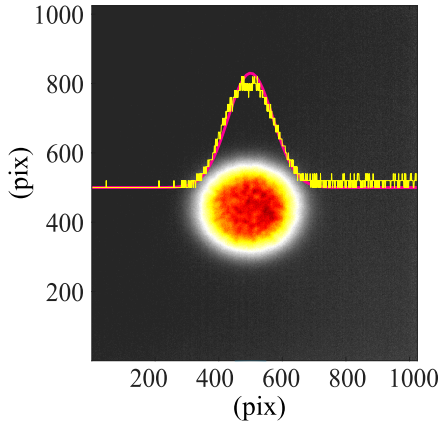

FIGURE 5.3: Experimental pump profile captured by CCD camera in the focus of the output lens of the lens tube. The camera pixel size is $5.3\,\mu\text{m}$.

The pump spot given by Fig. 5.3 is a multimode beam with a rich speckle structure. The yellow curve shows the horizontal cut of the cross-section at the maximal peak intensity of the beam. Its Gaussian fit is shown in red. The curves almost perfectly overlap. The experimental profile has a tiny top-hat center, which is often associated with a super-Gaussian beam or a few misplaced Gaussians.

An inclined pump under the angle 53° to the normal of the gain chip leads to an elliptical shape of the pump at the gain chip surface. The average power transmission coefficient in this case $T_{1/2VCSEL}$ is around 0.67, which can be calculated with the Fresnel coefficients. The final shape of the excitation area is shown in Fig. 5.3. It is given by an ellipse with half-axes: $a = 50\,\mu\text{m}$, $b = 40\,\mu\text{m}$. These are the typical dimensions at the focus of the pump, i.e. at the focus of the output lens. However, in the experiment we defocus the pump to increase the spot of the pumping area, i.e.

we move the lens tube away from the structure. In this case, the half-axes of the spot increase up to $a = 75\,\mu m$, $b = 60\,\mu m$.

5.1.2 Pump induced thermal lens

The pump power absorbed by the gain chip generates both a thermal and an electronic lens effect on the facet. The carrier profile creates a negative lens effect, while the thermal profile induces a positive one. This positive converging lens dominates over the negative electronic lens in VECSELs [Laurain 2009]. The presence of such a thermal lens has been observed in various works [Laurain 2009; Gredat 2019a; Bartolo 2022]. The typical temperature distribution induced by the pump beam with a Gaussian profile has been deeply investigated by [Gredat 2019a]. The profile is shown in Fig. 5.4.

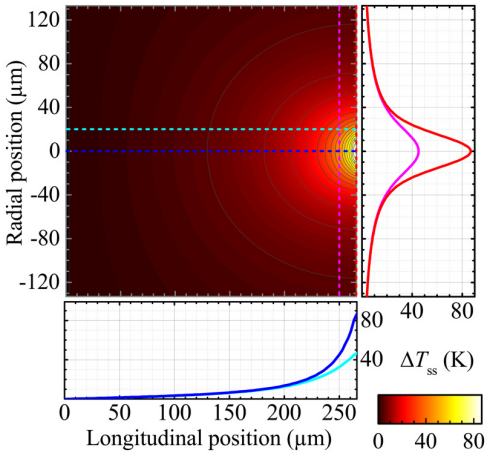

FIGURE 5.4: [Gredat 2019a]: Calculated steady-state spatial distribution of the temperature increase in the semiconductor structure. The longitudinal (respectively radial) temperature profiles at the bottom (respectively at the right side) of the map are plotted along the blue and cyan (respectively red and magenta) dotted lines.

Except for the pump beam profile, the temperature profile depends a lot on the combination of the gain chip material and heat dissipating system [Kemp 2006]. The formula (5.1) obtained by [Laurain 2009] gives an estimated value of the thermal lens focal distance f_{th}.

$$f_{th} \approx \sqrt{\frac{\pi}{\ln(2)^3}} \left(L_{\mu c} \frac{dn}{dT} \right)^{-1} \frac{w_p^3 \kappa}{\varepsilon P_p}, \tag{5.1}$$

where $L_{\mu c}$ is the wave penetration length in the 1/2-VCSEL structure. The average refraction index change is $\frac{dn}{dT} = 2.4 \times 10^{-4} K^{-1}$, κ is the thermal conductivity

of GaAs, the incident pump power is P_p and $\varepsilon \sim 0.3$ is the fraction of heat power generated.

In the experiment, the 1/2-VCSEL structure is optically pumped in a continuous wave (CW) regime by a commercial fiber-coupled high-power multimode laser diode within a power range $P_p = 0.5 - 1.1$ W. If the gain chip is excited by the nearly focused pump beam, the pump spot radius varies from $w_0 = 40\,\mu$m to $75\,\mu$m. Based on these values, the thermal focal length can vary in a wide range from $f_{th} \approx 40$ to 500 mm depending on the gain chip distance to the lens tube focus. The existence of the thermal lens changes the cavity stability. This effect will be considered in subsection. 5.3.

5.2 VECSEL gain chip

The gain chips are grown by MOVPE in a VEECO-D180 reactor on GaAs substrates by our collaborators from C2N. The chips consist of a multi-layered semiconductor structure including a distributed Bragg reflector (DBR), and a gain region containing different numbers of InGaAs/GaAsP quantum wells. Some of the tested samples have additional Al layers for improved internal heat redistribution and dissipation. Heat is extracted from the gain chip by attaching it to a Peltier cooler using a thermal paste. The Peltier cooler itself is mounted with thermal glue on a copper radiator, in which cooling water is circulated. The Peltier temperature is maintained at 20°C in all of the experiments. Heat dissipation plays a significant role in preventing efficiency rollover [Guina 2017b]. The efficiency rollover limits the output power range and consequently the number of lasers in the VECSEL array.

A semi-confocal cavity laser setup is built to test the available gain chips for thermal rollover and efficiency for potential usage in degenerate cavity VECSEL. Fig. 5.5 shows the output power dependence on the pump power for the several 1/2 VCSEL gain chips.

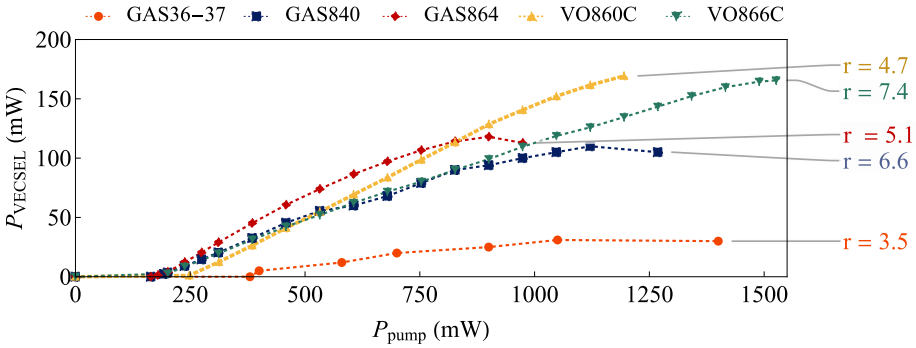

FIGURE 5.5: Experimental dependencies of the VECSEL output power P_{VECSEL} on the pump power P_{pump}. All gain chips were investigated in the same cavity configuration. Measurements are made a the semi-confocal cavity ($R_{OC} = 0.99$ at $1.064\,\mu$m) with a Lumics pump laser diode (808 nm, SN02477494)

A typical value of the pumping rate allowing to stay in the linear regime of a bare VECSEL is shown to be not much higher than $r = 4$ for the majority of the structures. The gain chips have different inner schematics, resonance wavelengths, and coatings.

The structures labeled GAS864 and VO860C are chosen for the degenerate cavity VECSEL experiment. These structures have an anti-reflection coating for $\sim 1.00\,\mu m$. Their central resonance wavelengths are $\lambda = 1.064\,\mu m$ and $\lambda = 1.04\,\mu m$. Those lasers have the best efficiency performances. GAS864 has a resonance wavelength close to the Nd:YAG laser, which has a huge application area. At the same time, V0860C has a wide range without thermal rollover thanks to the additional Al layers in the gain chip. The structure used in the particular experiment is specified at the place where data is presented.

5.3 Stability of degenerate cavity

An optical cavity is spatially degenerate when an arbitrary ray retraces its path after a single round trip. Spatial degeneracy of the laser cavity could be achieved with a different configuration of intracavity optical elements [Arnaud 1969]. Some examples of the degenerate cavities are shown in Fig. 5.6.

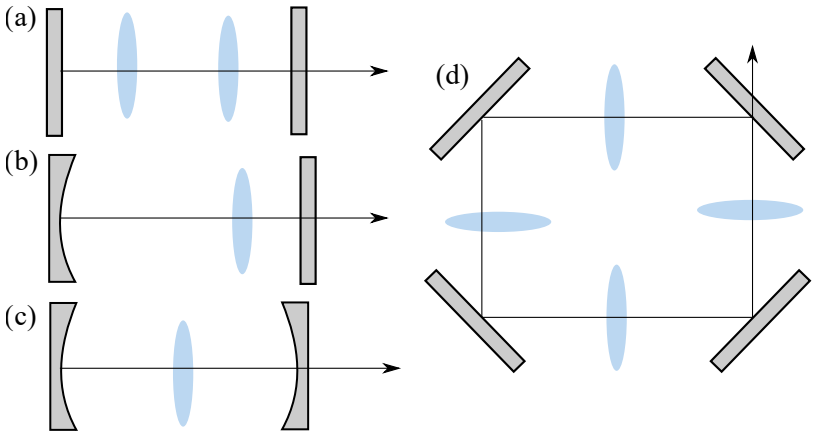

FIGURE 5.6: Degenerate cavities geometries. The planar and convex mirrors are shown in gray. Lenses are given in light blue colors. Practically the geometries very widely and successfully implemented are: (a) [Nixon 2013a] and (b) by [Hachair 2008] as degenerate cavity VECSELs. (c), (d) are more common as mode converters [Cheng 2017]

The propagation in this kind of system is associated with equivalent optical paths for each ray trace. The intensity profile at the input is reproduced at the output. Due to this, the system is also often referred to as self-imaging. The cavities can satisfy imaging conditions for a full round trip, as shown in Fig. 5.6 (a-c) or twice for

a round-trip (Fig. 5.6 (d)). In the first case (a-c), the output is given by the inverted image of the pumping spot relative to the axis, while in the second case (d) the image reproduces the object.

Since the main aim of the project is to develop a VECSEL array, one mirror should be replaced with the 1/2 VCSEL gain chip. Another mirror must be consistent with the planar loss mask. Only the planar geometry of the cavity shown in Fig. 5.6 (a,d) can satisfy those conditions. The optical pump will excite the field propagating from the gain toward the output coupler. A mask will be placed in the focal plane of the intracavity telescope to divide the gain into independent regions.

The planar degenerate cavity is marginally stable and its imaginary properties are degraded by any lens misalignment and aberration. Thus, the next step is to investigate the stability and imaging properties of the cavity.

5.3.1 ABCD matrix analysis

The cavity has a cylindrical symmetry and obeys the paraxial approximation. The stability of the paraxial cavity is easily described by ABCD matrices [Siegman 1986]. The ABCD matrices represent an optical system as a 2×2 matrix, so one can calculate how the optical system affects the path and properties of a beam of light passing through it.

A ray arriving on an optical element can be parametrized by the coordinates (r, ϕ), where r is the distance from the optical center and ϕ is the angle with respect to the optical axis. The beam at the output of the system can be calculated by $r' = Mr$, where M is the optical system ABCD matrix of constants:

$$\begin{bmatrix} r' \\ \phi' \end{bmatrix} = \begin{bmatrix} A & B \\ C & D \end{bmatrix} \begin{bmatrix} r \\ \phi \end{bmatrix}.$$

The laser cavity can be presented as a succession of free propagation and lenses. The reflection on the OC and perfect gain chip will give an identity matrix, while the transfer matrices of the free propagation and a lens are the following:

- Free propagation on a distance l : $M_{\mathrm{P}}(l) = \begin{bmatrix} 1 & l \\ 0 & 1 \end{bmatrix}$.
- Lens of focal length f : $M_{\mathrm{L}}(f) = \begin{bmatrix} 1 & 0 \\ -1/f & 1 \end{bmatrix}$.

Let us now consider a degenerate cavity formed by two planar mirrors and an intracavity telescope (see Fig. 5.7). The alignment parameter l_1 represents the distance between the gain chip and the first lens (with focal lens f_1) and l_2 gives the distance between the second lens (f_2) and OC. The misalignment parameter δ is given by the difference between the distance between the two lenses and the sum of their focal lengths.

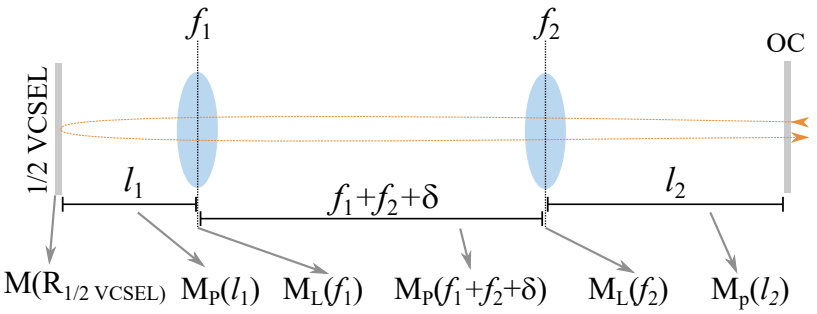

FIGURE 5.7: Planar degenerate cavity scheme and graphical notation of the misalignment parameters l_1, l_2, δ.

Since we are interested in the parameter of the beam at the output of the VECSEL at the OC plane, we investigate the beam transformation, when the beam starts its propagation at the OC, passes the second lens (f_2), it passes the first lens (f_1), reflects the 1/2 VCSEL gain chip and then pass the same elements in the reversed order.

The propagation matrices in the back ($M_{\leftarrow}$) and forward ($M_{\rightarrow}$) directions of the intracavity telescope are given below:

$$M_{\leftarrow} = M_P(l_1).M_L(f_1).M_P(f_1+f_2+\delta).M_L(f_2).M_P(l_2) = \begin{bmatrix} 1 & l_1 \\ 0 & 1 \end{bmatrix} \begin{bmatrix} 1 & 0 \\ -1/f_1 & 1 \end{bmatrix} \begin{bmatrix} 1 & f_1+f_2+\delta \\ 0 & 1 \end{bmatrix} \begin{bmatrix} 1 & 0 \\ -1/f_2 & 1 \end{bmatrix} \begin{bmatrix} 1 & l_2 \\ 0 & 1 \end{bmatrix}, \tag{5.2}$$

$$M_{\rightarrow} = M_P(l_2).M_L(f_2).M_P(f_1+f_2+\delta).M_L(f_1).M_P(l_1) = \begin{bmatrix} 1 & l_2 \\ 0 & 1 \end{bmatrix} \begin{bmatrix} 1 & 0 \\ -1/f_2 & 1 \end{bmatrix} \begin{bmatrix} 1 & f_1+f_2+\delta \\ 0 & 1 \end{bmatrix} \begin{bmatrix} 1 & 0 \\ -1/f_1 & 1 \end{bmatrix} \begin{bmatrix} 1 & l_1 \\ 0 & 1 \end{bmatrix}. \tag{5.3}$$

Then, the full transfer matrix for a round-trip inside the cavity is

$$\begin{pmatrix} A & B \\ C & D \end{pmatrix} = M_{\rightarrow}.M_{1/2\,\mathrm{VCSEL}}.M_{\leftarrow} \tag{5.4}$$

Here the matrix $M_{1/2\,\mathrm{VCSEL}}$ corresponds to the reflection on the gain-chip. The matrix corresponds to the identity matrix in case the gain chip is not deformed and thermal lensing is negligible.

The equality of the round-trip ABCD matrix with the identity matrix is the definition of a degenerate cavity. However, in the experiment, we start from a stable cavity situation to have the laser oscillations. We thus investigate the stability limits of the cavity given by [Siegman 1986]:

$$-1 \leq \frac{A+D}{2} \leq 1. \tag{5.5}$$

The stability criterion eq. (5.5) is met within some range of the mispositioning l_1, l_2, δ of cavity elements along the optical axis of the cavity (graphical definition of such

variables is given in Fig. 5.7). It is important to understand then, what kind of adjustments must be made to reach the proximity of the degeneracy when stable lasing is achieved. Additionally, it is important to understand, which elements mispositioning makes more impact the degenerate cavity VECSEL stability.

When solving the stability requirements of the cavity, one finds that the laser is stable for two bands of focus-to-focus misalignments δ. The values are bounded between four stability limits, $\delta_1 < \delta < \delta_2$ and $\delta_3 < \delta < \delta_4$, given by:

$$\begin{aligned}
\delta_1 &= 0, \\
\delta_2 &= \frac{f_2^2}{l_2 - f_2}, \\
\delta_3 &= \frac{f_1^2}{l_1 - f_1}, \\
\delta_4 &= \delta_2 + \delta_3 = \frac{f_2^2}{l_2 - f_2} + \frac{f_1^2}{l_1 - f_1}.
\end{aligned} \tag{5.6}$$

These stability limits can be named according to the mode size behavior on the cavity end mirrors as illustrated in Fig. 5.8 (a,b,c,d).

The first solution δ_1 (a) is a case where the lenses are separated by $f_1 + f_2$, forming a perfect telescope, which produces a collimated beam in both arms. For the next one δ_2 (b) the lenses are separated by $f_1 + f_2 + \delta_2$, such that the focal point between the lenses is imaged on OC. The third solution δ_3 (c) corresponds to a stability limit for which the lenses are separated by $f_1 + f_2 + \delta_3$, and the focal point between them is imaged on the gain chip plane. The last one is the δ_4 (d) point-point limit, where the lenses are separated by $f_1 + f_2 + \delta_4$, and the focus points of the lenses are imaged on both cavity ends.

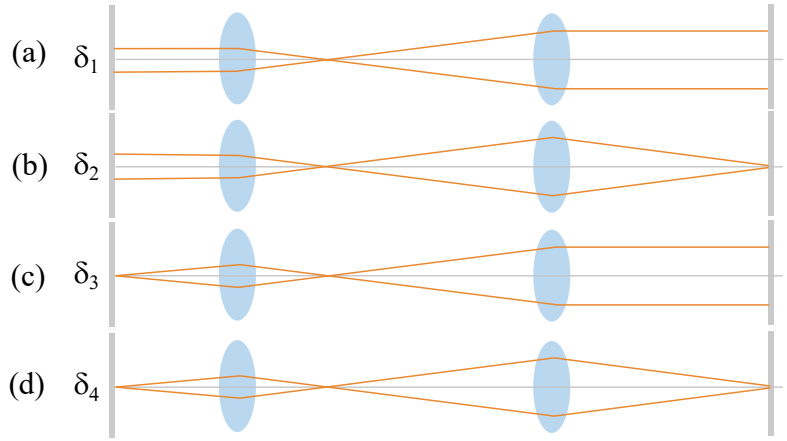

FIGURE 5.8: Geometrical representation of the cavity mode at the stability limits: (a) planar limit; (b) planar-to-point limit; (c) point-to-planar limit; (d) point-point limit. These results are consistent with the analysis performed by [Yefet 2013].

These conditions are stability limits. At the same time, the degeneracy condition is true only for $A = 1, D = 1, B = 0, C = 0$. This condition is possible to satisfy with a lens-to-lens mispositioning equal to δ_1 and δ_4, when a relation between along-axis mispositioning of the lenses $\Delta_1 = l_1 - f_1, \Delta_2 = l_2 - f_2$ is defined according to:

$$\frac{\Delta_1}{f_1^2} = \frac{\Delta_2}{f_2^2}.$$

From this, we can see that the mispositioning of the lens requires an adjustment of another lens proportional to the square ratio of their focal distances, i.e. $\Delta_2 = \Delta_1 \frac{f_1^2}{f_2^2}$. In the experiment, we use lenses with focal lengths $f_1 = 50\,\text{mm}$ and $f_2 = 200\,\text{mm}$. This means, for example, that once the first lens is misaligned ($\Delta_1 \neq 0$), the second one will have to compensate for the misalignment with a factor of 16, i.e. $\Delta_2 = \Delta_1 \frac{f_2^2}{f_1^2} = 16\Delta_1$. Otherwise, the cavity will not be degenerate.

5.3.2 Thermal lens compensation

As we have already seen, the pump induces a thermal lens effect in the VECSEL chip affecting cavity stability. The ABCD matrix describing reflection on the 1/2 VECSEL is now:

$$M_{1/2\,\text{VCSEL}} = \begin{pmatrix} 1 & 0 \\ -1/f_{th} & 1 \end{pmatrix}, \tag{5.7}$$

where f_{th} is the focus of the thermal lens. The updated stability criterion is then bounded between four stability limits covering the effect of the thermal lens:

$$\begin{aligned} \delta_1' &= \frac{f_1^2}{\Delta_1 - 2f_{th}}, \\ \delta_2' &= \frac{f_1^2}{\Delta_1}, \\ \delta_3' &= \frac{f_1^2}{\Delta_1 - 2f_{th}} + \frac{f_2^2}{\Delta_2}, \\ \delta_4' &= \frac{f_1^2}{\Delta_1} + \frac{f_2^2}{\Delta_2}. \end{aligned} \tag{5.8}$$

Stability range of δ are also $\delta_1' < \delta < \delta_2'$ and $\delta_3' < \delta < \delta_4'$ and can be associated with graphical illustrations in Fig. 5.8 (a,b,c,d). The degeneracy conditions are modified as well. The relations between cavity element misalignment $\delta, \Delta_1, \Delta_2$ are:

$$\Delta_1 = \frac{f_1^2}{\delta} + 2f_{th}, \quad \Delta_2 = \frac{f_2^2}{\delta} + \frac{f_1^2 f_2^2}{2f_{th}\delta^2}. \tag{5.9}$$

where $\Delta_1 = l_1 - f_1, \Delta_2 = l_2 - f_2$. From this, we can see again that the misalignment of the lens from its perfect telescopic position requires an adjustment proportional to the square of the focal distances ratio, as it was shown earlier for the case with no thermal lensing. Also, it is clear, that the positive thermal lens compensation, requires a negative δ. I.e. the distance between two lenses must be less, than the sum of their focuses.

5.3.3 Beam radius dependency on mispositioning of the cavity elements and thermal lens

As we mentioned, in the experiment, the VECSEL cavity is typically not degenerate with the primary cavity alignment. A simple parameter helping to estimate proximity to the spatial degeneracy while aligning is highly valued. The most convenient one is the radius of the output beam. The Gaussian mode propagating in the cavity can be represented by the complex beam parameter q. This parameter is obtained through the ABCD-matrix coefficients as [Siegman 1986; Yefet 2013]:

$$\frac{1}{q} = \frac{D-A}{2B} \mp i\frac{\sqrt{1-m^2}}{|B|}.$$

The real part of q gives a radius of curvature R and the imaginary part contains the radius spot size w.

We consider the case when the OC position is fixed and only the position of the first and the second lenses can be adjusted. Then, we have $\delta = -(\Delta_2 + \Delta_1)$. In this case, the beam radius of the fundamental Gaussian mode varies according to Fig. 5.9.

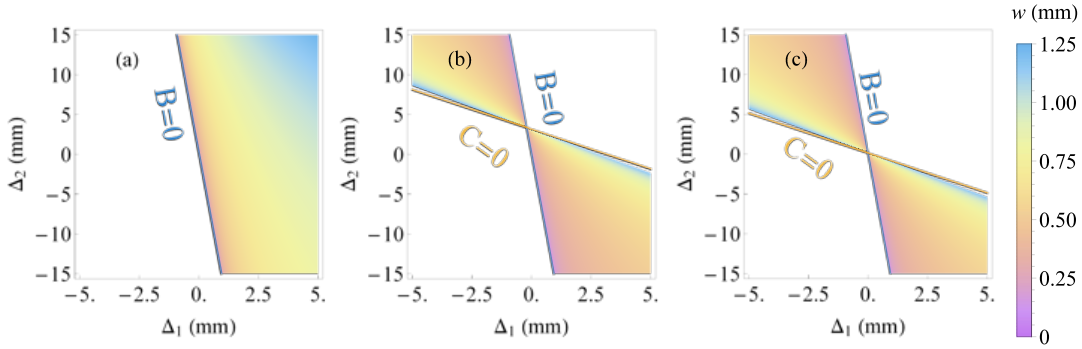

FIGURE 5.9: The beam radius of the fundamental Gaussian beam at the output of the cavity as a function of cavity misalignment Δ_1, δ. Here $f_1 = 50$ mm, $f_2 = 200$ mm. Where thermal lens focus is (a) $f_{th} = 40$ mm, (b) $f_{th} = 400$ mm and tends to infinity in (c). The blue and yellow curves represent zero-values of the B and C coefficients of the ABCD matrix for the one round-trip based on the eq. 5.4. The cross-section of those lines corresponds to the degeneracy of the cavity.

The subplots (a,b,c) are calculated for different values of the thermal lens f_{th}. They illustrate the changes in the output beam radius from the VECSEL. The borders of the real-valued data of the radius w are marked by two lines of blue and yellow color. These lines are given by zero-values of the B and C coefficients of the matrix defined by eq. 5.4 [1]. The cross-section of these lines corresponds to the cavity degeneracy.

In the first case, (a) the thermal lens is strong ($f_{th} = 40\,\text{mm}$). Degeneracy in this case can not be reached in the considered case within the millimeter range of the lens adjustment. As we mentioned before, the value of its focus f_{th} varies with the pump variation. In the experiment, when the pump spot is defocused and the thermal lens is approximately $f_{th} = 400\,\text{mm}$ for GAS864 at pump power $0.7 - 0.8\,\text{W}$. Subplot (b) is calculated for a less-curved thermal lens with focal length $f_{th} = 400\,\text{mm}$. We can see, that the degeneracy condition is now satisfied when $\Delta_1 = 3.3\,\text{mm}$ and $\Delta_2 = -0.2\,\text{mm}$. The first lens must be misplaced away from the gain chip and the second lens must be moved a little bit towards the first lens. This case corresponds to our experimental alignment. This case is similar to the one shown in Fig. 5.9 (c) for the negligible effect of the thermal lens, where no thermal lens correction is needed.

The characterization of the beam radius w is also presented in Fig. 5.10 for different thermal lens focal distances (a) and mispositioning of the intracavity elements (b).

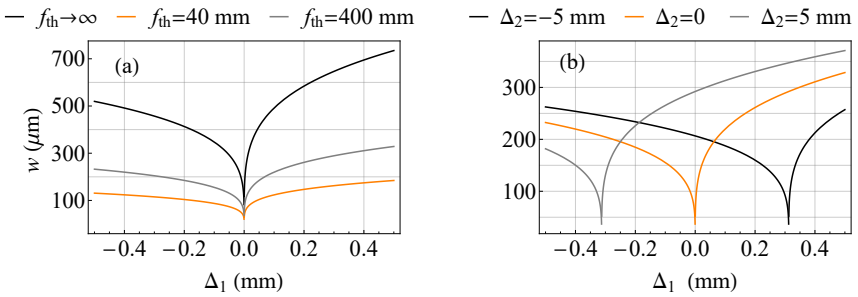

FIGURE 5.10: Beam waist w dependency on the thermal lens focal distance (a) and the OC mispositioning (b). For the subplots calculations was used (a) $\Delta_1, \Delta_2 = 0\,\text{mm}$, (b) $\delta = 5\,\text{mm}$. Degenerate conditions are satisfied with the minimal beam radius size.

In case all elements have no mispositions from the perfect telescope configuration, the beam radius will decrease with an increase of the thermal lens effect (i.e. f_{th} decrease). This case is shown in subplot (a). The beam radius is minimal in the point of degeneracy at $\Delta_1 = 0$. Subplot (b) illustrates the case when both the OC can be moved and the coordinate of the second lens can be chosen to adjust the first lens move to have $\delta = 0$. The distance between lenses then is given by the sum of their focuses. The beam radius then will be changed according to the subplot (b).

[1] The dependencies of the matrix coefficients A and D equal to one also separate the real-valued beam radius values and repeat the borders drawn by B and C lines.

Here different curves correspond to different values of the misalignment of the OC for Δ_2. We can see, that the degeneracy point (with the minimal beam radius) is then different from Δ_1 equal to 0. In this case, the adjustment of the first lens is needed to restore the degeneracy of the VECSEL cavity.

By this, we can conclude, that the thermal lens, the same as any misalignment can be compensated in a reasonable range of adjustments. Also, we find it rational to adjust the cavity in a way when the first lens position is chosen last. In this case, we obtain a sixteen times more accurate control on cavity telescope alignment.

5.4 VECSEL with degenerate cavity

All experimental data presented in this thesis were obtained with the same setup with minor modifications. The experimental setup is shown in Fig. 5.11.

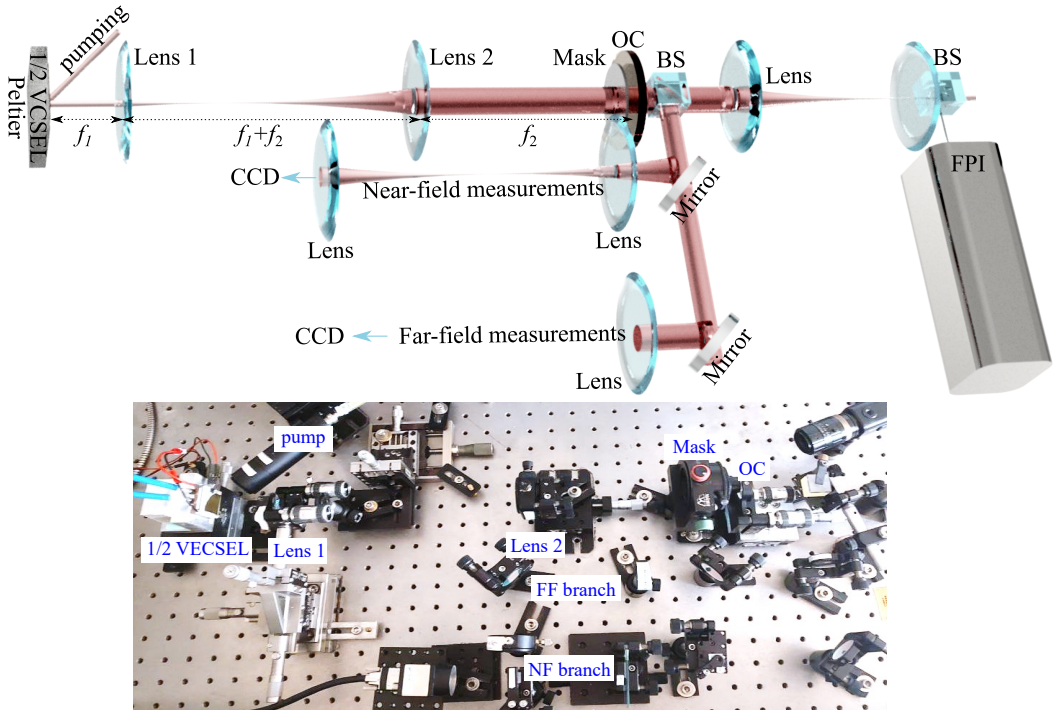

FIGURE 5.11: Experimental setup. Lenses 1,2 form an intracavity telescope ($f_1 = 5\,\text{cm}$, $f_2 = 20\,\text{cm}$). The metal mask placed at the self-imaging position forms the laser array. Near-field and far-field of the array are captured by CCD cameras (u-eye UI-3240 NIR). Fabry-Perot interferometer (FPI) – FPI100 (FSP – 1 GHz, finesse - 280) is used for spectral measurements.

Excitation of the chip is provided by optical pumping at 808 nm in a power ranging between 0.3 and 1.1 W. Heat is extracted from the gain chip according to the method described in section 5.2. The cavity is closed by a planar output coupler with

a 0.8% transmission at the $\lambda = 1.06\,\mu m$ laser wavelength. An intracavity telescope in a self-imaging configuration provides spatial degeneracy and stability of the cavity. Two positive lenses (focal lengths $f_1 = 5\,cm$ and $f_2 = 20\,cm$) provide a magnification of 4 in the 50 cm long cavity. The setup allows one to capture the near-field, far-field, and optical spectrum simultaneously with the time synchronization accuracy of electronic devices. The near-field and far-field images of the laser array emission are captured by a CCD camera (u-eye UI-3240 NIR, exposition time $9\,\mu s$). A Fabry-Perot interferometer (1 GHz free spectral range, finesse = 290) is used for spectral diagnostics.

5.4.1 Misalignment and mispositioning effects

The alignment of the system is challenging due to the low gain of the laser, small pumping area, and marginal stability of the cavity. Additionally, the cavity must provide high-quality imaging. During alignment, we can see various intensity patterns at the output.

Their interpretation gives a hint of the misalignment type through the aberration interpretation. The effect of spatial degeneracy affected by spherical aberration is studied in detail (including the impact on laser dynamics) in several works, such as [Gurevich 2024]. Our interest is to estimate what kind of misalignments do we have in the experiment based on the VECSEL output. Consequently, we can estimate what alignment is required.

An advantageous method of describing aberrations in systems like telescopes, microscopes, and other optical instruments is a family of orthogonal Zernike polynomials on the unit disc. This family includes both odd and even polynomials:

$$\text{odd: } Z_n^m = R_n^m(\rho)\cos m\phi,$$

$$\text{even: } Z_n^m = R_n^m(\rho)\sin m\phi,$$

where m and n are non-negative integers with $n \geq m \geq 0$, R_n^m are the radial polynomials defined below. Zernike polynomials have the property of being limited to a range of -1 to $+1$, $R_n^m(1) = 1$ and R_n^m is defined according to:

$$R_n^m(\rho) = \sum_{n=1}^{\frac{n-m}{2}} 2^{-n} \frac{(-1)^k (n-k)!}{k!(\frac{n+m}{2}-k)!(\frac{n-m}{2}-k)} \rho^{n-2k}$$

Each Zernike polynomial represents a specific type of aberration, such as defocus, astigmatism, coma, spherical aberration, etc. They provide a convenient and compact way to describe complex wavefront aberrations in terms of a set of coefficients corresponding to different polynomial terms. They provide a convenient and compact way to describe complex wavefront aberrations in terms of a set of coefficients corresponding to different polynomial terms.

The aberration type associated with Zernike polynomials Z_n^m is shown in Fig 5.12.

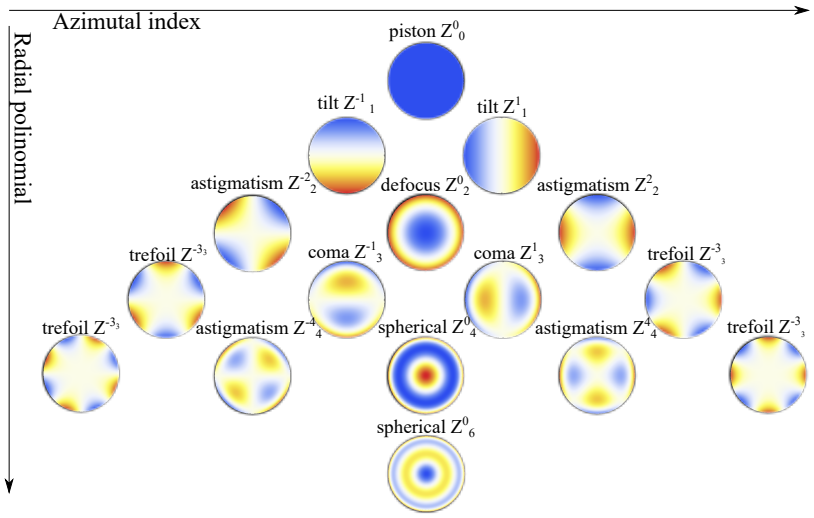

FIGURE 5.12: Zernike polynomials Z_n^m associated with aberrations of different kinds.

The far-field (FF) pattern of the radiation passing through the system with a particular aberration is given by the Fourier transform of the initial field profile convoluted with the polynomial Z_n^m. The FF patterns of an elliptic Gaussian beam profile (similar to the pump beam) affected by optical aberrations of different orders Z_n^m are shown in Fig. 5.13. Here the experimental misalignment is caused only by the first lens mispositioning along the optical axis and in transverse directions.

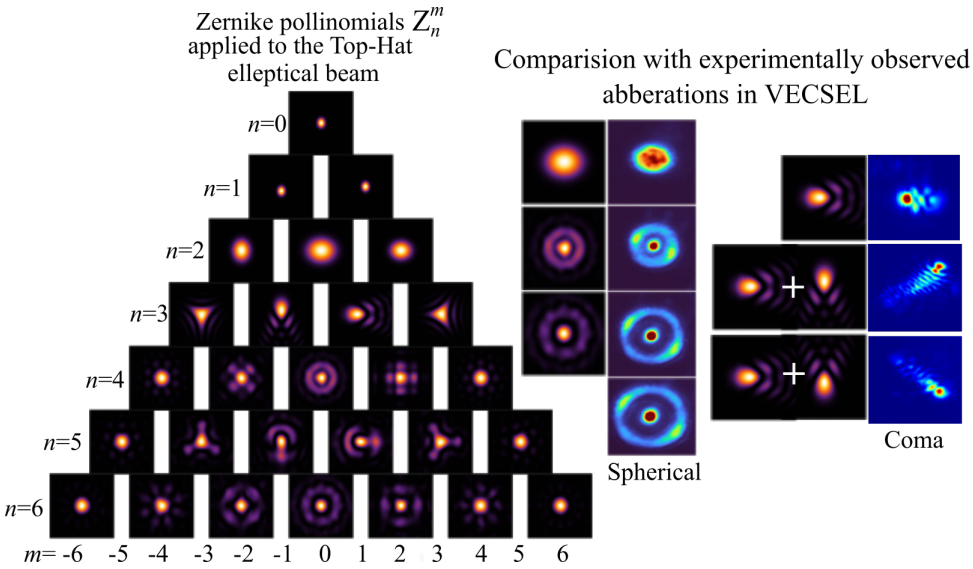

FIGURE 5.13: The FF intensity patterns transformed of an elliptic Gaussian beam by the Zernike polynomials. On the right, the comparison with experimental examples of the spherical aberration and coma effects are presented.

For example, an effect similar to spherical aberration (shown in Fig. 5.13) occurs when the first lens is too close to the gain chip, but the cylindrical symmetry of the cavity is saved. Experimental results are shown in blue-red colors on the right. In this case, we have strong on-axis emission and off-axis concentric rings of different thicknesses. The output is given by a high-order LG beam [Sheng 2022]. The total radius of the beam increases when the first lens moves closer to the gain chip.

In the case where the lens is vertically or horizontally misaligned or tilted, we expect to see a coma aberration effect. It is given by the rays from an off-axis emission imaged by different zones of the lens. The beam, in this case, looks like a comet spot. The spot has multiple minima and maxima if the lens is simultaneously not in the focal distance from the gain chip and is transversely misaligned. The output then corresponds to the superposition of the Hermite-Gaussian modes $HG_{m,n}$ having different phase accumulations during the round-trip inside the cavity. For example, Fig. 5.14 shows the effect of both a significant mispositioning of the first lens (f_1) longitudinal and transverse directions.

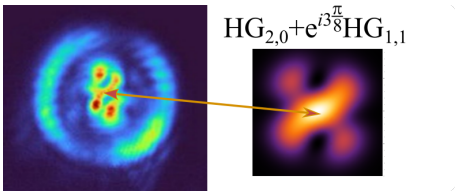

FIGURE 5.14: VECSEL laser output patterns when the lens/pumping is displaced in the vertical and horizontal directions by 0.1 mm. The on-axial part of the beam can be approximated by HG modes superposition, such as $HG_{2,0} + \exp^{i\frac{3\pi}{8}} HG_{1,1}$.

In this case, the central part is similar to the superposition of two HG modes with a $3\pi/8$ phase difference. When the cylindrical symmetric is preserved, the output is a combination of Laguere-Gaussian beams. Then degeneracy is easy to achieve with alignment only along the optical axis of the cavity.

Finally, we also noticed an interesting phenomenon driven by the change in the thermal lens profile. Let us look at the changes in the NF and FF of the aligned laser.

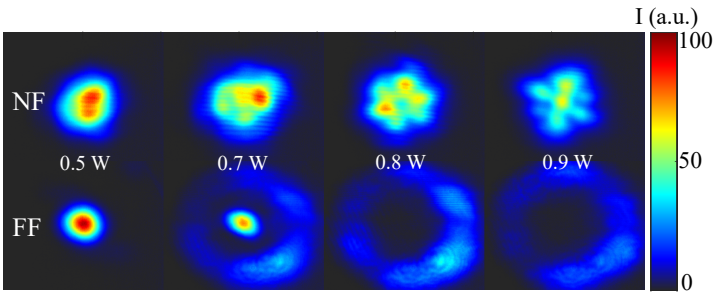

FIGURE 5.15: Far field and near-field patterns of the VECSEL output beam. The pump power increases from 0.5 W to 0.9 W. The lasing in the central spot stops with an increase in the pumping power.

The patterns are given in Fig. 5.15 from left to right for an increasing value of optical pump power. We can see that the increase in the pumping power leads to an effect similar to the spherical aberration. The thermal lens effect increases and the output spot shows different profiles. We detect a decrease in the VECSEL output power from around 50 mW (at 0.5 W) to almost 12 mW (at 0.9 W).

At some value of the pump power (0.8 W), the central spot (the on-axial emission) disappears. Potentially this is connected to the non-uniform curvation of the induced thermal lens. In general, we avoid significant pump power changes when the VECSEL cavity is aligned.

5.5 Experimental validation of the VECSEL degeneracy

Let us now consider more precisely the changes in the on-axis emission profile close to degeneracy. The cavity is properly aligned and we manipulate only the first lens position (with $f_1 = 50\,\text{mm}$) without any intracavity mask. Fig. 5.16 shows the NF and FF intensity distributions of the beam at the different mispositioning values Δ_1 of the first lens along the optical axis from degeneracy[2].

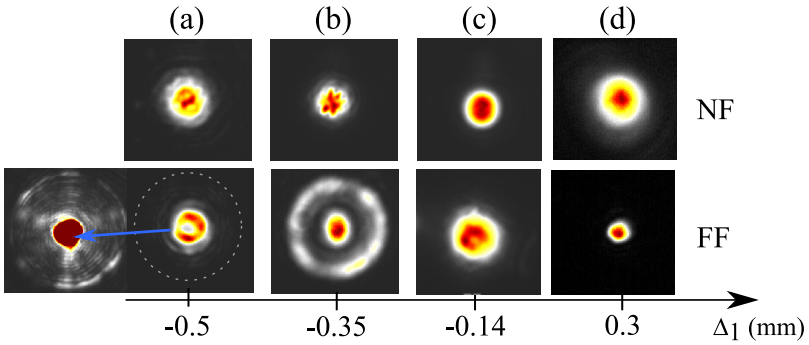

FIGURE 5.16: The effect of the first lens mispositioning (Δ_1) on the near-field (NF) and far-field (FF) patterns of the output VECSEL beam.

The first situation is when the first lens is moved along the optical axis in the negative Δ_1 range. Figs. 5.16 (a, b) display dramatically different structures in the NF and FF. The FF clearly shows an intense on-axis emission and an off-axis family of concentric rings. In subplot (a) the off-axis emission is almost invisible due to the NDFs, which were used to prevent on-axis emission saturation. These can be seen in the inset on the left, where the NDF was removed. The misalignment we implemented led to the effective diffraction length change and passing from a low-Fresnel number to a high-Fresnel number configuration [Hachair 2008]. The total beam diameter increases when Δ_1 decreases, and more and more off-axis rings are observed. Finally, the emission stops with Δ_1 close to $-2.65\,\text{mm}$.

[2]The cavity is aligned according to the previously determined $\Delta_1 = 3.3\,\text{mm}$ and $\Delta_2 = -0.2\,\text{mm}$ by the *ABCD*-analysis.

The NF patterns are not Gaussian in these cases as shown in top-row subplots (a, b) in Fig. 5.16. The NF is given by a set of bright spots aligned around the optical axis of the cavity. This phenomenon has also been detected in several works [Hachair 2008; Bartolo 2022]. The captured NF is a combination of the on-axis emission and the off-axis in this experiment. In case the on-axis part is switched off with an annular aperture, it is possible to see the transition between regular patterns having several leaves to hexagons and more complicated intensity distributions, such as demonstrated in [Bartolo González 2022; Vigne 2022]. This can be partially recognized in subplots (a,b) in the top row of Fig. 5.16.

On the other hand, a positive Δ_1 misalignment along the optical axis of the cavity leads to complete extinction of the off-axis emission (Fig. 5.16(d)) in our case. On-axis beam transforms to the Gaussian beam. The cavity is notably less stable in this range and emission stops close to $\Delta_1 = 0.5\,\text{mm}$.

The closer to degeneracy the lens position (see Fig. 5.16(c)) the closer the cavity is to a zero-length optical system ($B = 0$). The NF and FF have similar profiles. The output power is stronger in this case. The beam has an extremely multimode structure in this case. A couple more examples of the FF outputs of the degenerate cavity VECSEL are given in Fig. 5.17.

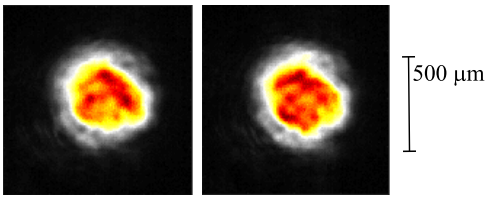

FIGURE 5.17: Far-field patterns of the degenerate cavity VECSEL output beam captured with the same alignment at different times.

5.5.1 Degenerate cavity VECSEL output with limited cavity aperture

The easiest practical test for degeneracy is to introduce some partial loss inside the cavity. In the degenerate configuration, each part of the gain is considered to be able to act as an independent laser. Then, the partial closing of the laser cavity with a blade, for example, will not affect the rest of the output beam. Schematically the idea is shown in Fig. 5.18.

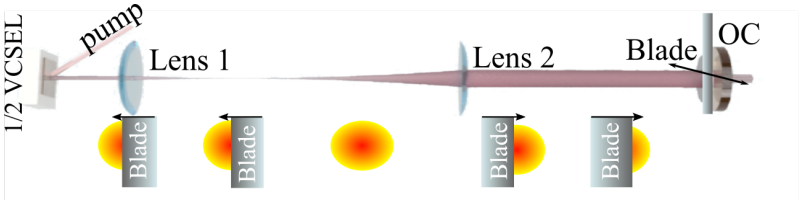

FIGURE 5.18: The scheme of the spatial intracavity losses controllable changes by the blade. The blade was installed at 1 millimeter from the OC. The blade moves parallel to the OC plane.

The blade sequentially blocks the optical path in the cavity. Fig. 5.19 shows the changes in the NF and FF when the blade covers the optical path from the right and the left.

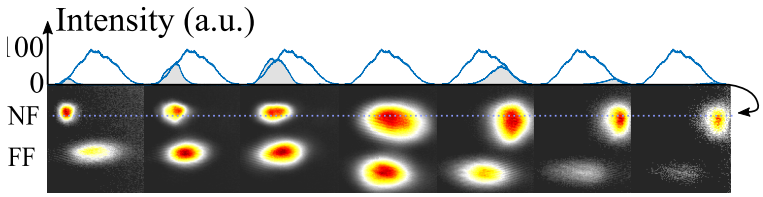

FIGURE 5.19: Near-field (NF) and far-field (FF) patterns of the VECSEL output beam. The cavity is considered to be degenerate.

It is clear, that the two side-ended sub-plots for both sides show laser emission when the on-axis path is blocked. Blue profiles at the top of Fig. 5.19 represent the cross-sections of the NF presented just below. The NF profile is almost perfectly given by the part of the total VECSEL output. The mounts of the blade and OC do not allow the movement of the blade close enough to the OC plane, thus the NF contains a part of the scattered light of the blade edge. The blade introduces a simple method of spatial filtering of the spatial components of the laser output.

This filtering can be also done through the far-field point of the intracavity telescope. A degenerate cavity VECSEL was shown to work as a laser source with a controllable coherence [Knitter 2016] when a pinhole with variable diameter is introduced at the far-field point. The scheme is shown in Fig. 5.20 (a).

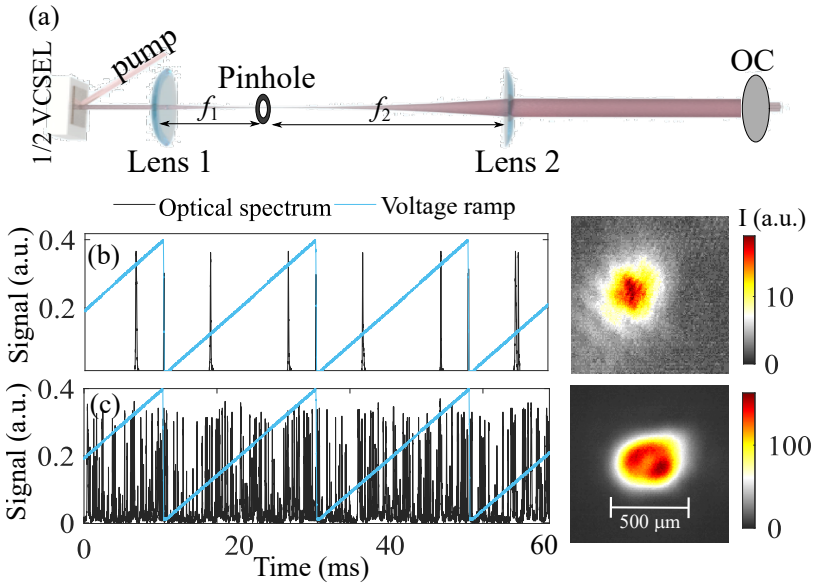

FIGURE 5.20: Changes in the optical spectrum of the VECSEL when the pinhole is closed ($\sim 300\,\mu$m) and completely open when the laser cavity is close to a degenerate configuration. The optical spectrum is measured with Fabry-Perot interferometer FPI100.

The measured optical spectra with closed and open pinholes are shown in Fig. 5.20 (b, c) respectively. Both subplots show the blue voltage ramp sawtooth signal and a black signal giving the optical spectrum. The voltage is applied to a piezo actuator in the FPI. The change of the applied voltage changes the optical length of the FPI resonator. Here the ramp parameters are chosen to show the FPI response over a full free spectral range.

The laser in this work is highly multimode when the pinhole is opened. The same results are obtained with the electrically pumped VECSEL developed earlier [Knitter 2016]. Its spatial coherence is low. On the other hand, a closed pinhole with a diameter around 300 µm leads to the single-frequency operation. The spectrum shows two peaks. Thus we conclude that the laser output is single mode. At the same time, the spectrum is slightly unstable. The laser oscillates in the free-running regime and the peaks drift and jump in time.

5.6 VECSEL arrays

The developed rate-equation models assume that each laser operates in a single transverse mode. To ensure this is the case, we determined the optimal parameter of the mask in the experiment with a "ruler" mask. The ruler mask is an array of holes with different diameters as shown in Fig. 5.21.

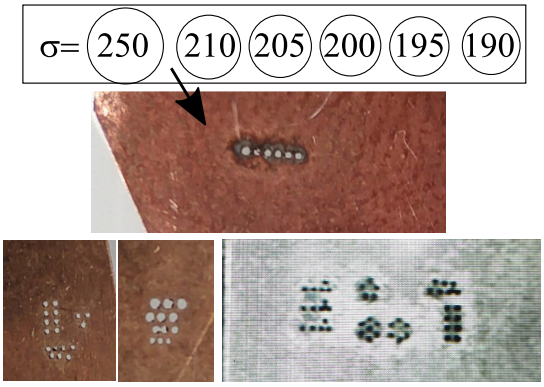

FIGURE 5.21: Mask rule scheme and different mask's photos.

By trying different masks, we noticed that the number of spatial modes sustained by each laser and the laser array spectrum significantly depends on the diameter of the holes. Each hole corresponds to a single nearly Gaussian fundamental mode only when the hole diameter σ is no larger than 200 µm. No stable emission is observed for the lower diameters. The edge-to-edge separation between holes is chosen to be $a = 50\,\mu\text{m}$. The figure also shows photos of different masks and a mask placed inside the cavity.

The laser arrays developed with one, two-, three, and five-hole masks according to the above-mentioned dimensions are shown in Fig. 5.22.

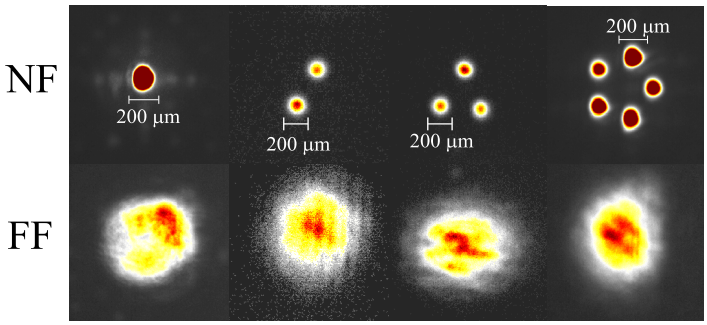

FIGURE 5.22: VECSEL array with a different number of lasers, when the mask is placed very close to the OC $z \sim 0$.

In Fig. 5.22, each laser array emission is not phase-locked as shown by the incoherent superposition obtained in the far field. The distance between the loss mask and OC is less than 50 µm, which explains why the coupling is too weak to lock the lasers. The output power of a single laser is in the range from $P = 0.27$ to 1 mW depending on the number of lasers and pump power. In all cases, the diameters of the holes are equal to $\sigma = 200\,\mu\text{m}$ with an edge-to-edge separation $a = 50\,\mu\text{m}$.

Note on VECSEL polarisation

VECSELs typically have a linearly polarised output along the [110] crystallographic axis of the gain chip. Thanks to this the polarisation is controlled by the rotation of the gain-chip around the optical axis of the cavity. Typical VECSEL linear polarisation indicatrice is shown in Fig. 5.23.

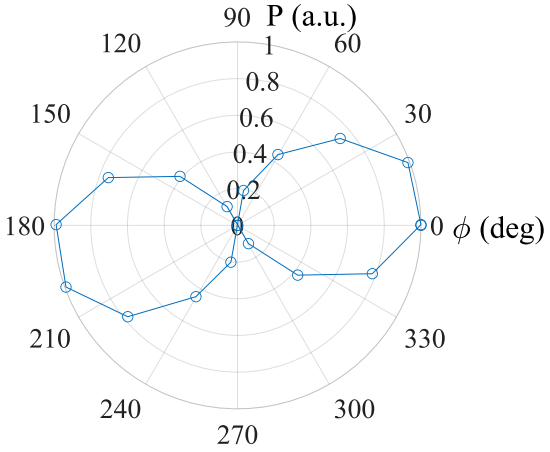

FIGURE 5.23: Polarisation plot of the VECSEL radiation. Power is normalized to its maximal value.

5.7 Conclusion to chapter 5

In this chapter, we analyzed the degeneracy of the planar cavity of the VESCEL with the ABCD matrix method taking into account the thermal lens effect of the structure. We presented the rule of thumb, that a lens misalignment requires a realignment of the second lens proportional to the square of the ratio of the focal lengths.

The developed experimental setup is presented. The degenerate cavity alignment is discussed in detail. The pump delivery system, thermal management, and gain chip choices are explained. Several evidences of spatial degeneracy of the cavity are demonstrated in this chapter. The evidences are NF and FF intensity analysis, spatial coherence modified by the pinhole, and the laser oscillation in the presence of extreme losses (when the on-axis path is closed).

We chose the optimal parameters of the loss mask and demonstrated several non-phase-locked VECSEL arrays. On this basis, we move forward to the laser array phase-locking investigation.

CHAPTER 6

Noise in coupled low-dimensional VECSEL arrays

Contents

The description of the degenerate cavity VECSEL array continues in this chapter. Here we study the laser noise based on the example of a few lasers. As was mentioned in the introduction, noise in lasers can act negatively. It can destabilize phase-locking, decrease the number of lasers, etc. Nevertheless, it also carries valuable information on the intrinsic properties of the laser system.

The noise is investigated experimentally, numerically, and analytically in this chapter. Phase-locking and noise properties an observed for the two- and three-laser arrays. Both arrays are investigated in two regimes. In one of them, the laser array is phase-locked and in the second regime, the lasers are not phase-locked.

The investigation aims at connecting the properties of laser array noise correlations with coupling parameters and investigating the role of the Henry factor. We start with the introduction of the experimental scheme and experimental results. Then we interpret the obtained experimental results. In the modeling part, we introduce noise into the rate-equation models obtained for the two-laser array and ring laser in chapter 2 and chapter 3. We calculate cross-correlation spectra numerically and analytically. We investigate the influence of the Henry factor on the amplitude of the laser noise cross-correlations. Finally, we compare these results and comment on the current experimental state of the developed VECSEL laser array.

6.1 Experimental setup

The experimental scheme is shown in Fig. 6.1.

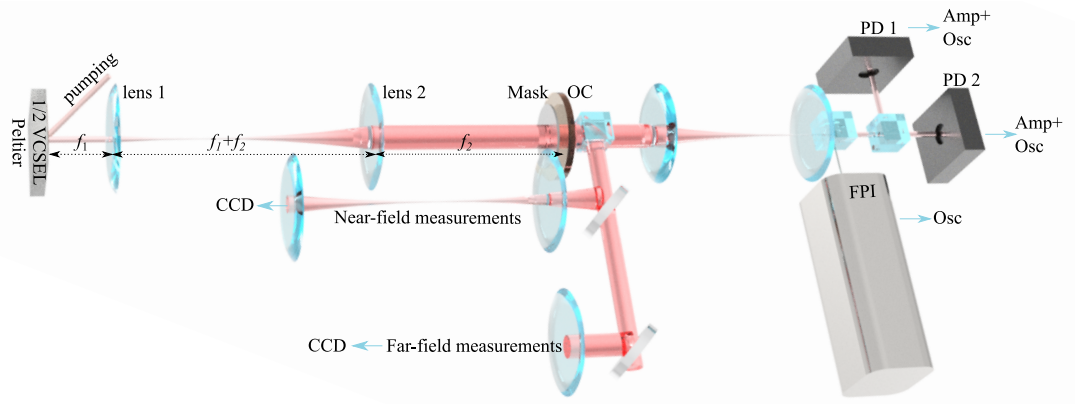

FIGURE 6.1: Experimental setup. Lenses 1,2 form an intracavity telescope ($f_1 = 5\,$cm, $f_2 = 20\,$cm). Near-field and far-field images of the array emission are captured by CCD cameras (u-eye UI-3240 NIR). Fabry-Perot interferometer (FPI) – FPI100 (FSP – 1 GHz, finesse - 280) is used for the spectral measurements. Noise measurements are performed with amplified photodiodes PDA015C2/M (380 MHz bandwidth, $180\,\mu m^2$) with signal amplifiers ZFL-1000LN+ Low Noise Amplifier (0.1-1000 MHz, 20 dB gain).

The scheme includes an OP-VECSEL and some characterization schemes to capture the NF and FF intensity patterns and measure optical spectra, and noise. The cavity is closed by a planar output coupler with a 0.8% transmission at the $\lambda = 1.06\,\mu m$ laser wavelength. Spatial degeneracy and stability of the cavity are provided by an intracavity telescope in 4f-configuration. Two positive lenses (focal lengths $f_1 = 5\,cm$ and $f_2 = 20\,cm$) provide a magnification of 4 in the 50-cm long cavity. The setup allows one to capture the near-field, far-field, optical spectrum, and intensity signals simultaneously with the time synchronization accuracy of electronic devices. The laser array is created using a metal mask placed very close to the output coupler. It consists of circular holes of diameter $\sigma = 200\,\mu m$ with an edge-to-edge separation $a = 50\,\mu m$. The near-field and far-field images of the laser array emission are captured by a CCD camera (u-eye UI-3240 NIR, exposition time $9\,\mu s$). A Fabry-Perot interferometer (1 GHz free spectral range, finesse = 290) is used for spectral diagnostics. Intensity noise measurements are performed with a series of preamplified photodiodes PD1, PD2 (Thorlabs PDA015C/M: bandwidth 380 MHz, sensor area $180\,\mu m^2$) followed by low noise signal amplifiers (Mini-circuits ZFL-1000LN+: bandwidth 1-1000 MHz, gain 20 dB). The gain chip is GAS864.

6.2 Phase-locking of two and three laser array

The changes in the coupling strength permit control of the phase-locking of the laser array, as is now going to be evidenced. Fig. 6.2 represents near-field (NF) and far-field (FF) images of the VECSEL output in different conditions: (a) without any mask, (b,c) with a mask consisting of two holes, and (d, e) with a mask consisting of three holes in a triangular geometry.

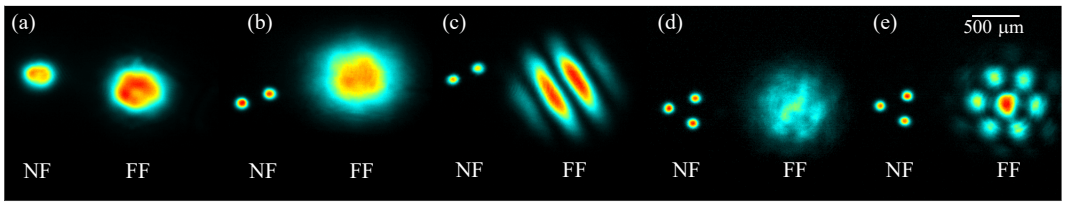

FIGURE 6.2: Near-field (NF) and far-field (FF) images of the laser emission. (a) No mask, (b) two unlocked lasers, (c) two phase-locked lasers, (d) three unlocked lasers, (e) three phase-locked lasers. Subplots (c, e) obtained for the distance $z \sim 550 - 600\,\mu m$.

The coupling between the lasers is changed by translating the mask along the laser axis. This permits to change from an unlocked (Figs. 6.2 (b,d)) to a locked (Figs. 6.2 (c,e)) regime, as can be seen from the far-field patterns. To obtain phase-locking, the distance between the mask and the output coupler is of the order of $400 - 600\,\mu m$.

It is worth mentioning that in all cases the independence of the different lasers of the array can be checked by blocking each of them individually without affecting the powers of the other ones. Then, let us study the phase-locked regime in more detail for two and three lasers separately.

6.2.1 Steady-state interpretation for two phase-locked lasers

When the length z of the diffraction cavity increases the coupling increases. In the case of two lasers, the intensity of the lasers starts to change its values based on the NF measurement. The far-field patterns reveal different interference patterns. Examples of the near-field and far-field intensity distributions are given in Fig. 6.3 for different lengths of diffraction cavity $z_1 < z_2 < z_3$.

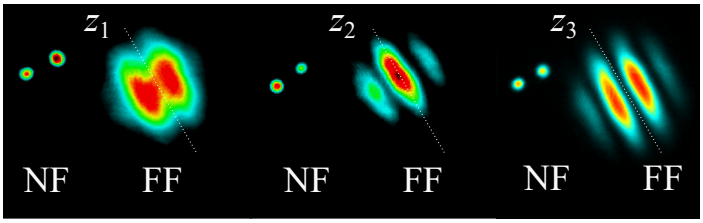

FIGURE 6.3: Near-field and far-field patterns, at three different distances of the diffraction cavity, i.e. mask to OC distances $z_1 < z_2 < z_3$. The case z_3 corresponds to Fig. 6.2 (c).

In the cases z_1 and z_2 the intensities of the lasers are different. The smallest of the presented distances is z_1. It has a value around $100-200\,\mu$m and corresponds to a low visibility of the FF pattern. This case is at the border of phase-locking. Smaller distances lead to intensity fluctuations and the optical spectrum is unstable. The steady-state solution is close to being out-of-phase. Contrary to this, the "in-phase" solution is observed at a bigger diffraction length $z = z_2$ closer to $300-400\,\mu$m. The intensities are quite stable in this case, but not equal. Their difference is around 60%. Any attempt to equalize the intensities by the mask or the pump realignment leads to phase unlocking. The laser with a smaller intensity has an output power of less than 0.2 mW. It is extremely difficult to study the noise in this case. The intensities of the lasers are the same only in the case z_3. This case with diffraction length z_3 around $500-600\,\mu$m is chosen for noise investigation.

These experimental results are easy to interpret because we obtained an analytical steady-state solution dependency on the coupling strength in chapter 2. The amplitudes in the steady-state are given by eqs. 6.1.

$$A_{1,2,\mathrm{st}} = \sqrt{F_{\mathrm{sat}}(r-1)}\left(\frac{r}{r-1}|\eta|\cos(\psi_{\mathrm{st}} \pm \theta) + 1\right). \tag{6.1}$$

Equal intensities for the two lasers $A_{1,\mathrm{st}} = A_{2,\mathrm{st}}$ may only be observed when the coupling argument is $\theta = 0$ or $\pm\pi$. The experiment agrees with that statement. The

corresponding image of equal-intensity lasers is given by the subplot corresponding to z_3. This solution is perfectly symmetric, and the steady-state phase-difference is around π. The coupling argument θ can be estimated with Fig. 2.20 in chapter 2. For example z close to $200,300$ and $600\,\mu$m gives a coupling argument $\theta = \pm\pi$. This explains our experimental results given by "out-of-phase" phase-locking with z_1, z_3. The case corresponding to z_2 is given by a coupling argument different from 0 and π and thus the two intensities are different.

In these experiments, we can't detect a significant effect of detuning between the lasers. This is also a good sign of conditions close to degeneracy. Approximately the detuning value can be estimated based on the marginally phase-locked case noted z_1 in Fig. 6.3. We estimate the coupling strength in this case to be at the border of phase-locking, i.e. close to η_{cr}. Then, detuning between lasers can't exceed tens of kHz: $\Omega/2\pi < 15\,$kHz.

6.2.2 Steady-state interpretation for three phase-locked lasers

A laser array of three lasers is characterized by almost equal amplitudes of the lasers at any distance z in the investigated range. The intensity in the near-field does not significantly vary with the change of mask position. We managed to see only stable "in-phase" phase-locking, which is easy to recognize by the strong maximum in the center of the FF beam. Fig. 6.4 shows the FF image obtained in the experiment at the same distance z_3 as the "out-of-phase" phase-locking of two lasers ($z_3 \sim 500 - 600\,\mu$m).

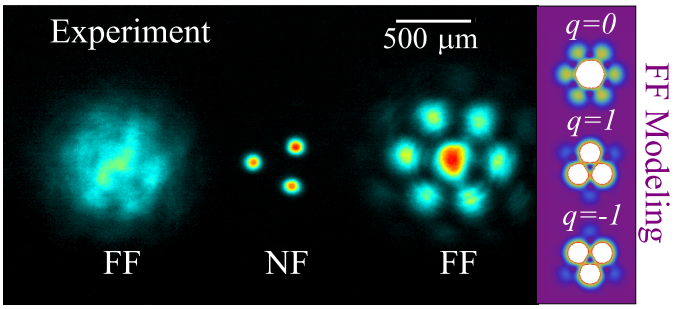

FIGURE 6.4: Laser array output. Black background: experiment. Left to right: unlocked array FF, NF of the three lasers, FF of the phase-locked lasers with $q = 0$. Pictures on the purple background: Modeling of the array phase-locking with different topological charges q.

This figure shows the NF and FF when the laser array is unlocked (the FF on the left) and phase-locked (the FF on the right). In the right inset of the figure three FF intensity patterns were calculated for different topological charges q. The observed TC is clearly zero in this case.

Neglecting the influence of detuning, the steady state solution can be approximated by eqs. (6.3) obtained in chapter 3:

$$A_{st} = \sqrt{F_{\text{sat}}}\sqrt{\frac{r}{1-2|\eta|\cos\psi_{\text{st}}\cos\theta}-1}\,, \tag{6.2}$$

$$\psi_{\text{st}} = \frac{2\pi q}{n},\ m \in \mathbb{Z}. \tag{6.3}$$

In case detuning is not zero, we have already seen with the modeling in chapter 3 that the order parameter then decreases. The visibility of the FF should decrease too and the position of maxima will not be symmetrically distributed. In the experiment, we consider $\Omega/2\pi < 15\,\text{kHz}$, i.e. the same average detuning as for the two laser arrays.

6.2.3 Optical spectrum of phase-locked laser arrays

In the perfectly degenerate cavity [Mahler 2021], the frequency detuning between the different lasers is supposed to be close to 0. But in practice, the intracavity aberrations create some spurious detunings between the lasers.

Nevertheless, when the lasers are phase-locked, they share the same frequency and operate in a single-frequency regime [1]. This is evidenced by the optical spectrum shown in Fig. 6.5.

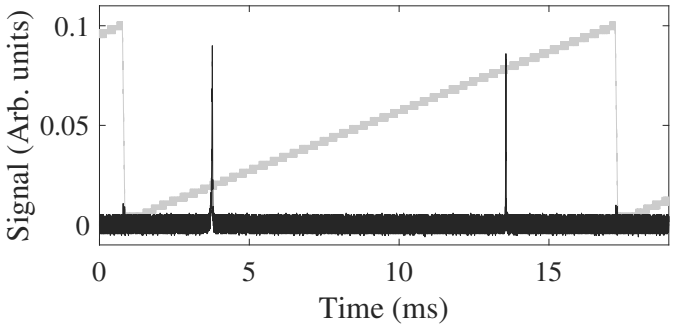

FIGURE 6.5: Black line: the optical spectrum obtained from the FPI for the array of two phase-locked lasers. Gray line: scan voltage of ramp applied to FPI. The free spectral range of the FPI is 1 GHz.

The phase-locking of the laser array makes it remarkably robust: the laser single-frequency operation remains stable without any mode hop for several seconds in a standard laboratory environment. The same optical spectra are observed for three laser arrays. On the contrary, in the case where the laser array is unlocked, the laser spectrum is much more unstable. This single-frequency operation will allow us in the following to establish a simple analytical model to describe the laser evolution.

Moreover, it simplifies the understanding of the origin of laser noise by excluding mode beating and other effects related to multimode operation.

[1] The optical spectrum of the single free-running laser is nearly single-mode but very unstable.

6.3 Noise of the laser array

The noise is typically weak in VECSELs. As mentioned before, we use amplified photodiodes (bandwidth 380 MHz, sensor area 180 µm^2) and additional low-noise amplifiers (0.1-1000 MHz, 20 dB gain) to detect the intensity fluctuations. This bandwidth of the noise amplifiers gives a lower limit of the measurement bandwidth. Also, the frequency range of the measuring noise will be limited by the bandwidth of the VECSEL cavity transfer function. The high-frequency component is typically filtered starting from the cavity cut-off frequency.

Cavity cut-off frequency

The cavity cut-off frequency for a class-A laser can be obtained from optical cavity transfer functions [Baili 2007; Baili 2008] given by the formula:

$$\mathrm{T}(f) = \frac{1}{\tau_{\mathrm{cav}}^2} \frac{1}{\left[\frac{1}{\tau_{\mathrm{cav}}} \frac{r-1}{r}\right]^2 + (2\pi f)^2}, \tag{6.4}$$

and the cut-off frequency is

$$f_{\text{cut-off}} = \frac{1}{2\pi\tau_{\mathrm{cav}}} \frac{r-1}{r}. \tag{6.5}$$

Using the photon lifetime we can calculate $f_{\text{cut-off}} = \frac{1}{2\pi\tau_{\mathrm{cav}}} \frac{r-1}{r} = 0.48\,\mathrm{MHz}$ with $r = 1.1, \tau_{\mathrm{cav}} = 30\,\mathrm{ns}$ for two lasers.

Noise measurement covering the range close to the cavity cut-off frequency allows us to distinguish the dynamical class of the lasers [Baili 2009]. Class-A dynamics never show a kink close to the cuff-off frequency and the attenuation of the noise happens according to the first-order low-frequency filter. To observe such behavior in our system we process the measured data in the range from 100 kHz to several MHz.

6.3.1 Noise spectra in the two laser array

In the next step, we investigate the amplitude noise of the lasers in the unlocked and phase-locked cases for two-laser and three-laser arrays. Thanks to the small sensor area, we can dedicate each photodiode to a single laser in the NF. We characterize the noise by the RIN spectra, defined as:

$$\mathrm{RIN}_i(f) = \frac{\langle|\widetilde{\delta I_i(f)}|^2\rangle|}{\bar{I}_i^2}, \tag{6.6}$$

where $\langle|\widetilde{\delta I_i(f)}|^2\rangle$ is the power spectral density obtained by the Fourier transform of the intensity noise of i-th laser and $\overline{I_i}$ is $i-$th laser mean intensity.

We measured the time series of the intensity noise with a time sampling of 2.5 ns and a length of 2 million points each. The measurements of its RIN spectrum are presented in Fig. 6.6 for both phase-locked and unlocked cases. The noise of the first laser is presented in the subplot (a) and the noise of the second laser is shown in subplot (b). As was mentioned, the noise below 100 kHz is filtered by the noise amplifiers. The upper bandwidth limit was chosen to observe the cavity cut-off frequency around 0.48 MHz.

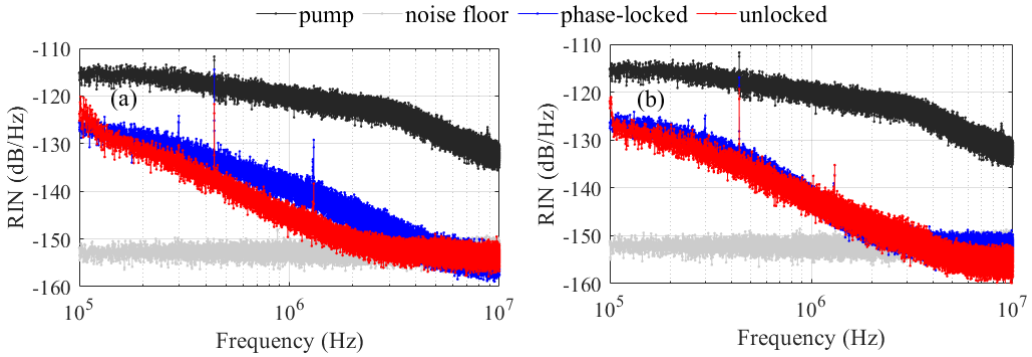

FIGURE 6.6: Experimental RIN spectra of the lasers in the array of two lasers. Subplot (a) illustrates the noise spectra for the first laser, subplot (b) illustrates the spectra for the second laser. Phase-locked data are shown in blue (laser output power of the order of 2 mW) and unlocked data are shown in red (laser output power of the order of 0.4 mW). Grey curve: noise floor. Black curve: pump laser RIN. Thin peaks originate from some spurious modulations of the laser power.

Fig. 6.6 compares the laser RIN when the two lasers are locked (blue line) and unlocked (red line). Apart from a difference in noise levels, which can be attributed to several reasons, such as a variation of the laser losses and power between the two cases, no significant difference appears between the two situations. The difference between the RIN levels of the locked and unlocked laser arrays in Fig. 6.6 is due to the presence of extra losses in the unlocked case. Measurements of the pump noise (black curve in Fig. 6.6) are performed outside the laser setup [2]. The pump spectrum contains frequency components, which affect the noise of the array's lasers around $f = 300, 420$ kHz and 1.5 MHz and are always present in the spectra. When one compares the laser RIN spectrum with the pump RIN spectrum (black line in Fig. 6.6), the filtering effect of the cavity above a 3 dB cut-off frequency of the order of 480 kHz is visible. The VECSEL cavity indeed behaves as a first-order filter with a -20 dB/decade attenuation, while class-B attenuation is -40 dB/Hz [Baili 2009]. In all cases, these spectra are typical of a class-A laser.

[2] Details of the pump noise measurements are given in subsection 6.3.3

Noise spectra in two laser array

We also checked that the same kind of RIN spectrum is obtained for an array of three lasers (see Fig. 6.7). In the case of the three laser arrays, we detect similar noise characteristics. The RIN of the first (1) and the second laser (2) among three lasers in total are shown in Fig. 6.7.

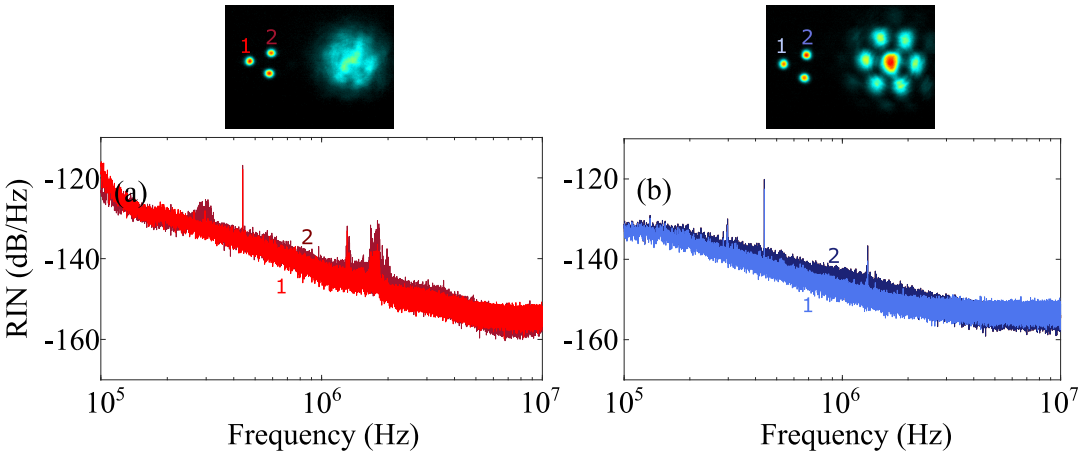

FIGURE 6.7: Experimental RIN spectra of two lasers in the array of three lasers. The unlocked noise spectra are given in subplot (a) by red and dark-red curves for lasers 1 and 2 marked by corresponding color in the NF intensity pattern above (laser output power of the order of 0.3 mW). Subplot (b) shows phase-locked noise spectra given by blue curves for laser 1 and 2 by corresponding color in NF intensity pattern above, laser output power of the order of 0.6 mW).

The pump-induced spikes are present at the same frequencies ($f = 300, 420$ kHz and 1.5 MHz). In the unlocked case (a) we can also see that additional laser frequency components are given by the mods beating induced. The lasing threshold is slightly different in the case of three lasers. The pumping rate is lower than r=1.07. This leads to a small modification in the cavity cut-off frequency.

6.3.2 Cross-correlation spectra

Much more information on the laser array behavior can be gained by measuring the spectrum of the correlations between the intensity noises of the different lasers of the array. The definition of the cross-correlations coefficient is given by eq. (6.7).

$$\mathrm{CC}(\widetilde{\delta I}_1, \widetilde{\delta I}_2) = \frac{\mathrm{Cov}(\delta\widetilde{I}_1, \delta\widetilde{I}_2)}{\sqrt{\mathrm{Var}(\delta\widetilde{I}_1)\mathrm{Var}(\delta\widetilde{I}_2)}}\,, \tag{6.7}$$

where Var holds for the variance and Cov for the covariance of the intensities Fourier spectra. The coefficient is a complex value. We refer to its modulus as correlation amplitude and its argument as correlation phase.

6.3.3 Pump spatial correlations

First of all, it is important to study the pump laser spatial correlations. These correlations of the laser noise can be enhanced due to the partial correlation between the injected parts of the pump beam. The pump noise measurements scheme is shown in Fig. 6.8.

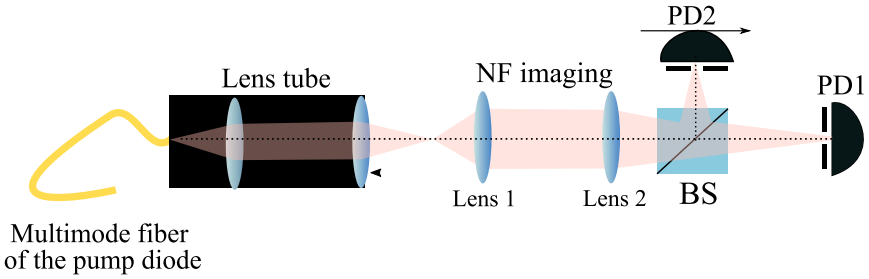

FIGURE 6.8: Experimental scheme for the pump laser noise measurements. Photodiodes are Thorlabs PDA15C2 with integrated 50 µm pinholes. Lens 1 and lens 2 have focal distances of 50 mm and 200 mm.

The pump laser is studied at the electrical current $j = 1.1$ A. This value corresponds to the typical value used in the VECSEL arrays studies. The intensity of the beam was significantly decreased by beam-splitters and NDFs, but this part of the scheme is not presented in Fig. 6.8. Then, the two-lens imaging system is installed. The lenses have 50 and 200-mm focal distances (LBF254-50-B and LBF254-200-B). This telescope repeats the intracavity telescope with a magnification 1/4 to mimic the edge-to-edge mask separation by the pinholes integrated with photodiodes. The beam of the pump laser is divided by a 50/50 beam-splitter and directed to the two amplified photo-diodes. Each photo-diode has an integrated pinhole of 50 µm. This pinhole size was chosen because it corresponds to the edge-to-edge separation of the holes in the mask. Such size of the edge was chosen to increase the coupling. It is easier to obtain phase-locking with such separation than for example with 100 µm. Also, the size of the pump spot can be smaller. At the same time, such a small loss profile can cause the pumping of both lasers by the same spatial mode of the pump. Then the correlations of the laser noise will depend not only on the laser's phase-locking but on the correlations of the injected pump noise.

The initial position of the photodiodes is chosen based on the maximal detected signal, which corresponds to the central maximum of the Gaussian pump. One of the photodiodes is fixed, and the transverse position of the second one can be precisely

varied. We measured twenty spectra of one million points each for several positions of the second photodiode PD2.

The correlation amplitude decreases with the distance between PD2 and the image of PD1 through the beamsplitter. The translation was performed in both directions. Then, the cross-correlation spectra for PD1 and PD2 were calculated and their modulus and arguments are given in Fig. 6.9 as correlation amplitude (a) and phase (b). The sampling period of the measurement is 2.5 ns. Each point of the presented curve is obtained by averaging over 250 points. The modulus of the PD2 translation distance is marked between the subplots.

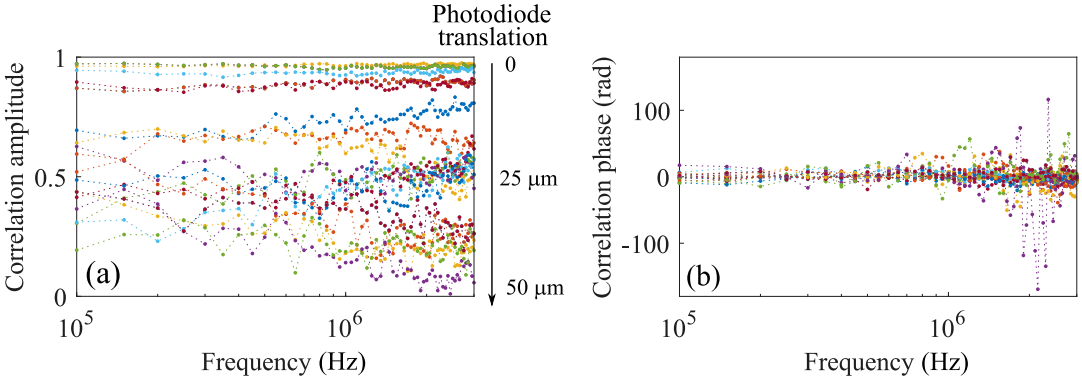

FIGURE 6.9: Cross-correlation spectra between the pump noise along the beam cross-section. The PD2 is translated, and the position of the PD1 is fixed. See Fig. 6.8 for details of the measurement scheme.

The correlation amplitudes decrease fast and they are almost zero for 50 µm separations. In all cases, the correlations decrease when the noise frequency reaches 3 to 4 MHz which corresponds to the pump laser frequency cut-off. Moreover, the phase of the correlations is always 0 (see Fig. 6.9 (b): the correlated parts of the pump noises are all in phase). The variance of the correlation phase increases only in the frequency range when the noise is very low (close to 3-4 MHz). We can conclude, that within the VECSEL noise transfer bandwidth, the pump noises seen by different lasers are weakly correlated at a distance given by the mask edges (50 µm) the correlations thus become completely negligible between the centers of the holes.

One can notice that the RIN of the pump presented in Fig 6.6 as black dots is higher than the VECSEL's RINs. It also exceeds its datasheet value, which is -130 dB/Hz at 10 kHz and -140 dB/Hz at 1 MHz.

When measuring n uncorrelated spatial modes with the same detector, the variance of the measurement result scales proportionally to n, meaning the standard deviation is proportional to the square root of the number of modes $\sqrt{n}$. Similarly, the average power is also proportional to n. Consequently, as the number of measured modes increases, the RIN decreases. Therefore, the RIN measured with a pinhole is larger than the RIN of the full beam. We use such measurement to characterize the spectrum of the pump, but we quantify the RIN value by the average datasheet number, i.e. -135 dB/Hz.

6.3.4 Noise cross-correlations in the VECSEL array

Knowing that the pump correlation between lasers is negligible, we can characterize the cross-correlation of the laser noises in the VECSEL array. As we mentioned the sampling period is 2.5 ns in our measurements and the length of the measured dataset is 2 million points. This gives us a wider frequency bandwidth (down to kHz) than we need to characterize the VECSEL cut-off frequency. Thus, we reshape the datasets to 250 smaller datasets in which low-frequency resolution is given by the amplifier's bandwidth of 100 kHz. The cross-correlation value at each frequency is then obtained by 250 values and averaged over 20 measurements. Fig. 6.10 shows an example of such measurements for two (a, b) and three lasers (c, d).

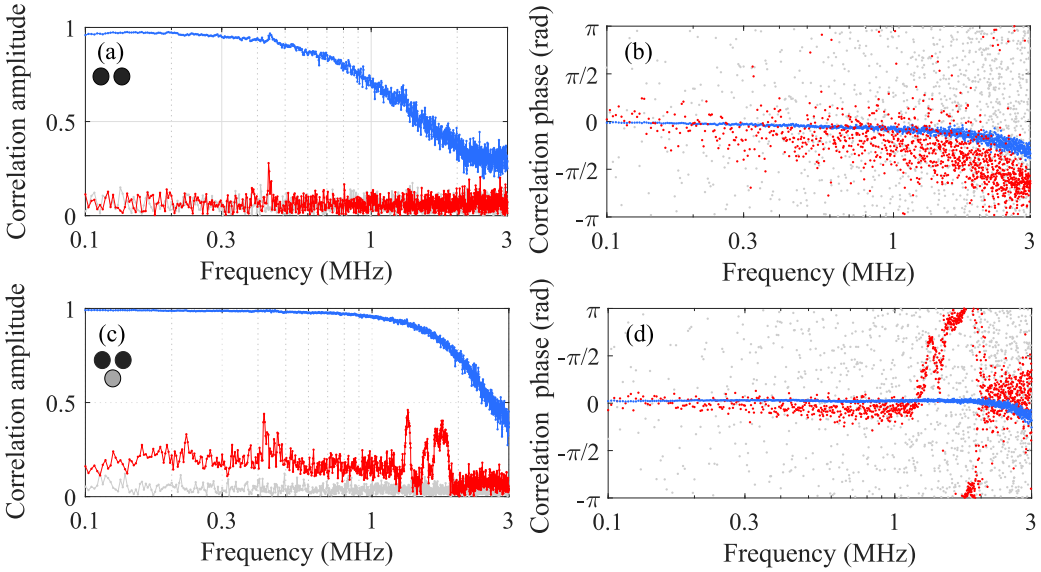

FIGURE 6.10: Measured correlation spectra between the intensity fluctuations of two lasers in the array. (a, c) Amplitude and (b, d) phase of the correlation. Blue curves: phase-locked laser array, red curves: unlocked laser array; light gray curves: noise floor. (a, b) array of two lasers, (c, d) array of three lasers.

Subplots (a) and (c) of Fig. 6.10 correspond to the amplitude of the normalized correlation spectrum between the intensity noises of two of the lasers in the array, while Figs. 6.10 (b) and 6.10 (d) display the phase of this correlation. In each plot, the blue (red) curve corresponds to the situation where the lasers of the array are phase-locked (unlocked). Figs. 6.10 (a, b) correspond to an array of two lasers while Figs. 6.10 (c, d) is obtained for an array of three lasers. A comparison of the two cases in this figure shows a dramatic difference between phase-locked and independent lasers. Indeed, while the correlation between the intensity noises between the lasers cannot be distinguished from noise when the lasers are unlocked (see the red curves in Fig. 6.10 (a) and 6.10 (c)), these intensity fluctuations become almost completely

correlated when the array is phase-locked (blue curves). This illustrates the fact that the lasers behave like completely independent oscillators when they are unlocked and that the laser array behaves like a single super-laser in a single super-mode when the lasers are phase-locked.

Additionally, we have to pay attention to the phase of the correlations. The phase is close to zero for the phase-locked cases (blue curve in (b) and (d)) for two and three lasers. The unlocked case shows more randomness in the correlations phase distribution (red curve in (b) and (d)). However, it does not correspond to the totally random situation for the base noise correlation phase (shown as gray dots). This means, that both lasers have a very small in-phase noise component injected from the pump laser injected. We have already seen the cause of this in Fig. 6.9, where the correlations are negligible, but the phase within the laser bandwidth is always around zero.

In the case of three lasers, the unlocked case (red curves in (c)) corresponds to a stronger coupling than the so-called "zero coupling" case for two lasers (a). The argument exhibits less dispersion in this case and it is close to zero. This is caused by the mask positioning imperfections. Complete zero of the correlations expected, when there is no gap between the mask and OC. Even though the coupling strength is not exactly zero, it is not enough to observe the phase-locking of the array.

There are also several peaks, where the correlations increase for each presented curve in Fig. 6.10. These peaks are transferred from the pump laser to each laser. Moreover, there is also evidence of anti-phase oscillations around 1.5 MHz, which is probably excited by the intense pump noise component at this frequency.

6.4 Modeling of the VECSEL array noise

The model used to describe the laser intensity noise is based on a system of rate equations. In the following, we present how the noise is introduced in the two- and three- laser models obtained in chapter 2 and chapter 3. First of all, the physical source of noise has to be defined. Our VECSEL arrays are optically pumped, thus the pump noise is always present in the system. Additionally, the output is affected by mechanical and thermal noises and spontaneous emission noise. In case where the lasers are not single-mode or not phase-locked, we can observe intensity variations excited by the mode beating, mode hopping, etc. Eventually, we are interested mostly in the intensity noise and its correlations. We believe that we can use its characteristics for the laser dynamics classification and use it for the laser array phase-locking investigation.

Fig. 6.11 illustrates the different noise sources' impacts on intensity and phase noise components. Black curves illustrate spontaneous emission noise, red curves are for pump-induced noise, and blue curves are for the shot noise.

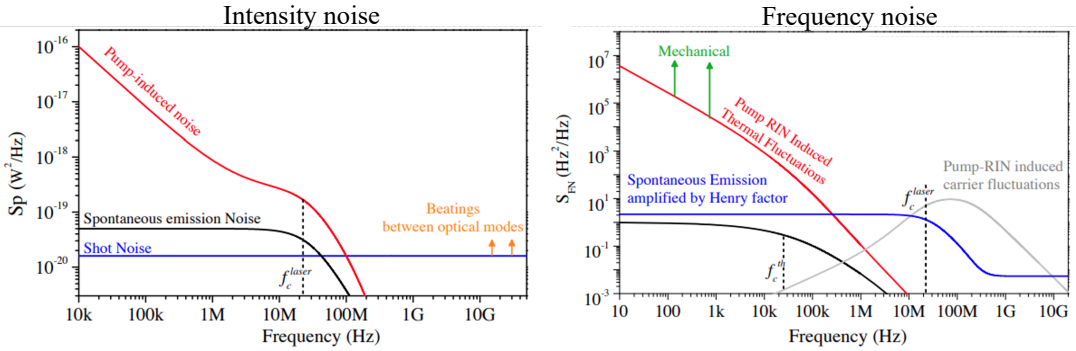

FIGURE 6.11: Noise origin in the OP VESCEL array. Adapted from [Myara 2013]. Black curves - spontaneous emission noise, red curves - pump-induced noise, blue curves - shot noise.

The noise of the optical pump prevails over the noise of spontaneous emission and shot noise. Thermal noise affects mostly the phase-noise characteristics [Gredat 2019b; Liu 2018a; Gredat 2018; Gredat 2020b; De 2013a; De 2013b]. The laser exhibits a stable single-frequency output when phase-locked. We thus introduce inside our model only the optical pump noise.

6.4.1 Rate equations with pump noise

The pump noise is introduced as a fluctuation $\delta r_i(t)$ in the pumping rate $r_i(t) = r + \delta r_i(t)$ of the laser i in the array, where r is the average pumping rate common to all the lasers.Then, the dynamics of the two laser arrays is governed by the following rate equations:

$$\begin{aligned}
\frac{dA_1}{dt} &= -\frac{A_1}{2\tau}\left(1-\frac{r_1(t)}{1+A_1^2/F_{sat}}\right)+\frac{|\eta|}{2\tau}\cos(\psi+\theta)A_2\,,\\
\frac{dA_2}{dt} &= -\frac{A_2}{2\tau}\left(1-\frac{r_2(t)}{1+A_2^2/F_{sat}}\right)+\frac{|\eta|}{2\tau}\cos(\psi-\theta)A_1\,,\\
\frac{d\psi}{dt} &= \frac{\alpha}{2\tau}\left(\frac{r_2(t)}{1+A_2^2/F_{sat}}-\frac{r_1(t)}{1+A_1^2/F_{sat}}\right)\\
&\quad -\frac{|\eta|}{2\tau}\left(\frac{A_2}{A_1}\sin(\psi+\theta)+\frac{A_1}{A_2}\sin(\psi-\theta)\right)+\Omega\,,
\end{aligned} \tag{6.8}$$

where A_1 and A_2 are the amplitudes of the two laser fields, normalized in such a way that their squares correspond to the respective photon numbers. The third variable ψ is the phase difference between the lasers and F_{sat} the saturation photon number. The Henry factor α, mean value of the excitation ratio r, and photon lifetime τ_{cav} are the same, as were used in the previous calculations.

Numerically we can investigate both cases of the phase-locked lasers and the unlocked case. When the coupling strength is too weak to overcome the detuning

effect, the noise spectra will exhibit intensity oscillations. The amplitude dynamics of these oscillations have been studied in chapter 2. In the simplest case where the lasers have equal pumping rates $r_1 = r_2$ and photon lifetimes $\tau_1 = \tau_2$ the value of the beatnote frequency defined by the detuning between the lasers Ω and the so-called laser locking frequency ω_L given by eq. (6.9):

$$f_{\text{bt}} = \frac{1}{2\pi}\sqrt{\Omega^2 - \omega_L^2}, \quad \text{where } \omega_L = \frac{|\eta|}{\tau_{\text{cav}}}. \tag{6.9}$$

Let us consider this case ($r_1 = r_2$, $\tau_1 = \tau_2$) with uncorrelated pump noises δr_1 and δr_2. Both of these noise components are considered as white noise with a RIN=-135 dB/Hz given by the mean value of the pump RIN in the datasheet. We are interested in the investigation and comparison of different cases of phase-locked laser arrays. We want to compare the noise of one of the lasers in the unlocked case with the phase-locked laser. Additionally, we are interested in the study of the detuning effect and the influence of the coupling strength.

In total we investigate four cases: zero-coupling $|\eta| = 0$; small coupling $|\eta| = 0.0001$, which can not overcome detuning between lasers; and strong coupling strength $|\eta| = 0.11$ with two different coupling arguments $\theta = 0$ and $\theta = 0.95\pi$. Strong coupling is enough to overcome detuning. The corresponding numerically calculated RIN spectra are shown in Fig. 6.12 for one laser.

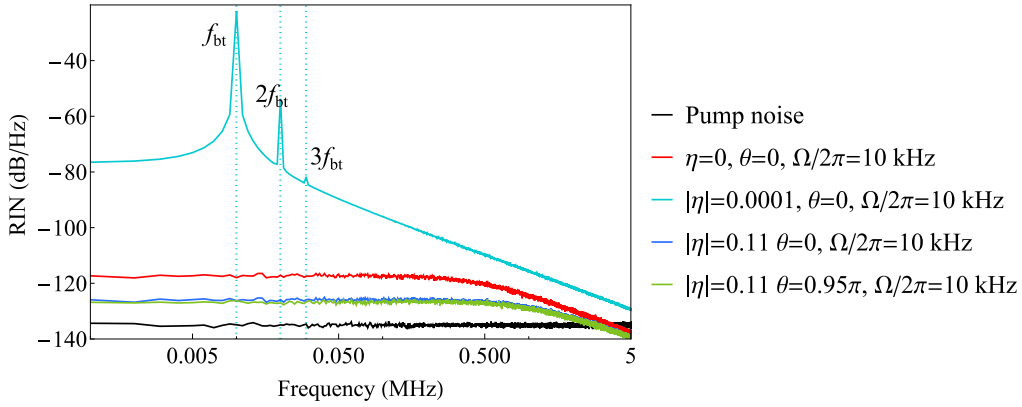

FIGURE 6.12: Numerically calculated laser RIN spectra for one of the lasers in a two laser array. Different colors correspond to the different values of the coupling strength ($|\eta| = 0$, 0.0001 and 0.11). The pump noises are fully uncorrelated in the considered frequency range with a RIN $= -135\,\text{dB/Hz}$. The presented data correspond to the averaging of over 100 noise spectra. The spectra are calculated with $\alpha = 6$, $r = 1.1$, $\tau = 30\,\text{ns}, \Omega/2\pi = 10\,\text{kHz}$.

The input white noise with RIN=-135dB/Hz is shown as black curve. The light blue curve characterizes the noise of the laser with a very small coupling $|\eta| = 0.0001$ lasers with detuning $\Omega/2\pi = 10\,\text{kHz}$. There are several peaks that evidence

intensity oscillations. Their frequencies are given by harmonics of the beatnote frequency $f_{bt} = 9.98$ kHz. The beatnote frequency decreases if the coupling strength increases and rises if detuning increases.

On the contrary, when the coupling is zero (red dataset in Fig. 6.12) and when the lasers are coupled and phase-locked (blue dataset in Fig. 6.12) the noise copies the input white noise, but with the filtering effect of the cavity. One can notice that these RIN spectra exhibit the typical first-order filter shape of a class-A laser, as observed experimentally. Indeed, we can see that the cut-off frequency with experimental parameters is around 0.5 MHz. The difference between the phase-locked and unlocked situations consists of a small change in the noise level. The RIN in the phase-locked case is smaller than in the case with unlocked lasers due to the changes in the mean intensity value, which depends on the coupling strength.

The difference between the unlocked and phase-locked cases is much more striking when one considers the correlations between the noises of the two lasers, as shown by the simulation results reproduced in Fig. 6.13. The cross-correlation spectra are obtained with a thousand noise spectra for each laser. Each value of the cross-correlation coefficient at a chosen frequency is a cross-correlation coefficient of two spectral datasets with a length of one thousand points. Here we study four cases where the lasers are unlocked or phase-locked with different coupling arguments.

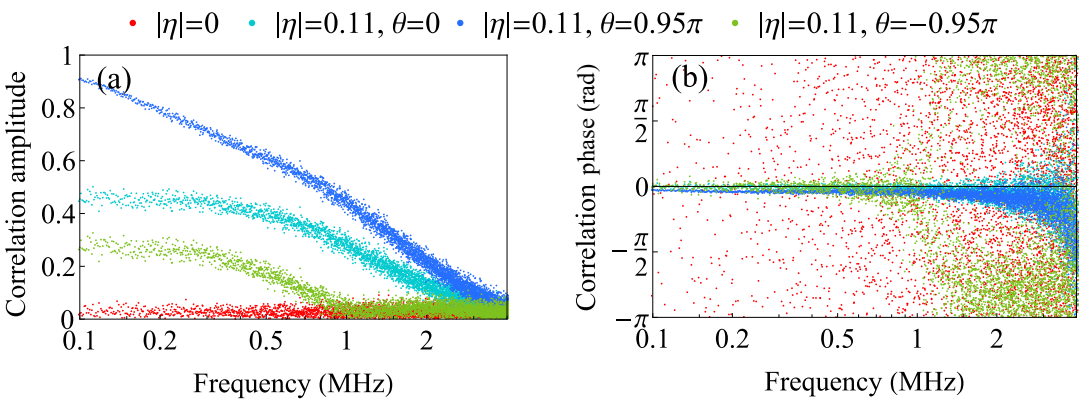

FIGURE 6.13: Amplitude (a) and phase (b) of the noise correlation spectrum between the intensity noises of the two lasers obtained with the numerical model. The data were calculated with the same parameters as Fig. 6.12. The presented data corresponds to the averaging of over 1000 noise spectra. The spectra are calculated with $\alpha = 6$, $r = 1.1$, $\tau = 30\,\text{ns}, \Omega/2\pi = 10\,\text{kHz}$.

The unlocked lasers show negligible correlation amplitude with a completely random argument of the correlations. This confirms the increase of the correlation phase variance in our experimental results. The argument of coupling strength θ affects the amplitude of the correlation a lot. The amplitude of the correlations for the phase-locked case is always non-zero. However, it depends a lot on the sign of θ. We study this phenomenon more precisely with an analytical model in the following.

6.4.2 Analytical model of the noise

To develop an analytical model, let us introduce a vector $\mathbf{S}$ whose three components are given by the right part of the three rate equations of eqs. 6.8. The fluctuations of the lasers can be obtained by linearizing the vector components around the steady state solution given by vector $\{A_{1,\mathrm{st}}, A_{2,\mathrm{st}}, \psi_{\mathrm{st}}\}$. Following [De 2013a], the three variables are written in vector form as $\mathbf{A} = \{A_{1,\mathrm{st}}, A_{2,\mathrm{st}}, \psi_{\mathrm{st}}\} + \delta\mathbf{A}$, where the vector $\delta\mathbf{A} = \{\delta A_1, \delta A_2, \delta\psi\}$ contains the fluctuations around the steady-state values $\{A_{1,\mathrm{st}}, A_{2,\mathrm{st}}, \psi_{\mathrm{st}}\}$. The pump fluctuations around the average values $\mathbf{r} = \{r, r\}$ are written as a vector $\delta\mathbf{r} = \{\delta r_1, \delta r_2\}$.

Then eqs. (6.8) can be formally written as:

$$\dot{\mathbf{A}}(t) = \mathbf{S}(\mathbf{A}, \mathbf{r})(t) = \mathbf{S}(\mathbf{A}_{\mathrm{st}} + \delta\mathbf{A}, \mathbf{r} + \delta\mathbf{r}). \tag{6.10}$$

Linearization consists of expanding the right-hand side up to the first order in $\delta\mathbf{r}$ and $\delta\mathbf{A}$, leading to:

$$\dot{\delta\mathbf{A}}(t) = \underbrace{RS(\mathbf{r}_0, \mathbf{A}_{\mathrm{st}})}_{=0} + \frac{\partial\mathbf{S}(\mathbf{r}, \mathbf{A})}{\partial\mathbf{A}}|_{r_0, A_{\mathrm{st}}}\delta\mathbf{A} + \frac{\partial\mathbf{S}(\mathbf{r}, \mathbf{A})}{\partial\delta\mathbf{r}}|_{r_0, A_{\mathrm{st}}}\delta\mathbf{r}\,. \tag{6.11}$$

Here, the partial derivative of a vector $\mathbf{S}$ over vector $\mathbf{A}$ stands for a matrix with elements $\left[\frac{\partial\mathbf{S}}{\partial\mathbf{A}}\right]_{ij} = \frac{\partial\mathbf{S}_i}{\partial\mathbf{A}_j}$ and over vector $\delta\mathbf{r}$ it is $\left[\frac{\partial\mathbf{S}}{\partial\delta\mathbf{r}}\right]_{ij} = \frac{\partial\mathbf{S}_i}{\partial\delta\mathbf{r}_j}$.

Thanks to the Fourier transform of eq. (6.11) we obtain the intensity noise of the lasers defined according to the eq. 6.12. The full process with details of this transformation is given in the appendix A.

$$\widetilde{\delta\mathbf{I}}(\omega) = 2\mathbf{A}_{st}\left[i\omega - \frac{\partial\mathbf{S}(\mathbf{r}, \mathbf{A})}{\partial\mathbf{A}}|_{r_0, A_{st}}\right]^{-1}\frac{\partial\mathbf{S}(\mathbf{r}, \mathbf{A})}{\partial\mathbf{r}}|_{r_0, A_{st}}\widetilde{\delta\mathbf{r}}(\omega) = 2\mathbf{A}_{st}\begin{bmatrix} a_1 & a_2 \\ b_1 & b_2 \end{bmatrix}\widetilde{\delta\mathbf{r}}(\omega). \tag{6.12}$$

Then, the cross-correlation coefficient has the shape of eq. 6.13:

$$CC(\widetilde{\delta I_1}, \widetilde{\delta I_2}) = \\ = \frac{a_1 b_1^* + a_2 b_2^* + (a_1 b_2^* + a_2 b_1^*)CC(\delta r_1, \delta r_2)}{\sqrt{|a_1|^2 + |a_2|^2 + 2\mathrm{Re}[a_1 a_2^*]CC(\delta r_1, \delta r_2)}\sqrt{|b_1|^2 + |b_2|^2 + 2\mathrm{Re}[b_1 b_2^*]CC(\delta r_1, \delta r_2))}}. \tag{6.13}$$

if pump noises are not correlated, $CC(\delta r_1, \delta r_2) = 0$, the formula for the cross-coefficient is then:

$$CC(\delta I_1, \delta I_2) = \frac{a_1 b_1^* + a_2 b_2^*}{\sqrt{(|a_1|^2 + |a_2|^2)(|b_1|^2 + |b_2|^2)}}. \tag{6.14}$$

6.5 Analytical modeling of the noise in VECSEL arrays

The model developed above allows obtaining the intensity noises of the laser in response to any input noise.

We consider the cross-correlation spectra with an assumption that the pump noise is white and has a constant RIN=-135 dB/Hz. We calculate the cross-correlation spectra with eq. (6.14) for different values of the coupling argument θ. The results are shown in Fig. 6.14. The data are presented in a comparison with numerically calculated values.

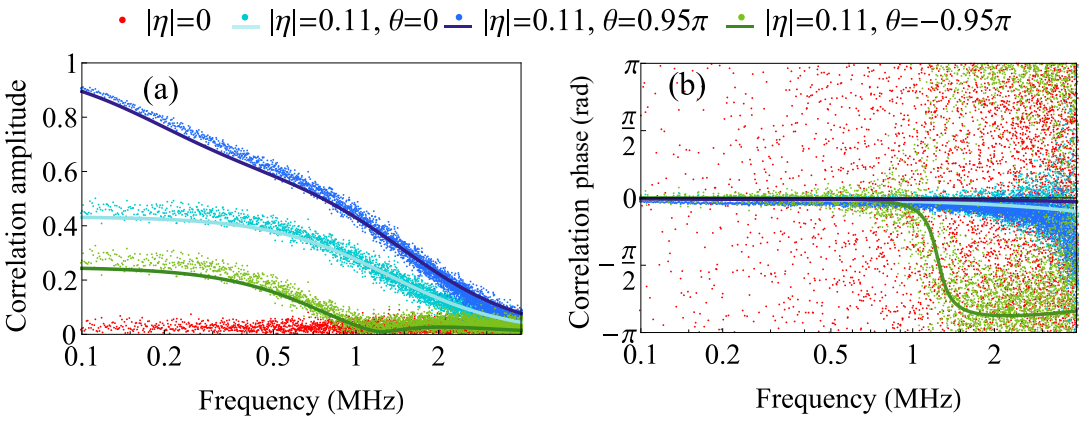

FIGURE 6.14: Amplitude (a) and phase (b) of the correlation spectrum between the intensity noises of the two lasers obtained with the numerical (dots) and analytical solid line model. The data are calculated for $r = 1.1$, $F_{\text{sat}} = 10^{10}$, $\tau = 30\,\text{ns}, \Omega/2\pi = 10\,\text{kHz}$. Different colors correspond to the different values of coupling parameters. The red curve corresponds to the unlocked case, which can not be approximated in our analytical model. Green, light blue and blue curves correspond to $|\eta| = 0.11$ with different θ values.

Indeed, the analytical model accurately reproduces the numerically calculated correlation spectra. Each of the presented analytical curves shows a slightly smaller correlation amplitude the the numerically calculated data. We connect this difference with the small-coupling approximation. One can notice that a negative coupling argument θ leads to a decrease in the amplitude of the correlations, while a positive one leads to an increase. In both cases ($\theta = 0.95\pi$ and $\theta = -0.95\pi$) the real part of the coupling strength is negative and the phase difference is close to π. Thus the increase or decrease of the correlations depends on the imaginary part of the coupling strength.

The phase of the correlation is always zero within the laser cavity bandwidth. Nevertheless, positive and negative θ lead to the zero and $\pm\pi$ phase after the cut-off frequency. In total we can see that both the blue numerically calculated dataset and blue analytical curve are very close to the experimental results. We also notice that

there is a strong dependence on the correlation spectra on the Henry factor, when θ is not zero, as shown in Fig. 6.15.

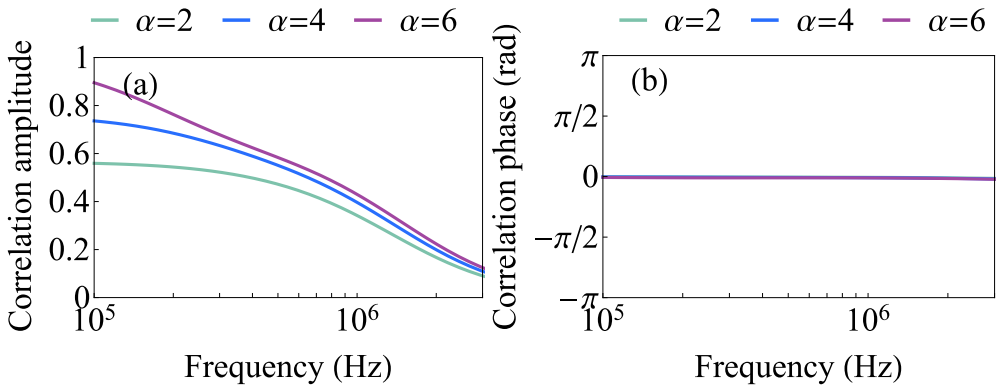

FIGURE 6.15: The amplitude (a) and phase (b) of the correlation spectrum between the intensity noises of the two lasers obtained with the analytical model. The data are calculated for $\theta = 0.95\pi, r = 1.1$, $F_{\text{sat}} = 10^{10}$, $\tau = 30\,\text{ns}, |\eta| = 0.11, \Omega/2\pi = 10\,\text{kHz}$. Different colors correspond to the different Henry factor values.

The correlation amplitude increases with an increase of the α factor if the imaginary part of the coupling strength is positive. On the contrary, the correlation amplitude decreases when $\text{Im}[\eta]$ is negative. The correlations with zero coupling argument do not depend on the α factor.

The correlation amplitude can be increased or decreased by the coupling strength $|\eta|$ variations. The dependency of the coupling strength is shown in Fig. 6.16.

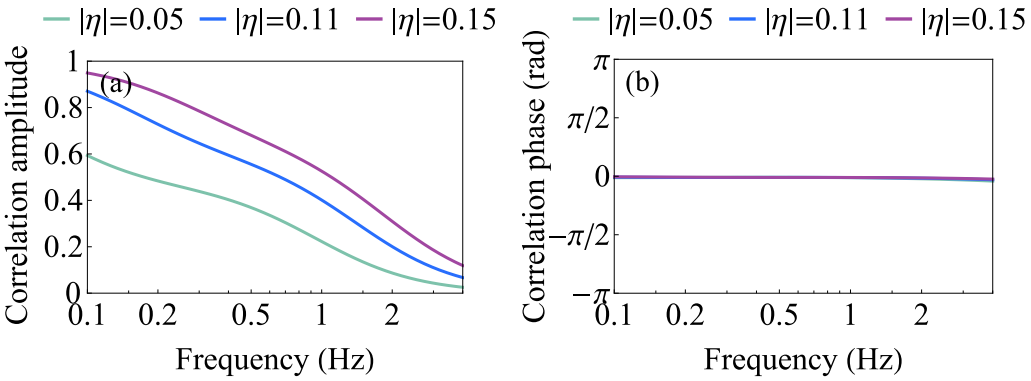

FIGURE 6.16: The amplitude (a) and phase (b) of the correlation spectrum between the intensity noises of the two lasers obtained with the analytical model. The data are calculated for $\theta = 0.95\pi, r = 1.1$, $F_{\text{sat}} = 10^{10}$, $\tau = 30\,\text{ns}, \alpha = 6, \Omega/2\pi = 10\,\text{kHz}$. Different colors correspond to different values of the coupling strength.

The values of the coupling modulus taken to plot Fig. 6.15 are larger than those obtained by calculating the overlap of the diffracted beam with neighboring lasers

along the lasers of chapter 2. This discrepancy can be attributed to the fact that the laser beams are not top-hat and also to uncertainties in the positions of the holes. In total, we can see that the correlation amplitude is always higher in the phase-locked case, such as in the experiment. The same results were obtained for the three laser arrays.

6.6 Three laser array noise correlations

Rate equations for the three laser arrays are the same as those used in chapter 3. We inject the pump noise to these equations as a fluctuation $\delta r_i(t)$ in the pumping rate $r_i(t) = r + \delta r_i(t)$ into each laser.

Then the rate equations for the three laser arrays are:

$$\begin{aligned}
\frac{\mathrm{d}A_i}{\mathrm{d}t} &= -\frac{1}{2\tau_{\mathrm{cav}}}\left(1-\frac{r_i(t)}{1+A_i^2/F_{\mathrm{sat}}}\right)A_i + \frac{|\eta|}{2\tau_{\mathrm{cav}}}\left[\cos(\psi_i+\theta)A_{i+1}+\cos(-\psi_{i-1}+\theta)A_{i-1}\right] \\
\frac{\mathrm{d}\psi_i}{\mathrm{d}t} &= \frac{\alpha}{2\tau_{\mathrm{cav}}}\left(\frac{r_{i+1}(t)}{1+A_{i+1}^2/F_{\mathrm{sat}}}-\frac{r_i(t)}{1+A_i^2/F_{\mathrm{sat}}}\right)+\frac{|\eta|}{2\tau_{\mathrm{cav}}}\left(\frac{A_{i+2}}{A_{i+1}}\sin(\psi_{i+1}+\theta)-\right. \\
&\quad \left.-\frac{A_i}{A_{i+1}}\sin(\psi_i-\theta)-\frac{A_{i+1}}{A_i}\sin(\psi_i+\theta)+\frac{A_{i-1}}{A_i}\sin(\psi_{i-1}-\theta)\right). \qquad (6.15)
\end{aligned}$$

where A_i stands for the amplitudes of the three laser fields, normalized in such a way that their squares correspond to the respective photon numbers. The variables ψ_i are the phase differences between the lasers, F_{sat} the saturation photon number. The Henry factor α, mean value of the excitation ratio r and photon lifetime τ_{cav} are the same as were used in the previous calculations in chapter 3.

We can follow an identical approach of the analytical model derivation. The approach is general and it can be applied to any shape of the laser array. Details of these calculations are also presented in appendix A.

We consider only two lasers out of three-laser phase-locked array, as was done in the experiment. Those lasers have intensity noises $\delta I_1, \delta I_2$ now have three components.

The eq. (6.14) is then replaced by eq. (6.16).

$$CC(\delta I_1, \delta I_2) = \frac{a_1 b_1^* + a_2 b_2^* + a_3 b_3^*}{\sqrt{(|a_1|^2+|a_2|^2+|a_3|^2)(|b_1|^2+|b_2|^2+|b_3|^2)}}. \qquad (6.16)$$

Results obtained with this formula are shown in Fig. 6.17 for different coupling values and different α factor values. In this case, the rate equation system was linearized around the in-phase steady-state solution ($q = 0$).

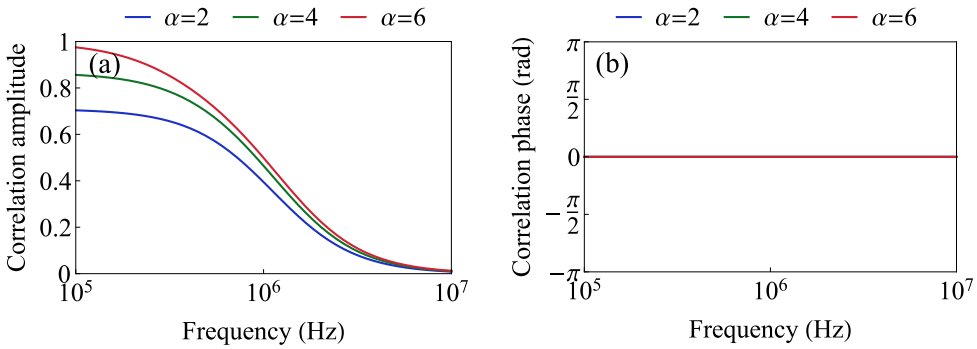

FIGURE 6.17: Amplitude (a) and phase (b) of the correlation spectrum between the intensity noises of two lasers from the three-lasers phase-locked array obtained with the analytical model. The data are calculated for $r = 1.1$, $F_{sat} = 10^{10}$, $\tau = 30\,\text{ns}$, $|\eta| = 0.11$, $\theta = 0.95\pi$. Different colors correspond to the different α values.

The amplitude of the correlations increases with the increase of the Henry factor if the imaginary part of the coupling coefficient is negative $\text{Im}[\eta] < 0$. We also checked that there is no dependency on the Henry factor if $\theta = 0$ and the coupling is real.

The same conclusions hold for the case of two phase-locked lasers. However, in the three-laser case, we can see that the correlation amplitude is stronger than for two lasers. The comparison is shown in Fig. 6.18. Both cases were studied with the same parameters of the pumping rate, photon lifetime, coupling strength (same $|\eta|$ and θ), etc.

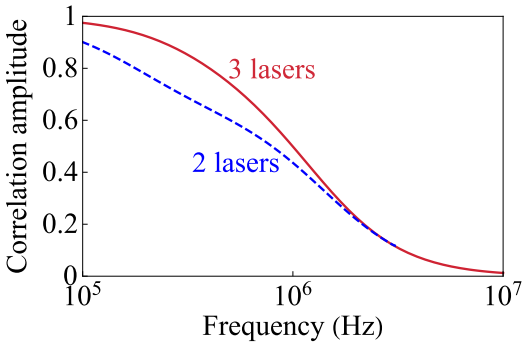

FIGURE 6.18: Amplitude of the correlation spectrum between the intensity noises of the two lasers obtained with the analytical models for three phase-locked lasers (red) and two lasers (blue). The data are calculated for $r = 1.1$, $F_{sat} = 10^{10}$, $\tau = 30\,\text{ns}$, $|\eta| = 0.11$, $\theta = 0.95\pi, \Omega/2\pi = 0$. Different colors correspond to the different number of lasers.

The increase of the correlation in the ring array of three lasers is associated with the impact of the coupling with two neighboring lasers. Each laser in our array

supports and is supported by its neighbors. Each of them receives a fraction of the neighbor intensity variations. In the case of two lasers, it was only a fraction of one laser, in the case of three the impact is double.

Also, this analytical model demonstrates good agreement with measurements presented in Fig. 6.10 for the phase-locked three-laser array.

6.6.1 Noise in the vortex solution

Earlier in chapter 3 we established that there are also vortex and anti-vortex solutions in which a three-laser array can be phase-locked. Linearization of the rate equation system around these vortex steady-states leads to new correlation spectra dependencies. An example of the noise correlation spectrum of the phase-locking in vortex with $|\eta| = 0.11$ and $\theta = -0.55\pi$ is shown in Fig. 6.19.

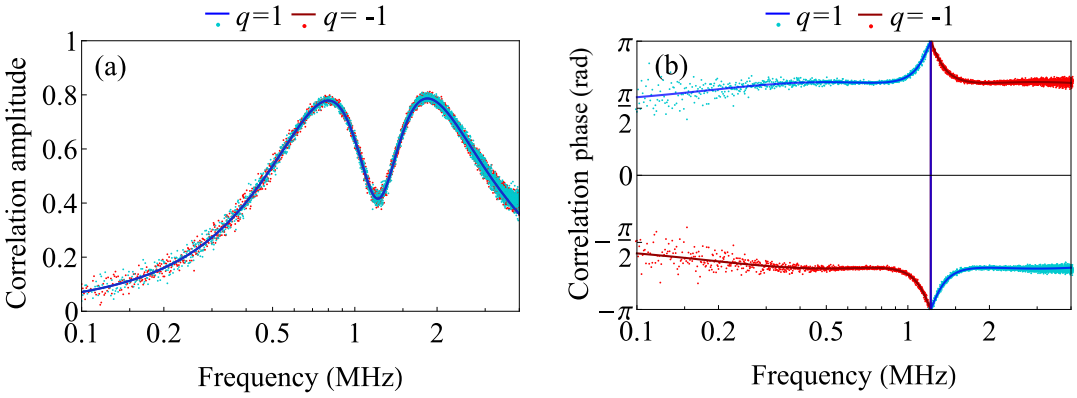

FIGURE 6.19: Cross-correlation amplitude and phase spectra $CC(\delta I_2, \delta I_1)$ for the phase-locking in a vortex in anti-vortex. Red color corresponds to the vortex $q = 1$ and blue data corresponds to the antivortex. Numerically calculated values are shown as dots and analytically obtained curves are shown in solid lines.

The correlation spectra in this case differs significantly from the in-phase solution. Based on the calculations the correlation coefficients are always complex. This means that the noises are delayed from one to the other. At first, we can see, that based on the numerical and analytical model, the delay is either positive or negative. The noise of the first laser is delayed positively from the second laser for the vortex solution and negatively for the anti-vortex. This occurs within the laser bandwidth, i.e. at frequencies less than the VECSEL cavity cut-off frequency ($\sim 500\,\text{kHz}$).

This situation (shown in Figs. 6.19) reminds us of the investigation of the orbit solution in the chapter 3 (see Fig. 3.15 and Fig. 3.16). In that orbit solution, some delay between the intensity oscillations was observed. As was mentioned, such delayed dynamics can be used to investigate the sign of the vortex charge. It is very complicated to investigate such an orbit solution experimentally. On the contrary, the noise measurements are easier to implement and it happens, that they provide the

same information. In this case, we can identify the sign of the vortex by the noise measurement, such as was done for the in-phase solution characterization.

We can also see, that close to the cavity cut-off frequency we have an intense increase in the correlation amplitude localized in two bands. We can see that the correlation phase experienced a π shift after passing $f \sim 650\,\text{kHz}$. Thus two correlation bands in the amplitudes have orthogonal phases. Such dependencies must be validated experimentally. The origin of the occurred bands requires further investigation. Unfortunately, the experimental measurement for this case faced some difficulties. This study goes beyond the scope of this manuscript. The current experimental state of this study is given in the Perspectives section of chapter 8.

6.7 Conclusions to chapter 6

In this chapter, we have conducted both theoretical and experimental investigations into the phase-locking and noise characteristics of an array of lasers utilizing a degenerate cavity VECSEL operating as a class-A laser. Both measurements and theory demonstrate that the magnitude of correlation strongly depends on the phase-locking.

Additionally, we noticed that the amplitude of the correlations increases with an increase of the Henry factor if the imaginary part of the coupling coefficient is negative $\text{Im}[\eta] < 0$. There is no dependency if $\theta = 0$ and the coupling is real. The correlation amplitude decreases if $\text{Im}[\eta] > 0$.

The physical explanation behind this α-dependence of the correlation amplitude when η is complex lies in the fact that a complex coupling coefficient breaks the system symmetry, while the α factor enhances any system asymmetry. The same kind of phenomenon can be shown to occur if there is an unbalance between some parameters of the investigated lasers, such for example the pump fluctuations δr_i.

The model and analytical approach we have developed offer a versatile framework that can be readily applied to arrays of lasers in higher dimensions and with varying mask topologies. All of the dependencies obtained for two laser arrays are reproduced in the three laser arrays.

We also started an investigation of the noise in the three laser array phase-locked in the vortex configuration. It was noticed, that the sign of the cross-correlation phase of the laser array noises provides information about the sign of the vortex.

CHAPTER 7

Optical computation with phase-locked laser arrays

Contents

One of the interests of coupled laser arrays is their possible application for optical computations. This chapter presents the modeling results of potential laser array applications in this domain. We can call a laser array a network if lasers are coupled. In this case, the coupling channels are used for information exchange. Different network topologies, i.e. topology of the mask, are used to solve different problems. Examples of the network topologies used for computer network classification are given in Fig. 7.1.

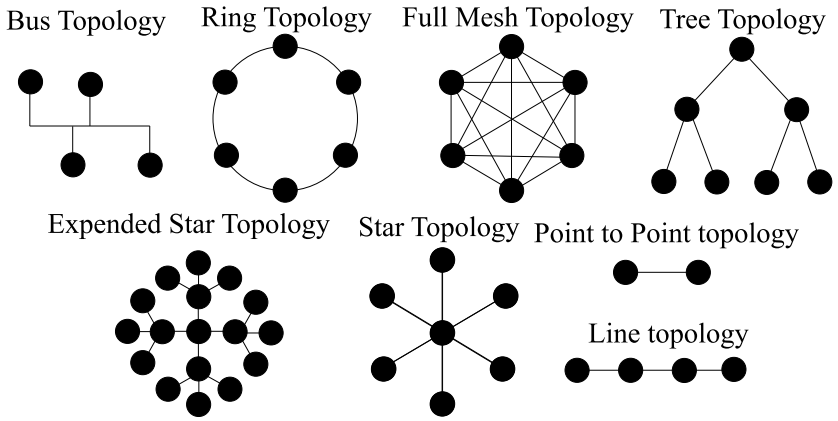

FIGURE 7.1: Examples of the network topologies by IPCisco. Network Certifications of Top Network Vendors - Cisco, Juniper, Nokia (Alcatel-Lucent), and Huawei.

The most general case is given by the full mesh topology, where each node of the network is coupled to every other node. This case represents the parallel computing architecture, known as the Ising model. This model has been widely investigated, including its all-optical implementation. The particular cases of a mesh topology are also used for laser solvers ([Tradonsky 2019; Pal 2020], LightSolver). A laser solver is a laser network aiming at solving optimization problems. The problem, i.e. input data, is introduced to the laser array through the loss or phase profile (for example with SLM). Then the lasers phase-lock in the global steady-state. The result readout is obtained by measuring the output far-field pattern.

Today, we are unable to investigate the full mesh in our experiment. We can implement point-to-point, ring, and star coupling topologies experimentally, as shown in Fig. 7.2.

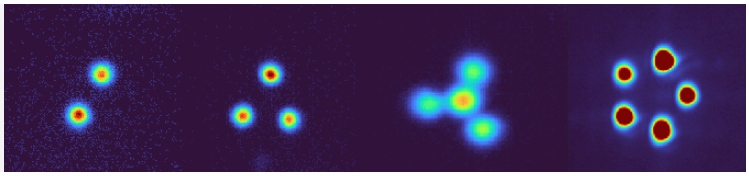

FIGURE 7.2: VECSEL laser arrays available in our experiment.

The point-to-point coupling topology is supported by two lasers, and ring topology can be implemented with three and five lasers, while the star one is given by four lasers, where one laser is created in the center of the ring array of three lasers.

Usually, the full mesh can not be implemented in the optical system without optical feedback. Nevertheless, each of the already existing arrays can solve some math problems when phase-locked. Thus, in this chapter, we investigate the properties of the VECSEL array as an optical data processor.

7.1 Optical computations with VECSEL arrays

The input data can be injected into the laser array solver by the pump modulations. Each laser will obtain a different logical sequence. For example, this can be done with a beam-shaped optical pump. The concept of such an optical pump is shown in Fig. 7.3.

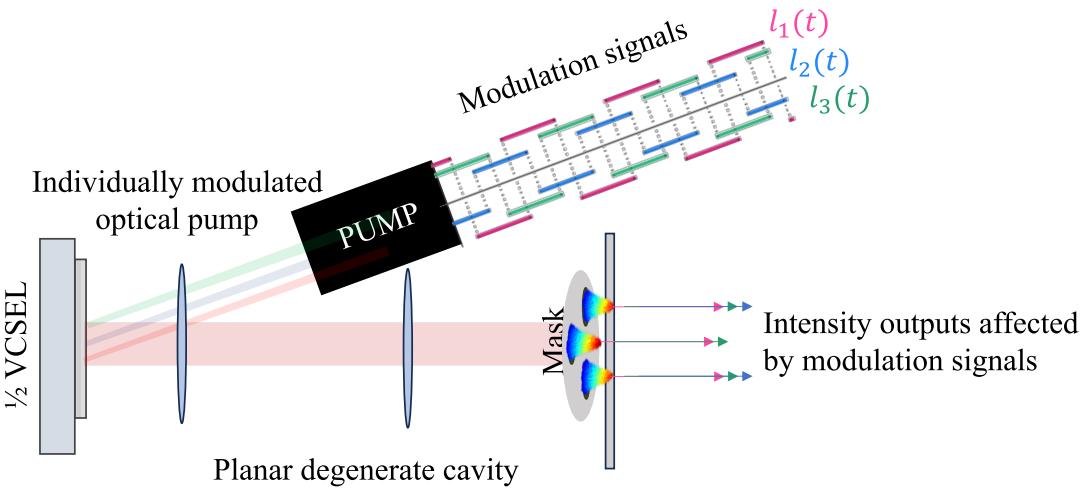

FIGURE 7.3: The concept of the different modulation signal injection to the VECSEL array through the beam-shaped pump.

Each laser in the array will be pumped above the threshold, but additionally receive a logical sequence with the pump modulation. The local modulation, i.e. for a single laser, can be introduced for example by the method described in [Bartolo González 2022]: the main pumping beam provides an exaltation for the lasing threshold and the hot-spot activation beams can be modulated by choppers.

Thanks to the coupling channels provided by the diffraction of the mask, each laser output will have an output intensity that should be modified by the logical signals mixed with a neighboring laser pump. This phenomenon is studied below with an example of two lasers and a ring laser array of three lasers.

7.1.1 Boolean math in point-to-point VECSEL network

The dynamics of the two laser arrays is governed by the following rate equations:

$$\begin{aligned}
\frac{dA_1}{dt} &= -\frac{A_1}{2\tau}\left(1-\frac{r+l_1(t)}{1+A_1^2/F_{\text{sat}}}\right)+\frac{|\eta|}{2\tau}\cos(\psi+\theta)A_2\,,\\
\frac{dA_2}{dt} &= -\frac{A_2}{2\tau}\left(1-\frac{r+l_2(t)}{1+A_2^2/F_{\text{sat}}}\right)+\frac{|\eta|}{2\tau}\cos(\psi-\theta)A_1\,,\\
\frac{d\psi}{dt} &= \frac{\alpha}{2\tau}\left(\frac{r+l_2(t)}{1+A_2^2/F_{\text{sat}}}-\frac{r+l_1(t)}{1+A_1^2/F_{\text{sat}}}\right)\\
&\quad -\frac{|\eta|}{2\tau}\left(\frac{A_2}{A_1}\sin(\psi+\theta)+\frac{A_1}{A_2}\sin(\psi-\theta)\right)+\Omega\,,
\end{aligned} \tag{7.1}$$

where A_1 and A_2 are the amplitudes of the two laser fields, normalized in such a way that their squares correspond to the respective photon numbers. The third variable ψ is the phase difference between the lasers, F_{sat} the saturation photon number. Here we inject two independent logical sequences $l_1(t)$, $l_2(t)$. Examples of the signals, such as two square signals are presented in Fig. 7.4.

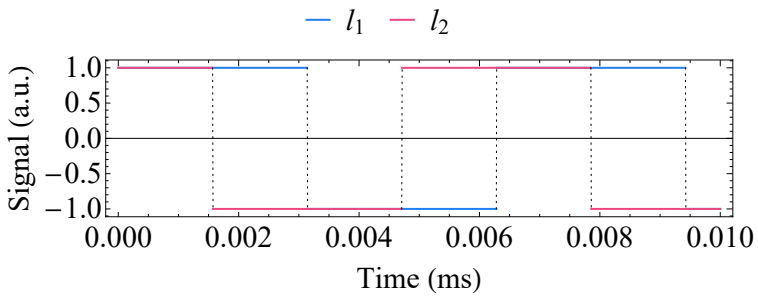

FIGURE 7.4: Examples of the logical sequences injected to lasers through the pumping rates. The amplitudes of the signals are normalized to one.

Applied signals can have any amplitude levels, but allowing for the laser to operate over the threshold, i.e. their amplitudes must be less than $(r-1)$. Each classical logical signal in the information theory operates by two states "1" and "0". In our case "1" corresponds to the l_i amplitude 1 and "0" with amplitude -1 in Fig. 7.4.

We investigate the time, when we can observe combinations of the l_1 and l_2 having different states, such as "1"+"1", "1"+"0", "0"+"1" and "0"+"0".

Let us investigate the output of the laser array in three cases: when the laser array is unlocked, almost phase-locked, and phase-locked. Detuning between lasers is $\Omega/2\pi = 200$ kHz, Henry factor $\alpha = 6$, excitation ratio $r = 1.1$ and photon lifetime in the cavity $\tau_{\text{cav}} = 30$ ns. The modulation frequency of the applied signals is $f = 100$ kHz, their amplitudes are equal to $r/1000$. The laser amplitudes at the output are presented in Fig. 7.5 for three different values of real coupling strength.

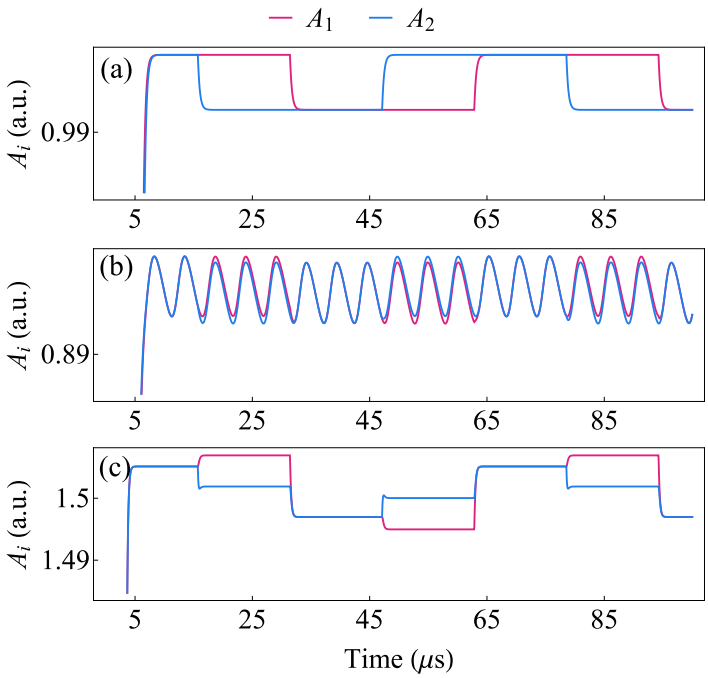

FIGURE 7.5: Examples of the logical sequences injected to lasers through the pumping rates. The amplitudes of the signals are normalized. Subplot (a) illustrates an unlocked case when $|\eta| = 0$. Subplot (b) shows the beating between lasers occurred with small coupling $|\eta| = 0.01$. The phase-locked case is given in subplot (c) for $|\eta| = 0.11$.

The amplitudes repeat injected signals in the unlocked case as expected when the coupling is zero. This case is illustrated in subplot (a) of Fig. 7.5. When the coupling increases, we observe oscillations in subplot (b). These signals are typical when the coupling does not overcome detuning. This makes the output useless for the interpretation without referring to its Fourier spectra. Finally, the third case illustrates the existence of four different amplitude levels for each laser. These levels are given by a combination of the injected signals I_1, I_2 depending on the laser system parameters. Due to this dependency, we believe we can use the system for optical computations.

7.1.2 Optical level interpretation

First, we present an example of how the phase-locking of two lasers can be useful for Boolean data processing.

Boolean algebra operates by the True and False variables, usually denoted as "1" and "0", on the contrary to the elementary algebra where the values are numbers. In classical computers, the values of "0" and "1" are associated with "LOW" and "HIGH" voltage states. Typically "0" is below 30% and "1" is above 70% of a maximal digital voltage level for a given data transfer protocol in a nowadays microcontrollers (standard values of the voltage could be 5V, 3.3V, 1.8V, and more).

However, there is not a general method of laser intensity interpretation. We can introduce an optical reference level specific to our system. By this level, we mean a virtual threshold between the True "1" and False "0" states.

For example Fig. 7.6 (a) shows the amplitudes of the phase-locked solution with $|\eta| = 0.109$ and the chosen optical reference level.

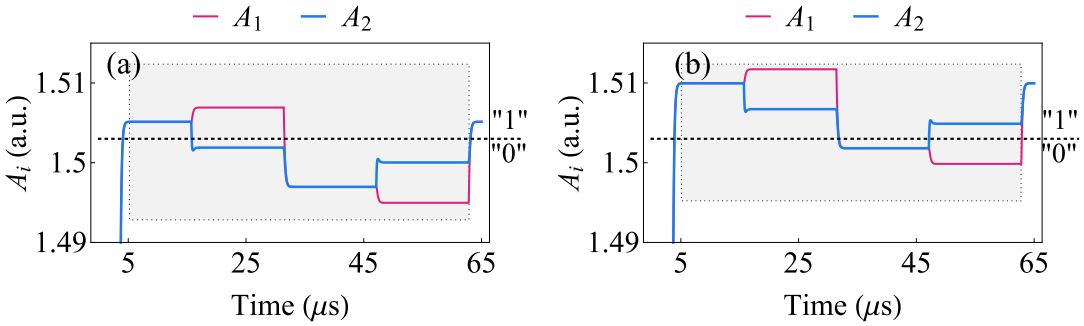

FIGURE 7.6: Amplitudes of the two phase-locked lasers with different coupling strengths (a) $|\eta| = 0.109$ and (b) $|\eta = 0.11|$. And the amplitude levels interpretation with respect to the reference level.

Subplot (b) shows the same optical reference level, but the amplitudes are obtained with stronger coupling $|\eta| = 0.11$.

Let us study only the output of the second laser A_2 shown by the thick blue color within the grey window. This window illustrates the time, when all combinations of the input l_1, l_2 signals ("11","10","01","00") can be observed. Subplot (a) gives the output interpreted as "1000", while subplot (b) gives "1101" within the period from 5 µs to 60 µs. These results are summarized in Table 7.1.

l_1	l_2	A_2 with $\|\eta\| = 0.109$	A_2 with $\|\eta\| = 0.11$
1	1	1	1
1	0	0	1
0	0	0	0
0	1	0	1
		Boolean AND	Boolean OR

TABLE 7.1: Interpretation of the amplitude levels shown in Fig. 7.6 by Boolean variables.

As we can see, the output of the one laser A_2 at different coupling strengths can be used to perform the AND and OR operation among the input signals l_1 and l_2. The coupling strength variation is simply performed by the mask positioning.

This is a naive example of one of the wide range of applications. The transformation of the input l_i signals by the phase-locked lasers is a non-linear function. It depends on the Henry factor α, coupling strength η, excitation ratio r, and saturation number of photons F_{sat}.

However, we can estimate the output with a simplified formula. We separate amplitudes A_i for its constant $A_{1,DC}$ and variable $A_{i,AC}$ components. The constant component of amplitude at the steady-state A_{DC} is obtained earlier in chapter 2 and equal $A_{DC} = \sqrt{\frac{r}{1-|\eta|\cos\psi}} - 1$. The variable component $A_{i,AC}$ is given by eq. (7.2) for real positive coupling.

$$A_{i,AC} = c_0 \left(c_1 l_i + \frac{\alpha}{2}(c_2 l_i + c_3 l_j) \right) \tag{7.2}$$

Coefficients c_0, c_1, c_2, c_3 have a complicated dependency on the laser array parameters. In case detuning is zero ($\Omega = 0$) the coefficients c_2 and c_3 are equal and correspond to 1. If not, the coefficient changes anti-proportionally to each other. Coefficients c_0, c_1 depend mostly on the coupling strength. Examples of results given by eq. (7.2) are shown in Fig. 7.7.

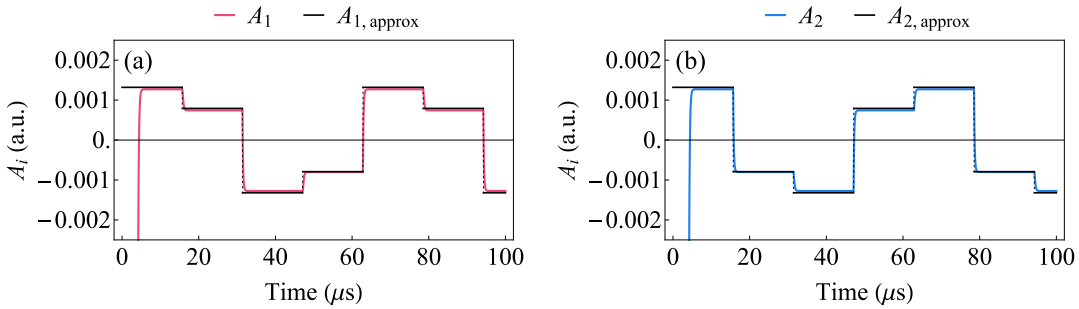

FIGURE 7.7: Approximation of the variable component of the laser amplitudes. Here $\alpha = 6$, $\eta = 0.11$, $\Omega = 0$. Coefficients of the approximation are $c_0 = 0.08$, $c_1 = 8$, $c_2 = c_3 = 1$.

The approximation with eq. (7.2) gives a good agreement with numerical modeling. However, the exact formula covering dependency on the detuning, coupling strength, pumping rate, etc. values is undetermined.

7.2 Optical computations in the ring VECSEL array

We investigate the output properties with the simplest case of three lasers. The logical signals injected into the laser array l_1, l_2, l_3 are shown in Fig. 7.8. The signals are normalized in different ranges for visualization. Here l_1 is normalized in the range from -1 to 1, l_2 has an amplitude of 0.75, and l_3 has an amplitude of 0.5. We also add a phase-shift to the l_2 and l_3 given respectively by $\pi/3$ and $2\pi/3$.

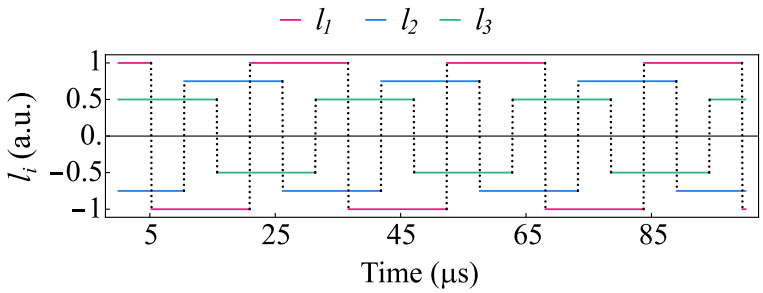

FIGURE 7.8: Amplitudes of the input logical signals. The modulations have different amplitudes and a phase delay for a quarter of the signal period. The modulation frequency is $f = 100$ kHz.

If such modulation l_i is injected into the ring laser array each laser then obeys eqs. (7.3).

$$\begin{aligned}
\frac{dA_i}{dt} &= -\frac{1}{2\tau}\left(1-\frac{r+l_i}{1+A_i^2/F_{\text{sat}}}\right)A_i + \frac{|\eta|}{2\tau}\left[\cos(\psi_i+\theta)A_{i+1}+\cos(-\psi_{i-1}+\theta)A_{i-1}\right] \\
\frac{d\psi_i}{dt} &= \frac{\alpha}{2\tau}\left(\frac{r+l_{i+1}}{1+A_{i+1}^2/F_{\text{sat}}}-\frac{r+l_i}{1+A_i^2/F_{\text{sat}}}\right)+\frac{|\eta|}{2\tau}\left(\frac{A_{i+2}}{A_{i+1}}\sin(\psi_{i+1}+\theta)-\right. \\
&\left.-\frac{A_i}{A_{i+1}}\sin(\psi_i-\theta)-\frac{A_{i+1}}{A_i}\sin(\psi_i+\theta)+\frac{A_{i-1}}{A_i}\sin(\psi_{i-1}-\theta)\right)+\Omega_i. \qquad (7.3)
\end{aligned}$$

We know that the cavity transfer function has a cavity cut-off of around 480 MHz. The frequency of the modulation is chosen equal to $f = 500$ kHz to illustrate as well the cut-off influence. The output amplitudes in the case $|\eta| = 0.04$, $\alpha = 6$ are shown in Fig. 7.9 (a) for equal amplitude logical signals and (b) for the amplitudes with a ratio 1/0.75/0.5 of the l_1, l_2, l_3 amplitudes.

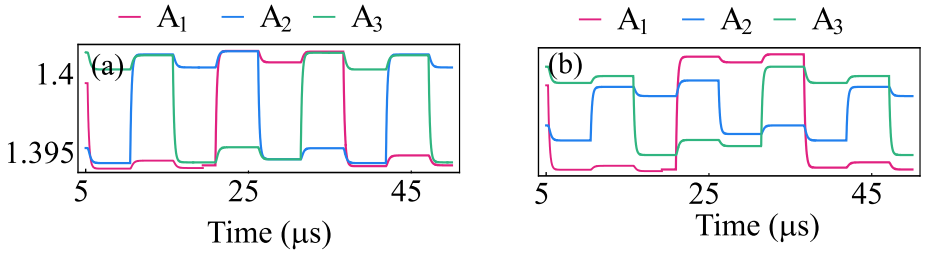

FIGURE 7.9: Amplitudes at the output. (a) Injected logical signals have the same amplitudes of $r/1000$. Subplot (b) illustrates the impact of the different l_i amplitudes. Here $|\eta| = 0.02$

The laser array is phase-locked during the time between the logical signal fronts. We can see that the output signals do not reproduce injection signals. This is easier to notice in subplot (b), where the amplitudes of the injected logical sequences have a ratio of 1/0.75/0.5. The output is a linear combination of the applied signals. The

formula is estimated in the same way as with two lasers:

$$A_{i,AC} = c_0 \left(c_1 I_i + \frac{\alpha}{2} (c_2 I_i - c_3 I_{i+1} - c_4 I_{i-1}) \right). \tag{7.4}$$

The estimation sequences superimposed with the first laser amplitude ($i = 1$) are given in Fig. 7.10

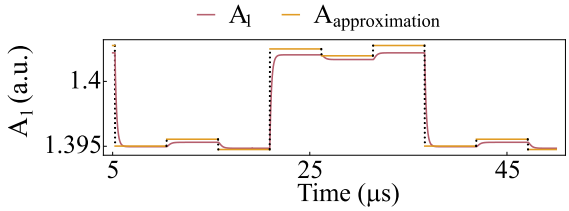

FIGURE 7.10: Amplitudes at the output of the first laser from the phase-locked array of three lasers and its approximation with eq. 7.4. The coefficients of the approximation are $c_0 = 4, c_1 = -0.02$, $c_2 = 1$, $c_3 = c_4 = 1$.

The formula also gives a fine approximation. One can notice, that the level interpretation, i.e. is it True "1" or False "0" levels, can be difficult. At the same time, thanks to Henry factor dependency, we can choose the proper difference between amplitude levels. The amplitude outputs of the three lasers calculated numerically with different α values are shown in Fig. 7.11.

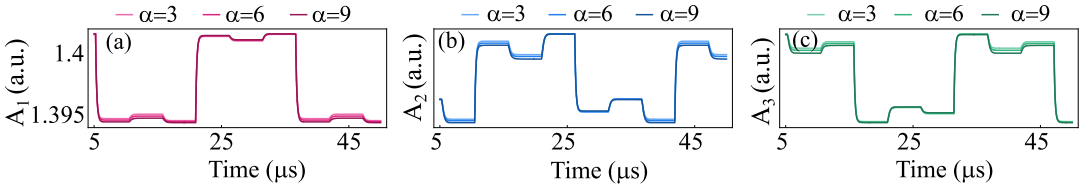

FIGURE 7.11: Amplitudes at the output of the first (a), the second (b), and the third (c) with different values of the Henry factor.

By this, we conclude that the choice of the Henry factor can be used to improve the contrast between levels.

7.2.1 Conclusions to chapter 7

Phase-locking of the VECSEL laser array creates a powerful method of optical data processing. Here we presented a potential application of the laser array phase-locking for two different Boolean operations, where the choice of the operation is based on the coupling strength control. Indeed, by changing the distance between the loss mask and OC, we can perform AND and OR operations by measuring the output of one of the lasers. At the same time, the output of the second laser can be used in parallel for the other operation.

We partially obtained an analytical approximation of the injected signal processing in the phase-locked VECSEL array. Even though the approximation is linear, it was obtained for the implied case for zero detuning. The exact formula for the general case is undetermined yet.

CHAPTER 8

Conclusions and perspectives

8.1 Conclusions

The results presented in this thesis address fundamental and practical aspects of VECSEL array studies. A significant part of this work focused on the dynamics of laser arrays, investigating phase-locking regularities, and developing a general model for the investigated array topologies.

For the first time, we introduced several important analytical dependencies. The first one gives a critical coupling value for phase-locking between two lasers with a complex coupling coefficient. Phase-locking requires a coupling strength modulus exceeding a critical coupling value. The formula for this value, as well as the dependency of steady-state amplitude and phase difference on it, is provided in the conclusions of chapter 2.

Using a generalized model for a ring laser array, we examined its steady-state solutions. We highlighted that the probability of obtaining a vortex solution in class-A VECSEL arrays is higher compared to class-B lasers. Another analytical result presented for the first time is the dependency of steady-state amplitudes and phase differences of the ring array on the complex coupling value. These formulas are presented in conclusions of chapter 3. We also showed theoretically the method of asymmetric vortex creation.

Overall, the manuscript primarily investigates the influence of the Henry factor on phase-locking. We demonstrated that it enhances the variation in phase-differences, when the laser array is in the process of stabilization. This leads to longer synchronization times for the laser array with larger Henry factors. Our third important analytical relation describes the dependency of the limiting Henry factor on the argument of the complex coupling and topological charge. Different topological charges are shown to have different limiting Henry factor values. This can be used as a sorting method for the laser array phase-locked solution. It was presented that the

Henry factor's natural tendency to increase asymmetry in the laser system. Different pumping rates, photon lifetimes, and detunings are standard parameters causing this asymmetry. The impact of asymmetry enhancement was further demonstrated through noise studies and logical signal operations. The correlation of noise was shown to be increased with a higher Henry factor when phase-locking is close to being out-of-phase. As a rule of thumb, this dependency can be conceptualized as the dependency of the amplitude of the cross-correlation on the term proportional to the Henry factor multiplying the difference of the injected noises $\sim \alpha(\delta r_1 - \delta r_2)$. Similar relations were derived in chapter 7 for the optical sum of a logical sequence. In the same chapter 7 we also showed an example of the VECSEL array applications to build an optical boolean computer.

Most importantly we experimentally developed laser arrays with a few lasers and confirmed some of the predicted analytical relations. Based on the VECSEL RIN spectra we obtained a class-A laser array. We proved its cavity degeneracy in several ways in chapter 5. Furthermore, we investigated the phase-locking of the obtained laser arrays and studied their noise to validate both the numerical and analytical models.

However, there remain important cases that have not yet been studied experimentally. Numerically we showed that the optical feedback can be realised to control phase-locking solution. More specifically, the vortex can be supported by the vorticity created between two neighboring lasers, when the fraction of the one is injected to the second one. The experimental validation was not yet implemented.

The manuscript highlighted a problem with recognizing vortex charge when far-fields are indistinguishable (for example, see chapter 3, the case for 10 lasers in Fig. 3.4). We presented two possible solutions to this problem. Both methods rely on measuring the intensities of VECSELs in the near-field. One method involves observing the orbit solution discussed in chapter 3. The second one is simpler and requires measuring the noise correlations of the lasers. These experiments are intriguing challenges for future research.

8.2 Perspectives

The presented work faced some experimental difficulties. The obtained laser array is too small to investigate the whole spectrum of the theoretically predicted phenomena. This problem requires an update of the gain chip. The chips with higher gain and less thermal lens effect are extremely valued for our experiment.

Additionally, an update of the systems in terms of intracavity magnification can be beneficial for the quality of the array. For example, laser magnification would reduce the role of the defects of the mask, and would be allowed to get more lasers.

Noise measurement of the vortex steady-state

The noise measurement of the lasers phase-locked in a vortex is fascinating for noise studies. As was presented in chapter 6 such measurements give information about the sign of the vortex based on the noise spectra cross-correlation phase.

Unfortunately, the first experimental measurements of this case faced some difficulties. Only in the three and four laser arrays, we can choose vortex solutions in the experiment by the choice of coupling argument θ[1]. Such θ must provide Re[η]<0 and Im[η]<0. I.e. we need θ to be in the range from $\pi/2$ to $-\pi$. These values correspond to the diffraction coupling distance z either close to 300-400 µm or in the wide range starting from 600 µm. In the experiment with three lasers small distances do not provide enough coupling strength to observe a phase-locked array. Additionally, θ varies too fast with z. On the contrary, the coupling is enough, but the losses at $z > 600$ µm are too big to observe stable phase-locking. Due to this, we changed the gain chip GAS864 for VO860C.

Indeed, we obtained the far-field (FF) patterns proving as the coexistence of two vortices with $q = -1$ and $q = 1$. Such phase-locking is very unstable. We managed to extract two of the most contrasting FF patterns shown in the second row of Fig. 8.1.

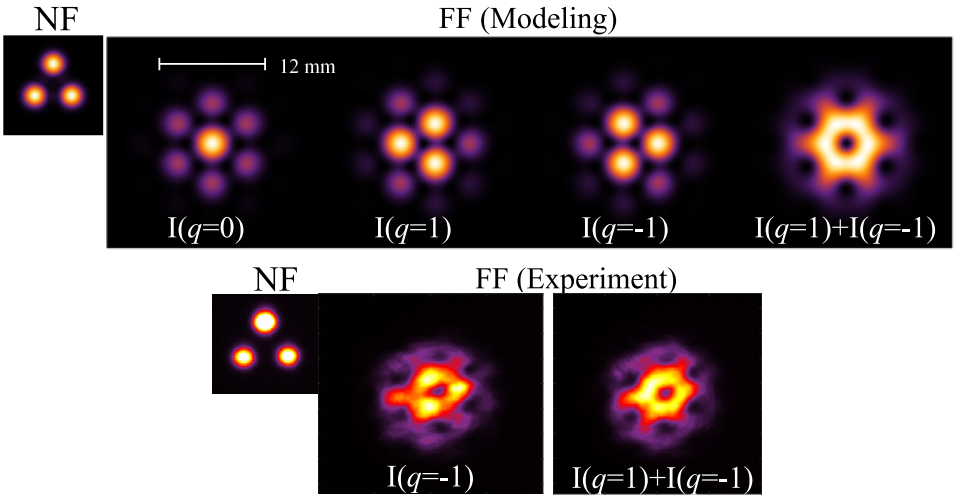

FIGURE 8.1: Modeling of the far-fields of the laser array phase-locked with different phase-differences.

To interpret the experimentally obtained far-field patterns we did a modeling of the FF with different topological charges and the case when OV ($q = 1$) and AV ($q = -1$) coexist. The modeling patterns are shown in the first row of Fig. 8.1. The FF are similar thus, we are glad to state that we observed vortex solutions in our

[1]The in-phase and vortex solutions are separable by the coupling choice only for $n \leq 4$. An increase in the number of lasers makes the system multistable for any coupling value. In the negative coupling range, the phase-locking with the highest topological charge becomes beneficial. On the positive the in-phase is beneficial.

system. At the same time, the phase-locking is highly unstable and thus it requires additional study with a careful OF control.

Alternatively, we can study the vortex with $|q| = 2$ case with four lasers. The vortex and anti-vortex have identical phase-difference distributions and same far-fields. Thus, the phase-locking would be stable and no phase-locking solutions method is needed. At the same time, negative coupling leads to the phase-locking with the highest possible topological charge. The topological charge will be equal to two ($|q| = 2$) for four negatively phase-locked lasers. Then the phase-differences are $\psi_q = 2\pi q/4$ equal to $\pm\pi$. This fact was studied and detected in numerous works with solid-state lasers.

Indeed we obtained the corresponding phase-locking in the updated setup shown in Fig. 8.2.

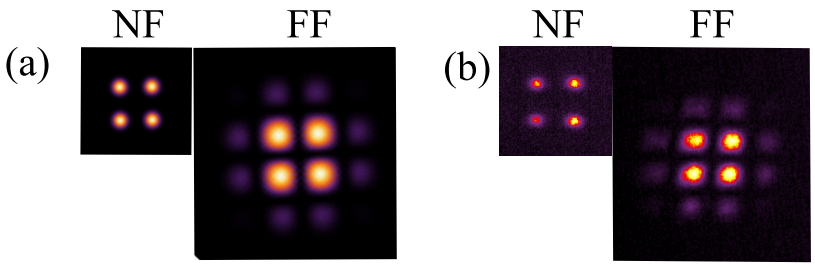

FIGURE 8.2: Near field and far field patterns of the four lasers phase-locking with TC $q = \pm 2$. (a) is modeling and (b) is experimental data.

The neighboring lasers are phase-locked out of phase in this case. This leads to an in-phase locking of the two lasers along the diagonal of the square. The noise study of this case hasn't been performed yet and the experimental noise measurements of this case are beyond the scope of the manuscript.

Phase-locking of such a square laser array was shown to be useful as an optical solver. The Hamiltonian of such solid-state laser array was shown possible to map to the XY Hamiltonian [Pal 2020; Gershenzon 2020]. The mapping can be performed by assuming that each of the π or 0 phase-difference is associated with a spin orientation of the array element. Such systems are useful for the optimization problem-solving including NP-hard problem class and modeling of the other XY-Hamiltonian systems.

CHAPTER A

Analytical formula for spectral cross-correlations

A.1 Analytical model of the noise

In this chapter, we provide additional details of the derivation of the analytical formula for the cross-correlation.

In chapter 6 we introduced a vector $\mathbf{S}$ whose three components are given by the right part of the three rate equations of by eqs. 6.8. We did this to obtain an analytical model for the laser intensity fluctuation and its correlation spectra.

The fluctuations of the lasers can be obtained by linearizing the vector components around the steady state solution given by vector $\{A_{1,\mathrm{st}}, A_{2,\mathrm{st}}, \psi_{\mathrm{st}}\}$. Following [De 2013a], the three variables are written in vector form as $\mathbf{A} = \{A_{1,\mathrm{st}}, A_{2,\mathrm{st}}, \psi_{\mathrm{st}}\} + \delta\mathbf{A}$, where the vector $\delta\mathbf{A} = \{\delta A_1, \delta A_2, \delta\psi\}$ contains the fluctuations around the steady-state values $\{A_{1,\mathrm{st}}, A_{2,\mathrm{st}}, \psi_{\mathrm{st}}\}$. The pump fluctuations around the average values $\mathbf{r} = \{r, r\}$ are written as a vector $\delta\mathbf{r} = \{\delta r_1, \delta r_2\}$.

Then eqs. (6.8) can be formally written as:

$$\dot{\mathbf{A}}(t) = \mathbf{S}(\mathbf{A}, \mathbf{r})(t) = \mathbf{S}(\mathbf{A}_{\mathrm{st}} + \delta\mathbf{A}, \mathbf{r} + \delta\mathbf{r}). \tag{A.1}$$

Linearization consists of expanding the right-hand side up to the first order in $\delta\mathbf{r}$ and $\delta\mathbf{A}$, leading to:

$$\dot{\delta\mathbf{A}}(t) = \underbrace{RS(\mathbf{r}, \mathbf{A}_{\mathrm{st}})}_{=0} + \frac{\partial\mathbf{S}(\mathbf{r}, \mathbf{A})}{\partial\mathbf{A}}|_{r,A_{\mathrm{st}}}\delta\mathbf{A} + \frac{\partial\mathbf{S}(\mathbf{r}, \mathbf{A})}{\partial\mathbf{r}}|_{r,A_{\mathrm{st}}}\delta\mathbf{r}\ . \tag{A.2}$$

Here, the partial derivative of a vector $\mathbf{S}$ over vector $\mathbf{A}$ stands for a matrix with elements $\left[\frac{\partial\mathbf{S}}{\partial\mathbf{A}}\right]_{ij} = \frac{\partial\mathbf{S}_i}{\partial\mathbf{A}_j}$ and over vector $\mathbf{r}$ it is $\left[\frac{\partial\mathbf{S}}{\partial\mathbf{r}}\right]_{ij} = \frac{\partial\mathbf{S}_i}{\partial\mathbf{r}_j}$.

Taking the Fourier transform of eq. (A.2) leads to the following algebraic expression:

$$\int_{-\infty}^{+\infty} \dot{\delta\mathbf{A}}(t)\exp^{-i\omega t}\,\mathrm{d}t = \int_{-\infty}^{+\infty}\left(\frac{\partial \mathbf{S}(\mathbf{r},\mathbf{A})}{\partial \mathbf{A}}|_{r_0,A_{st}}\delta\mathbf{A} + \frac{\partial \mathbf{S}(\mathbf{r},\mathbf{A})}{\partial \mathbf{r}}|_{r_0,A_{st}}\delta\mathbf{r}\right)\exp^{-i\omega t}\,\mathrm{d}t,$$

$$i\omega\widetilde{\delta\mathbf{A}}(\omega) = \frac{\partial \mathbf{S}(\mathbf{r},\mathbf{A})}{\partial \mathbf{A}}|_{r_0,A_{st}}\int_{-\infty}^{+\infty}\delta\mathbf{A}\exp^{-i\omega t}\,\mathrm{d}t + \frac{\partial \mathbf{S}(\mathbf{r},\mathbf{A})}{\partial \mathbf{r}}|_{r_0,A_{st}}\int_{-\infty}^{+\infty}\delta\mathbf{r}\exp^{-i\omega t}\,\mathrm{d}t,$$

$$i\omega\widetilde{\delta\mathbf{A}}(\omega) = \frac{\partial \mathbf{S}(\mathbf{r},\mathbf{A})}{\partial \mathbf{A}}|_{r_0,A_{st}}\widetilde{\delta\mathbf{A}}(\omega) + \frac{\partial \mathbf{S}(\mathbf{r},\mathbf{A})}{\partial \mathbf{r}}|_{r_0,A_{st}}\widetilde{\delta\mathbf{r}}(\omega). \tag{A.3}$$

Then the amplitude noise of the variables is defined according to the eq. A.5:

$$i\omega\widetilde{\delta\mathbf{A}}(\omega) = \frac{\partial \mathbf{S}(\mathbf{r},\mathbf{A})}{\partial \mathbf{A}}|_{r_0,A_{st}}\widetilde{\delta\mathbf{A}}(\omega) + \frac{\partial \mathbf{S}(\mathbf{r},\mathbf{A})}{\partial \mathbf{r}}|_{r_0,A_{st}}\widetilde{\delta\mathbf{r}}(\omega), \tag{A.4}$$

$$\widetilde{\delta\mathbf{A}}(\omega) = \begin{bmatrix}\widetilde{\delta A_1}(\omega)\\ \widetilde{\delta A_2}(\omega)\\ \widetilde{\delta\psi}(\omega)\end{bmatrix} = \left[i\omega - \frac{\partial \mathbf{S}(\mathbf{r},\mathbf{A})}{\partial \mathbf{A}}|_{r_0,A_{\mathrm{st}}}\right]^{-1}\frac{\partial \mathbf{S}(\mathbf{r},\mathbf{A})}{\partial \mathbf{r}}|_{r_0,A_{\mathrm{st}}}\widetilde{\delta\mathbf{r}}(\omega). \tag{A.5}$$

where the tilde denotes the Fourier-transformed variables. Let us focus on amplitude fluctuation, specifically intensity fluctuations, which can be measured experimentally. The intensity fluctuations $\delta I(t)$ of one laser are then obtained from the amplitude fluctuations. The intensity is defined as a square modulus of the field or

$$I(t) = |A_{st}|^2 + A_{st}(\delta A(t)^* + \delta A(t)) + \underbrace{|\delta A(t)|^2}_{\text{small}}.$$

On the other hand, intensity is given by its steady-state value and fluctuation part $I(t) = I_{st} + \delta I(t)$ then $\delta I(t) = |A(t)|^2 + A_{st}[\delta A(t)^* + \delta A(t)]$ which is given by $\widetilde{\delta I(\omega)} = A_{st}[\widetilde{\delta A(-\omega)}^* + \widetilde{\delta A(\omega)}] = 2A_{st}\widetilde{\delta A(\omega)}$ in the frequency domain. Here "*" stands for complex conjugation.

Finally, the intensity fluctuations in the frequency domain are given by the eq. A.6.

$$\widetilde{\delta\mathbf{I}}(\omega) = \begin{bmatrix}\widetilde{\delta I_1}(\omega)\\ \widetilde{\delta I_2}(\omega)\end{bmatrix} = 2\mathbf{A}_{\mathrm{st}}\left[i\omega - \frac{\partial \mathbf{S}(\mathbf{r},\mathbf{A})}{\partial \mathbf{A}}|_{r_0,A_{\mathrm{st}}}\right]^{-1}\frac{\partial \mathbf{S}(\mathbf{r},\mathbf{A})}{\partial \mathbf{r}}|_{r_0,A_{\mathrm{st}}}\widetilde{\delta\mathbf{r}}(\omega)\ , \tag{A.6}$$

With this formula, one can deduce the RIN spectra of the two lasers and the cross-correlation spectrum between their amplitude fluctuations, is then defined in the following way:

$$\mathrm{CC}(\widetilde{\delta\mathbf{I}}_1, \widetilde{\delta\mathbf{I}}_2) = \frac{\mathrm{Cov}(\widetilde{\delta A_1}, \widetilde{\delta A_2})}{\sqrt{\mathrm{Var}(\widetilde{\delta A_1})\mathrm{Var}(\widetilde{\delta A_2})}}\ , \tag{A.7}$$

in which Var holds for the variance and Cov for the covariance.

Cross-correlation spectrum dependency on the pump correlation

The formula A.7 can be presented through the vector elements directly. The amplitudes are defined as presented below, and can be represented as follows:

$$\begin{aligned}\widetilde{\delta\mathbf{I}}(\omega) =& 2\mathbf{A}_{st}\begin{bmatrix}\widetilde{\delta A_1}\\ \widetilde{\delta A_2}\end{bmatrix} = 2\mathbf{A}_{st}\begin{bmatrix}a_1 & a_2\\ b_1 & b_2\end{bmatrix}\widetilde{\delta\mathbf{r}}(\omega) = \\ &= 2\mathbf{A}_{st}\left[i\omega - \frac{\partial\mathbf{S}(\mathbf{r},\mathbf{A})}{\partial\mathbf{A}}|_{r_0,A_{st}}\right]^{-1}\frac{\partial\mathbf{S}(\mathbf{r},\mathbf{A})}{\partial\mathbf{r}}|_{r_0,A_{st}}\widetilde{\delta\mathbf{r}}(\omega),\end{aligned} \tag{A.8}$$

I.e. $\widetilde{\delta A_1(\omega)} = a_1\widetilde{\delta r_1(\omega)} + a_2\widetilde{\delta r_2(\omega)}$ and $\widetilde{\delta A_2} = b_1\widetilde{\delta r_1(\omega)} + b_2\widetilde{\delta r_2(\omega)}$.

The noise components of the pump are characterized by the same standard deviation σ and zero mean value, i.e.

$$Var(\delta r_1) = \sigma^2, \overline{\delta r_1} = 0 \text{ and } Var(\delta r_2) = \sigma^2, \overline{\delta r_2} = 0,$$

and in the general case, they can be correlated. We name the pump noise cross-correlation coefficient by $CC(\delta r_1, \delta r_2)$. The variances of the amplitude fluctuations and its covariance are:

$$\begin{aligned}Var(\delta A_1) &= Var(a_1\widetilde{\delta r_1} + a_2\widetilde{\delta r_2}) = |a_1|^2\sigma^2 + |a_2|^2\sigma^2 + 2Re[a_1a_2]CC(\delta r_1,\delta r_2)\sigma^2,\\ Var(\delta A_2) &= Var(b_1\widetilde{\delta r_1} + b_2\widetilde{\delta r_2} = |b_1|^2\sigma^2 + |b_2|^2\sigma^2 + 2Re[b_1b_2]CC(\delta r_1,\delta r_2)\sigma^2,\\ Cov(\delta A_1,\delta A_2) &= \overline{\delta A_1\delta A_2^*} - \underbrace{\overline{\delta A_1}\ \overline{\delta A_2}}_{=0} = a_1b_1^*\sigma^2 + a_2b_2^*\sigma^2 + (a_1b_2^* + a_2b_1^*)CC(\delta r_1,\delta r_2)\sigma^2.\end{aligned}$$

Then, the cross-correlation coefficient has the shape of eq. A.9:

$$CC(\widetilde{\delta I_1},\widetilde{\delta I_2}) = \frac{a_1b_1^* + a_2b_2^* + (a_1b_2^* + a_2b_1^*)p_{cc}}{\sqrt{|a_1|^2 + |a_2|^2 + 2Re[a_1a_2^*]CC(\delta r_1,\delta r_2)}\sqrt{|b_1|^2 + |b_2|^2 + 2Re[b_1b_2^*]p_{cc}}}. \tag{A.9}$$

If pump noises are not correlated, $CC(\delta r_1,\delta r_2) = 0$, the formula for the cross-coefficient is then

$$CC(\delta I_1,\delta I_2) = \frac{a_1b_1^* + a_2b_2^*}{\sqrt{(|a_1|^2 + |a_2|^2)(|b_1|^2 + |b_2|^2)}}. \tag{A.10}$$

A.1.1 Intensity correlations in three lasers array

The approach applied to the array of two lasers is general and we can follow the same procedure. In the case of the three-laser array, eq. (A.8) becomes:

$$\widetilde{\delta \mathbf{I}}(\omega) = 2\mathbf{A}_{st}\left[i\omega - \frac{\partial \mathbf{S}(\mathbf{r},\mathbf{A})}{\partial \mathbf{A}}|_{r_0,A_{st}}\right]^{-1}\frac{\partial \mathbf{S}(\mathbf{r},\mathbf{A})}{\partial \mathbf{r}}|_{r_0,A_{st}}\widetilde{\delta \mathbf{r}}(\omega) = 2\mathbf{A}_{st}\begin{bmatrix} a_1 & a_2 & a_3 \\ b_1 & b_2 & b_3 \\ c_1 & c_2 & c_3 \end{bmatrix}\widetilde{\delta \mathbf{r}}(\omega). \tag{A.11}$$

We consider only two lasers out of three-laser phase-locked arrays, as was done in the experiment. The noise components of the pump we consider uncorrelated. The choice of the lasers does not play any role in the in-phase solution, the case is symmetrical. Those lasers have intensity noises $\delta I_1, \delta I_2, I_3$. The eq. A.10 is then replaced by eq. A.13 for the correlation of the first laser with the second one and the second laser with the third one.

$$CC(\delta I_1, \delta I_2) = \frac{a_1 b_1^* + a_2 b_2^* + a_3 b_3^*}{\sqrt{(|a_1|^2 + |a_2|^2 + |a_3|^2)(|b_1|^2 + |b_2|^2 + |b_3|^2)}}, \tag{A.12}$$

$$CC(\delta I_2, \delta I_3) = \frac{b_1 c_1^* + b_2 c_2^* + b_3 c_3^*}{\sqrt{(|b_1|^2 + |b_2|^2 + |b_3|^2)(|c_1|^2 + |c_2|^2 + |c_3|^2)}}. \tag{A.13}$$

where $a_1, a_2, a_3, b_1, b_2, b_3, c_1, c_2, c_3$ -are the $\delta A_{1,2,3}$ coefficients at $\delta r_{1,2,3}$. The identical approach can be applied to any array with two neighbors.

Bibliography

[Alexoudi 2020] Theoni Alexoudi, George Kanellos, and Nikos Pleros. "Optical RAM and integrated optical memories: a survey". *Light: Science & Applications* 9 (Dec. 2020). DOI: 10.1038/s41377-020-0325-9 (cit. on p. 3).

[Alkhazraji 2023] Emad Alkhazraji et al. "Linewidth narrowing in self-injection-locked on-chip lasers". *Light: Science & Applications* 12.1 (June 2023), p. 162. DOI: 10.1038/s41377-023-01172-9 (cit. on p. 24).

[Allen 1992] L. Allen et al. "Orbital angular momentum of light and the transformation of Laguerre-Gaussian laser modes". *Physical Review A* 45 (11 June 1992), pp. 8185–8189. DOI: 10.1103/PhysRevA.45.8185 (cit. on p. 58).

[Ambrosio 2012] Antonio Ambrosio et al. "Light-induced spiral mass transport in azo-polymer films under vortex-beam illumination". *Nature Communications* 3.1 (Aug. 2012), p. 989. DOI: 10.1038/ncomms1996 (cit. on p. 74).

[Anderegg 2019] Loïc Anderegg et al. "An optical tweezer array of ultracold molecules". *Science* 365 (Sept. 2019), pp. 1156–1158. DOI: 10.1126/science.aax1265 (cit. on p. 3).

[Arecchi 1984] F.T. Arecchi et al. "Deterministic chaos in laser with injected signal". *Optics Communications* 51.5 (1984), pp. 308–314. DOI: 10.1016/0030-4018(84)90016-6 (cit. on p. 9).

[Arnaud 1969] J.A. Arnaud. "Degenerate optical cavities". *Applied Optics* 8.1 (1969), pp. 189–196 (cit. on pp. 3, 101).

[Arwas 2022] Geva Arwas et al. "Anyonic-parity-time symmetry in complex-coupled lasers". *Science Advances* 8.22 (2022), eabm7454. DOI: 10.1126/sciadv.abm7454. eprint: https://www.science.org/doi/pdf/10.1126/sciadv.abm7454 (cit. on p. 93).

[Baili 2007] G Baili et al. “Shot-noise-limited operation of a monomode high-cavity-finesse semiconductor laser for microwave photonics applications”. *Opt Lett* (2007) (cit. on pp. 9, 125).

[Baili 2008] Ghaya Baili et al. “Experimental Investigation and Analytical Modeling of Excess Intensity Noise in Semiconductor Class-A Lasers”. *J. Lightwave Technol.* 26.8 (Apr. 2008), pp. 952–961 (cit. on pp. 9, 125).

[Baili 2009] G. Baili et al. “Direct observation of the class-B to class-A transition in the dynamical behavior of a semiconductor laser”. *Europhysics Letters* 87.4 (Sept. 2009), p. 44005. DOI: 10.1209/0295-5075/87/44005 (cit. on pp. 29, 97, 125, 126).

[Baili 2014] Ghaya Baili et al. “Ultralow Noise and High-Power VECSEL for High Dynamic Range and Broadband RF/Optical Links”. *J. Lightwave Technol.* 32.20 (Oct. 2014), pp. 3489–3494 (cit. on p. 9).

[Barland 2002] Stephane Barland et al. “Cavity solitons as pixels in semiconductor microcavities”. *Nature* 419.6908 (Oct. 2002), pp. 699–702. DOI: 10.1038/nature01049 (cit. on p. 5).

[Bartolo González 2022] Adrián Alejandro Bartolo González. “Spatial organization of localized pulses in a self-imaging vertical external cavity surface emitting laser”. Thesis. Université Côte d’Azur, June 2022 (cit. on pp. 6, 113, 145).

[Bartolo 2022] A. Bartolo et al. “Temporal localized Turing patterns in mode-locked semiconductor lasers”. *Optica* 9.12 (Dec. 2022), pp. 1386–1393. DOI: 10.1364/OPTICA.471006 (cit. on pp. 6, 97, 99, 113).

[Bartolo 2023] A. Bartolo et al. “Spatiotemporally reconfigurable light in degenerate laser cavities”. *Photon. Res.* 11.10 (Oct. 2023), pp. 1751–1756. DOI: 10.1364/PRJ.495892 (cit. on pp. 6, 7).

[Basov 1966] N. Basov, O. Bogdankevitch, and A. Grasuk. “Semiconductor lasers with radiating mirrors”. *IEEE Journal of Quantum Electronics* 2.4 (1966), pp. 154–154. DOI: 10.1109/JQE.1966.1073948 (cit. on p. 14).

[Benedikovič 2020] Daniel Benedikovič et al. “Silicon-germanium receivers for short-waveinfrared optoelectronics and communications High-speed silicon-germanium receivers (invited review)”. *Nanophotonics* -1 (Dec. 2020). DOI: 10.1515/nanoph-2020-0547 (cit. on p. 23).

[Bernard 1961] Maurice G. A. Bernard and Georges Duraffourg. "Laser Conditions in Semiconductors". *physica status solidi (b)* 1.7 (1961), pp. 699–703. DOI: https://doi.org/10.1002/pssb.19610010703. eprint: https://onlinelibrary.wiley.com/doi/pdf/10.1002/pssb.19610010703 (cit. on p. 23).

[Bouchereau 2022] Yann Bouchereau et al. "Effect of linewidth enhancement factor on the generation of optical vortices in a class-A degenerate cavity semiconductor laser". *Opt. Express* 30.9 (Apr. 2022), pp. 15648–15658. DOI: 10.1364/OE.456946 (cit. on pp. 9, 12, 35, 53, 64, 65, 67).

[Bouwmans 2000] G. Bouwmans et al. "Modeling coupled microchip lasers requires complex coupling coefficients". *J. Opt. Soc. Am. B* 17.5 (May 2000), pp. 781–789. DOI: 10.1364/JOSAB.17.000781 (cit. on p. 41).

[Burd 2016] S. C. Burd et al. "VECSEL systems for the generation and manipulation of trapped magnesium ions". *Optica* 3.12 (Dec. 2016), pp. 1294–1299. DOI: 10.1364/OPTICA.3.001294 (cit. on p. 3).

[Chen 2011] Chin-Hui Chen et al. "All-optical memory based on injection-locking bistability in photonic crystal lasers". *Opt. Express* 19.4 (Feb. 2011), pp. 3387–3395. DOI: 10.1364/OE.19.003387 (cit. on p. 3).

[Cheng 2017] Ze-Di Cheng et al. "Degenerate cavity supporting more than 31 Laguerre-Gaussian modes". *Opt. Lett.* 42.10 (May 2017), pp. 2042–2045. DOI: 10.1364/OL.42.002042 (cit. on p. 101).

[Chriki 2018] Ronen Chriki et al. "Rapid and efficient formation of propagation invariant shaped laser beams". *Opt. Express* 26.4 (Feb. 2018), pp. 4431–4439. DOI: 10.1364/OE.26.004431 (cit. on pp. 7, 8).

[Consoli 2012] Antonio Consoli et al. "Self-validating technique for the measurement of the linewidth enhancement factor in semiconductor lasers". *Opt. Express* 20.5 (Feb. 2012), pp. 4979–4987. DOI: 10.1364/OE.20.004979 (cit. on pp. 9, 24).

[Cookson 2021a] Tamsin Cookson et al. "Geometric frustration in polygons of polariton condensates creating vortices of varying topological charge". *Nature Communications* 12.1 (Apr. 2021), p. 2120. DOI: 10.1038/s41467-021-22121-3 (cit. on p. 7).

[Cookson 2021b] Tamsin Cookson et al. "Geometric frustration in polygons of polariton condensates creating vortices of varying topological charge". *Nature Communications* 12 (Apr. 2021), p. 2120. DOI: 10.1038/s41467-021-22121-3 (cit. on p. 52).

[DAmato 1989] F X D'Amato, E T Siebert, and C Roychoudhuri. "Coherent operation of an array of diode lasers using a spatial filter in a Talbot cavity". *Applied physics Letters* 55.9 (Dec. 1989), pp. 816–818. DOI: 10.1063/1.101768 (cit. on p. 9).

[Dave 2020] Harshil Dave, Zihe Gao, and Kent Choquette. "Complex coupling coefficient in laterally coupled microcavity laser diode arrays". *Applied Physics Letters* 117 (July 2020), p. 041106. DOI: 10.1063/5.0014468 (cit. on p. 41).

[Davidson 2022] Nir Davidson et al. "Complex-Light Lasers". *Opt. Photon. News* 33.5 (May 2022), pp. 26–33. DOI: 10.1364/OPN.33.5.000026 (cit. on p. 8).

[De 2013a] S S De et al. "Intensity noise correlations in a two-frequency VECSEL". *Optics Express* 21.3 (Feb. 2013), pp. 2538–2550. DOI: 10.1364/oe.21.002538 (cit. on pp. 8, 132, 135, 157).

[De 2013b] Syamsundar De et al. "Theoretical and experimental analysis of intensity noise correlations in an optically pumped, dual-frequency Nd:YAG laser". *Journal of the Optical Society of America B* 30.11 (2013), p. 2830. DOI: 10.1364/josab.30.002830 (cit. on pp. 8, 132).

[De 2015] Syamsundar De et al. "Intensity- and phase-noise correlations in a dual-frequency vertical-external-cavity surface-emitting laser operating at telecom wavelength". *Phys. Rev. A* 91 (5 May 2015), p. 053828. DOI: 10.1103/PhysRevA.91.053828 (cit. on p. 97).

[Dev 2021] Vasu Dev and Vishwa Pal. "Divergence and self-healing of a discrete vortex formed by phase-locked lasers". *Journal of the Optical Society of America B* 38.12 (2021), p. 3683. DOI: 10.1364/josab.440587 (cit. on p. 4).

[Einstein 1917] Albert Einstein. "Zur Quantentheorie der Strahlung". *Phys. Z.* 18 (1917), pp. 121–128 (cit. on p. 14).

[El-Nashar 2009] Hassan F. El-Nashar et al. "Transition to complete synchronization in phase-coupled oscillators with nearest neighbor coupling". *Chaos: An Interdisciplinary Journal of Nonlinear Science* 19.1 (Jan. 2009), p. 013103. DOI: 10.1063/1.3056047. eprint: https://pubs.aip.org/aip/cha/article-pdf/doi/10.1063/1.3056047/13483531/013103_1_online.pdf (cit. on pp. 40, 59, 61).

[Eliezer 2021] Yaniv Eliezer et al. "Suppressing meta-holographic artifacts by laser coherence tuning". *Light: Science & Applications* 10.1 (May 2021), p. 104. DOI: 10.1038/s41377-021-00547-0 (cit. on p. 5).

[Engay 2020] Einstom Engay and Peter John Rodrigo. "Nonlinear optical vortex coronagraph". *Optics Letters* 45.6 (Mar. 2020), pp. 1579–1582. DOI: 10.1364/OL.383311 (cit. on p. 74).

[Erneux 2010] T. Erneux and P. Glorieux. *Laser Dynamics*. Cambridge University Press, 2010 (cit. on pp. 27, 37, 39, 89).

[Eshaghi 2021] Mahdi Eshaghi and Aristide Dogariu. "Phase Memory of Optical Vortex Beam Scattered by Random Phase Screens". *2021 IEEE Photonics Society Summer Topicals Meeting Series (SUM)*. 2021, pp. 1–2. DOI: 10.1109/SUM48717.2021.9505869 (cit. on p. 74).

[Fabiny 1993] Larry Fabiny et al. "Coherence and phase dynamics of spatially coupled solid-state lasers". *Phys. Rev. A* 47 (5 May 1993), pp. 4287–4296. DOI: 10.1103/PhysRevA.47.4287 (cit. on p. 40).

[Fan 2021] Haihao Fan et al. "Flower-Shaped Optical Vortex Array". *Annalen der Physik* 533.4 (2021), p. 2000575. DOI: https://doi.org/10.1002/andp.202000575 (cit. on p. 58).

[Flunkert 2011] Valentin Flunkert. "Lang Kobayashi Laser Equations". *Delay-Coupled Complex Systems: and Applications to Lasers*. Berlin, Heidelberg: Springer Berlin Heidelberg, 2011, pp. 111–119. DOI: 10.1007/978-3-642-20250-6_11 (cit. on p. 89).

[Fordell 2007] Thomas Fordell and Asa Marie Lindberg. "Experiments on the Linewidth-Enhancement Factor of a Vertical-Cavity Surface-Emitting Laser". *IEEE Journal of Quantum Electronics* 43.1 (2007), pp. 6–15. DOI: 10.1109/JQE.2006.884583 (cit. on pp. 9, 24).

[Fridman 2010a] Moti Fridman et al. "Passive phase locking of 25 fiber lasers". *Optics letters* 35.9 (May 2010), pp. 1434–1436. DOI: 10.1364/ol.35.001434 (cit. on p. 8).

[Fridman 2010b] Moti Fridman et al. "Phase locking of two coupled lasers with many longitudinal modes". *Optics letters* 35.4 (Feb. 2010), pp. 526–528. DOI: 10.1364/ol.35.000526 (cit. on p. 8).

[Friesem 2013] A A Friesem et al. "Efficient method for controlling the spatial coherence of a laser". *Optics letters* 38.19 (Oct. 2013), pp. 3858–3861. DOI: 10.1364/ol.38.003858 (cit. on p. 9).

[Gao 2018] Zihe Gao et al. "The Complex Coupling Coefficient of Coherent VCSEL Arrays". Sept. 2018, pp. 1–2. DOI: 10.1109/ISLC.2018.8516184 (cit. on p. 41).

[Genevet 2009] Patrice Genevet et al. "Stationary localized structures and pulsing structures in a cavity soliton laser". *Physical Review A : Atomic, molecular, and optical physics [1990-2015]* (2009), p. 033819 (cit. on p. 5).

[Genevet 2010] Patrice Genevet et al. "Bistable and Addressable Localized Vortices in Semiconductor Lasers". *Physical review letters* 104 (June 2010), p. 223902. DOI: 10.1103/PhysRevLett.104.223902 (cit. on p. 91).

[Gershenzon 2020] Igor Gershenzon et al. *Nanophotonics* 9.13 (2020), pp. 4117–4126. DOI: doi:10.1515/nanoph-2020-0137 (cit. on p. 156).

[Glova 2003] A F Glova. "Phase locking of optically coupled lasers". *Quantum Electronics* 33.4 (Apr. 2003), p. 283. DOI: 10.1070/QE2003v033n04ABEH002415 (cit. on pp. 2, 9, 31, 35, 37, 39).

[Gould 2017] Travis J. Gould et al. "STED Microscopy". *Fluorescence Microscopy*. John Wiley & Sons, Ltd, 2017. Chap. 10, pp. 321–338. DOI: https://doi.org/10.1002/9783527687732.ch10. eprint: https://onlinelibrary.wiley.com/doi/pdf/10.1002/9783527687732.ch10 (cit. on p. 74).

[Gredat 2018] Gregory Gredat et al. "Fully–correlated multi–mode pumping for low–noise dual–frequency VECSELs". *Optics Express* 26.20 (2018), pp. 26217–26226. DOI: 10.1364/oe.26.026217 (cit. on pp. 8, 132).

[Gredat 2019a] G. Gredat, H. Liu, and F. Bretenaker. "Thermal phase fluctuations in optically pumped dual-frequency vertical external-cavity surface-emitting lasers for cesium clocks based on coherent population trapping". *Journal of Applied Physics* 126.17 (Nov. 2019), p. 173104. DOI: 10.1063/1.5123444. eprint: https://pubs.aip.org/aip/jap/article-pdf/doi/10.1063/1.5123444/15235315/173104_1_online.pdf (cit. on p. 99).

[Gredat 2019b] Gregory Gredat, Hui Liu, and Fabien Bretenaker. "Thermal Noise in Optically Pumped DF-VECSELs". *2019 Conference on Lasers and Electro-Optics Europe & European Quantum Electronics Conference*. 2019, pp. 1–1. DOI: 10.1109/CLEOE-EQEC.2019.8872538 (cit. on p. 132).

[Gredat 2020a] Grégory Gredat. "Propriétés de bruit et dynamique de lasers à semiconducteurs en régime d'émission bifréquence pour l'optique micro-ondes et la métrologie". Theses. Université Paris-Saclay, June 2020 (cit. on p. 22).

[Gredat 2020b] Gregory Gredat et al. "Optimization of laser dynamics for active stabilization of DF-VECSELs dedicated to cesium CPT clocks". *Journal of the Optical Society of America B-Optical Physics* 37.4 (2020), pp. 1196–12. DOI: 10.1364/josab.389310 (cit. on pp. 8, 132).

[Grobe 2014] Klaus Grobe et al. "Access Networks Based on Tunable Lasers". *J. Lightwave Technol.* 32.16 (Aug. 2014), pp. 2815–2823 (cit. on p. 3).

[Grundmann 2016] Marius Grundmann. "Band Structure". *The Physics of Semiconductors: An Introduction Including Nanophysics and Applications*. Cham: Springer International Publishing, 2016, pp. 153–201. DOI: 10.1007/978-3-319-23880-7_6 (cit. on p. 18).

[Gu 2014] Min Gu, Xiangping Li, and Yaoyu Cao. "Optical storage arrays: a perspective for future big data storage". *Light: Science & Applications* 3.5 (May 2014), e177–e177. DOI: 10.1038/lsa.2014.58 (cit. on p. 3).

[Guina 2017a] M Guina, A Rantamäki, and A Härkönen. "Optically pumped VECSELs: review of technology and progress". *Journal of Physics D: Applied Physics* 50.38 (Aug. 2017), p. 383001. DOI: 10.1088/1361-6463/aa7bfd (cit. on pp. 14, 15, 21, 97).

[Guina 2017b] Mircea Guina, Antti Rantamäki, and A Härkönen. "Optically pumped VECSELs: Review of technology and progress". *Journal of Physics D: Applied Physics* 50 (Sept. 2017), p. 383001. DOI: 10.1088/1361-6463/aa7bfd (cit. on p. 100).

[Guo 2023] Pan Guo and Sha Wang. "Structured Light Laser Based on Intra-Cavity Modulation". *Photonics* 10.1 (2023). DOI: 10.3390/photonics10010001 (cit. on p. 7).

[Gurevich 2024] S. V. Gurevich, F. Maucher, and J. Javaloyes. "Aberration-driven tilted emission in degenerate cavities". *Phys. Rev. Res.* 6 (1 Feb. 2024), p. 013166. DOI: 10.1103/PhysRevResearch.6.013166 (cit. on p. 109).

[Hachair 2008] X. Hachair et al. "Transverse spatial structure of a high Fresnel number Vertical External Cavity Surface Emitting Laser". *Opt. Express* 16.13 (June 2008), pp. 9519–9527. DOI: 10.1364/OE.16.009519 (cit. on pp. 101, 112, 113).

[Harshith 2019] B. S. Harshith and G. K. Samanta. "Controlled generation of array beams of higher order orbital angular momentum and study of their frequency-doubling characteristics". *Scientific Reports* 9.1 (July 2019), p. 10916. DOI: 10.1038/s41598-019-47403-1 (cit. on p. 74).

[Henry 1982] C. Henry. "Theory of the linewidth of semiconductor lasers". *IEEE Journal of Quantum Electronics* 18.2 (1982), pp. 259–264. DOI: 10.1109/JQE.1982.1071522 (cit. on pp. 23, 24).

[Iga 1988] K. Iga, F. Koyama, and S. Kinoshita. "Surface emitting semiconductor lasers". *IEEE Journal of Quantum Electronics* 24.9 (1988), pp. 1845–1855. DOI: 10.1109/3.7126 (cit. on p. 14).

[Ikonnikov 2020] Denis A. Ikonnikov et al. "Two-dimensional Talbot effect of the optical vortices and their spatial evolution". *Scientific Reports* 10.1 (Nov. 2020), p. 20315. DOI: 10.1038/s41598-020-77418-y (cit. on p. 74).

[Kapon 1984] E Kapon, J Katz, and A Yariv. "Supermode analysis of phase-locked arrays of semiconductor lasers". *Optics letters* 9.4 (Jan. 1984), pp. 125–127. DOI: 10.1364/ol.9.000125 (cit. on p. 8).

[Karuseichyk 2023] Sopfy Karuseichyk et al. “Investigation of noise correlations in the phase-locked class-A VECSEL array”. *Opt. Express* 31.25 (Dec. 2023), pp. 41713–41725. DOI: 10.1364/OE.501051 (cit. on pp. 12, 41).

[Kemp 2006] A. J. Kemp et al. “Thermal lensing, thermal management and transverse mode control in microchip VECSELs”. *Applied Physics B* 83.2 (May 2006), pp. 189–194. DOI: 10.1007/s00340-006-2151-z (cit. on p. 99).

[Khanin 2006] I.A.I. Khanin. *Fundamentals of Laser Dynamics*. Cambridge International Science Publishing, 2006 (cit. on p. 24).

[Kittel 2004] C. Kittel. *Introduction to Solid State Physics*. Wiley, 2004 (cit. on p. 18).

[Knitter 2016] Sebastian Knitter et al. “Coherence switching of a degenerate VECSEL for multimodality imaging”. *Optica* 3.4 (Apr. 2016), pp. 403–406. DOI: 10.1364/OPTICA.3.000403 (cit. on pp. 5, 114, 115).

[Kotlyar 2016] V. V. Kotlyar, A. A. Kovalev, and A. P. Porfirev. “An optical tweezer in asymmetrical vortex Bessel-Gaussian beams”. *Journal of Applied Physics* 120.2 (July 2016), p. 023101. DOI: 10.1063/1.4958309 (cit. on p. 86).

[Kovalev 2016] Alexey A. Kovalev, Victor V. Kotlyar, and Alexey P. Porfirev. “Optical trapping and moving of microparticles by using asymmetrical Laguerre–Gaussian beams”. *Opt. Lett.* 41.11 (June 2016), pp. 2426–2429. DOI: 10.1364/OL.41.002426 (cit. on p. 86).

[Kovalev 2021] A. A. Kovalev and V. V. Kotlyar. “Propagation-invariant laser beams with an array of phase singularities”. *Physical Review A* 103 (6 June 2021), p. 063502. DOI: 10.1103/PhysRevA.103.063502 (cit. on p. 74).

[Kuwashima 2001] Fumiyoshi Kuwashima, Iwao Kitazima, and Hiroshi Iwasawa. “Theory of Chaotic Dynamics on Class A Laser with Optical Delayed Feedback”. *Japanese Journal of Applied Physics* 40.2R (Feb. 2001), p. 601. DOI: 10.1143/JJAP.40.601 (cit. on pp. 26, 89).

[Larisch 2020] Gunter Larisch, Sicong Tian, and Dieter Bimberg. “Optimization of VCSEL photon lifetime for minimum energy consumption at varying bit rates”. *Opt. Express* 28.13 (June 2020), pp. 18931–18937. DOI: 10.1364/OE.391781 (cit. on p. 29).

[Lau 2008] Erwin K. Lau et al. "Strong optical injection-locked semiconductor lasers demonstrating > 100-GHz resonance frequencies and 80-GHz intrinsic bandwidths". *Opt. Express* 16.9 (Apr. 2008), pp. 6609–6618. DOI: 10.1364/OE.16.006609 (cit. on pp. 3, 8).

[Laurain 2009] A. Laurain et al. "High power single–frequency continuously–tunable compact extended–cavity semiconductor laser". *Opt. Express* 17.12 (June 2009), pp. 9503–9508. DOI: 10.1364/OE.17.009503 (cit. on p. 99).

[Li 2018] Lin Li et al. "Generation of optical vortex array along arbitrary curvilinear arrangement". *Optic Express* 26.8 (Apr. 2018), pp. 9798–9812. DOI: 10.1364/OE.26.009798 (cit. on p. 74).

[Liu 2018a] Hui Liu et al. "Noise Investigation of a Dual-Frequency VECSEL for Application to Cesium Clocks". *Journal of Lightwave Technology* 36.18 (July 2018), pp. 3882–3891. DOI: 10.1109/jlt.2018.2852061 (cit. on pp. 8, 132).

[Liu 2018b] Hui Liu et al. "Ultra-low noise dual-frequency VECSEL at telecom wavelength using fully correlated pumping". *Opt. Lett.* 43.8 (Apr. 2018), pp. 1794–1797. DOI: 10.1364/OL.43.001794 (cit. on p. 97).

[Ma 2022] Yanhong Ma et al. "Phase-locking dynamics of a 2D VCSEL hexagonal array with an integrated Talbot cavity". *Opt. Express* 30.6 (Mar. 2022), pp. 9892–9903. DOI: 10.1364/OE.452548 (cit. on pp. 31, 34).

[Mahler 2019a] Simon Mahler et al. "Coupling of laser arrays with intracavity elements in the far-field". *OSA Continuum* 2.6 (June 2019), pp. 2077–2084. DOI: 10.1364/OSAC.2.002077 (cit. on pp. 7, 8).

[Mahler 2019b] Simon Mahler et al. "Dynamics of dissipative topological defects in coupled phase oscillators". *Journal of Physics B: Atomic, Molecular and Optical Physics* 52.20 (Sept. 2019), p. 205401. DOI: 10.1088/1361-6455/ab3d00 (cit. on p. 74).

[Mahler 2021] Simon Mahler et al. "Fast laser speckle suppression with an intracavity diffuser". *Nanophotonics* 10.1 (2021), pp. 129–136. DOI: doi:10.1515/nanoph-2020-0390 (cit. on pp. 8, 124).

[Mehuys 1991] David Mehuys et al. "Modal analysis of linear Talbot-cavity semiconductor lasers". *Opt. Lett.* 16.11 (June 1991), pp. 823–825. DOI: 10.1364/OL.16.000823 (cit. on p. 31).

[Miri 2023] Mohammad-Ali Miri and Vinod Menon. "Neural computing with coherent laser networks". *Nanophotonics* 12.5 (2023), pp. 883–892. DOI: doi:10.1515/nanoph-2022-0367 (cit. on p. 4).

[Mitsugi 2002] Satoshi Mitsugi et al. "Microoptical Two-Dimensional Devices for the Optical Memory Head of an Ultrahigh Data Transfer Rate and Density Sytem Using a Vertical Cavity Surface Emitting Laser (VCSEL) Array". *Japanese Journal of Applied Physics* 41 (July 2002), pp. 4835–4840. DOI: 10.1143/JJAP.41.4835 (cit. on p. 3).

[Myara 2013] Mikhaël Myara et al. "Noise properties of NIR and MIR VeCSELs". *Proceedings of SPIE - The International Society for Optical Engineering* 8606 (Feb. 2013). DOI: 10.1117/12.1000329 (cit. on p. 132).

[Nixon 2011] M. Nixon et al. "Enhanced coherence of weakly coupled lasers". *Opt. Lett.* 36.8 (Apr. 2011), pp. 1320–1322. DOI: 10.1364/OL.36.001320 (cit. on pp. 4, 39).

[Nixon 2012] Micha Nixon et al. "Controlling Synchronization in Large Laser Networks". *Phys. Rev. Lett.* 108 (21 May 2012), p. 214101. DOI: 10.1103/PhysRevLett.108.214101 (cit. on p. 8).

[Nixon 2013a] M. Nixon et al. "Efficient method for controlling the spatial coherence of a laser". *Opt. Lett.* 38.19 (Oct. 2013), pp. 3858–3861. DOI: 10.1364/OL.38.003858 (cit. on p. 101).

[Nixon 2013b] Micha Nixon et al. "Observing Geometric Frustration with Thousands of Coupled Lasers". *Physical Review Letters* 110 (18 May 2013), p. 184102. DOI: 10.1103/PhysRevLett.110.184102 (cit. on pp. 4, 74).

[Pabœuf 2011] David Pabœuf et al. "Volume Bragg grating external cavities for the passive phase locking of high-brightness diode laser arrays: theoretical and experimental study". *J. Opt. Soc. Am. B* 28.5 (May 2011), pp. 1289–1299. DOI: 10.1364/JOSAB.28.001289 (cit. on p. 8).

[Pal 2015] Vishwa Pal et al. “Phase locking of even and odd number of lasers on a ring geometry: Effects of topological-charge”. *Optics Express* 23.10 (Jan. 2015), pp. 13041–13050. DOI: 10.1364/oe.23.013041 (cit. on pp. 4, 32, 52, 84).

[Pal 2017] Vishwa Pal et al. “Observing Dissipative Topological Defects with Coupled Lasers”. *Physical Review Letters* 119.1 (July 2017), pp. 013902–5. DOI: 10.1103/physrevlett.119.013902 (cit. on pp. 4, 52, 53, 74, 81).

[Pal 2020] Vishwa Pal et al. “Rapid fair sampling of the XY spin Hamiltonian with a laser simulator”. *Physical Review Research* 2 (July 2020). DOI: 10.1103/PhysRevResearch.2.033008 (cit. on pp. 4, 144, 156).

[Pando 2023] Amit Pando et al. “Improved laser phase locking with intra-cavity adaptive optics”. *Opt. Express* 31.4 (Feb. 2023), pp. 6947–6955. DOI: 10.1364/OE.482196 (cit. on p. 8).

[Pedaci 2006] F. Pedaci et al. “Positioning cavity solitons with a phase mask”. *Applied Physics Letters* 89.22 (Nov. 2006), p. 221111. DOI: 10.1063/1.2388867. eprint: https://pubs.aip.org/aip/apl/article-pdf/doi/10.1063/1.2388867/14362188/221111_1_online.pdf (cit. on p. 5).

[Pedaci 2008] F. Pedaci et al. “All-optical delay line using semiconductor cavity solitons”. *Applied Physics Letters* 92.1 (Jan. 2008), p. 011101. DOI: 10.1063/1.2828458. eprint: https://pubs.aip.org/aip/apl/article-pdf/doi/10.1063/1.2828458/14386742/011101_1_online.pdf (cit. on p. 5).

[Petermann 1991] K. Petermann. *Laser Diode Modulation and Noise*. Springer, 1991 (cit. on p. 8).

[Piccardo 2022] Marco Piccardo et al. “Vortex laser arrays with topological charge control and self-healing of defects”. *Nature Photonics* 16.5 (May 2022), pp. 359–365. DOI: 10.1038/s41566-022-00986-0 (cit. on p. 7).

[Rafferty 2021] Aidan Rafferty and Thomas C. Preston. “Trapping positions in a dual-beam optical trap”. *Journal of Applied Physics* 130.18 (2021), p. 183105. DOI: 10.1063/5.0068183 (cit. on p. 74).

[Raja 1989] M.Y.A. Raja et al. "Resonant periodic gain surface-emitting semiconductor lasers". *IEEE Journal of Quantum Electronics* 25.6 (1989), pp. 1500–1512. DOI: 10.1109/3.29287 (cit. on p. 15).

[Reddy 2022] Andra Naresh Kumar Reddy et al. "Phase locking of lasers with Gaussian coupling". *Opt. Express* 30.2 (Jan. 2022), pp. 1114–1129. DOI: 10.1364/OE.439957 (cit. on p. 8).

[Rogister 2009] Fabien Rogister. *Nonlinear Dynamics of Semiconductor Lasers Subject to Optical Feedback*. 2009. DOI: 10.48550/ARXIV.0909.4449 (cit. on p. 89).

[Saxena 2022] Dhruv Saxena et al. "Sensitivity and spectral control of network lasers". *Nature Communications* 13 (Oct. 2022). DOI: 10.1038/s41467-022-34073-3 (cit. on p. 4).

[Seghilani 2016] Mohamed S. Seghilani et al. "Vortex Laser based on III-V semiconductor metasurface: direct generation of coherent Laguerre-Gauss modes carrying controlled orbital angular momentum". *Scientific Reports* 6.1 (Dec. 2016), p. 38156. DOI: 10.1038/srep38156 (cit. on pp. 7, 74).

[Shen 2019] Yijie Shen et al. "Optical vortices 30 years on: OAM manipulation from topological charge to multiple singularities". *Light: Science & Applications* 8.1 (Oct. 2019), p. 90. DOI: 10.1038/s41377-019-0194-2 (cit. on p. 74).

[Shen 2021] Zhe Shen et al. "Optical spanner for nanoparticle rotation with focused optical vortex generated through a Pancharatnam–Berry phase metalens". *Applied Optics* 60.16 (June 2021), pp. 4820–4826. DOI: 10.1364/AO.425892 (cit. on p. 74).

[Sheng 2022] Quan Sheng et al. "Intracavity spherical aberration for selective generation of single-transverse-mode Laguerre-Gaussian output with order up to 95". *PhotoniX* 3.1 (Feb. 2022), p. 4. DOI: 10.1186/s43074-022-00050-8 (cit. on p. 111).

[Siegman 1986] A.E. Siegman. *Lasers*. G - Reference,Information and Interdisciplinary Subjects Series. University Science Books, 1986 (cit. on pp. 27, 33, 37, 39, 102, 103, 106).

[Silber 1993] Mary Silber, Larry Fabiny, and Kurt Wiesenfeld. "Stability results for in-phase and splay-phase states of solid-state laser arrays". *J. Opt. Soc. Am. B* 10.6 (June 1993), pp. 1121–1129. DOI: 10.1364/JOSAB.10.001121 (cit. on p. 40).

[Singh 2023] Sumit Kumar Singh et al. “Tailoring Large Asymmetric Laguerre-Gaussian Beam Array Using Computer-Generated Holography”. *Photonics* 10.3 (2023). DOI: 10.3390/photonics10030247 (cit. on p. 86).

[Sinquin 2023] Brian Sinquin and Marco Romanelli. “Determination of the linewidth enhancement factor of semiconductor lasers by complete optical field reconstruction”. *Opt. Lett.* 48.4 (Feb. 2023), pp. 863–866. DOI: 10.1364/OL.483776 (cit. on pp. 9, 24).

[Spitz 2021] Olivier Spitz et al. “Private communication with quantum cascade laser photonic chaos”. *Nature Communications* 12.1 (June 2021), p. 3327. DOI: 10.1038/s41467-021-23527-9 (cit. on p. 2).

[Spitz 2022] O. Spitz et al. “Characterization of Optical Chaos in Mid-Infrared Interband Cascade Lasers: Towards High-Speed Free-Space Applications”. *Optica Advanced Photonics Congress 2022*. Optica Publishing Group, 2022, NpW2F.2. DOI: 10.1364/NP.2022.NpW2F.2 (cit. on p. 2).

[Stohs 2001] J. Stohs et al. “Gain, refractive index change, and linewidth enhancement factor in broad-area GaAs and InGaAs quantum-well lasers”. *IEEE Journal of Quantum Electronics* 37.11 (2001), pp. 1449–1459. DOI: 10.1109/3.958374 (cit. on pp. 9, 24).

[Takata 2012] Kenta Takata, Shoko Utsunomiya, and Yoshihisa Yamamoto. “Transient time of an Ising machine based on injection-locked laser network”. *New Journal of Physics* 14.1 (2012), p. 013052. DOI: 10.1088/1367-2630/14/1/013052 (cit. on p. 4).

[Takata 2014] Kenta Takata and Yoshihisa Yamamoto. “Data search by a coherent Ising machine based on an injection-locked laser network with gradual pumping or coupling”. *Physical Review A* 89.3 (2014), p. 032319. DOI: 10.1103/physreva.89.032319 (cit. on p. 4).

[Takata 2016] Kenta Takata et al. “A 16-bit Coherent Ising Machine for One-Dimensional Ring and Cubic Graph Problems”. *Scientific Reports* 6.1 (Sept. 2016), p. 34089. DOI: 10.1038/srep34089 (cit. on p. 4).

[Tartwijk 1995] G H M van Tartwijk and D Lenstra. "Semiconductor lasers with optical injection and feedback". *Quantum and Semiclassical Optics: Journal of the European Optical Society Part B* 7.2 (Apr. 1995), pp. 87–143. DOI: 10.1088/1355-5111/7/2/003 (cit. on p. 89).

[Thorette 2017] Aurélien Thorette, Marco Romanelli, and Marc Vallet. "Linewidth enhancement factor measurement based on FM-modulated optical injection: application to rare-earth-doped active medium". *Opt. Lett.* 42.8 (Apr. 2017), pp. 1480–1483. DOI: 10.1364/OL.42.001480 (cit. on pp. 9, 24).

[Tradonsky 2017] Chene Tradonsky et al. "Talbot diffraction and Fourier filtering for phase locking an array of lasers". *Appl. Opt.* 56.1 (Jan. 2017), A126–A132. DOI: 10.1364/AO.56.00A126 (cit. on pp. 8, 32).

[Tradonsky 2019] C. Tradonsky et al. "Rapid laser solver for the phase retrieval problem". *Science Advances* 5.10 (2019), eaax4530. DOI: 10.1126/sciadv.aax4530. eprint: https://www.science.org/doi/pdf/10.1126/sciadv.aax4530 (cit. on pp. 4, 7, 8, 144).

[Tradonsky 2021] Chene Tradonsky et al. "High-resolution digital spatial control of a highly multimode laser". *Optica* 8.6 (June 2021), pp. 880–884. DOI: 10.1364/OPTICA.423140 (cit. on p. 7).

[Vigne 2022] Nathan Vigne et al. "Non-linear structured light in a self-imaging laser cavity based on III-V semiconductor nanotechnology". *SPIE Photonics Europe*. Vol. 12141. Semiconductor Lasers and Laser Dynamics X. SPIE. Strasbourg, France: SPIE, Apr. 2022, p. 121410I. DOI: 10.1117/12.2621135 (cit. on p. 113).

[Vigne 2023] N. Vigne et al. "Spatially Localized Structures in a Self-Imaging Semiconductor Laser Cavity: Diffraction and Complex Non-linearity Management". *2023 Conference on Lasers and Electro-Optics Europe & European Quantum Electronics Conference (CLEO/Europe-EQEC)*. 2023, pp. 1–1. DOI: 10.1109/CLEO/Europe-EQEC57999.2023.10232525 (cit. on p. 6).

[Wang 2016] Jian Wang. *Advances in communications using optical vortices*. Oct. 2016. DOI: 10.1364/PRJ.4.000B14 (cit. on p. 74).

[Wang 2022] Xiaofan Wang et al. "Dynamics of mutual injection phase-locking of laser diode array with interference effect". *Optics Communications* 522 (2022), p. 128616. DOI: https://doi.org/10.1016/j.optcom.2022.128616 (cit. on p. 8).

[Wieczorek 2005] S. Wieczorek et al. "The dynamical complexity of optically injected semiconductor lasers". *Physics Reports* 416.1 (2005), pp. 1–128. DOI: https://doi.org/10.1016/j.physrep.2005.06.003 (cit. on p. 25).

[Winful 1988] H G Winful and S S Wang. "Stability of phase locking in coupled semiconductor laser arrays". *Applied physics Letters* 53.20 (Dec. 1988), pp. 1894–1896. DOI: 10.1063/1.100363 (cit. on p. 8).

[Xiang 2022] Zhiyuan Xiang, Zhe Shen, and Yaochun Shen. "Quasi-perfect vortices generated by Pancharatnam-Berry phase metasurfaces for optical spanners and OAM communication". *Scientific Reports* 12.1 (Jan. 2022), p. 1053. DOI: 10.1038/s41598-022-05017-0 (cit. on p. 74).

[Yang 2022] Qingshuai Yang et al. "Ultra-secure optical encryption based on tightly focused perfect optical vortex beams". *Nanophotonics* (2022). DOI: doi:10.1515/nanoph-2021-0786 (cit. on p. 74).

[Yefet 2013] Shai Yefet and Avi Pe'er. "A Review of Cavity Design for Kerr Lens Mode-Locked Solid-State Lasers". *Applied Sciences* 3.4 (2013), pp. 694–724. DOI: 10.3390/app3040694 (cit. on pp. 104, 106).

[Zhou 2018] Xiaoming Zhou et al. "Experimental investigation on optical vortex tweezers for microbubble trapping". *Open Physics* 16.1 (July 2018), pp. 383–386. DOI: 10.1515/phys-2018-0052 (cit. on p. 74).

[Zilkie 2008] Aaron J. Zilkie et al. "Time-Resolved Linewidth Enhancement Factors in Quantum Dot and Higher-Dimensional Semiconductor Amplifiers Operating at 1.55 μm". *J. Lightwave Technol.* 26.11 (June 2008), pp. 1498–1509 (cit. on pp. 9, 24).